Northumbria Research Link

Citation: Doyle, Lauren (2020) Solar and stellar flares and their connection. Doctoral thesis, Northumbria University.

This version was downloaded from Northumbria Research Link: http://nrl.northumbria.ac.uk/id/eprint/43890/

Northumbria University has developed Northumbria Research Link (NRL) to enable users to access the University's research output. Copyright © and moral rights for items on NRL are retained by the individual author(s) and/or other copyright owners. Single copies of full items can be reproduced, displayed or performed, and given to third parties in any format or medium for personal research or study, educational, or not-for-profit purposes without prior permission or charge, provided the authors, title and full bibliographic details are given, as well as a hyperlink and/or URL to the original metadata page. The content must not be changed in any way. Full items must not be sold commercially in any format or medium without formal permission of the copyright holder. The full policy is available online: http://nrl.northumbria.ac.uk/policies.html

Northumbria University NEWCASTLE

University Library

Northumbria University
NEWCASTLE

SOLAR AND STELLAR FLARES AND THEIR CONNECTION

L. DOYLE

PhD

2020

SOLAR AND STELLAR FLARES AND THEIR CONNECTION

LAUREN DOYLE

A thesis submitted in partial fulfilment of the requirements of the University of Northumbria at Newcastle for the degree of Doctor of Philosophy

Research undertaken in the Faculty of Mathematics, Physics and Electrical Engineering

July 2020

For my Mum and Dad, who gave me my love
for the stars.

Publications

Below are a list of publications (including hyperlinks) and conference proceedings which resulted from work presented in this thesis, including those which are in preparation or have been submitted. All of these publications form chapters within this thesis where the details are stated at the beginning of each chapter.

Doyle L., Ramsay G., Doyle J. G., Wu K., Scullion E., (2018), *Investigating the Rotational Phase of Stellar Flares on M dwarfs using K2 Short Cadence Data*, MNRAS, 480, 2153 – 2164

Doyle L., Ramsay G., Doyle J. G., Wu K., (2019), *Probing the Origin of Stellar Flares on M dwarfs Using TESS Sectors 1 - 3*, MNRAS, 489, 437 – 445

Doyle L., Wyper P., Sculion E. et al., (2019), *Multi-wavelength Observations and 3D MHD Modeling of a Confined Helical Jet Launched by the Eruption of a Filament*, ApJ, 887 (2), 246 The associated movies to the figures in Chapter 3 can be found at the above hyperlink or the following link: https://iopscience.iop.org/article/10.3847/1538-4357/ab5d39.

Doyle L., Ramsay G., Doyle J. G., (2020), *Superflares and Stellar Variability on Solar-Type Stars Using TESS*, MNRAS, 494(3), 3596-3610

Conference proceedings based on oral presentations given at conferences during my PhD.

Doyle L., Ramsay G., Doyle J. G., (2018), *Searching for the Origin of Flares in M dwarfs*, The 20th Cambridge Workshop on Cool Stars, Stellar Systems, and the Sun, Boston, USA, arXiv:1811.06594

Doyle L., et al., (2019), *Exploring Flaring Behaviour on Low Mass Stars, Solar-type Stars and the Sun*, IAU Symposium 354: Solar and Stellar Magnetic Fields, Copiapo, Chile, (in press)

Publications which have been submitted for review.

Ramsay, G., Doyle, J. G., **Doyle, L.**, (2020), *TESS Observations of Southern Ultra Fast Rotating Low Mass Stars*, Accepted for publication in MNRAS (in press)

Abstract

This thesis focuses on bridging the gap between solar and stellar physics through the study of flares. Solar flares are the most powerful explosions in the solar system and many stellar flares have been observed to be orders of magnitudes larger. However, is not yet known if these phenomena are formed through the same physical process. In this thesis we explore their common origins through a detailed case study of a solar flare and a robust statistical analysis of stellar flares with bespoke observations. Using data from the Swedish Solar Telescope, a detailed study of a solar flare associated with a filament eruption and jet was compared with advanced 3D MHD simulations. This amalgamation of observation and theory allows for a complete picture of the event including the pre-flare magnetic structure and the resulting kinematics of the jet post eruption. Overall, this study aims to characterise the physical environment capturing many evolutionary properties of the event providing a unique perspective on eruptive phenomena on the Sun.

With regards to stellar flares, observational data from both K2 and TESS are used to conduct a statistical analysis on flares from both low mass and solar-type stars. As a result of this, no relationship between the rotational phase of stellar flares and starspots is present. This was unexpected as there is a well-established relationship between solar flares and sunspots. This result yields potential implications for how the magnetic field in fully convective low mass stars is generated. Possibly, this result implies the surface of these stars is more complex than the Sun. Furthermore, groups of rapidly fast rotating low mass and solar-type stars were discovered to exhibit very little flaring activity. This is unusual, as rotation is linked to a star's dynamo mechanism and so faster rotating stars are expected to show higher levels of activity.

This research has raised new questions surrounding the underpinning mechanisms driving stellar flares. In an effort to address this the solar 3D MHD simulation is scaled up to replicate flare energies seen in the observed stellar flares. This comparative analysis allows for the exploration of the flare mechanism and potential magnetic structure on these stars, which will be a subject of future research, in order to explain such high energy flares.

Contents

List of Figures

List of Tables

Acknowledgements

Over the course of my PhD, I have received help and support from many friends, family and colleagues. Firstly, I must extend a thank you to my supervisors at Armagh, Dr. Gavin Ramsay and Prof. Gerry Doyle. Their encouragement, guidance and support throughout the past three and a half years has been extremely appreciated. I would not have been as successful or had as many opportunities during my PhD without them and I am incredibly grateful to have had them as my supervisors.

I would also like to thank my two supervisors at Northumbria University, Dr. Eamon Scullion and Prof. James McLaughlin. I always looked forward to my Skype calls and visits to Newcastle and overall, their experience and knowledge of solar physics has really helped me. It has been a pleasure to be a part of the solar physics group at Northumbria University, where I have really felt like part of the team. I must also thank my collaborator Dr. Peter Wyper where without his solar modelling knowledge a comparison between the solar and stellar aspects of my thesis would not have been possible.

I cannot forget all of my fellow students at Armagh Observatory and Northumbria University who were a vital support network throughout my PhD. A special mention must go out to my office mate Erin Higgins. We have supported each other through the whole journey and I could not have asked for a better office mate or friend.

Next, I have to thank all of my family and friends but especially my Mum and Dad, whom this thesis is dedicated to. They have always taught me to believe I can do anything and I would not be where I am today without them. Dad, thank you for buying me that space book all those years ago, now I'm writing one of my own.

Finally, a massive thank you goes to my partner Fraser. We started our academic journeys together as first year students in Glasgow and he has always encouraged and supported me in whatever I do. I would not have been able to do this without him and I really appreciate all the coding help, travelling to conferences with me and even reading the full thesis for mistakes. Hopefully you have learned something about stars and flares in all these years.

Declaration

I declare that the work contained in this thesis has not been submitted for any other award and that it is all my own work. I also confirm that this work fully acknowledges opinions, ideas and contributions from the work of others. The work was done in collaboration with the following: Dr Eamon Scullion (Northumbria University), Prof James McLaughlin (Northumbria University), Dr Gavin Ramsay (Armagh Observatory), Prof J. Gerry Doyle (Armagh Observatory), Dr Peter Wyper (Durham University) and Dr Kinwah Wu (Mullard Space Science Laboratory).

Any ethical clearance for the research presented in this thesis has been approved. Approval has been sought and granted by the University Ethics Committee on 22nd August 2017.

I declare that the Word Count of this thesis is 44,384 words.

Name: Lauren Doyle

Signature:

Date: 10 July 2020

1 Introduction

The Sun has been observed, studied and even worshipped for many centuries with the first records of early attempts to understand our nearest star dating back to 3300 BC (Tayler, 1997). The Sun is critical for life and our existence here on Earth and plays an important role in everyday life, signifying the beginning and end of each day. Today, the Sun is continuously observed and the knowledge gained from studying its many phenomena forms the basis for the understanding of other stars in the solar neighbourhood.

Over the years, solar and stellar flare research have each progressed in isolation with many solar flares being observed from radio through visible and infra-red to X-ray wavelengths, whereas stellar flares are mainly observed in white light. More recently, there have been observations of stellar flares in X-ray and radio wavelengths, however, with missions such as *Kepler* and *TESS* optical observations of stellar flares are more frequent and easier to access. One of the key reasons why activity, including solar flares, from our Sun is studied in such great detail is due to the implications these events can have on Earth. In fact, the effects of solar flares, coronal mass ejections and the solar wind can be seen through the entire solar system and so understanding these events is important. Additionally, a particularly large solar flare which is directed towards Earth can have consequences for satellites' functionality, including GPS and power grid failure and even impact upon health and safety astronauts.

Overall, as the Sun is our nearest star it offers a great opportunity to study the phenomena of sunspots and flares in a manner which is not possible on other stars. It is through these studies that we can gain a much greater insight into solar flares, gaining a deeper understanding of the processes and activity on other stars and the effects it can have on potential exoplanetary

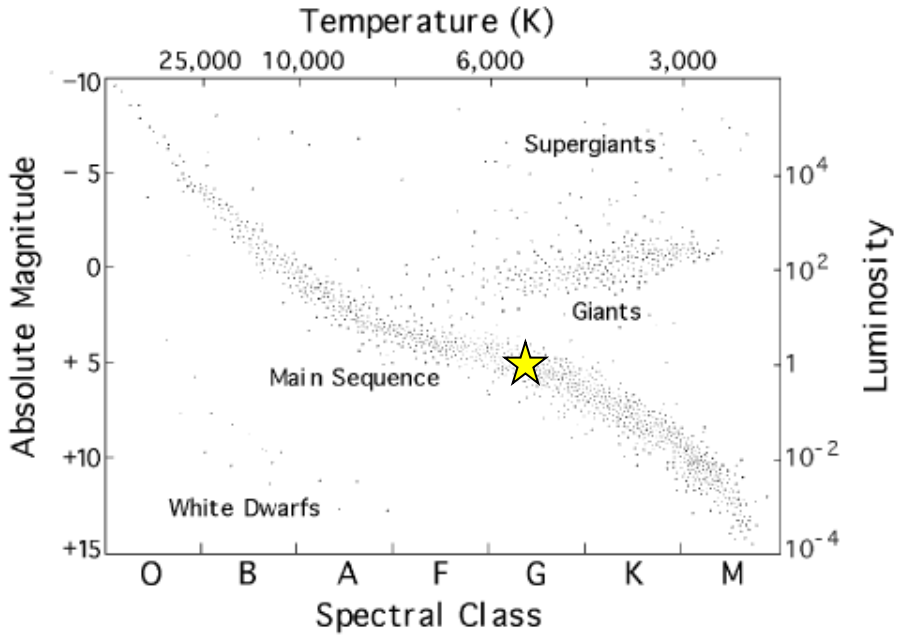

Figure 1.1: The Hertzsprung Russell Diagram for stars within the solar neighbourhood. A star has been added to show the location of the Sun and its place amongst other stars of varying types. *Image courtesy of NASA.*

systems.

1.1 The Sun

The Sun is a comparably average star in relation to the billions of other stars including low mass and solar-type stars which populate the universe. By average, I am referring to the level of flaring activity observed on the Sun in comparison to other active flare stars which show much larger flares more frequently. Astronomers have been studying the Sun for centuries and today the magnetic phenomena we observe is relatively well understood. The Sun is a G2 class star with a surface temperature of 5,800 K, placing it in the middle of the Hertzsprung Russell Diagram on the main sequence, see Figure 1.1. It is composed mainly of Hydrogen and Helium which contribute to 71% and 27% of the solar mass respectively, with the remaining 2% being heavier metals. The Sun is approximately 4.5 billion years old and is roughly half way through its life, generating energy in the core by converting hydrogen to helium via the proton-proton chain (Carroll and Ostlie, 2006). The solar rotation period at the equator is 24.5 days and this is known as the sidereal rotation period. Differential rotation plays a role with regards to the

rotation period of the Sun, where the rotation speed is different at varying latitudes on the solar surface. However, the synodic rotation period of 26.24 days is more commonly referred to as the solar rotation period as this is the time it takes for a fixed feature at the equator to rotate to the same apparent position viewed from Earth.

These properties of the Sun are important, especially later on in the thesis where rotation rates on other types of stars will be discussed and compared to our nearest star. However, there are many other aspects such as the atmospheric structure, including the interior and outer atmospheres, which are both important for understanding the processes which occur within the star. Furthermore, there is the solar dynamo which plays an important role in generating the magnetic activity observed on the Sun. In the remainder of this Chapter we will overview these aspects in more detail, discussing various observed phenomena and setting the scene for the remainder of the thesis.

1.1.1 The Solar Interior

Figure 1.2 shows the solar interior and atmospheric structure of the Sun. Firstly, **The Core** of the Sun is where thermonuclear reactions take place through a process known as nuclear fusion (Cox et al., 1991). Due to fusion the core is heated to a temperature of 15 M K as it converts hydrogen into helium, whereby today the mass fraction of hydrogen has decreased by 37% over the Sun's lifetime (Carroll and Ostlie, 2006). As a result, high energy photons are produced which propagate throughout the interior of the Sun. Overall, 99% of the Sun's energy is generated in the core but only accounts for half of the mass extending out to one quarter of the solar radius.

Next is the **Radiative Zone** where the high energy photons from the core are transported via radiation, reducing their temperature to between 2-7 MK. Additionally, the photons are scattered off ions and electrons as they travel through this layer of the solar interior, taking approximately 1 million years to reach the edge meeting the tachocline. Even though the photons are travelling at the speed of light they become trapped within the radiative zone for long periods of time due to radiative transfer evoking a random walk.

Between the radiative and convective zones lies a small interface layer known as the **Tachocline**.

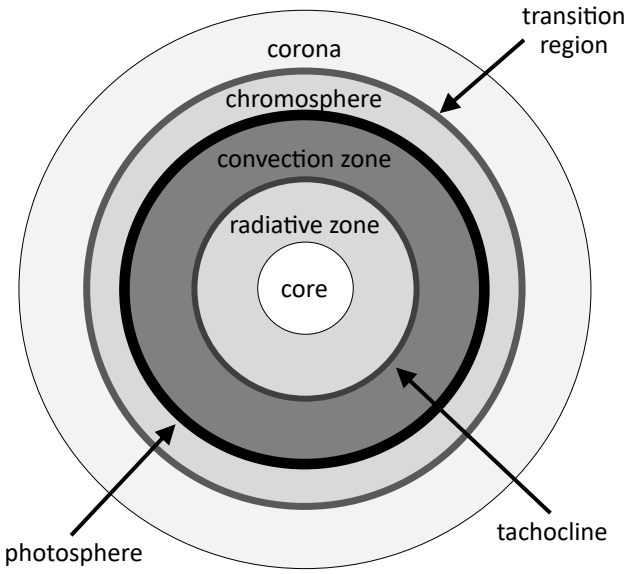

Figure 1.2: A diagram showing the structure of the solar interior and solar atmosphere, this has not been drawn to scale. The photospheric layer separates what we define as the solar interior from the solar atmosphere.

Many solar physicists believe the tachocline is where the global solar magnetic field is generated. It is a region where the energy transfer transitions from being radiative to convective, causing great shear as the rotation rate changes rapidly. This is a result of the radiative zone rotating as a solid body where the convective zone rotates as a fluid. Therefore, differential rotation also begins in the tachocline with its affects observed on the solar surface.

Finally, there is the **Convection Zone** the last layer within the solar interior which extends out to the visible surface. Once the high energy photons have left the tachocline, radiative transport has broken down and convection takes over. This is due to the decreasing temperature of the plasma allowing ions to recombine with electrons producing neutral hydrogen. As a result this leads to an increase in the opacity of the plasma were it becomes opaque to UV photons, therefore, radiation becomes inefficient for energy transfer so convection dominates. Overall, the convective zone is much more turbulent than the radiative zone and as a result, carries heat rapidly to the surface where the temperature drops from 2 MK to 5,800 K. The effects of these convective motions can be seen on the surface in the form of supergranulation and granulation. The convective zone is very important for generating solar phenomena such as flares and CME's as the motions twist up the magnetic field as it travels through the zone to

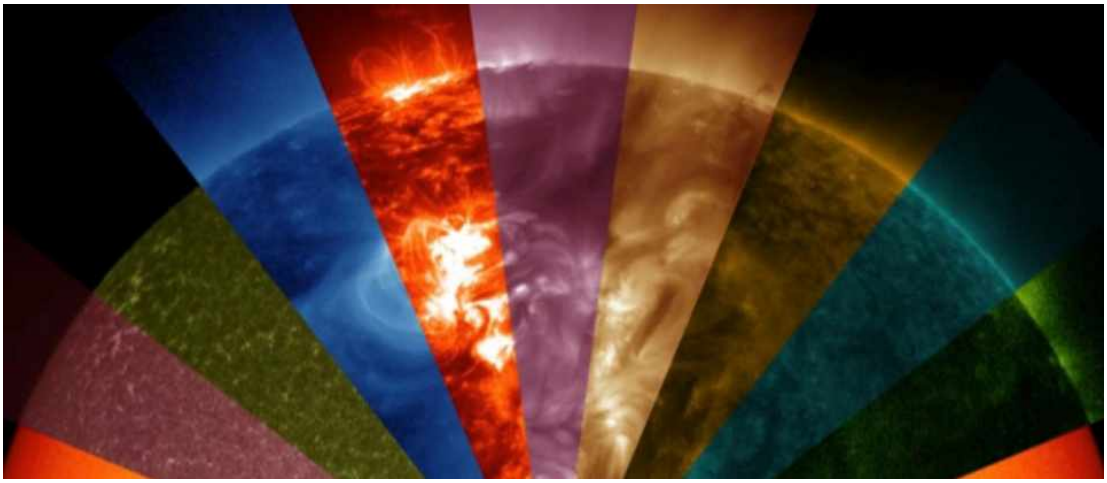

Figure 1.3: These images from The Solar Dynamics Observatory capture the different layers of the solar atmosphere at one instance in time. *Image courtesy of SDO/NASA.*

the surface (see alpha and omega effects in Figure 1.5).

1.1.2 The Solar Atmosphere

The solar atmosphere is composed of four main layers; the photosphere, the chromosphere, the transition region and the corona. When studying phenomena close to the surface it is impossible to only concentrate on one of these layers in isolation. Various parts of the solar spectrum are emitted at various optical depths, within a corresponding height scale, in the solar atmosphere. The emitted spectra at varying optical depths / heights in the solar atmosphere is also related to the temperature of the plasma which is emitting. Figure 1.3 from the Solar Dynamics Observatory is a perfect example of this multi-thermal structuring of the solar atmosphere. Therefore, it is vital to observe solar phenomena across a broad range of spectral lines sampling a broad range of the EM spectrum including the (E)UV, visible and near-infrared in order to adequately understand the physics driving them.

The **Photosphere** is the visible surface of the Sun as it is defined as the layer where visible light is seen and is largely emitted at 500 nm. Overall, 99% of the energy generated within the Sun is emitted in the photoshpere which has a temperature range of 3,800 K - 6,600 K and extends within a height range of approximately 400km. There are many phenomena observed within the photosphere including supergranulation and sunspots. Supergranulation is a pattern of the convective cells within the convective zone which are observed in the photosphere as

Figure 1.4: An image of the 2019 Chilean total solar eclipse taken by Aoife Maria Ryan. In this image you can see the structure of the corona along with the reddish tinge of the chromosphere in the bottom right edge.

horizontal velocity flows using Doppler velocity measurements. Sunspots contain the strongest magnetic field of the photosphere between 1 - 3 kG, however, a very weak field runs through the whole solar surface which can manifest as concentrated strong fields between granules (Phillips, 1995).

Above the photosphere we have the **Chromosphere** with a height range of approximately 2 Mm and a temperature range from 5,800 K at the photosphere to about 25,000 K at the edge (Carroll and Ostlie, 2006). The main characteristics of the chromosphere include a rise in temperature with height and a complex structure which is always changing. At the high temperatures, hydrogen emits H-alpha (Hα: 656.28 nm) and by using spectrograph filters in this wavelength many features of the chromosphere can be observed in absorption in Hα. For example, one feature observed in Hα is jet-like protrusions of plasma which are present in the chromosphere and can extend up to heights of 10,000 km. These are known as spicules which have lifetimes as short as 1 minute (De Pontieu et al., 2007) and up to 15 minutes, otherwise known as macrospicules (Scullion et al., 2009). Overall, it is estimated that around 30,000 of these can exist at any given time, covering 2-3% of the Sun's surface. The chromosphere is a layer of importance as this is where flares radiate most of their energy away.

Next, lies a thin region of approximately 100km in depth known as the **Transition Region**.

This region exhibits a rapid increase in temperature reaching between 2×10^5 - 10^6 K (Judge, 2008). As you move outwards in the solar atmosphere the gas pressure drops exponentially, whereas the magnetic pressure drops much slowly. Therefore, the plasma beta (β) (ratio of gas pressure to magnetic pressure) becomes $\beta < 1$ and the magnetic field shapes the plasma (Mariska, 1992). As a result of this, flows and dynamic activity dominate where the magnetic field defines the structures (i.e. coronal loops and spicules) which are observed.

Finally, we have the **Corona** which can be observed as a halo surrounding the Sun in white light during a total solar eclipse, see Figure 1.4. Observational features of the corona include streamers, plumes and loops where the temperature range is a few million Kelvin. The visible corona extends out to several million kilometres, however, it could be said its effects extends to the edge of the heliosphere at 100 AU. Emission from the corona is also observed in a wide range of wavelengths including X-rays, Extreme Ultraviolet (EUV) and radio. Close to the Sun, it has a very low density, typically 10^8 - 10^9 particles cm^{-3}, and so is essentially transparent to most electromagnetic radiation, therefore, it is not in local thermal equilibrium (Carroll and Ostlie, 2006). One of the biggest unanswered questions in solar physics is the *Coronal Heating Problem* as it is still unknown how magnetic energy dissipates within the corona to heat the plasma to such high temperatures. Additionally, the solar wind is a phenomenon which originates from the corona where the effects can be seen throughout the entire solar system. The slow solar wind is made up of streams of ions and electrons which flow outwards from the Sun at a speed of 440 km/s and temperature of 83,000 K (Richardson, 2010), higher solar wind speeds originating from open magnetic flux regions (coronal holes) can reach speeds of thousands of km/s at 1 AU (Tu et al., 2005).

1.2 The Solar Dynamo

Over the course of the $\sim$ 11-year solar cycle the Sun displays a vast array of magnetic phenomena across varying temporal, spatial and energy scales. The solar dynamo is a mechanism which should explain the origins of the atmospheric solar magnetic field and the manifestation of the magnetic phenomena. Additionally, advances in our understanding of the solar dynamo are important for explaining the magnetic fields and stellar dynamos in other stars.

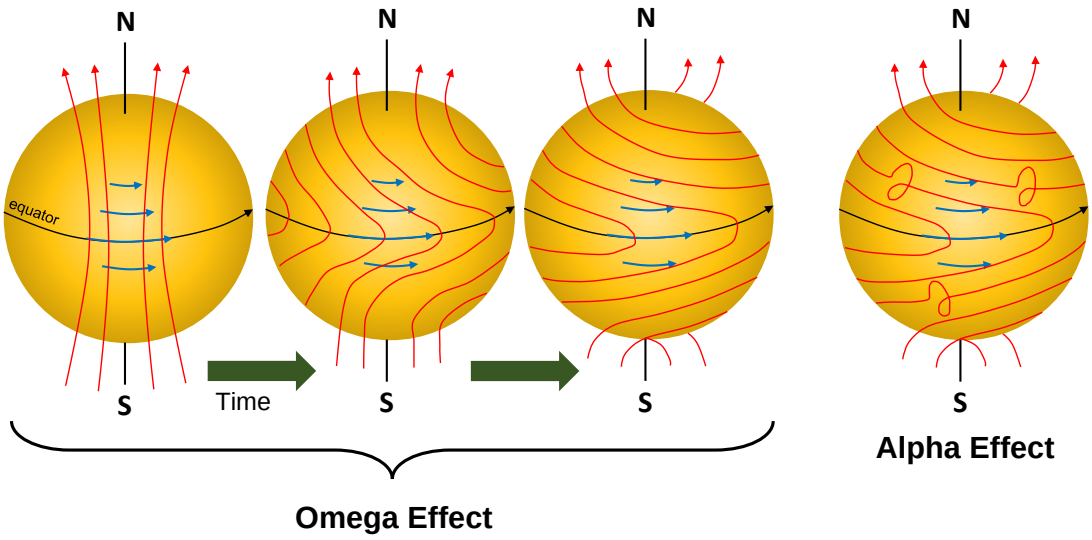

Figure 1.5: A series of diagrams showing the alpha (α) and omega (Ω) effects on the magnetic field structure in the Sun.

Dynamo action is a term used to describe the maintenance of the Sun's magnetic field as a result of its interactions with plasma motions. The question of dynamo action as an answer to the Sun's magnetic field was a big scientific question in the 1950s - 1980s. During this time, it was shown that turbulence driven by convection within a rotating system can produce a magnetic field with scales comparable to those observed on the Sun. Today, solar physicists are still trying to replicate the dynamo mechanism through models to produce the magnetic field of the Sun we observe (Larmor, 1919; Parker, 1955; Herzenberg, 1958; Steenbeck et al., 1966).

The solar dynamo is a physical process which generates and maintains the Sun's magnetic field. It is a naturally occurring electric generator within the solar interior, producing an electric current and consequently a magnetic field. It does this through the laws of magneto-hydrodynamics, however, we do not need to go into such detail here as it is beyond the scope of this thesis. Overall, the solar dynamo is seen as an alpha-omega ($\alpha\Omega$) dynamo where a poloidial field threads through the photosphere. The omega effect is the winding up of this poloidal field through differential rotation to produce a toroidal field, see Figure 1.5. The alpha effect is the twisting of the magnetic field which is thought to result from rising flux ropes deep within the solar interior following the convective motions. This alpha effect is responsible for sunspot groups which follow Joy's Law (Hale et al., 1919) where they are observed to be tilted

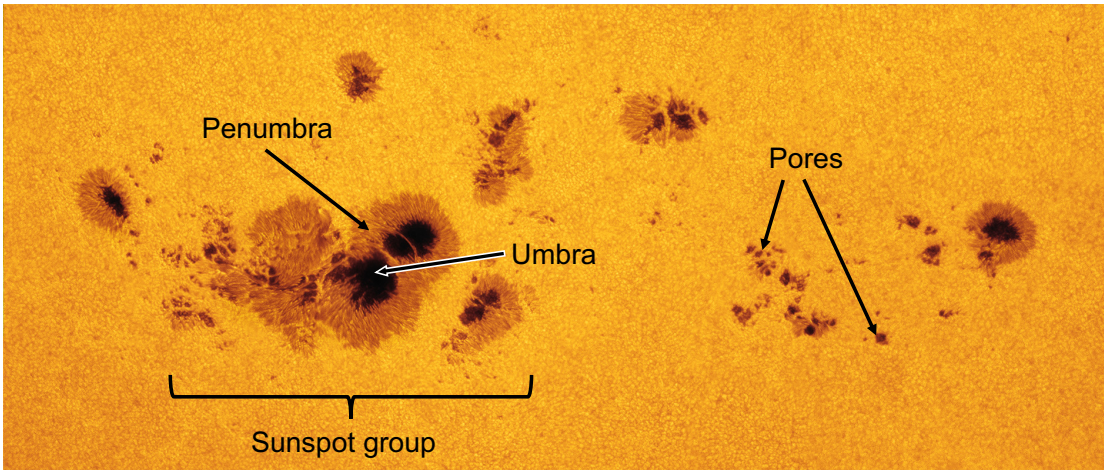

Figure 1.6: An image of sunspot group in Active Region 1520 (July 2012) showing the overall structure of sunspots. The largest spot on the left has a size approximate to 11 Earths and the whole array of sunspots stretches across 322,000 km. *Image courtesy of Alan Friedman/ NASA Goddard.*

with the trailing spots further from the equator in comparison with the leading spot.

1.3 Solar Activity

1.3.1 Sunspots

Sunspots have been observed for centuries with continuous observations dating back to the 1600s and even some records as old as 1128AD (Bray and Loughhead, 1964, : see Chapter 7). They are continuously used as an indicator of solar activity and are closely correlated with solar flares. Sunspots appear as dark features on the solar surface and are the most visible manifestations of the magnetic field. The characteristics of a sunspot include a dark centre known as the umbra and a slightly lighter halo known as the penumbra, see Figure 1.6. They always occur in active regions and typically possess a bipolar magnetic structure. Sunspots are restricted to the activity belts on the Sun and therefore, are not observed beyond $\pm 30^{\circ}$ latitude on each side of the equator (Solanki, 2003). In the photosphere, these dark spots are cooler than their surroundings with temperatures in the range of 3500 – 4550 K. The cooler temperature of sunspots is a result of their high magnetic field strengths which suppress the convective transport of heat giving them their darker appearance. Overall, the magnetic field is vital for sunspots as it determines their physical properties where strengths lie between 2 –

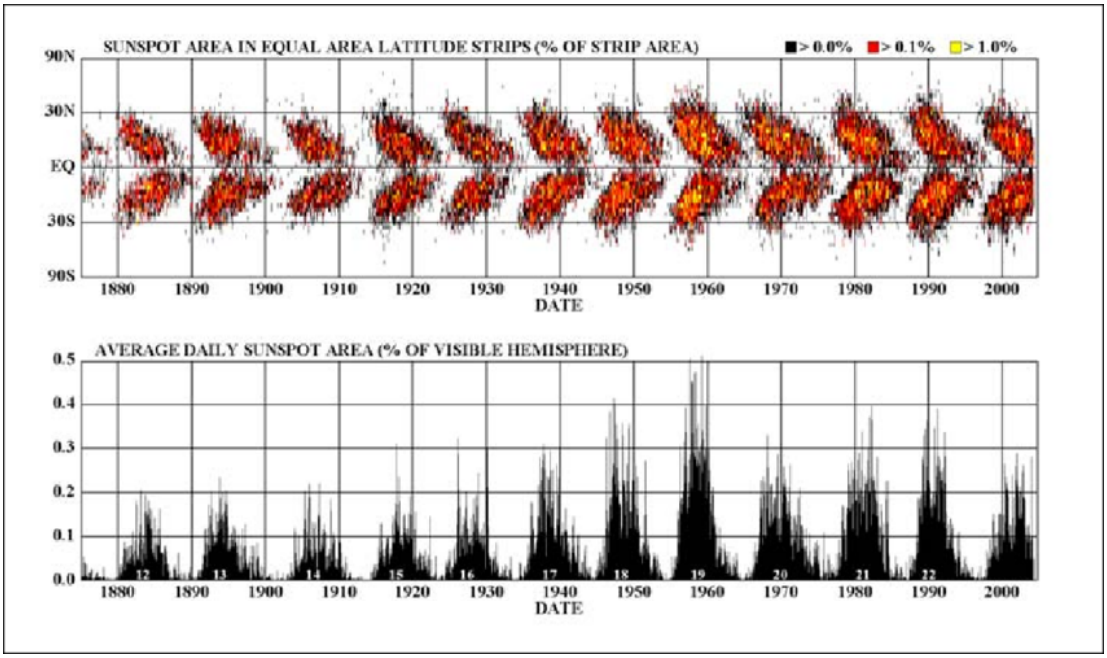

Figure 1.7: The daily sunspot area averaged over individual solar rotation, plotted for multiple solar cycles. This is commonly known as the 'butterfly' diagram, detailing the increase/decrease of sunspot coverage during solar maximum/minimum. *Image sourced from (Baykan and Özçelik, 2006).*

4 kG depending on the region of the sunspot (Solanki, 2003).

During a solar cycle there is a great variation in the size distribution of sunspots. For example, a very large sunspot can reach 60,000 km in diameter whereas a smaller spot can be 3,500 km (Bray and Loughhead, 1964). Typically, the larger sunspots are less common than the smaller ones with the distribution of sizes following a log-normal function (Bogdan et al., 1988). In relation to sunspot sizes, there is a classification system by McIntosh (1990) using white light observations. The classification is based on three factors; (i) the size of a sunspot group and the distribution of the penumbrae, (ii) the principle and largest spot in the group and (iii) the degree of compactness (i.e. these classifications are determined by eye). This classification is an expansion on the Zurich classes producing 60 different types of sunspot groups. On the Sun, sunspots can have lifetimes lasting from hours to months, where the lifetime increases linearly with size. Generally, sunspots last for days with longer lifetimes being difficult to monitor due to the setting Sun or the spot moving behind the solar disk.

Observations of sunspots show their number and area varies over the solar cycle and this can be observed in the butterfly diagram in Figure 1.7. The 11-year solar cycle and the 27-day

rotation period are well known and studied in solar physics and are linked directly to sunspot number. At solar minimum there are few sunspots and overall the Sun is very quiet. However, by solar maximum there are multiple groups of spots which interact producing high levels of flaring activity.

1.3.2 Solar Flares

Solar flares have been studied for over one hundred years with the first record of a solar flare being observed by Richard Carrington in 1859 (Carrington, 1859). While making drawings of the sunspots present on the surface of the Sun, Carrington observed brightenings in the same area as the sunspots which is now known as a white light flare. Following Carrington's observations there were problems with telegraphs worldwide and Northern Lights were observed as far south as Cuba, marking the first ever recorded space weather event. This paved the way into solar flare research which today has become a thriving field with great importance not only with regards to the effects on Earth but the applications to exoplanets.

A solar flare is observed as a sudden and localised brightening in the solar corona which is visible across all wavelengths and results from a rapid reconfiguration of the magnetic field. Flares are an increase in radiation and are often accompanied by a mass motion of fast moving high energy particles, known as a Coronal Mass Ejection (CME). Overall, flares are powerful and energetic events and can reach energy outputs of 10^{32} ergs (Fletcher et al., 2011). Prior to the release of a solar flare the magnetic field becomes stressed and twisted, resulting in a build up of magnetic energy in the form of a build up of current. This is converted into kinetic energy, thermal energy and particle acceleration when the magnetic field structure simplifies through a process described as magnetic reconnection, see Figure 1.8.

Magnetic reconnection is a process by which a magnetic field in an almost ideal plasma (i.e. $E + v \times B = 0$) changes its topology. As mentioned earlier, prior to a solar flare, the magnetic field becomes twisted producing a build up of magnetic energy. Think of this scenario within a set of coronal loops where fully ionised plasma of the corona becomes guided by a magnetic field. If the topology of the magnetic field has to change, then the path the particles and plasma follow must also change. Magnetic reconnection occurs within a region called the diffusion

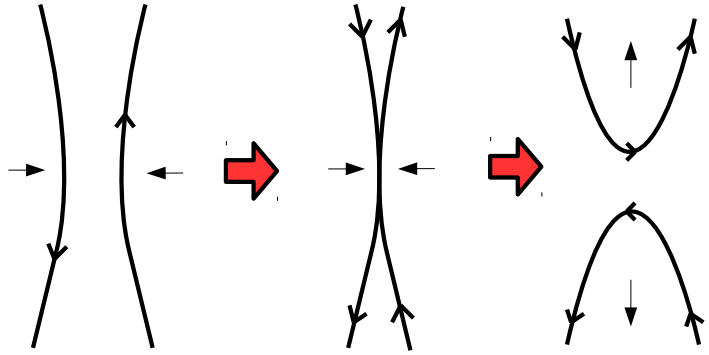

Figure 1.8: A simple schematic diagram showing magnetic reconnection. Two parts of the magnetic field of opposite polarity are forced together causing them to break and snap back to a different configuration releasing a large amount of magnetic free energy in the form of heating and kinetic processes.

region which is a boundary layer where the disconnection and reconnection takes place. Within this layer, dissipation is responsible for the changing of the magnetic field topology (Shibata and Magara, 2011). The increase in diffusivity is caused by large gradients in the magnetic field, B. Due to this, the particles of the plasma can change to different parts of the magnetic field which can then reconnect. This process results in energy being liberated from the system which is followed by a relaxation of the magnetic field to a lower energy state. This liberated energy is responsible for many of the phenomena observed on the Sun's surface but also other events which occur in the solar system.

Solar flares are known to originate from active regions which typically host sunspots, however, there are other observable phenomena associated with flares which occur in or around the active region. Firstly, two or more footpoints are always present during a flare release, appearing as bright patches within the active region in the lower atmosphere. These footpoints form the ends of coronal loops with one positive and one negative polarity, connecting the loop to the photosphere.

In addition, footpoints are connected to another phenomena, flare ribbons, which result from particle beams accelerated via magnetic reconnection. They are often observed in Hα and ultraviolet (UV) wavelengths and are the most prominent feature of a solar flare. These ribbons occur at the same time as the flare release and can be observed to separate from each other as the flare progresses (Janvier et al., 2016). Eventually, they brighten briefly before

Table 1.1: A table showing the peak X-ray brightness in the 1–8Å range for each of the flare classifications (Harra et al., 2016).

Class	Peak (W/m^2) between 1 – 8Å
X	$> 10^{-4}$
M	10^{-5} – 10^{-4}
C	10^{-6} – 10^{-5}
B	10^{-7} – 10^{-6}
A	$< 10^{-7}$

dissipating and then disappearing. Flare ribbons represent the footpoints of coronal loops within the chromosphere which have reconnected. As a result of the reconnection, accelerated particles flow down from the site of reconnection along the magnetic field producing bright ribbon shaped features in the lower chromosphere (Masson et al., 2009). Overall, flare ribbons are important for providing details regarding the topology of the magnetic field during the reconnection (e.g. Fletcher and Hudson, 2001).

Finally, there are post-flare arcades/coronal loops which form and grow around the active region experiencing a brightening upon a flare release which produces high fluxes of Soft X-ray (SXR) emission (Fletcher et al., 2011). Following the release of the flare, the loops are observed to cool through EUV temperatures.

There are three key stages which are observed in larger solar flares (Doyle, 2017).

1. **Preflare Phase** – During this stage SXR emission gradually increases and very little Hard X-Rays (HXRs) or gamma rays are detected above background instrument level.
2. **Impulsive Phase** – Next, gamma rays and HXRs rise impulsively in short bursts of emission. These bursts only last between a few to tens of seconds where the SXR flux also rises rapidly.
3. **Gradual Phase** – The last stage results in the rapid decay of the HXRs and gamma rays with a time consistent of a few minutes. The SXRs follow a similar pattern but with a significantly longer decay time of approximately hours.

Flares are classified using their peak X-ray brightness between 1Å and 8Å as observed by the Geostationary Operational Environmental Satellite (GOES: see section 2.1.3 for more details). The individual classes are noted in Table 1.1 with the classes of X, M, C, B and A which are

also divided into nine subdivisions. This is of particular importance later in the thesis as we begin to discuss flaring activity from other solar-type and low mass stars.

1.3.3 Other Magnetic Phenomena

There are many other magnetic phenomena on the Sun including prominences, filaments, plage regions and many more. For the purposes of this thesis we will go into a couple of these in more detail as they will appear in further discussions.

Filaments (or prominences when observed at the limb) are long-lived, stable features which are present in the solar atmosphere and appear as long, thin, dark structures when viewed against the solar disk (Engvold, 2015, and references therein). However, filaments within active regions tend to be shorter in length, lower in height and have shorter timescales than those present in the quiet Sun (Parenti, 2014). They consist of relatively cool, dense plasma suspended against gravity by the magnetic field in the corona. Both quiet Sun and active region filaments form along a polarity inversion line (PIL) in photospheric magnetic fields (Parenti, 2014; Chen, 2017). They exist in force balance, with the outward magnetic pressure of the filament channel balanced by the downward tension of the strapping field above. Filament eruption follows from the catastrophic loss of this force balance via resistive processes, e.g. breakout reconnection (Antiochos, 1998; Antiochos et al., 1999) and tether-cutting (Moore et al., 2001), and/or via an ideal instability (Chen, 2011, and references therein), e.g. the kink (Török and Kliem, 2005) and torus (Kliem and Török, 2006) instabilities.

Plages are bright patches which are often observed surrounding sunspots in the photosphere. They are associated with concentrations of the magnetic field but unlike sunspots are not large enough to appear dark in colour. They are formed from many small flux tubes giving them their bright appearance which is mainly observed in Hα. Typically, plage regions can be anywhere from 500 – 5,000 km in diameter, however, solar active region plage can cover a surface area of at least one order of magnitude more than sunspots (Solanki, 1999).

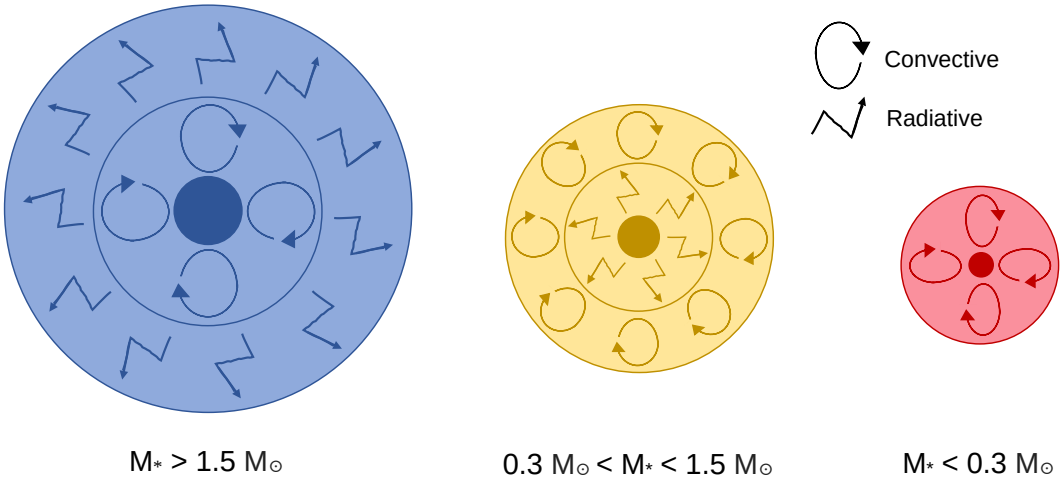

Figure 1.9: A graphic showing the differing interiors of varying star types including massive, solar-type and low mass stars as a result of their mass.

1.4 Solar-Type Stars

There are many terms in stellar physics which are used to define stars similar to the Sun, namely solar analogues, solar twins and solar-type (Cayrel de Strobel, 1996). Solar analogues have detailed properties such as temperature and metalicity which is similar to the Sun, whereas solar twins are indistinguishable from the Sun in terms of their stellar properties. Solar-type is a definition which is more fluid and the stars are similar to the Sun in both mass and evolutionary state. The key feature of solar-type stars is they have a convective envelope like the Sun and are not fully convective like low mass stars. For the purposes of the research within this thesis, solar-type stars are defined as being between spectral types F8 – K2.

1.5 Low Mass Stars

Low mass stars (namely M dwarfs) make up 70% of the stars in the solar neighbourhood. They are small, cool main sequence stars with temperatures in the range of 2400 - 3400 K and radii between 0.20 - 0.63 $R_{\odot}$ (Gershberg, 2005). For stars with spectral type later than M4 it is thought their interiors are fully convective (Hawley et al., 2014), see Figure 1.9. Although more recent work by Mullan and Houdebine (2020), suggest the dynamo mode transition may be narrowed down to between M2.1 and M2.3. However, since these stars have no tachocline

(a boundary zone between the radiative and convective zones) the star would have a negligible magnetic field but, this is not the case and some late M dwarfs do show strong flaring activity suggesting these flares are generated by a different mechanism. The study of magnetic activity on these small, cool stars is of particular interest due to the implications and effects it can have on orbiting exoplanets.

Twenty-five years ago, there were no known exoplanets. However, over the course of my life nearly 4,000 have been discovered with many more candidates awaiting confirmation. We now know that most main sequence stars from solar-like to low mass are likely to possess planetary systems. Low mass stars have become increasingly popular targets for exoplanet surveys due to their abundance in the solar neighbourhood and the relative ease of detecting planets around them. Flares have been observed from many low mass stars over decades including our nearest star Proxima Centauri (Walker, 1981; Güdel et al., 2004). After the discovery of 7 planets, including five Earth-sized, orbiting an ultra-cool red dwarf known as TRAPPIST-1 (Gillon et al., 2017), the study of low mass stars and their flaring activity has become increasingly prominent.

1.6 Fully Convective Dynamos

It is widely accepted that large scale magnetic fields are created in the Sun, solar-type stars and early M dwarfs through differential rotation on a poloidal field (Ω-effect) in the tachocline between the radiative core and convective envelope. This shear layer creates large scale toroidal fields and this process is known as the $\alpha\Omega$-dynamo which has a strong correlation between activity and rotation. To date the origin of the magnetic field on M dwarf stars which are fully convective has been speculated. In fully convective stars there is the absence of a tachocline and the topology of the magnetic field within these stars exhibits a multipole structure differing from the aligned dipole field generated by the $\alpha\Omega$-dynamo on the Sun. Therefore, the $\alpha\Omega$-dynamo is not feasible for the generation of the complex large scale magnetic field seen in these M dwarfs.

Durney et al. (1993) proposed a dynamo generated by a turbulent velocity field causing the generation of chaotic magnetic fields in the absence of rotation. This produces a self-maintained

small-scale magnetic field where rotation is not a factor and when rotation is included only increases the generation rate of the field mildly. In light of this, a small-scale field can produce and maintain certain levels of activity, however, not the high levels observed in certain M dwarfs. Chabrier and Küker (2006) attempt to answer the question: what very active dynamo is responsible for the magnetic field in cool, fully convective objects? The magnetic field generation does not disappear in such objects such as low mass stars and brown dwarfs, therefore, there must be a change in dynamo mechanism for fully convective stars. Mullan and Houdebine (2020) use Ca II data with projected rotational velocities ($vsin(i)$) to explore the spectral range where the transition to of the dynamo mechanism occurs. They conclude that between spectral types M2 - M3 (0.3 - 0.35 $M_{\odot}$) the dynamo mechanism of M dwarfs changes corresponding to a change in the interior of the star to fully convective.

Chabrier and Küker (2006) explore the possibility of an α^2-dynamo generating a large scale magnetic field. In this dynamo model the strength of the field depends on the stellar parameters, rotation rate and a larger Coriolis force yields a stronger field. The Coriolis force is an effect on a mass which is moving within a rotating system and experiences a force which acts perpendicular to the direction of motion and axis of rotation. The α^2 dynamo requires a high Rossby number (ratio of inertial force to Coriolis force) producing large Coriolis forces. These Coriolis forces will act in the plasma of the star producing helical motions rising from the convective core and hence produce a stable large scale magnetic field. This can then be affected by the rotation of the star, as a higher rotation period will churn up the fields making them more stressed and twisted which should result in a greater number of flares with higher energies.

However, in a study by Donati et al. (2006) they use spectropolametric data to construct a Zeeman-Doppler magnetic map of the fully convective, rapidly rotating M dwarf V374 Peg. Surprisingly, these maps show this star has a strong large scale field which is largely axisymmetric. Both the turbulent dynamo and α^2 dynamo models produce a large scale magnetic field which is non axisymmetric. Overall, the mapping of magnetic fields through Zeeman Doppler Imaging (ZDI) allows for the mapping of the large scale magnetic field but not the small scale features such as spots. To do this, many studies use Zeeman Broadening as an indication of the magnetic flux associated with these smaller scale features (e.g. Lang et al.,

2014; Llama et al., 2018; See et al., 2019). Despite the efforts of these studies on low mass stars the dynamo mechanisms at play generating the magnetic fields is still an unanswered question. Additionally, there is the possibility of multiple dynamos operating simultaneously on the star to produce the observed magnetic fields (Mullan and Houdebine, 2020).

In solar physics the presence of a tachocline is regarded as being important in various solar dynamo theories for organising the Sun's magnetic field (see Dikpati and Charbonneau, 1999; Ossendrijver, 2003; Charbonneau, 2010). However, in a recent study Bice and Toomre (2020) show that the convective zone of fast rotating early M dwarfs is capable of generating and organising strong magnetic fields without the presence of a tachocline. In addition, rotation plays an important role and would suggest is a key factor in the dynamo mechanism of fully convective stars. Therefore, it is possible to generate fields strong enough in fully convective M dwarfs capable of producing the high flaring activity observed.

1.7 Stellar Magnetic Activity

1.7.1 Spots and Rotation

The earliest observations of magnetic activity on the Sun are dark sunspots which appear and disappear as they travel across the solar disk. The sunspots are widely associated with flares and have been observed for centuries. Solar-type and low mass stars can show considerable amplitude variations in their lightcurves which have been explained by the presence of large dominant starspots on the surface moving in and out of view as the star rotates, see Figure 1.10. These changes in brightness represent one way of determining the stars rotation period and has produced accurate values of rotation periods for thousands of low mass stars observed by Kepler/K2 (see e.g. McQuillan et al., 2013).

Figure 1.11 shows an example of a photometric lightcurve from the star TIC 229141941, a M3.5 star with a rotation period of 1.6 days observed by TESS, which displays clear rotational modulation. The size of spots observed on solar-type and low mass stars are vastly larger than the sunspots we observe on the solar disk. Typically during solar maximum, sunspots can cover up to 1% of the visible solar disk, however, on M dwarfs starspots can cover up to 50% of the

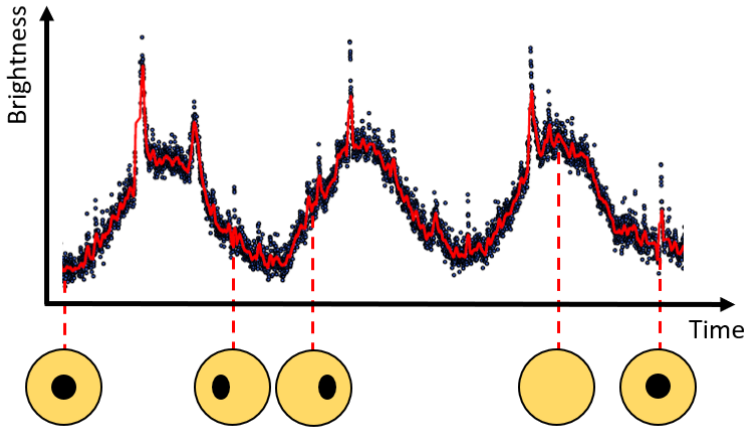

Figure 1.10: A diagram showing the location of a dominant starspot on a star, and the corresponding photometric *TESS*lightcurve. This highlights the observed change in brightness as the cooler and darker starspot passes across the stellar disk. The sharp spikes amongst the rotational modulation represent stellar flares.

visible stellar surface (Tregloan-Reed and Unda-Sanzana, 2019).

Determining rotation periods for low mass stars has become an increasingly popular topic especially as it is considered to drive the magnetic field generation of stars and is directly related to magnetic activity. In Stelzer et al. (2016) they used K2 observations of 134 M dwarfs to focus on the relation between magnetic activity and stellar rotation. They found a difference between slow and fast rotating M dwarfs where for periods greater than approximately 10 days there is an abrupt change in activity.

Newton et al. (2016) use photometry from the MEarth project to derive rotation periods of 387 mid-to-late M dwarfs finding values between 0.1 – 140 days. They find the rotation period distribution is dependent on mass. In addition, these M dwarf stars maintain a fast rotation period for the first several gigayears before spinning down quickly. This aligns with their findings, where a gap between the fast and slow rotators is observed, indicating an age-rotation relation.

Rotation is not only important as it relates to age but also magnetic activity in general. Rapidly rotating low mass stars are expected to produce increased levels of activity as rotation is strongly related to their dynamo mechanism (Hartmann and Noyes, 1987; Maggio et al., 1987). This is known as the rotation-activity-age relation and becomes an important paradigm throughout discussions in this thesis.

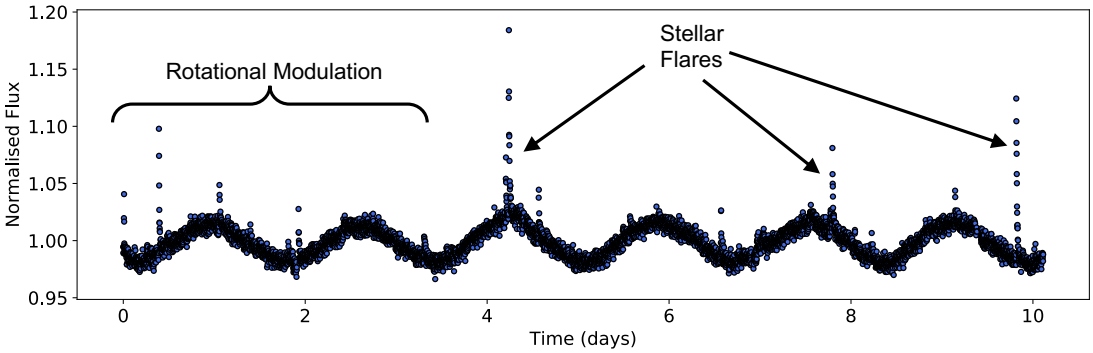

Figure 1.11: A *TESS*lightcurve of TIC 229141941 which has a rotational period of 1.6 days, spectral type M3.5 and was observed in both Sectors 2 and 3. This lightcurve shows an example of the rotational modulation which is observed on many solar-type and low mass stars and also includes some evidence of flaring activity.

1.7.2 Stellar Flares

Stellar flares are a phenomena which have been studied for a century. Some of the first detailed optical observations of stellar flares on M dwarfs were made by Bopp and Moffett (1973) and Gershberg and Shakhovskaya (1983). Amongst the first X-ray observations of stellar flares were made by Heise et al. (1975) using *EXOSAT* which detected an X-ray flare from the M4.5V star YZ CMi. Since then, the physics of stellar flares has been studied by many over the years and in the full energy range from γ-rays to radio frequencies.

More recently, the *Kepler* (Borucki et al., 2010) mission allowed almost uninterrupted observations of stars lasting many months, or in some cases years, allowing many studies into the flare properties of stars. The M dwarf star GJ 1243 was of particular interest because it shows frequent flaring in its lightcurve. This star has a spectral type of M4 making it a great example of a star which possesses a fully convective core. Several papers have been published on this star including Ramsay et al. (2013) where they observed many short-duration low energy flares on the star using short cadence Kepler data. Hawley et al. (2014) used the same data of this star to analyse classical and complex flares, finding correlations between flare energy, amplitude, duration and decay time.

Further to this Stelzer et al. (2016) focused on the relation between magnetic activity and stellar rotation using K2 data of 134 M dwarfs. They found a difference between slow and fast rotating M dwarfs where after a period of approximately 10 days there is an abrupt

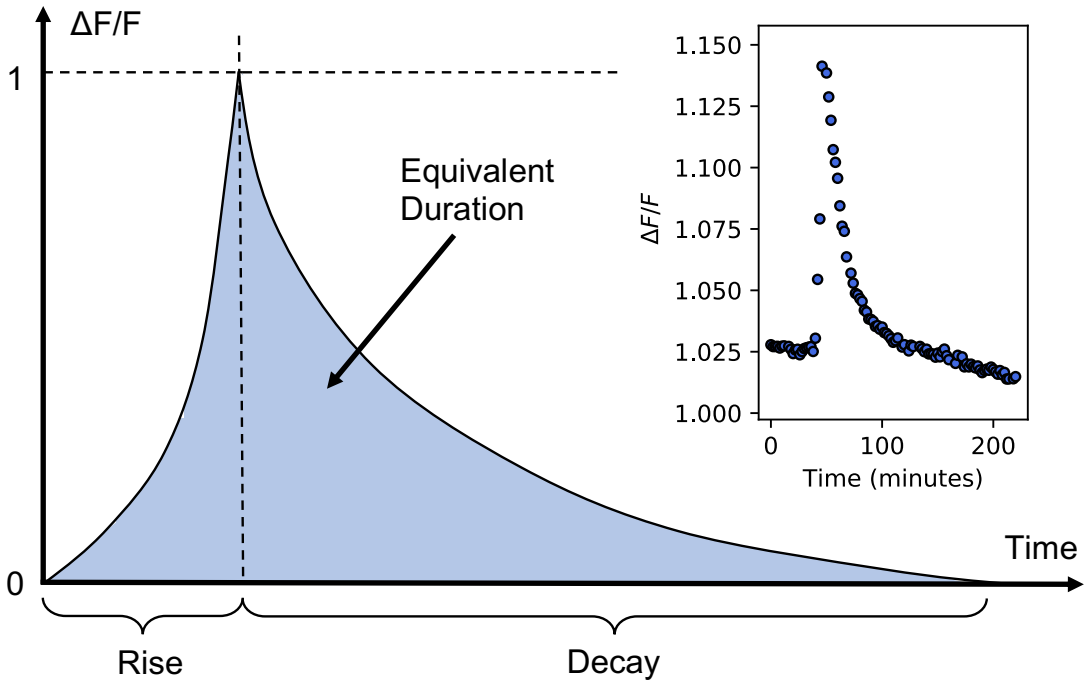

Figure 1.12: This schematic shows the properties of a classical flare profile which are observed in white light by missions such as *Kepler* and *TESS*. Overall, a classical flare has a sharp rise and exponential decay with the equivalent duration being the area under the flare lightcurve profile.

change in activity, suggesting a link between activity and rotation. However, with the vast majority of targets only having long cadence (30 min) data, short duration flares would be missed (for context solar flares can have timescales in the range of minutes to hours), leading to an incomplete analysis of flare statistics. Other studies into the flaring activity of stars includes Davenport (2016) where they used every available Kepler light curve to search for and catalogue stellar flares from stars of all spectral types, opening a new avenue in stellar flare statistics.

A classical stellar flare profile (Figure 1.12) possess a sharp rise and exponential decay whereas complex profiles contain multiple peaks. These flares can last from a few minutes up to a couple of hours in duration with energies significantly exceeding the largest 10^{32} erg flares observed on the Sun. In recent years the study of highly active stars has become more popular due to the increased discovery of planetary systems orbiting these stars which can have drastic effects on the atmospheres of any orbiting exoplanets.

1.8 Thesis Aims

As the Sun is our nearest star, we are able to collect detailed spatial observations of its many phenomena from large scale flares and CMEs to the smaller scale granulation and spicules. In addition, there are historical data including spot and flare observations dating back to the 1600s and since the launch of the Solar Dynamics Observatory in 2010 the Sun is observed continuously. Along with all these observations comes a deep knowledge and understanding of the mechanisms which are at play on our nearest star and how they can affect the Earth and Solar System. In stellar physics, although the number of stars now observed by missions such as Kepler, TESS and Gaia are nearing 2 billion, the lack of detailed (multi-spectral and high temporal cadence) and long-term observations remains an issue. The capabilities of our technology and the vast distances between us and our neighbouring stars restricts our ability to produce observations which show details of the magnetic activity. Therefore, we should attempt to apply the knowledge gained from detailed solar observations to illuminate our understanding of stellar flares.

In this thesis, I look at the solar-stellar flare connection through detailed observations of both a confined solar flare event and stellar flares from solar-type and low mass stars. Using the results from these studies I aim to provide insights into large scale flare events observed on other stars. Chapter 2 details the observational data both from solar and stellar physics missions and telescopes which will be used throughout this thesis.

In Chapter 3, I present a detailed analysis of a confined filament eruption and jet associated with a C1.5 class solar flare. Multi-wavelength observations from both the Global Oscillations Network Group and Solar Dynamics Observatory are used to reveal the details of the formation of the filament. Utilising high-resolution Hα observations from the Swedish Solar Telescope/CRisp Imaging Spectro Polarimeter, velocity maps of the outflows are constructed, demonstrating their highly structured but broadly helical nature. The observations are contrasted with a 3D magnetohydrodynamic (MHD) simulation of a breakout jet in a closed-field background where a close qualitative comparison is found with the observations. This Chapter discusses the details of both the observations and simulations which are important for the subsequential chapters as the key to investigating the solar-stellar flare connection.

In Chapters 4 & 5 data from both *Kepler*/K2 and *TESS* are used to conduct statistical analyses into the flares from other stars. Chapter 4 looks at the stellar flares from a small sample of low mass stars observed with K2. In this study the rotational phase of the flares is investigated where I explore a correlation between the starspot causing the modulation and flare number. In Chapter 5, this study is then expanded using *TESS* data of a much larger sample of low mass stars to study this relationship on a greater sample.

Chapter 6 expands on the studies of low mass stars looking at solar-type stars with *TESS*. Again the relationship between starspots and flare number is tested with historic solar flare and sunspot data, brought in to make a comparison of this relationship on the Sun. Additionally, two of the solar-type stars possess one year worth of *TESS* observations, allowing for a more detailed study into the magnetic variability of these stars.

Finally, in Chapter 7 all of the studies from both solar-type stars, low mass stars and the Sun are brought together to discuss the solar-stellar flare connection. The future work which stems from this thesis is also discussed with studies already underway to investigate the magnetic activity in general of solar-type and low mass stars.

2 Observational Data

The research presented in this thesis has used observational solar and stellar data from several telescopes and instruments. There is a mixture of both ground based and space based observations and in this chapter I detail the specifics of each telescope/instrument.

2.1 Solar Flare Observations

2.1.1 Solar Swedish Telescope

The Swedish 1-m Solar Telescope (SST: Scharmer, Bjelksjo, Korhonen, Lindberg and Petterson, 2003) is a solar telescope in La Palma which is run by the Institute for Solar Physics of the Royal Swedish Academy of Sciences. It received first light on 2nd March 2002 without any adaptive optics and a smaller aperture of 60 cm. Once the adaptive optics were installed the telescope was opened to a full aperture on the 21st May 2002 (Scharmer, Bjelksjo, Korhonen, Lindberg and Petterson, 2003).

The SST is a vacuum telescope which uses its single 1 meter lens to seal it off. The vacuum is filled with Helium gas which reduces the heating of the optics and gas by the sunlight producing a crisp and clear image. There are two main instruments at the SST: 1) CRisp Imaging SpectroPolimeter (CRISP) and 2) CHROMospheric Imaging Spectrometer (CHROMIS).

The instrument used to collect data for the study in this thesis is the CRisp Imaging SpectroPolarimeter (CRISP: Scharmer et al., 2008), a spectropolarimeter based on a dual Fabry-Pérot interferometer design which operates in the red beam from 510 - 860 nm. It has three cameras,

two of which are narrowband of 0.3 - 0.9 nm and one wideband. The CRISP spectral scans are centred on the Hα 6562.8 Å absorption line of the chromosphere. The field of view (FOV) of these observations is approximately $60\,\mathrm{arcsec} \times 60\,\mathrm{arcsec}$ with an image scale of 0.0592 arcsec per pixel. CHROMIS is also a dual Fabry-Pérot system, similar to CRISP, but at the moment does not measure polarimetry. It has been designed to be used between wavelengths of 380 nm to 500 nm, observing lines such as Ca K, Ca H and Hβ, which form in the upper chromosphere. For the purposes of the research in this thesis, data from only the CRISP instrument is used, see Chapter 3.

2.1.2 Global Oscillations Network Group

The Global Oscillations Network Group (GONG: Harvey et al., 1996) is a global network of six identical telescopes with the goal of observing the Sun continuously. The products of the GONG network include full disk images of the velocity, intensity and magnetic flux of the Sun every minute. In addition, there are high-cadence, high-sensitivity magnetograms and 2K x 2K Hα intensity images obtained in 20-second cadence mode.

There are six GONG locations across the world which allows for the Sun to be observed 24 hours a day. These include; The Big Bear Solar Observatory (BBSO) in Southern California, the Learmonth Solar Observatory in Australia, the Udaipur Solar Observatory in India, the El Teide Observatory in the Canary Islands, the Cerro Tololo Interamerican Observatory in Chile and the Mauna Loa Solar Observatory in Hawaii.

For the research within this thesis, Full-Disk Hα (FDHA) images were acquired from GONG (Harvey et al., 2011) hosted by the National Solar Observatory. In particular FDHA images were collected from the Big Bear Solar Observatory and the El Teide Observatory. FDHA images are taken with a cadence of 1 minute and each 2k $\times$ 2k image has a spatial sampling of 1 arcsec.

2.1.3 The Geostationary Operational Environmental Satellites

The Geostationary Operational Environmental Satellites (GOES: Menzel and Purdom, 1994) are a group of, currently, four geosynchronous satellites which are owned and operated by the

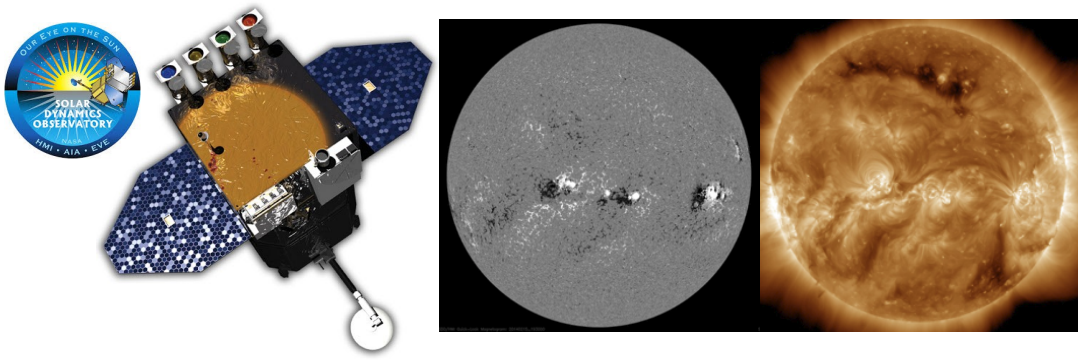

Figure 2.1: The Solar Dynamics Observatory satellite which has AIA, HMI and EVE onboard. The two solar images show a HMI magnetogram and an AIA image in 171Å detailing the relationship between strong magnetic fields and active regions on the Sun. *Images courtesy of NASA.*

United States' National Oceanic and Atmospheric Administration (NOAA). These satellites are used to monitor many weather related phenomena on Earth including weather forecasting, severe storm tracking and meteorology research. In addition, these satellites are important in the solar physics community as they provide solar imagery, magnetometer data, solar X-ray data and data on high energy solar protons at Earth. The solar X-ray data is of particular importance as it is used to classify and monitor flaring activity which occurs on the Sun.

2.1.4 Solar Dynamics Observatory

The Solar Dynamics Observatory (SDO: Pesnell et al., 2012) is a NASA mission which is part of the 'Living With a Star' program. It was launched in February 2010 and consists of three separate instruments; the Atmospheric Imaging Assembly (AIA), the Helioseismic and Magnetic Imager (HMI), and the Extreme-Ultraviolet Variability Experiment (EVE), see Figure 2.1. SDO is positioned in a circular geosynchronous orbit at an altitude of 35,789 km, at 102 degrees West longitude and inclined at 28 degrees (Pesnell, 2015). This orbit was chosen as the optimal position to observe the Sun continuously with minimal distribution. The Solar Dynamics Observatory was built with the primary objective to understand the physics of solar variability which will improve our knowledge and understanding of how the Sun drives global change and space weather.

The Atmospheric Imaging Assembly

The Atmospheric Imaging Assembly (AIA: Lemen et al., 2012) consists of four 20cm dual-channel telescopes which provide multiple simultaneous full-disk filtergram images (image scale of 0.6 arcsec in AIA) of emission lines of the corona and transition region. Overall it has a 1.5 arcsec spatial resolution, 12 second temporal resolution and FOV of 41 arcmin, observing in ten different wavelength channels. These channels include, narrowband images in seven EUV channels centred on specific Fe lines and one He line; 94Å, 131Å, 171Å, 193Å, 211Å, 304Å and 335Å. One of the telescopes is used to observe C IV near 1600Å and the nearby continuum at 1700Å and has a filter which observes in the visible to enable co-alignment with images from other telescopes. Overall, AIA covers a temperature range of 6×10^4 K to 2×10^7 K (Lemen et al., 2012) and has been extremely valuable in the solar community, advancing our understanding of the mechanisms of solar variability.

Helioseismic and Magnetic Imager

The Helioseismic and Magnetic Imager (HMI: Scherrer et al., 2012) was designed to study the origins of solar variability and to understand the Suns interior along with the multiple components of magnetic activity. The HMI instrument takes measurements of polarisation in specific spectral lines tracking motions in the solar photosphere to image the components of the photospheric magnetic field. It is essentially an enhanced version of the Michelson Doppler Imager (MDI) on board the Solar and Heliospheric Observatory (SOHO). In comparison with SOHO, HMI has higher resolution, higher cadence and an extra camera providing additional polarisation measurements. Every 45 seconds HMI provides 1 arcsecond resolution full-disk, Doppler velocity, line-of-sight magnetic flux images. Vector magnetic field maps are provided every 90 or 135 seconds depending on the frame sequence. Similar to AIA, HMI provides images which fill the 4096 $\times$ 4096 CCD camera on-board where every pixel is approximately 0.5 arcseconds.

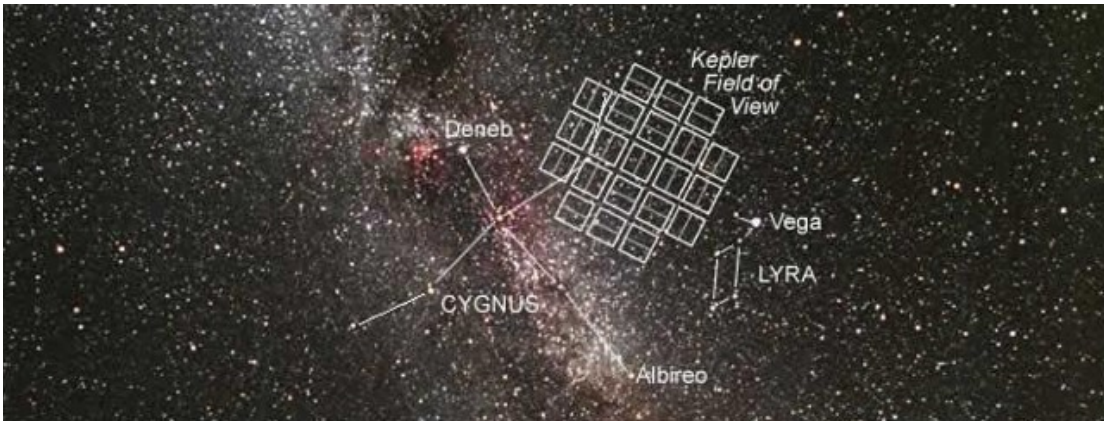

Figure 2.2: In this image the Field of View (FOV) which *Kepler* monitored for four years is shown to be located between the constellations of Cygnus and Lyra. *Kepler*ś field of view covers a total of 115 square degrees which is around 0.25 percent of the sky. *Image courtesy of Carter Roberts / Eastbay Astronomical Society*.

2.2 Stellar Flare Observations

2.2.1 Kepler/K2

Kepler, a NASA mission, was launched in 2009 and stared at the same 115 square degree patch of sky just north of the Galactic plane for 4 years (see Figure 2.2), providing extensive photometric data for over 100,000 stars (Koch et al., 2004). It was originally launched with the purpose of finding Earth-sized planets around other stars near or in habitable zones but, surpassed its planned mission time and continued to exceed expectations. The telescope itself is of Schmidt design with a 1.4 m primary mirror and is in an Earth-trailing heliocentric orbit. The data obtained by *Kepler* revolutionised the study of astrophysics especially in the field of exoplanets, where it is responsible for finding the majority through the transit method. In addition, *Kepler* data has also revolutionised the field of Asteroseismology, the number of stars with known rotation periods and interacting binaries. *Kepler* also provided the means to study stellar flares due to the high precision and length of the light curves. It can operate in two observation modes, short cadence (SC) 1 minute exposure and long cadence (LC) 30 minute exposure.

In August 2013 *Kepler* lost the use of two of its reaction wheels and it was decided to abandon the attempts to fix them. As a result the current mission would need to be modified, however,

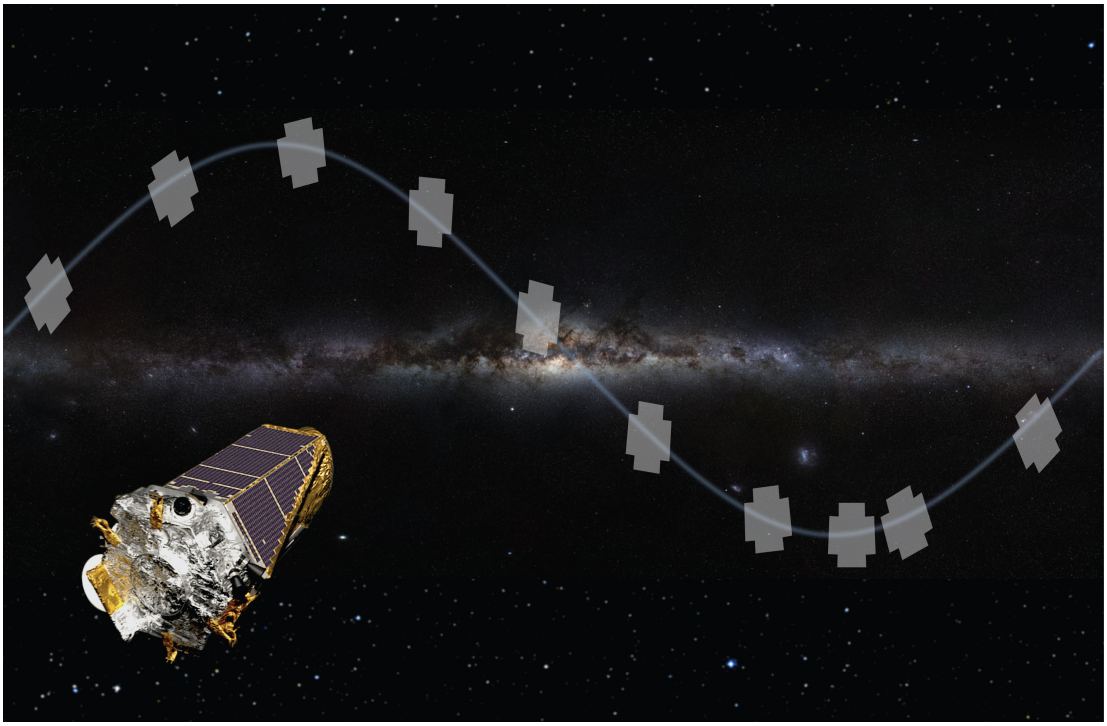

Figure 2.3: This graphic shows a selection of the K2 FOV's along the ecliptic which are each observed for approximately 70 days. In total there were 18 separate FOV's observed during the duration of the K2 mission. *Image courtesy of W. Stenzel / NASA Ames.*

it did not signify the end for *Kepler*. New life was given to the mission when it was re-purposed as K2 which began taking observations in June 2014 where fields are observed along the ecliptic (see Figure 2.3) for a duration of two months each (Howell et al., 2014).

Because of the way that K2 is pointed, stars typically move by $\sim$1 pixel over the course of 6 hours (Van Cleve et al., 2016). Without applying a photometric correction the resulting root mean square (rms) on a lightcurve can be considerably higher than for *Kepler*. For instance for stars in the 10 – 11 mag range, *Kepler* gave an rms of 18 parts per million (ppm). For K2 the uncorrected rms is 170 ppm. Amongst the first to provide readily available corrected data were Vanderburg and Johnson (2014) who were able to bring the rms for 10–11 mag stars down to 31 ppm.

A number of other groups have developed software which corrects for the instrumental effects which are present in raw K2 data. Not all of these techniques are suitable for SC mode data and some approaches can remove astrophysical effects. For the targets observed by K2 in Chapter 4, the corrected K2 data was obtained using the EPIC Variability Extraction and Removal for Exoplanet Science Targets (EVEREST) pipeline (Luger et al., 2016) in all but

one star in our sample. For GJ 1224 observed in Field 9 the SC lightcurve was obtained from Andrew Vandenburg, (Van Cleve et al., 2016).

The lightcurves of each source come with a range of data values and characteristics including a 'QUALITY' flag which can highlight various potential issues with the photometric values for that specific photometric measurement. This is of particular importance when trying to find events such as flares which could, in principal, be mistaken for an instrumental effect. The EVEREST pipeline keeps the original flags from *Kepler*, but adds additional 'bit values'. For instance, bits '23' and '25' could be detector anomalies but could also be events such as eclipses or flares (Luger et al., 2016; Luger et al., 2018).

In searching for photometric variations longer than the typical duration of flares, such as the stellar rotation period, we were cautious and removed all events which did not conform to QUALITY=0. This removes all points which could have potential issues but also removes any flaring activity. This is to allow for the rotation period to be derived without any interference from other phenomena observed in the lightcurves. When we searched for flares we removed photometric points which were identified as bad in the *Kepler* Archive Manual[1] and points corresponding to bit values which were clearly identifying times when the spacecraft thruster was used such as bit value 20 and 21. We kept points which had bit values 23 and 25.

After nine years of observations including the legacy of 2,600 exoplanet discoveries, NASA announced the retirement of the *Kepler*/K2 space telescope on 30th October 2018. This was a result of the spacecraft running out of fuel which was needed for further science operations. Despite this, the discoveries of *Kepler* will continue with the wealth of data collected and available within the astrophysics community. The retirement of *Kepler* also paves the way for its successor *TESS* to continue its legacy.

2.2.2 Transiting Exoplanet Survey Satellite

The Transiting Exoplanet Survey Satellite (*TESS*: Ricker et al., 2015) was launched in April 2018. Unlike *Kepler* and K2, during its initial two year mission *TESS* will make a near all-sky survey, observing 200,000 of the closest stars to our Sun. It will target 500,000 stars, with

[1] https://archive.stsci.edu/kepler/manuals/archive_manual.pdf

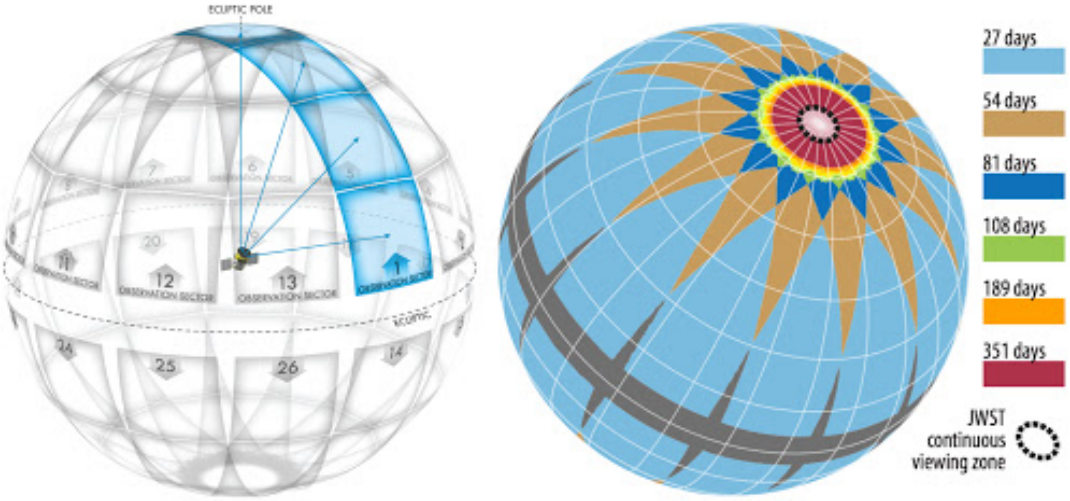

Figure 2.4: These images shows the observing sequence of *TESS* detailing the overlapping of the various sectors to produce the continuous viewing zone near the poles. *Images courtesy of NASA and MIT*.

a focus on nearby G, K and M type with thousands of the closest red dwarfs being included in the 2-min cadence programme. The primary mission for *TESS* is to search for exoplanets via the transit method around low mass M dwarf stars. Therefore, *TESS* has a band-pass of 600 - 1000 nm and is centred on 786.5 nm (Ricker et al., 2015). *TESS* is fitted with four CCD cameras which act as a 1×4 array providing a total FOV of $24^{\circ} \times 96^{\circ}$. Each of the hemispheres are split into 13 equal sectors which *TESS* will observe for a duration of 27.4 days each. Close to the poles there are overlaps within Sectors producing certain areas which are observed in excess of ~ 300 days, this includes a continuous viewing zone (see Figure 2.4). *TESS* data releases include Full Frame Images (FFIs) and Short Cadence (2-min) lightcurves. For this study we will be using the 2-min lightcurves as they allow for the observation of the shorter and typically less energetic flares.

The first batch of *TESS* data was released in late 2018/early 2019 and included observations of the southern hemisphere from sectors 1 – 3 made between July 25th and October 17th 2018. The data release included both Full Frame Images (FFIs) and Short Cadence (2-min) lightcurves. The 2-min lightcurves allow for the detection of short duration, low amplitude flares, and it is these lightcurves which form the basis of the research in this thesis. The calibrated *TESS* lightcurves for each of our target stars in all samples discussed, were downloaded

from the MAST data archive[2]. The data values for PDCSAP_FLUX are used, which are the Simple Aperture Photometry values, SAP_FLUX, after the removal of systematic trends common to all stars in that chip. Each photometric point is assigned a QUALITY flag which indicates if the data may have been compromised to some degree by instrumental effects, similar to K2 data. Those points which did not have QUALITY $\neq$ 0 are removed and each lightcurve is normalised by dividing the flux of each point by the mean flux of the star. The *TESS* data is different to the K2 data and bit values such as 23 and 25 are not used in terms of the QUALITY flags.

Since the release of *TESS* data for sectors 1 – 3 in early 2019, all sectors in the southern hemisphere have now been observed, with data available up to sector 13. This data is utilised in the solar-type star sample in Chapter 6. *TESS* is now due to finish observations in the northern hemisphere by April 2020 where data will be available shortly after. This includes the *TESS* observations of the *Kepler* FOV which will see interesting comparisons over the next few years. *TESS* has already had confirmation of an extension to the mission, which will see it return to the southern hemisphere and includes a 20 second cadence mode for lightcurve observations. It is safe to say, there are exciting times ahead for the *TESS* mission as it continues to play a great role in stellar variability and exoplanet research.

2.2.3 TESS vs. Kepler/K2

Since there are observations from both *Kepler*/K2 and *TESS* within this thesis, therefore, there are various factors which we need to take into account for the analysis. First, the *TESS* camera's have a 10.5 cm aperture compared to *Kepler's* 95 cm diameter mirror. For the same magnitude, *TESS* will therefore provide lightcurves with a greater noise level than *Kepler*. The CCD's in the *Kepler* detector had a pixel scale of $4''$ – this contrasts with $21''$ in *TESS*. Indeed, the 90 percent encirclement radius for a stars flux in *TESS* is $42''$ (Ricker et al., 2015), which compares with a 95 percent encirclement radius in *Kepler* of $8.4''$. There is therefore a potential issue of dilution of the flux of the target stars with other stars falling into the same aperture.

We therefore used the Gaia DR2 (Gaia Collaboration, 2018) to search for stars within $42''$ of

[2]https://archive.stsci.edu/tess/

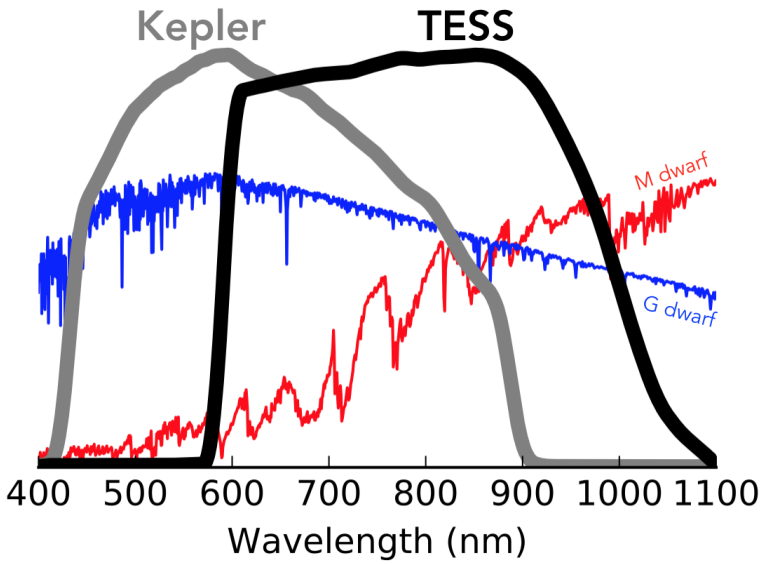

Figure 2.5: This graph shows the difference between the *TESS* and *Kepler* band-passes with *TESS* extending further into redder wavelengths. This was in order to observe more planets orbiting low mass M dwarf stars. *Image courtesy of Zach Berta-Thompson with data from Sullivan at al. (2015).*

the stars in our target list, see Chapter 5. All those targets which had another star with a magnitude of up to 1.5 mag fainter (1/4 in flux) were flagged. Of the 167 low mass stars in the sample, 46 had a star which was up to 1.5 mag fainter and within $42''$ of the target. Of these, nine were actually brighter than the target. Whilst this does not affect the prime goal of investigating the rotational phase of the flare it makes us less sensitive to lower energy flares than for stars with no spatially coincident stars and we will underestimate the energy of the flares unless we take into account the flux from the nearby star. Similarly, some flares may originate from the nearby star and be mistaken as flares from the target star. The spectral type of those nine stars were determined using the `SIMBAD` database and seven of them are classified as M dwarfs. Therefore, we cannot exclude that a small fraction of flares from these stars could originate from the nearby star. We come back to this issue in §5.6 where we investigate the rotational phase distribution of the flares.

Additionally, it is important to mention the differing band-passes between *Kepler* and *TESS*, see Figure 2.5. The *TESS* band-pass spans from 600 – 1000 nm and is centred on 786.5 nm (Ricker et al., 2015), whereas the *Kepler* band-pass spans 400 – 900 nm. This redder band-pass was chosen specifically to observe a larger number of M dwarfs as planets are easier to

detect around these smaller, cooler stars. As the *TESS* band-pass is more sensitive to redder wavelengths, *TESS* will not detect the less energetic events as flares typically have their peak emission towards the blue. Overall, the rms of the *TESS* lightcurves for the M4 low mass star GJ 1243 is 4.6 times lower than the *Kepler* lightcurves, this will differ for stars of other spectral types. As a result, *TESS* will be unable to detect short duration, low amplitude flares (Ramsay et al., 2020). However, this is related to the brightness of the stars where lower energy flares could be detected on brighter targets, therefore, the key factor in detecting low energy flares is the SNR of the lightcurve.

3 Observations and Modelling of a Confined Jet and Solar Flare

The research outlined in this chapter has been published in the Astrophysical Journal (ApJ) as Doyle et al., 2019, ApJ, 887(2), 246. This work was done in collaboration with Peter Wyper from Durham University who was responsible for the modelling aspect of the research.

3.1 Introduction

Solar flares are a sudden increase in radiation caused by energy conversion resulting from a rapid reconfiguration of the coronal magnetic field. These events are powerful bursts of radiation with energy outputs sometimes exceeding 10^{32} erg and can be observed across the entire electromagnetic spectrum (Fletcher et al., 2011, and references therein). Having been studied for over 150 years, the underlying physical mechanisms leading to energy conversion during solar flares remains a focus of investigation.

Magnetic energy release in solar flares can manifest itself in a number of different observables, notably flare ribbons and post-flare arcades, but also in filament eruptions (e.g. Rust, 2001; Sterling and Moore, 2005; Schmieder et al., 2013), CMEs (e.g. Moore et al., 2001; Emslie et al., 2005; Karpen et al., 2012) and blow-out jets (e.g. Moore et al., 2010; Moore et al., 2013; Young and Muglach, 2014). It is clear the pre-flare magnetic field topology dictates the manifestation of any number (or all) of these phenomena in a solar flare. Here the focus is on the role of a filament eruption (discussed in Section 1.3.3) in a confined solar flare.

Confined flares are flare events where the solar atmosphere is bound to the surface and there is no eruption of plasma out into space. Confined flares are often associated with the failed

eruption of a filament (e.g. Ji et al., 2003). Simulations and observations have revealed that there are two main scenarios for confined filament eruptions. A pre-existing flux rope in a bipolar active region becomes ideally unstable (usually to the kink instability), but the overlying field is too strong or has a low decay index and halts the eruption (e.g. Török and Kliem, 2005; Hassanin and Kliem, 2016; Amari et al., 2018; Liu et al., 2018). In some cases the decay index may be high enough, but the development of the instability destroys the coherence of the flux rope before it can erupt (Zhou et al., 2019). The kink instability is associated with the conversion of twist (internal twisting of flux tubes which make up the flux rope) to the dimensionless quantity of writhe, i.e. the measurement of the helical deformation of the flux rope about its axis. Often there is a clear development of writhe in these events (e.g. Ji et al., 2003; Török and Kliem, 2005). Alternatively, the filament forms in a multi-polar topology and the erupting material is redirected along nearby coronal loops by reconnection of the erupting structure, (e.g. DeVore and Antiochos, 2008; Sun et al., 2013; Joshi et al., 2014; Reeves et al., 2015; Masson et al., 2017; Yang and Zhang, 2018). These events are associated with multiple flare ribbons, and in particular several have been observed with circular ribbons indicative of a coronal null point topology (e.g. Sun et al., 2013; Masson et al., 2017). The reconnection and redirection of the erupting material is also sometimes associated with a jet-like surge of plasma (e.g. Yang and Zhang, 2018).

Multi-polar confined filament eruptions and their associated redirected plasma flows are locally similar in nature to coronal jets generated by the eruption of so-called "mini-filaments" – small-scale filaments typically of length 10 to 30 Mm (e.g. Panesar et al., 2016). Coronal jets are a solar phenomenon with a constant presence throughout the solar cycle and have been observed since the launch of Yohkoh in X-ray emission (Shibata et al., 1993; Shimojo et al., 1996). They are commonly found in coronal holes (and also active regions) and posses a collimated, beam like structure originating from coronal bright points. Recent observations have revealed that the majority of coronal jets are generated by mini-filament (or sigmoid) eruptions (e.g. Sterling et al., 2015; Kumar et al., 2019). Typically these jets begin with a brightening at the base followed by rapid helical plasma outflows guided by the surrounding magnetic field. They are smaller than typical flares or CMEs with energies in the range of approximately 10^{26} - 10^{27} erg (Pucci and Velli, 2013). Overall, jet properties include lengths, velocities and lifetimes which

are in the range of 1.5 $\times$ 10^5 km (large side), 100 - 400 km/s and 100 - 16,000 seconds, respectively.

Wyper et al. (2017, 2018) developed a three-dimensional simulation model for mini-filament jets in coronal holes, building upon concepts introduced in previous jet/CME simulations and observations (e.g. Shibata and Uchida, 1986; Antiochos et al., 1999; Lynch et al., 2008; Pariat et al., 2009; Archontis and Hood, 2013; Moreno-Insertis and Galsgaard, 2013; Sterling et al., 2015). In their model, surface motions are used to form a filament channel along a section of a quasi-circular PIL beneath a coronal null point. In an analogous manner to how breakout CMEs occur (Antiochos, 1998; Antiochos et al., 1999), breakout reconnection (reconnection between upper and lower systems where a transfer of flux occurs at the two sides of the system) at the null point allows the filament channel to rise, inducing tether cutting reconnection (redistributed shear within a system to the edge of sheared region produces reconnection leading to an eruption; Moore et al., 2001) that forms a flux rope if one is not already present. When the flux rope reaches the breakout current layer, it is explosively reconnected on to the ambient open field, launching non-linear Alfvén waves and driving a helical jet as the twist within the opened section of flux rope propagates away.

This chapter, discusses the mechanisms for confined filament eruptions in multi-polar topologies and the links to solar flares and jets. Multi-wavelength observations are utilised of a confined filament eruption from the Swedish Solar Telescope, Solar Dynamics Observatory, Big Bear Solar Observatory and El Teide Observatory. These observations provide a unique perspective of the area surrounding the filament eruption and also the inferred magnetic field topology prior to the flare. To aid in the interpretation, reference is made to a modification of the Wyper et al. (2017, 2018) jet model, where a filament channel eruption launches a jet confined along coronal loops. The details of the observations are given in §3.2 to §3.5 describing the filament eruption and jet. The observations are contrasted with the MHD simulation in §3.6, where an excellent qualitative agreement is found. Finally, §3.7 summarises the interpretation of the observations, whilst §3.8 discusses the broader ramifications of the work and presents the conclusions.

3.2 Observations

3.2.1 Ground Based

The SST observed a filament eruption associated with a C1.5 class solar flare on the 30th June 2013 in AR 11778 close to the disk centre, where the observations were made using CRISP. The observations consist of a series of images scanning the Hα spectral line in the range of $\pm$1.38Å with 50 milli-Angstrom equidistant steps resulting in 33 spectral line positions scanned. Overall, the active region was observed for approximately one hour at a temporal resolution of 7.27 seconds with the eruption and flaring occurring within the first 5 minutes.

The CRISP FOV is corrected for solar tilt and the bright points in the wideband images are cross-correlated with those in SDO/AIA 1700Å for co-alignment, achieving a sub-AIA pixel accuracy in the CRISP pointing and establishing a heliocentric coordinate system for CRISP. Sub-AIA pixel alignment of the CRISP pointing is achieved as a result of a cross-correlation of the most intense CRISP pixel within the AIA pixel space of 10 coincident bright points (initially identified by eye within a Graphic User Interface (GUI)). Then the CRISP pixel space, within the AIA bright point, is explored for each of the 10 bright points in order to maximise the correlation and a correction to the pointing information of CRISP is established. As a result, the CRISP observations are centred on $(x, y) = (323.36\,\mathrm{arcsec}, -287.91\,\mathrm{arcsec})$ with a roll angle of 62.04°. Each pixel contains the 33-point spectral scan of Hα and this makes up the spectral data cube for investigation using the CRisp SPectral EXplorer (CRISPEX: Vissers and Van Der Voort, 2012)). The standard procedure for the reduction of CRISP is given by de la Cruz Rodriguez et al. (2015), and includes a correction for differential stretching. Post-processing was applied to the data sets using the image restoration technique Multi-Object Multi-Frame Blind Deconvolution (MOMFBD), as outlined by Van Noort et al. (2005). Overall, this data reducing process was completed by Eamon Scullion a collaborator within this project who was also responsible for the observation and collection of the data.

GONG full-disk Hα images were used as context observations to identify and monitor the filament emergence from its first appearance until it eventually erupts. These images were vital in the determination of the events which unfolded within the eruption.

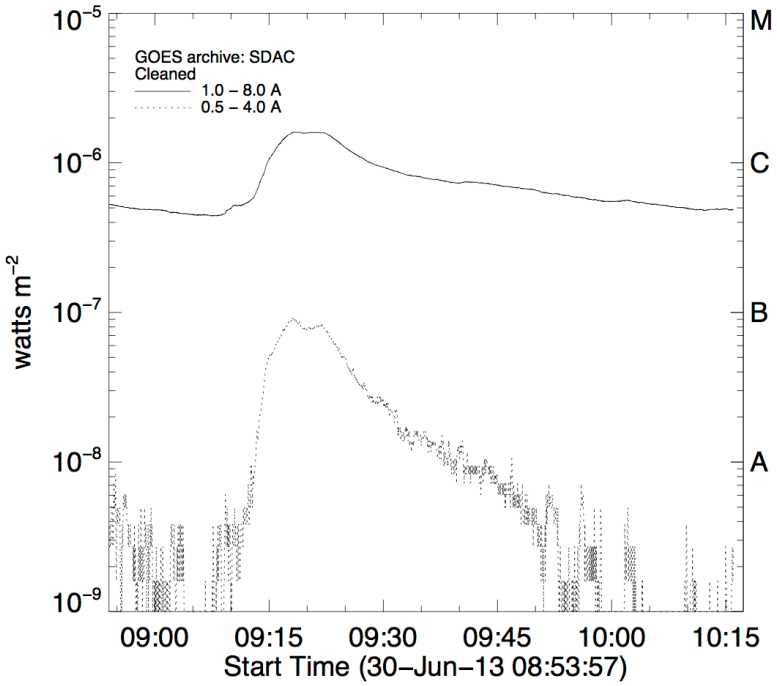

Figure 3.1: The GOES lightcurve for the time of the SST/CRISP observations which show this flare event as a C1.5 class flare in the 1.0 - 8.0Å channel.

3.2.2 Space Based

The GOES (Bornmann et al., 1996) soft X-Ray lightcurve of the C1.5 solar flare is presented in Figure 3.1, showing the flare beginning at 09:11UT with a peak at 09:18UT. For analysis of the flare ribbons in this flare event in particular, including HXR and high energy signatures, refer to Druett et al. (2017).

Data was utilised from AIA as well as HMI on board the Solar Dynamics Observatory (SDO). In this chapter, observations across multiple AIA channels are utilised, including 131Å (1.9×10^5 - 2.5×10^7 K), 171Å (2×10^5 - 2.5×10^6 K), 211Å (63,000 - 6.3×10^6 K) and 304Å (40, 000 - 2×10^6 K) where the temperatures correspond to the passbands of each AIA channel according to the AIA response functions. Additionally, the peak temperature of 131Å, 171Å, 211Å, and 304Å are 6.3×10^5 K, 7.9×10^5 K, 1.7×10^6 K and 80,000 K respectively, covering flaring regions, transition region, the corona and chromosphere within the solar atmosphere. This allows us to view the flaring active region, thereby, providing a larger FOV (in comparison with CRISP) and broader context of the overlying magnetic topology and subsequent evolution of the filament eruption prior to the flare. HMI magnetic flux images are also used to provide

a clear interpretation of the magnetic topology of the active region photosphere containing the filament. Data reduction was carried out using SSWIDL `aia_prep` for SDO instruments and for GONG preprocessed data from the online data archive[1] was acquired.

3.3 Pre-eruption Magnetic Configuration

In order to determine the origin of the flaring event and filament eruption, HMI magnetograms from SDO are used together with coronal loop observations from AIA to infer the topology of the active region magnetic field. Two days prior to the flare (27th June 2013) the active region exhibited a simple bipolar photospheric magnetic field footprint. Throughout the 28th June 2013, a patch of negative field (hereafter referred to as the *parasitic polarity*) emerges into the positive field region, creating the embedded bipole surface field associated with a coronal null point (e.g. Antiochos, 1990; Masson et al., 2009; Sun et al., 2013; Kumar et al., 2018). Between the 29th and 30th June 2013, the parasitic polarity appears to weaken and fragment as it evolves into the positive field.

Figure 3.2 shows the pre-flare bipolar magnetic field structure of the active region before, (a), and after, (b), the emergence of the parasitic polarity region. Note the negative polarity within panel (a) is a result of transient flux emergence and does not become a part of the parasitic polarity. Panels (d) to (f) show Hα and EUV images after the emergence. In the Hα sequence associated with image (d) a ring filament can be seen appearing in the upper right hand corner which corresponds to the location of the PIL surrounding the parasitic polarity in the HMI magnetogram (b). The filament forms and develops over 24 hours and this is simultaneous with the beginning of the flux emergence in HMI. The EUV images in panels (e) and (f) show that new connections have been formed between the negative parasitic polarity and the surrounding positive polarity in the classic anemone shape associated with a coronal null point (Shibata et al., 1994). From comparing the large-scale coronal loops, the filament position and magnetogram it can be inferred the ring filament has formed beneath the spine-fan topology of a coronal null. An outer spine is therefore expected to follow the large-scale loops and connect to the surface in the negative magnetic flux concentrations on the left hand side of

[1] http://halpha.nso.edu/

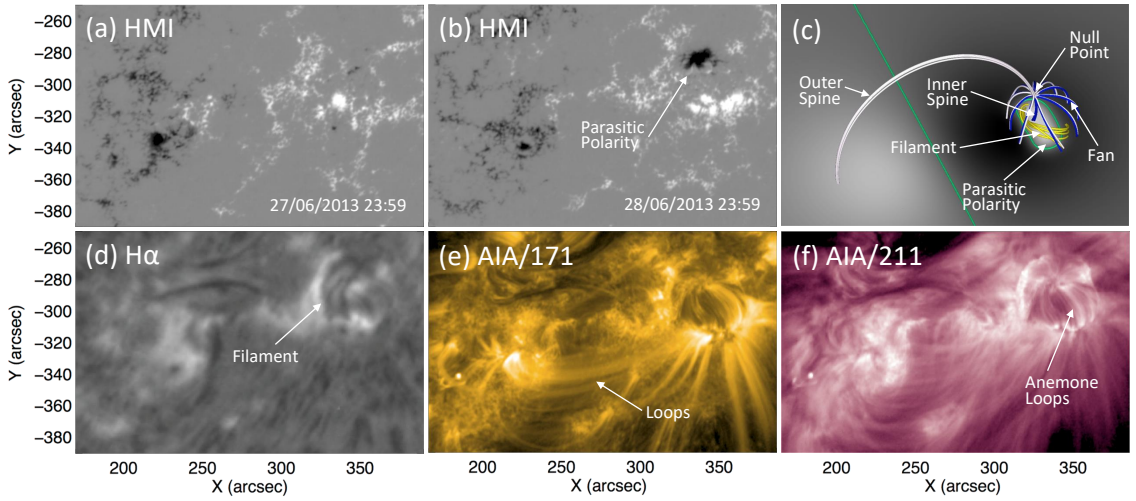

Figure 3.2: Here multi-wavelength observations of the active region are shown where (a) and (b) represent the HMI magnetograms before and after the parasitic polarity appears, respectively. These images are taken 24 hours apart on the 27/06/2013 23:59UT and 28/06/2013 23:59UT. Panel (c) shows the pre-flare magnetic field of the simulation where the green lines denote the PILs. Surface shading shows the normal component of the magnetic field scaled between ± 240 G. Panels (d) - (f) show the active region after the parasitic polarity emerges at 23:59UT on 28/06/2013 in Hα, 171Å and 211Å. The FOV for each of the HMI, AIA and Hα images is $220\,\mathrm{arcsec} \times 140\,\mathrm{arcsec}$ and is centred on $(x, y) = (280\,\mathrm{arcsec}, -320\,\mathrm{arcsec})$.

the magnetogram. For an illustrative comparison, in Figure 3.2(c) the pre-flare magnetic field structure of the 3D MHD simulation is shown which contains the basic constituent features of the observations described. Note that the surface field polarity is reversed with respect to the observation.

Figure 3.3 describes the temporal evolution of magnetic flux and the average magnetic field strength of the parasitic polarity, spanning before and after the flare. To construct the time profiles in panel (b), the parasitic polarity field concentrations are identified within the enclosed box of panel (a) using intensity contours at the level of -100 Gauss; this is denoted by the yellow contour in (a). Panel (b) shows that the parasitic polarity first appears on 27th June 2013 at 15:59 UT and it grows in size and strength for approximately 1.5 days reaching a peak intensity on 29th June 2013 at 00:00 UT.

After this the parasitic polarity begins to fragment and disperse covering a larger area ondisk and by 2nd July 2013 it had disappeared. Overall, it had a total lifetime of 3 - 4 days, with the flare under study occurring approximately 33 hours after the peak in magnetic flux. During the cancelling of magnetic flux there were brightenings in the AIA hot channels at the Hα filament

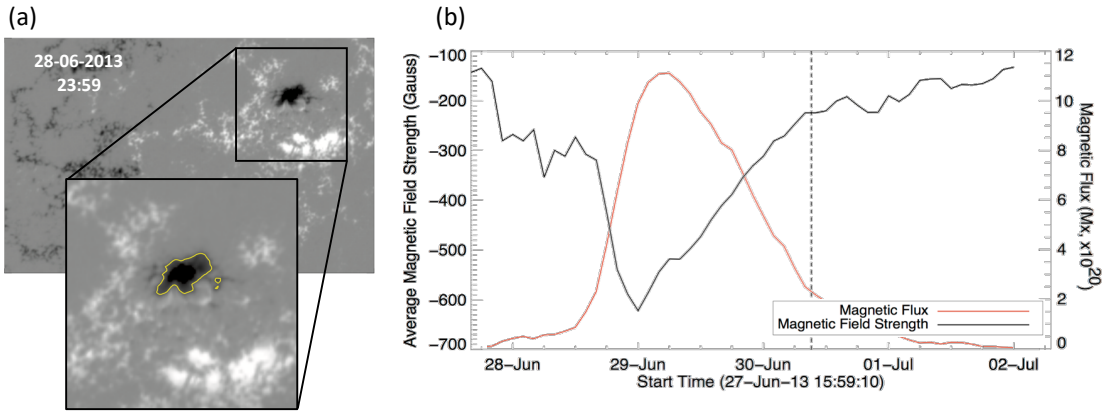

Figure 3.3: Panel (a) is a zoomed in view of the parasitic polarity detailing the contoured region in yellow as the area used to derive the magnetic field strength and magnetic flux. Panel (b) shows the average magnetic field strength (black line) of the contoured area of the parasitic polarity and corresponding magnetic flux (red line) with respect to time. The black dashed line represents the flare onset time of 09:11UT.

location, which may be indicative of small scale magnetic reconnection events.

3.4 The Filament Eruption

Figure 3.4 is a four image sequence from (a) - (d) spanning 10 minutes before and during the eruption with respect to 171Å. Equivalent image sequences in Figure 3.5 are presented in panels (a) - (d) with respect to 304Å and panels (e) - (h) with respect to the hot coronal "flaring" line 131Å. For context, the FOV is shown by the zoomed image of the magnetogram in Figure 3.3(a). In panel (a) the clear structure of the filament lying along the left section of the quasi-circular PIL is observed. Four minutes later, as shown in panel (b), the filament has started to erupt. At this time bright loops appear to the right of the rising filament which increase in brightness over time as the filament erupts, panels (c) and (d). Further brightenings are also observed immediately adjacent to the rising filament at these times in 171Å and in 131Å. As will be discussed further in §3.6 these brightenings are signatures of breakout and flare reconnection, respectively. Throughout this phase of the eruption the filament material is accelerated, moving from the north east to the south west of the region.

In Figure 3.6, the AIA observations in 304Å, 171Å, and 131Å detail the next phase of the eruption. Panels (a) - (d) demonstrate that soon after beginning to erupt the filament material is transferred to the extended (overlying) active region coronal loops, where it then propagates

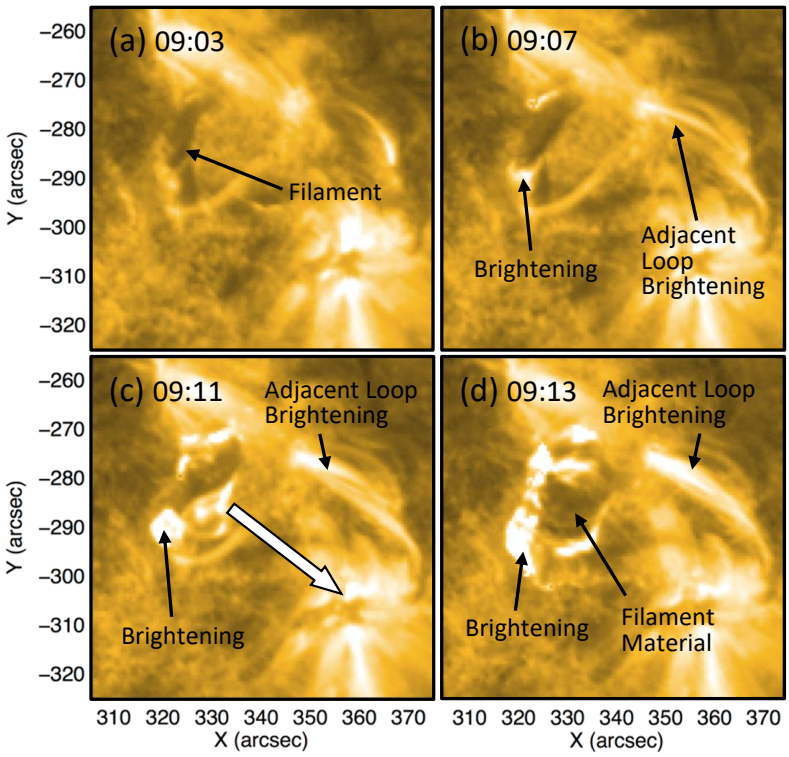

Figure 3.4: Observations in AIA 171Å of the active region before and during the filament eruption detailing the brightenings adjacent to the filament as a consequence of magnetic reconnection. The white arrow represents the direction of the erupting filament material. The FOV is $70\,\mathrm{arcsec} \times 70\,\mathrm{arcsec}$ and is centred on $(x, y) = (340\,\mathrm{arcsec}, -289\,\mathrm{arcsec})$, it is the same FOV as the zoom in box in Figure 3.3(a).

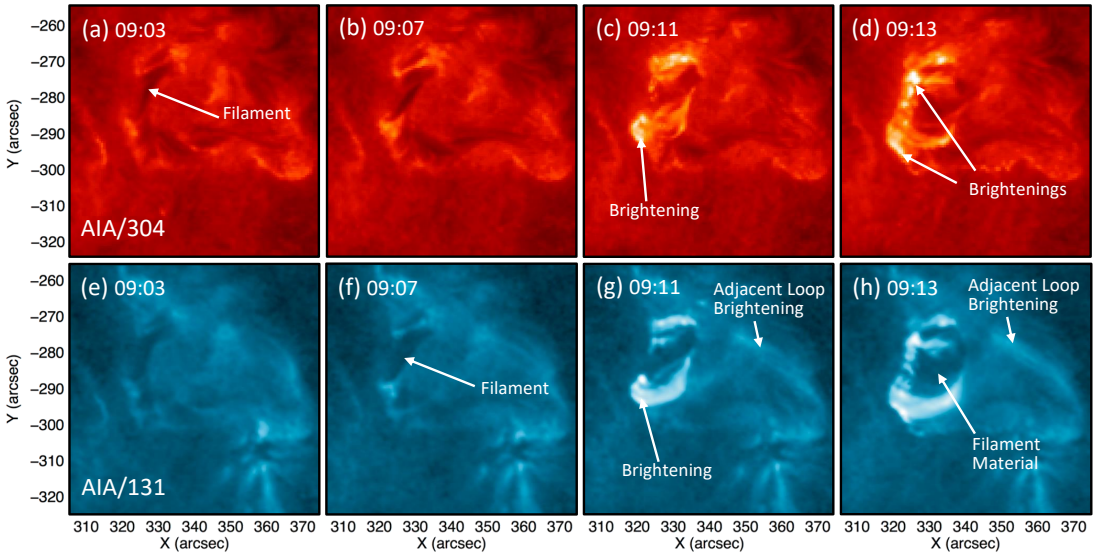

Figure 3.5: Observations in AIA 304Å and 131Å of the active region before and during the filament eruption detailing the brightenings adjacent to the filament as a consequence of magnetic reconnection. The FOV is $70\,\mathrm{arcsec} \times 70\,\mathrm{arcsec}$ and is centred on $(x, y) = (340\,\mathrm{arcsec}, -289\,\mathrm{arcsec})$, it is the same FOV as the zoom in box in Figure 3.3(a).

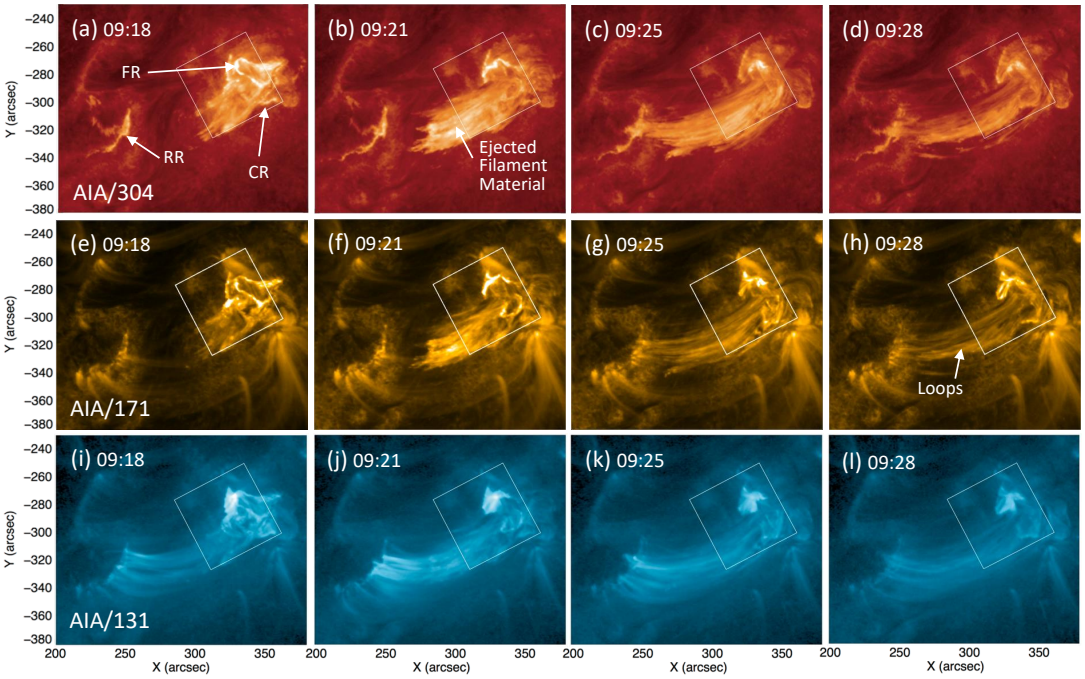

Figure 3.6: A sequence of AIA images in 304Å 171Å and 131Å spanning a total of 10 minutes after the filament eruption has started. The FOV is $180\,\mathrm{arcsec} \times 150\,\mathrm{arcsec}$ and is centred on $(x, y) = (290\,\mathrm{arcsec}, -305\,\mathrm{arcsec})$ and the white box represents the CRISP FOV. Abbreviations are as follows: Circular Ribbon = CR, Remote Ribbon = RR, Flare Ribbon = FR.

eastward in the form of a large-scale outflow (jet) back to the surface, making the eruption completely confined within the active region. Such a transfer is only possible if the field lines supporting the erupting filament material have been reconnected through the null point. Figure 3.6(e) - (l) shows that the jet is also multi-thermal, i.e. also containing a heated plasma component, consistent with this picture. The multi-thermal jet appears to flow within or beneath a set of substantially hotter overlying post-flare loops that already exist at the time of the formation of the jet, i.e. comparing panels (a) and (i).This is a result of the filament material being presumably denser that the hotter (outer) corona. Therefore, the filament was physically below these hot loops (seen in AIA/131) otherwise the loops would not be visible as their emissions would become absorbed by the filament.

Further evidence for reconnection through the null is provided by the flare ribbons. The brightest are the two parallel ribbons formed by flare reconnection beneath the erupting filament. However, also present is a remote flare ribbon and circular flare ribbon. All three ribbons (FR: Flare Ribbon; CR: Circular Ribbon; RR: Remote Ribbon) are shown in Figure 3.6(a). The remote and circular ribbons are the expected signatures of energy deposition in the chromo-

sphere from non-thermal particles accelerated near the null point that escape along the outer spine and fan plane, respectively (e.g. Masson et al., 2009). Druett et al. (2017) studied the Hα response of the southern section of the circular ribbon in this flare event and obtained excellent agreement with a 1D beam electron model.

SST/CRISP captured, in excellent detail, the crucial moments where the erupting material was transferred to the overlying loops and the jet was launched. Figure 3.7 shows the CRISP spectral image sequence of the filament eruption and flare ribbons, at four times in 50 s intervals, i.e. from 09:16:50 UT to 09:19:20 UT (rows) and at four wavelength positions (columns), sampling the Hα spectral profile. In panels (a) - (d), at the beginning of the sequence, the filament eruption is well underway. At this time the erupting filament material has formed an arch-like shape, having already erupted towards the south west (bottom right). The two flare ribbons are also visible near the continuum in the Hα wings of panels (a) and (d) which run parallel to the original location of the filament. The legs of the erupting structure appear to be connected to the surface near the ends of the parallel flare ribbons, as one would expect for a typical filament eruption. Also visible near the line core of panels (b) and (c) is the southward section of the circular ribbon which appears to connect to the base of the left-most flare ribbon at this time. The subsequent panels then show that over the next two and half minutes, filament material from around the southern leg of the erupting structure begins to be transferred to the overlying coronal loops, propagating away to the south east. This is most easily seen in the blue wing, e.g. (a), (e), (i) and (m). Accompanying this transfer of filament material is the development of a strong clockwise rotation of the filament structure. The above along with the simulation results (discussed below) further supports the conclusion that the flux rope supporting the erupting filament material has been reconnected on to the overlying loops near its apex, transferring plasma from its southward leg. This will be discussed in detail in §3.6.

3.5 Jet Kinematics from Hα profiles

In order to understand more about the plasma outflow and its development of rotation, a line fitting analysis was carried out on the CRISP Hα observations. This section looks to describing

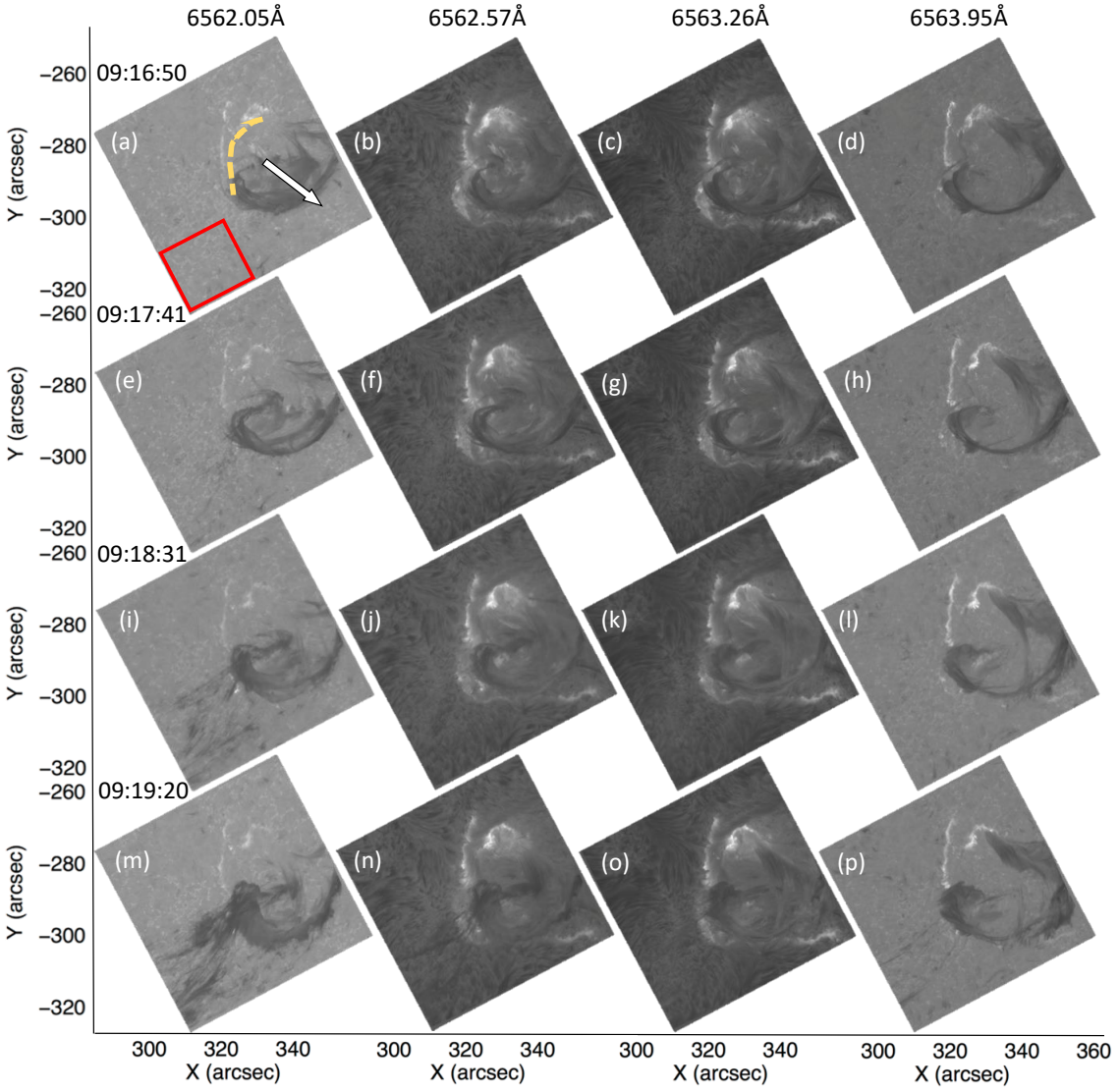

Figure 3.7: This mosaic of CRISP Hα spectral images from (a) - (p) shows the observed filament eruption in varying wavelengths at different times. Each column represent a different wavelength position within the Hα line profile. The rows then represent the time stamps which span a total of 2.5 minutes and show the evolving untwisting filament feature. The red box in panel (a) represents the quiet Sun region used to calculate the rest wavelength profile and the dashed yellow line is the filament location prior to erupting. Additionally, the white arrow represents the direction of the erupting filament material. The FOV for each image is $60\,\mathrm{arcsec} \times 60\,\mathrm{arcsec}$ and is centred on $(x, y) = (323.6\,\mathrm{arcsec}, -287.91\,\mathrm{arcsec})$.

the analysis techniques used and the resulting output which details the jet kinematics of the plasma flows.

3.5.1 Fitting the Hα profiles

Due to the complex spectral line deformations within various spatial pixels throughout the eruption, several multi-Gaussian fit functions were applied in order to identify which combination of Gaussian functions could achieve the overall best spectral line fit, following a reduced χ^2 minimisation test. Every pixel was fitted with a single, double and triple Gaussian and the χ^2 statistic was minimised to achieve the best fit to the line profile. For the double and triple Gaussian fits, constraints were placed on the centroid wavelength of each Gaussian. This enabled the Gaussian components to fit the various features of the profile, especially when it was highly blue or red shifted. The constraints for the centroids of the double Gaussian are 6561.62 - 6563.1Å and 6563.1 - 6564.37Å and the triple Gaussian 6561.62 - 6562.82Å, 6562.82 - 6563.25Å and 6563.25 - 6564.37Å. In addition, the background level was set as a standard polynomial fit with zero degrees (i.e. a constant) and was not constrained. The reduced χ^2 obtained could then be used to select the most appropriate fit function on a pixel-by-pixel basis and for all spectral scans in time. This process was completed for all pixels in the first 30 time frames of the observation, consisting of the full duration of the filament material transfer.

In order to simplify this process a block fitting routine was implemented, available within SSWIDL, called `cfit_block`. In addition, all of the profiles were normalised to each of their maximum y-values, making up the background (zero) level. Once the iterative fitting process is completed the resulting output is a data structure consisting of the centroid wavelength position, amplitude and Full Width at Half Maximum (FWHM) for each Gaussian fit component, for each time frame, from which investigations of the evolving spectral profiles are possible in greater detail.

Figure 3.8 shows example fits for a pixel within the filament eruption, (b), and a quiet Sun pixel away from the event, (c). The corresponding components of each of the fit functions are also shown, within 4 sub-panels to the right of (b) and (c), for completeness. By applying the

reduced χ^2 minimisation method and identifying the fitting combination that maximises the number of zero-line crossings in the goodness-of-fit residuals, it is possible to iterate through all pixels at all times. This process of selection of best fit functional form results in the assignment of a key value from 1 - 3 for each pixel, in order to create a map of the preferred fit as being either single (1), double (2) or triple (3) Gaussian. Further details on the distribution of functional fits for the FOV and more examples of line fits to complex absorption profiles are given in Figure 3.14.

There are other statistical methods to determine the best model to fit the spectral line profiles. For example, the Akaike Information Criterion (AIC) can be used as a tool for model selection as it estimates the quality of each model. It uses the number of model parameters and the maximum value of the likelihood function to determine this (see Morton et al., 2012). When AIC values are applied to the single, double and triple Gaussian models they consistently return the same best fit model to the spectral line profile as does using the reduced χ^2 and maximising the number of zero line crossings. Therefore, the approach used in this analysis is an acceptable method for determining the best model fit.

3.5.2 Producing Line-of-Sight Velocity Maps

An important parameter obtained from the fitting routine is the centroid wavelengths of each Gaussian component. These wavelengths can be used to calculate the corresponding Doppler velocities of the line profiles which can represent plasma upflows and downflows. To calculate the Doppler shift from the Gaussian fit components, a rest wavelength was obtained from the averaged quiet Sun profiles (see Figure 3.8a) summed over a section of pixels in the SST FOV away from the flaring and eruption regions (see Figure 3.7a). Using the rest wavelength of 6563.06Å determined from the profile obtained from the quiet Sun profiles, the Doppler velocity of each pixel at each of the 30 time frames can be computed to produce velocity maps as the erupting filamentary material is transferred into the confined jet. With regards to the triple Gaussian best fit pixels, it is possible to construct Doppler velocity maps of the plasma flows in the blue wing, core and red wing. Overall, the primary concerns are with the motions of the erupting filament material which focus on the highly blue-shifted and red-shifted components within the velocity maps, largely arising from double Gaussian best fits. Now I

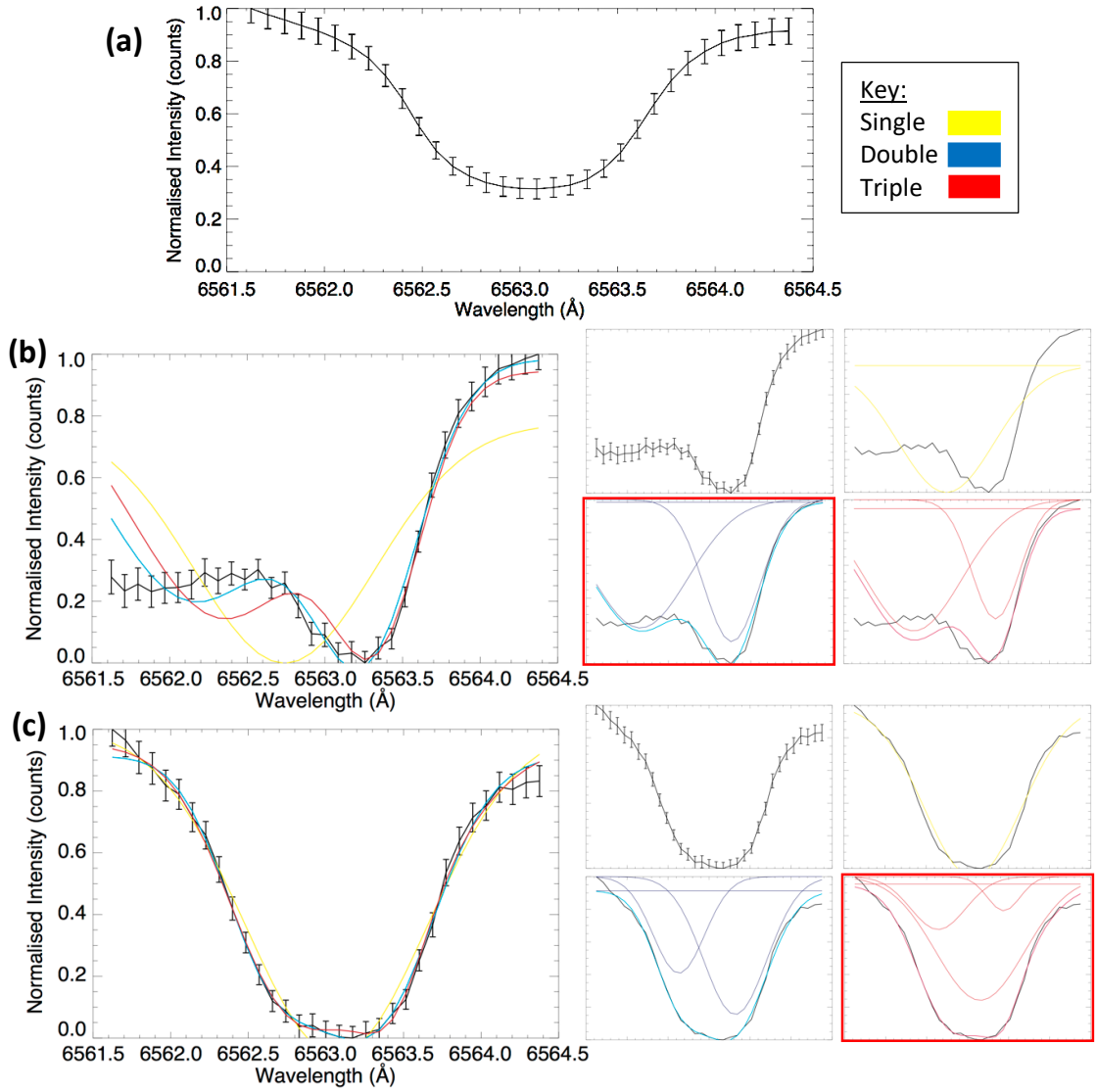

Figure 3.8: Gaussian fits to the Hα absorption profiles are presented for a number of cases in panel rows (a) - (c). Panel (a) presents the normalised, rest Hα line profile along with the associated errors on each wavelength point.This normalised profile is made up from the averaging of thousands of quiet sun profiles from the last frames in the SST data when the filament has erupted and is not within the FOV. Panel (b) presents spectral line profile fits for a pixel sampling the moving/outflowing filament which exhibits a highly blue-shifted wing component. As a result of this, the double Gaussian model, highlighted within the red-boxed sub-panel provides the best fit to the data. The individual components of each Gaussian model are also presented in the sub panels. Panel (c) presents the line profile fit for a quiet Sun pixel location showing a relatively unshifted Hα profile. The triple Gaussian model fits the line best here and is highlighted within the red-boxed sub-panel.

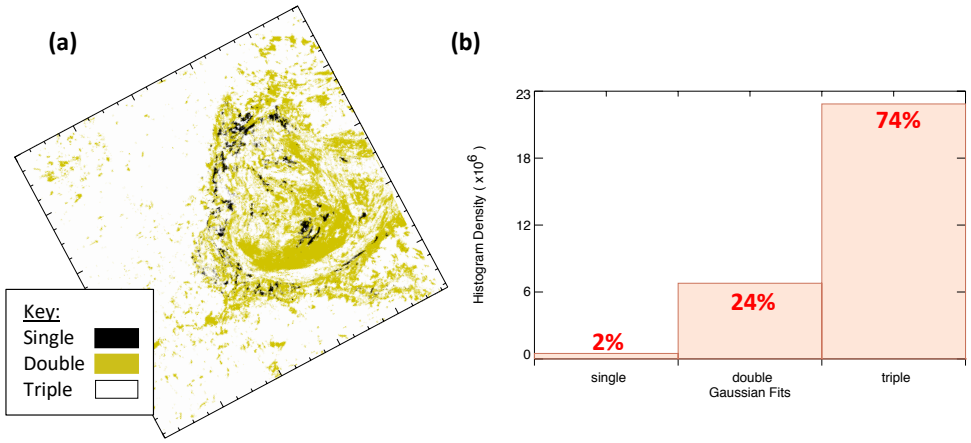

Figure 3.9: The two figures convey the statistics of the fitting method used. (a) A snapshot of which features within the SST/CRISP FOV prefer particular Gaussian fits. It can be seen that the majority of the filament eruption is fitted with a double Gaussian, whereas the background quiet Sun requires a triple Gaussian. (b) A histogram detailing the percentage of pixels in all time frames in the SST/CRISP FOV which preferred each of the three fits.

will discuss how these maps were constructed and the statistics of the fitting method as a whole.

Producing the velocity maps involves a selective process which iterates through all pixels at all times and assigns each pixel a key value from 1 - 3 which informs whether the pixel is best fitted by a single, double or triple Gaussian, according to the χ^2 minimisation together with maximising the number of residual crossings. This 'key', shown in Figure 3.9(a), can then be used to construct velocity maps in the blue wing, core and red wing. Where a single Gaussian was preferred the core map would be assigned the velocity component and the blue and red wings would be 0 km/s, as there is no component of large blue or red shift in these profiles. If a triple Gaussian was preferred then each Gaussian component was assigned to the blue, core or red wing. In addition, if the amplitude of the Gaussian in the blue or red wing was less than a background intensity it was removed from the maps. This was designed to eliminate all the random small velocity movements in the background quiet Sun (i.e. spicules etc.) as the main concern lies with the large velocity movements associated with the extended line wings corresponding to blue and red shifted components of the Hα component of the jet. Lastly, if a double Gaussian was preferred, and if centroids lie within the FWHM of the Hα profile then the velocity is calculated from an average of the two centroids and applied to the core map. Similarly, if one of the centroids lies within the FWHM it is applied to the core map and

the remaining Gaussian centroid lies outside the FWHM it is assigned to the red or blue maps depending on its location.

In Figure 3.9(b), the histogram details which Gaussian fits were preferred for the line profiles from all pixels during the first 30 time frames where the untwisting jet occurs. As you can see the triple Gaussian is the most preferred fit to the line profiles with 76%, double 24% and single 2%. From the key image, Figure 3.9(a), it can be seen the triple Gaussian fits are located in the background quiet Sun regions which is to be expected. This is because, these profiles are very similar to the rest Hα profile and by providing more free parameters reduces the χ^2. Double Gaussian fits were preferred in the region of the filament where the highly red and blue shifted plasma is located and single fits in the locations of the flare ribbons. This is a result of the fact that the core chromosphere is being emptied during the event at the location of the filament so, the core red and predominantly blue will become subsequently shifted which, then becomes best fitted with two distinct Gaussians that neglect the rest wavelength intensity. Overall, this histogram shows the significance of the fitting method implemented and the need for multiple fit functions. For full disclosure of the profile fitting of the Hα absorption line in this study a wide variety of single, double, triple and unsuccessful fits are shown in Figure 3.14.

3.5.3 The Velocity Maps

In Figure 3.10 each panel represents a different time step beginning at 09:15:54 UT and ending at 09:19:06 UT. Each panel image represents an amalgamation of the red and blue velocity maps which correspond to the red and blue wing components revealing the locations of the largest outflows. In Figure 3.10(a), the inferred shape of the erupting filament is shown as a dashed yellow line. The top portion of the arch shaped erupting filament is strongly blue-shifted (reaching at least 60 km/s), whilst plasma in the legs to the left and top right is red shifted ($\approx$ $+$45 km/s). The red shifts show that filament plasma in the legs is moving downward towards the solar surface, whilst the plasma near the top of the arch is being ejected upwards. Similar plasma motions are routinely observed in large-scale filament eruptions, (e.g. Pant et al., 2018, and references therein). Based on its similarity to large-scale eruptions in this phase, it can be conjectured that the downflows are predominantly due to mass draining along the legs as they

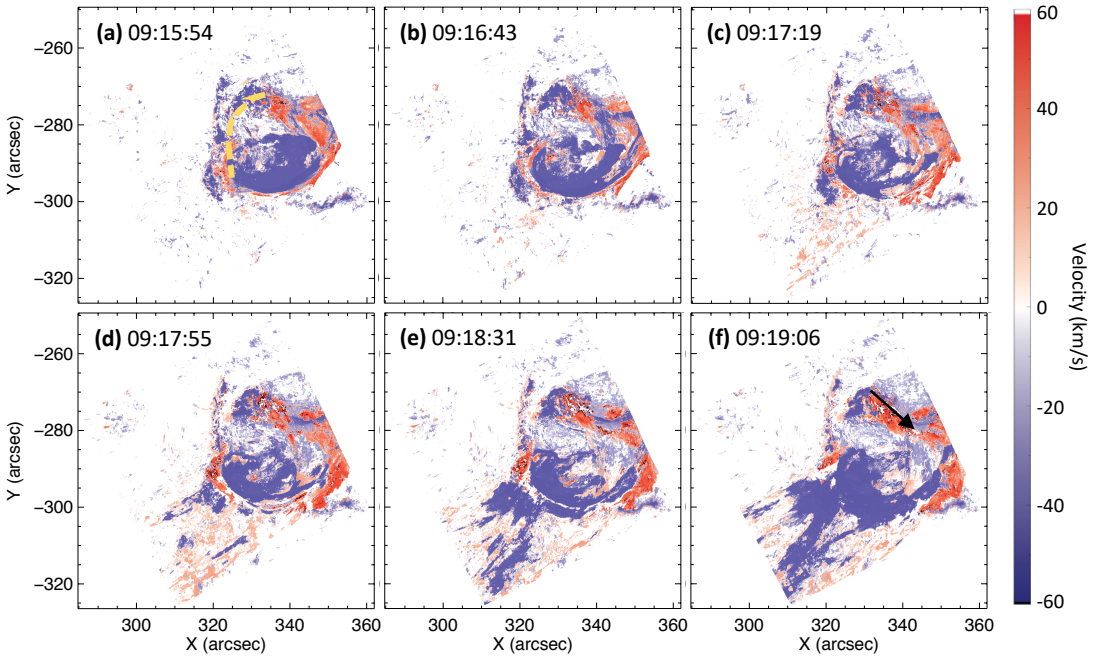

Figure 3.10: Velocity maps constructed as an amalgamation of the extremely blue-shifted and red-shifted components within the filament eruption. The dashed yellow line represents the filament location prior to erupting and the black arrow the flows which move downwards to the solar surface.

become angled upwards, however other mechanisms such as driving from pressure gradients or magnetic tension can not be discounted. Note that due to the wavelength window available for making these maps, the inferred velocities are effectively limited to ± 60 km/s. Therefore, the true line of sight velocity in the strongly blue shifted regions could be much higher.

Over the next few minutes, i.e. panels (b) - (d), the filament material develops fine structure and becomes transferred on to the longer active region loops (flowing towards the south-west in each panel). The transferred material remains strongly blue-shifted and begins to rotate clockwise as it propagates away to the bottom left. Although more structured, the red shifts of the right-most leg continue to generally show downflows throughout this time. Downflows near the foot point of the other leg are also visible next to the strongly blue-shifted material in the jet. Therefore it is found that downward as well as upward motions of the filament material occur during the filament eruption and further confirm the conjecture that reconnection of the erupting flux rope near its southern leg is responsible for launching the filament plasma into the jet.

3.6 3D MHD Simulation

This section was completed in collaboration with Peter Wyper from Durham University who was responsible for the simulations. I will discuss the simulations here with regards to the comparison to the observations, therefore, for the full details of the MHD simulation set up please refer to Doyle et al. (2019).

3.6.1 Setup

To explore the conjectures further a 3D MHD simulation was conducted with the Adaptively Refined Magnetohydrodynamics (ARMS code: DeVore and Antiochos, 2008) for qualitative comparison with the filament eruption and jet in the observed event. The key details of the simulation setup are described below. For further specifics please refer to the full published paper Doyle, Wyper, Scullion, McLaughlin, Ramsay and Doyle (2019).

The simulation was initialised with a uniform background plasma and a potential magnetic field containing a large-scale bipole with a small-scale embedded parasitic polarity. The resulting field has a similar 3D magnetic null point topology to the one inferred from the observations. The system was then energised using surface motions which formed a small-scale filament channel beneath the null point in a similar position to the observed filament. This method of creating the filament channel is simply a numerically convenient way of introducing the free magnetic energy where it is wanted and is not meant to reproduce how this particular filament was formed. The surface driving is then halted once the filament channel has formed, and the system allowed to evolve without external forcing from this point onward. Field lines showing the filament channel and the spine-fan topology of the null point in the simulation just before eruption are shown in Figure 3.2(c).

3.6.2 Eruption evolution

The simulated filament channel eruption proceeds in the same manner as the coronal hole jet simulations reported in Wyper et al. (2017, 2018). Figure 3.11(a) shows the filament channel (yellow field lines) prior to eruption. Four other field line regions are also shown: cyan –

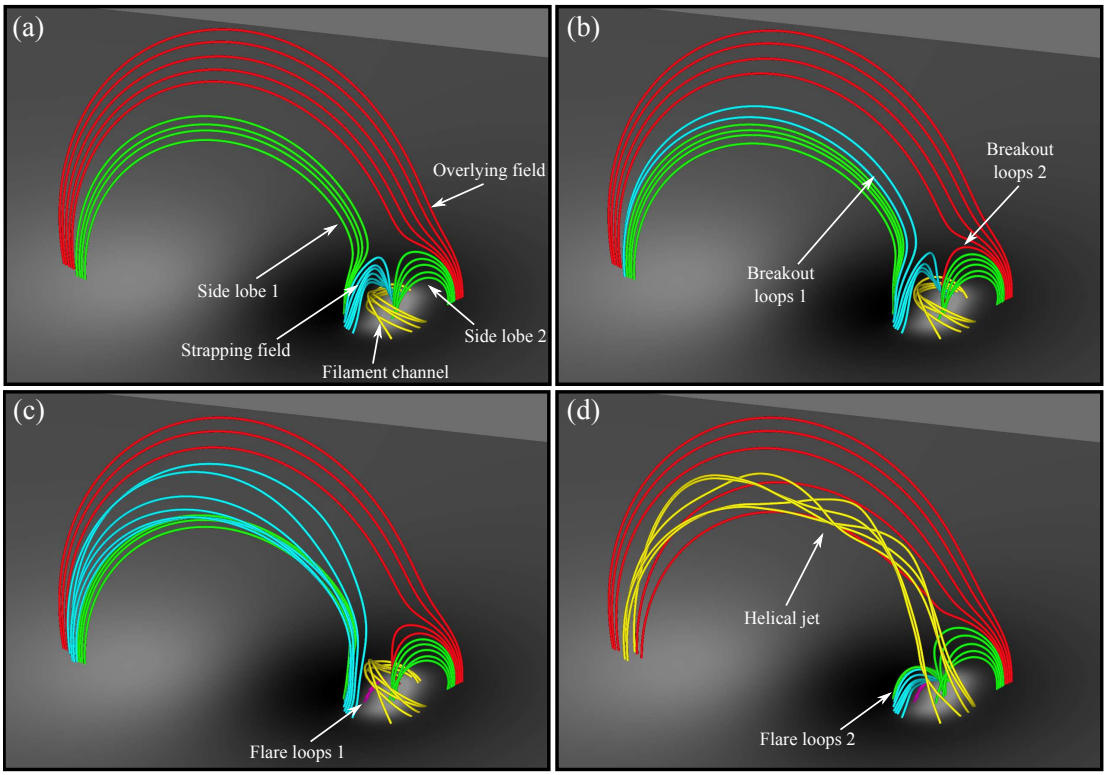

Figure 3.11: Field lines showing the eruption of the filament in the MHD model. Yellow: the filament channel. Cyan: overlying strapping field. Green: side lobe regions. Red: overlying background field. (a) t =12 min 55 s, (b) t =14 min 35 s, (c) t =16 min 15 s, (d) t =17 min 5 s.

overlying strapping field; green – side lobe regions (1 and 2) and red – overlying background field. The null point resides where the four regions meet each other, with the closed outer spine following the path between the overlying (red) and side lobe 1 (green) field lines.

The increasing magnetic pressure within the filament channel expands the overlying strapping field upwards, quasi-statically balancing the outward magnetic pressure with magnetic tension. However, this expansion also stresses the null point so that a current sheet forms there (the breakout sheet). Reconnection within the sheet then slowly transfers the strapping field to the side lobe regions, reducing the downward magnetic tension force on the filament channel and allowing it to rise, Figure 3.11(b). This leads to a faster rise, which in turn leads to faster breakout reconnection (the breakout feedback mechanism). Although the simulation does not include dense chromospheric plasma and the effects of gravity, you would still expect a similar qualitative evolution in a magnetically dominated low-β plasma. However, the timing and speed of the filament rise might be expected to alter slightly.

The reconnected strapping field forms new coronal loops in the two side lobe regions, labelled breakout loops 1 and 2 in Figure 3.11(b). Loops 1 form nearby to the original position of the outer spine, whereas loops 2 form beneath the domed fan plane separatrix. The rising filament channel also stretches the strapping field, creating a flare current layer beneath it. Tether cutting/slipping flare reconnection within this layer converts the sheared arcade into a twisted flux rope, whilst also forming short flare loops beneath, Figure 3.11(c) (flare loops 1).

Although not explicitly included in the simulation, one would expect enhanced coronal EUV emission associated with both the flare and breakout loops. As such, the origins of the observed brightenings shown in Figure 3.4(b) during the filament eruption now become clear. The adjacent loop brightening shows new loops formed by the breakout reconnection of the strapping field, i.e. breakout loops 2. Interestingly, at this time there is no clear coronal EUV signature of loop heating associated with breakout loops 1. This may be because the deposited energy from the breakout reconnection is spread over a much larger volume than that for breakout loops 2, reducing the intensity of emission. The brightening beneath the filament shows bright, heated plasma within the flare loops. Such energy release beneath the erupting filament material implies flare-like reconnection has set in beneath the erupting material. This flare reconnection forms a flux rope in the model (in common with all eruptive flare models). Therefore, it can be inferred that if a flux rope was not already present prior to eruption, it will be by this point in the evolution.

Returning to the simulation, the rise of the flux rope then accelerates as the feedback loop sets in between the flux rope rise and the removal of strapping flux via breakout reconnection. This continues until all of the strapping field is reconnected away, Figure 3.11(c). Such a feedback loop could explain the steadily increasing intensity of the flare and adjacent loop brightenings shown in Figure 3.4(c) - (d). Beyond this time in the simulation, the rising flux rope itself begins to reconnect with the overlying field. The end of the flux rope rooted in the background negative polarity is then connected on to distant closing field lines, whereupon the twist begins to propagate along the loops as a non-linear Alfvén wave, Figure 3.11(d) (yellow field lines). The end of the flux rope rooted in the minority polarity reforms the filament channel, but now with a reduced shear (not shown). A similar evolution of the erupting flux rope is inferred in the observed event from the filament plasma evolution in the SST/CRISP images (Figs. 3.7

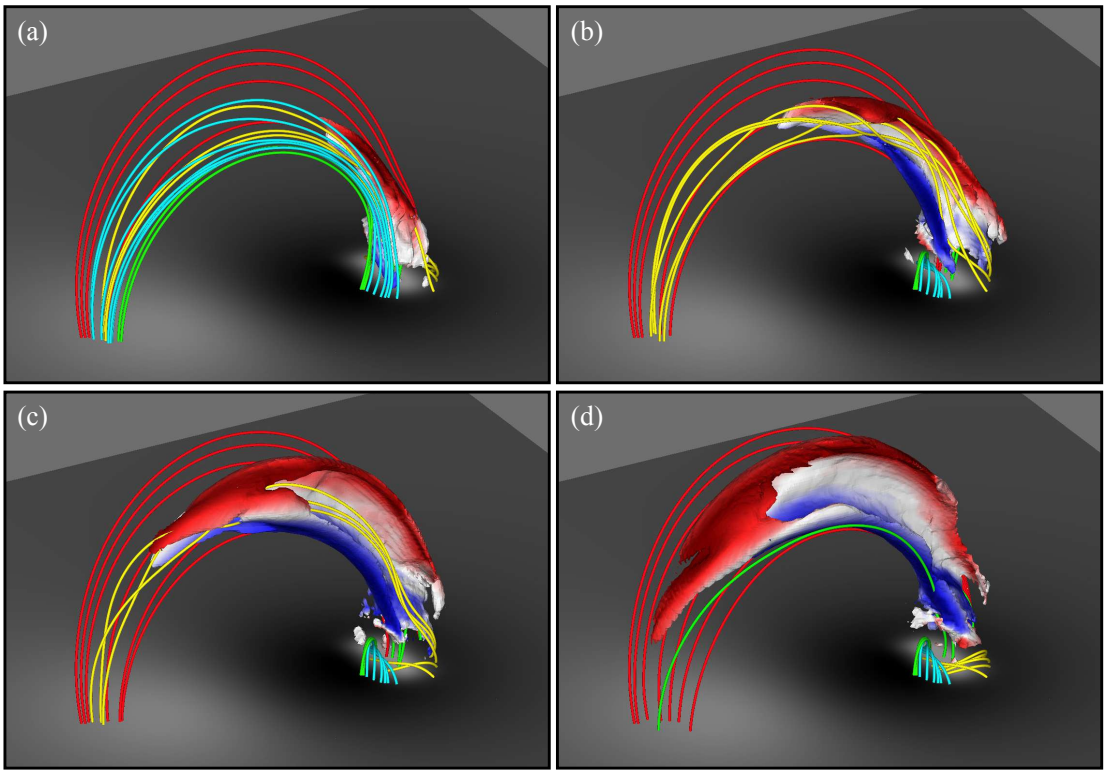

Figure 3.12: An isosurface of velocity ($|v| = 500\,\mathrm{km/s}$) showing the jet. The isosurface is shaded to show the v_z value (saturated at $\pm 500\,\mathrm{km/s}$), showing the jet rotation. (a): $t = 16\,\mathrm{min}\ 40\,\mathrm{s}$. (b): $t = 17\,\mathrm{min}\ 5\,\mathrm{s}$. (c): $t = 17\,\mathrm{min}\ 30\,\mathrm{s}$. (d): $t = 17\,\mathrm{min}\ 55\,\mathrm{s}$.

and 3.10). That is, in both the simulation and observation a rotating jet is produced when the erupting structure is reconnected, transferring its twist to the overlying field.

One further aspect of the field line evolution that is worthy of mention is that once the erupting flux rope is reconnected, the flare reconnection after this time transfers the flux moved into the side lobe regions in the breakout phase back into the overlying field and strapping flux regions, Figure 3.11(d) (red and cyan field lines). As discussed in detail in Wyper et al. (2018), once the flux rope is reconnected the null in the breakout current layer moves into the flare current layer beneath the erupting structure. Thus, the new flare loops formed after this time (flare loops 2) are through null point reconnection as opposed to tether cutting/slipping reconnection prior to this. Observationally, the signature of this transition should be that one of the parallel flare ribbons becomes part of the circular ribbon, as the two are now formed by energy deposition from the same reconnection region. This is precisely what is observed in the Hα (Figure 3.7) and EUV 304Å (Figure 3.6e) in the event as the jet is launched.

3.6.3 Helical Jet

Figure 3.12 shows an iso-surface of velocity depicting the plasma jet formed by the transfer of twist in the simulation. Qualitatively, the jet is very similar to the observation in that (i) it is helical in nature, (ii) it is guided along the ambient coronal loops back to the surface and (iii) it is formed from a mixture of ambient coronal plasma swept up by the reconnection and plasma from within the filament channel.

Quantitative comparison of the speeds, however, reveal that the simulation jet is significantly faster. In the simulated jet the plasma propagates at roughly the local Alfvén speed within the loop, reaching speeds of $\approx$ 450 km/s with typical coronal scaling values. This is higher than in the observation, where values of 60 km/s were recorded, Figure 3.10. However, as noted earlier, the wavelength window used for constructing the velocity maps leads to an effective cap of $\pm$60 km/s for the inferred velocities, with the real value expected to be higher. Additionally, the simulation uses a simplified atmosphere with a uniform background plasma and neglects gravity. As such, although the magnetic field structure of the filament channel is formed and evolved in a qualitatively correct manner, it does so in the absence of the denser, cooler filament material seen in the observation. It would not be unreasonable to expect that were such dense plasma be included, the propagation speed along the loop might be reduced by the locally slower Alfvén speed and the action of gravity. A more sophisticated simulation would be required to test this claim. Despite this, the close qualitative comparison between the observations and simulation, incorporating a simplified model atmosphere, serves to highlight the pertinence of reconnecting magnetic fields in dictating the overall dynamics of this event and the potential universality of this model in sufficiently describing a variety of similar events within differing atmospheres and on different scales.

3.7 Event Summary

In this work a detailed analysis of a confined filament eruption/flare and its associated helical jet is presented. Using observations from SDO/AIA/HMI, GONG and SST/CRISP the formation of the filament and its surrounding magnetic topology, the eruption and the subsequent jet

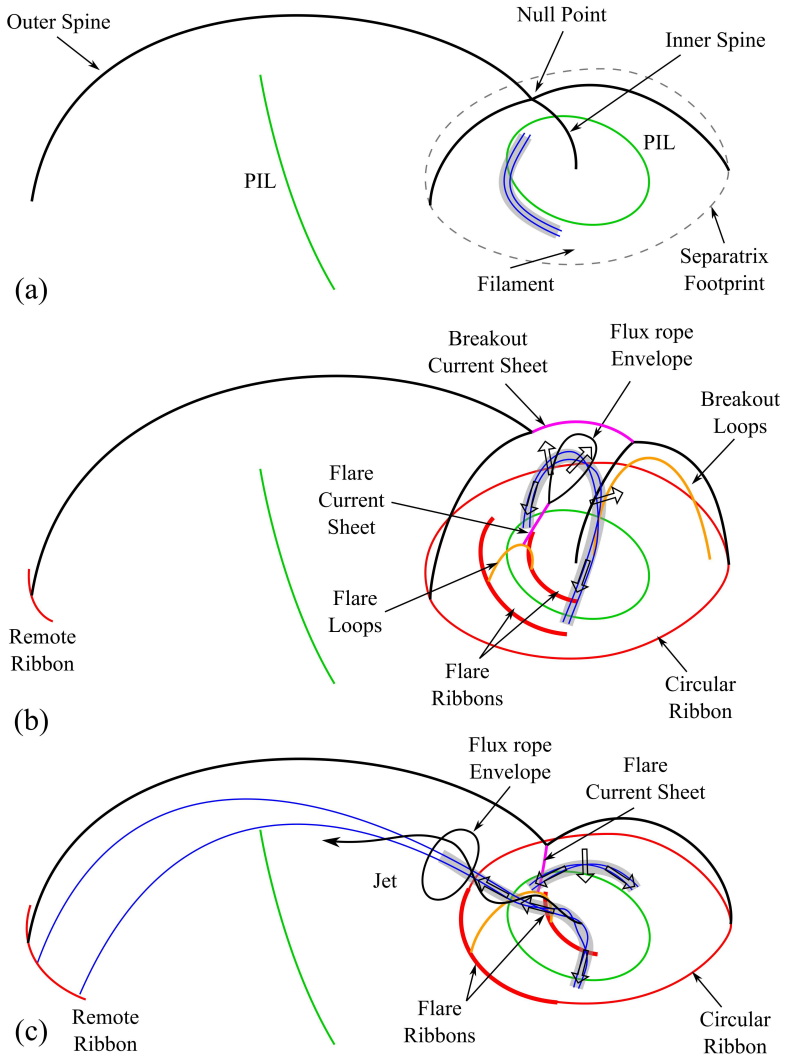

Figure 3.13: Schematic of the eruption. (a) pre-eruption. (b) during the breakout phase. (c) after the filament is reconnected and the jet is launched.

kinematics are all studied. In particular, the SST/CRISP observations gave us a detailed view of the transfer of filament material as the jet was launched. Qualitative comparison with a 3D MHD simulation of a closed-field breakout jet further aided the interpretation of the observations. Figure 3.13 shows a schematic which summarises the interpretation of the different stages of the confined eruption.

Figure 3.13(a) shows the configuration just prior to eruption. The filament (dark grey) resides along a section of the quasi-circular PIL (green) beneath the separatrix of the 3D null point. This configuration forms over ≈ 1.5 days as the parasitic polarity emerges. The evolution of magnetic flux in the parasitic polarity (Figure 3.3) suggest that a combination of flux emergence

and cancellation is involved in the formation of the filament.

Figure 3.13(b) shows the filament mid-eruption. The null point above the filament has collapsed into a breakout current sheet (pink). Breakout reconnection removes strapping field from above the filament, forming bright loops adjacent to the erupting material (breakout loops, orange). New loops should also be formed nearby the outer spine, but they are much less intense and not clearly observed in the event. Additionally, the upward stretching of the strapping field forms the flare current sheet beneath the filament material (pink). Reconnection in the flare sheet forms a flux rope if not already present (or adds further polodial flux if one is present initially) and bright flare loops (orange). The flux rope forms an envelope (cross section shown in black) around the erupting filament material which resides in its core. The material near the core is accelerated upwards with the erupting flux rope, whilst the material in the legs falls back to the surface (hollow arrows). Energy deposition from the breakout current layer creates circular and remote ribbons at the base of the fan and outer spine, respectively (thin red lines). Parallel flare ribbons also form at the base of the flare loops that stretch between the two feet of the erupting flux rope (thick red lines).

Once the erupting flux rope reaches the breakout current layer it is reconnected, Figure 3.13(c). This splits the flux rope near its apex, forming a new shorter closed loop along which downflows of filament plasma are observed (e.g. top right arrow, Figure 3.10(f)). The other section of flux rope is now connected to coronal loops with foot points nearby the original foot point of the outer spine. As the twist within the flux rope propagates along the loops, it drives a mixture of cooler, denser filament material and hotter, more tenuous heated plasma along these loops as a helical jet. At this point the flare current layer has reached the separatrix, so that the flare reconnection is actually null point reconnection. One of the parallel flare ribbons now forms a section of the circular flare ribbon, whilst the other outlines field lines near the foot point of the inner spine (thick red lines), e.g. Figure 3.6(a).

3.8 Discussion

The observations presented herein are consistent with the breakout picture for jet generation. However, the possibility that the triggering mechanism differs from breakout and is instead an

instability of the flux rope itself can not be ruled out. Figure 3.4 showed that the brightening associated with breakout reconnection occurred simultaneously with the brightening from flare reconnection. This could be consistent with slow, low-energy breakout reconnection prior to the eruption that speeds up once flare reconnection is initiated (as in Karpen et al. (2012); Wyper et al. (2018); Kumar et al. (2018) for example). Or equally the breakout reconnection could be reactionary, following from the eruption of the filament driven by an ideal instability (as suggested by e.g. Masson et al. (2017) for their event). The partial cancellation of the parasitic polarity flux suggests that a flux rope may have formed in the filament channel prior to the eruption, thus both of the above scenarios are a possibility. A non-linear force-free extrapolation of the pre-eruption magnetic field could potentially help to pin down the pre-eruptive field structure and aid in diagnosing the eruption trigger. However, this is outside the scope of the present work which is focused on understanding the eruption kinematics.

Regardless of the exact trigger, once the eruption is underway it is clear that breakout reconnection is heavily involved in the eruption as demonstrated by the similarities with the simulation and the high resolution CRISP and AIA observations. As with jets involving mini-filaments in coronal holes, the strength of the overlying field suppresses ideal expansion of the flux rope once flare reconnection ensues. Without being able to blast the overlying field outwards, breakout reconnection of the strapping field and then ultimately the erupting flux rope provides the only avenue to eject the twist/helicity from the filament channel. In the case of open-field coronal hole jets, the twist then propagates away along open field lines, whereas in these confined events it becomes trapped on overlying loops.

Why then do all confined flares in null topologies not show clear evidence of associated jets? This is likely to do with the relative size of the separatrix surface compared with the surrounding coronal loops. Wyper et al. (2016) quantified this with the ratio L/N, where L is the distance between the two spine foot points and N is the width of the footprint of the separatrix dome on the solar surface. They found in simulations of jets driven by rotating the parasitic polarity that in configurations where $L/N \approx 1$ minimal jets were produced, whereas for larger ratios the jets became more defined and higher energy. The classic jet producing topology of a parasitic polarity surrounded by open field corresponds to $L \to \infty$ (and therefore $L/N \to \infty$), consistent with this picture. Recently, Masson et al. (2017) studied a confined flare where

$L/N \approx 1$ finding little evidence of clear outflows, whereas in the event studied by Yang and Zhang (2018) estimate that $L/N \approx 2.1$ and a clear rotating jet spire was observed. In the event, based on the pre-flare EUV loops (Figure 3.2(e) and (f)), it is estimated that $L/N \approx 2.6$.

The event and simulation are relatively small compared to some confined events. DeVore and Antiochos (2008) studied homologous breakout eruptions that are much larger in scale. However, in a similar manner to the breakout jet simulation they find that a full scale breakout eruption and CME is suppressed when a strong overlying field is present. The erupting filament channel is instead reconnected across the breakout current layer, transferring its shear/helicity to the overlying field. The key differences from the present model is the larger scale of their simulation (allowing greater ideal expansion of the filament channel) and an L/N ratio of 1, giving less coherent jet-like outflows. However, the basic physics is the same in the two models. In this sense, the current simulation bridges the gap between the large-scale confined eruption simulations of DeVore and Antiochos (2008) and the open-field jet simulations of Wyper et al. (2017, 2018).

Taken together with previous studies of jets (e.g. Wyper et al., 2017; Kumar et al., 2019), CMEs (e.g. Lynch et al., 2008; Karpen et al., 2012; Chen et al., 2016) and other confined filament channel eruptions (with and without associated jets) (e.g. Sun et al., 2013; Masson et al., 2009; Yang and Zhang, 2018) the results support the conclusion that all of the above phenomena can be tied together by the shared topology of a filament channel formed beneath the separatrix of a coronal null. In such a configuration, breakout reconnection can and should be expected to be involved in the eruption. The present investigation demonstrates that in the context of confined filament eruptions, the breakout process provides and intuitive mechanism for confining the eruption by redirecting it along overlying field.

3.9 Conclusion

These observations provide the evidence to validate the simulation which can be applied not only to jets and CMEs but also confined eruptions and flares. Overall, the magnetic configuration observed in the event and in the simulation can be applied to multiple eruptive phenomena

on the Sun. In turn, this can then be applied to stellar scenarios, scaling up the simulation to replicate flare energies observed on other stars. By monitoring the effects this has on the size and strength of sunspots it is possible to determine whether it is likely these flares are generated through a similar magnetic field configuration or if it is more complex. I come back to discuss this further in Chapter 7 after looking at some stellar flare studies on solar-type and low mass stars.

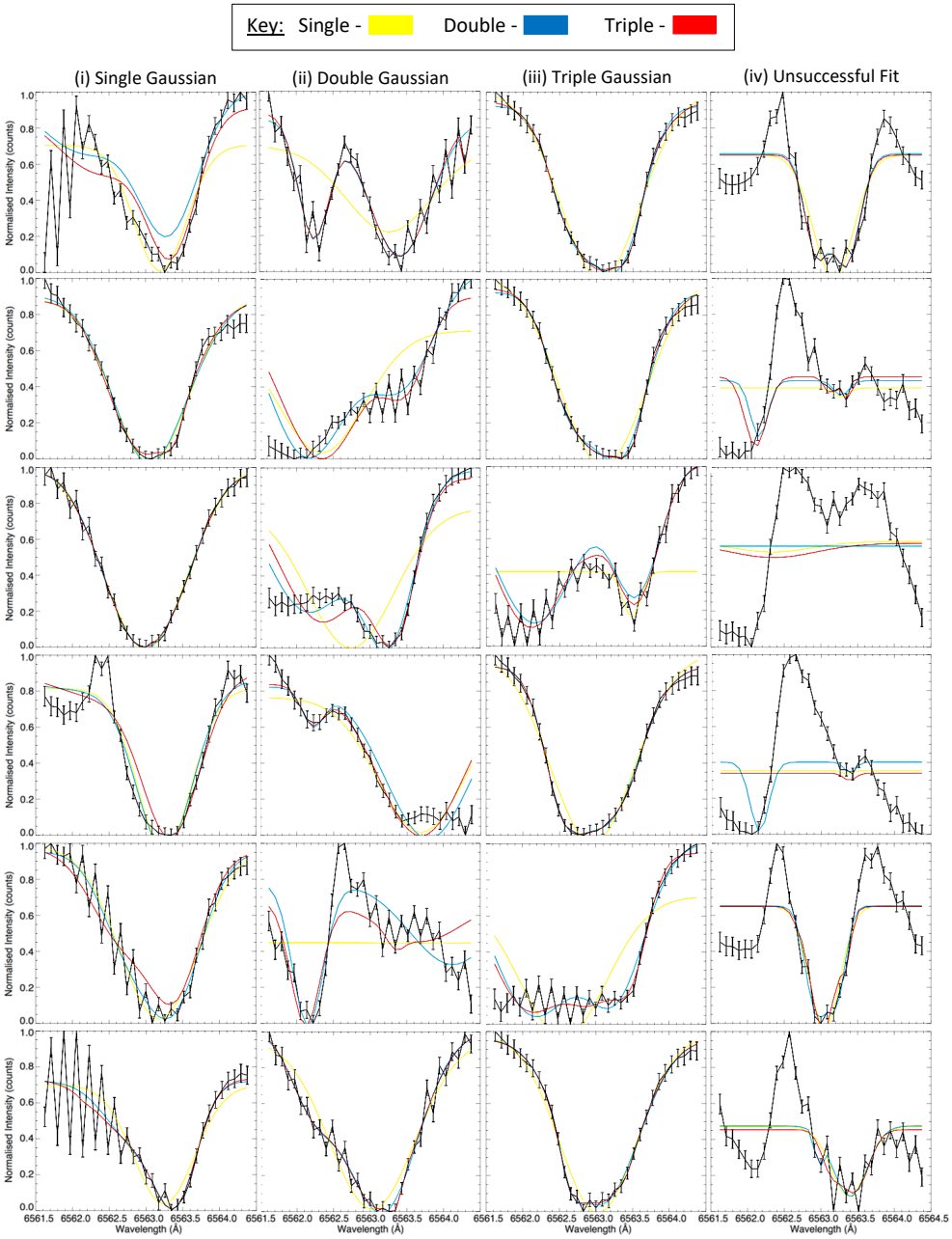

Figure 3.14: This selection of Hα line profiles along with their respected model fits shows the varying degrees of complex profiles and how the fitting method responds. Each column shows profiles which prefer a single, double and triple Gaussian fit with the last column representing unsuccessful fitted profiles. These unsuccessful profiles are a result of the flare ribbons which produce Hα in emission and cause issues within the fitting method resulting in none of the Gaussian fits being suitable. However, despite this the fitting of the ribbons are not of interest as the main concern lies with the kinematics of the erupting filament and jet so these profiles are insignificant.

4 The Rotational Phase of Stellar Flares on M dwarfs with K2

The research outlined in this chapter has been accepted for publication in the Monthly Notices of the Royal Astronomical Society (MNRAS) Doyle et al., 2018, MNRAS, 480, 2153.

4.1 Introduction

In solar physics, the relationship between sunspots and solar flaring activity has been studied for decades and it is generally accepted that these two phenomena are closely related. Guo et al. (2014) carried out a statistical study on the dependence of flares in relation to sunspots and phase in the 22nd and 23rd solar cycles. They found the occurrence of X-class flares was in phase with the solar cycle hence, flares closely follow the same 11 year cycle as sunspots. Maehara et al. (2017) investigated the correlation between starspots and superflares on solar-type stars using *Kepler* observations and identified starspots based on the rotational phase of the brightness minima in the lightcurve, showing superflares tend to originate from a larger starspot area.

Despite the extensive work over the years in stellar flare physics, one area which has not been investigated in depth is the rotational phase distribution of flares in M dwarfs. If the analogy between the physics of solar and stellar flares holds and these events occur from active regions which typically host spots, then you would expect to see a correlation between starspots and flare occurrence. A small number of stars have been studied to determine whether there is a correlation between stellar rotation phase and number of flares but so far nothing has been found. Ramsay et al. (2013), Ramsay and Doyle (2015), Hawley et al. (2014) and Lurie

et al. (2015) examine the phase distribution of the flares in a small sample of M dwarf stars using *Kepler*/K2. Each of the stars show flares at all rotational phases despite there being clear rotational modulation present in their lightcurves. There is no evidence for a correlation between rotational phase and number of flares. However, some do note the most energetic flares occur at flux minimum (starspot most visible) in a handful of their stars, while the other show flares near flux maximum.

This poses the question; do flares show any preference for rotational phase in M dwarfs in general? It is expected that more flares would occur during the minimum of the rotational modulation when the spot/active region producing the minimum is most visible. If this is not the case, what mechanisms are responsible and what is causing the generation of flares in these active stars? In this chapter, a sample of M dwarf stars is investigated which have been observed in short cadence by K2. For details of the data preparation refer to §2.2.1. By analysing the flare and stellar properties of this group of stars I aim to address some of the questions concerning the phase distribution of the flares.

4.2 The K2 Late Dwarf Sample

To create the sample of stars, all the sources observed in short cadence with K2 in Fields 1–9 were taken (observations made between May 2014 and Jul 2016) and cross referenced with SIMBAD[1](astronomical database), removing all stars which were not of spectral type M0 or later. In addition, those stars classed as BY Dra stars (variable late type stars) were removed from the sample since many of them are in binaries or triples and are therefore, not conducive to investigating stellar activity on single stars before and after the M4 spectral sub-type. The remaining stars were then cross referenced with the EPIC catalogue (Huber et al., 2016) and those which showed characteristics of a giant (e.g. have a radii $>1R_{\odot}$) were also removed. Stars which were too faint to show a clear detection in the K2 thumb print image were also removed from the sample.

This left us with a sample of late dwarf stars observed with K2 in short cadence mode, consisting of 33 M dwarfs and one L dwarf. Of this sample of stars, 32 percent were classed as known

[1]http://simbad.u-strasbg.fr/simbad

flare stars in the SIMBAD catalogue. They range in spectral type and mass from M0 to L1 and 0.58 $M_{\odot}$ to 0.08 $M_{\odot}$. Each target has been observed for $\sim$70 – 80 days producing a near continuous lightcurve over this period. The significance of short cadence data is it allows flares with a duration of a few minutes to be detected, giving a more comprehensive and robust overview of stellar activity. In addition, the wide range of spectral types provides a broader insight into how magnetic activity can vary in M dwarfs as a whole. The properties of the stars in the sample, including spectral type, previously known rotation period, mass, distance and magnitude are shown in Table 4.1.

Table 4.1: The properties of the M stars which are included in the survey where all data comes from the K2 EPIC Catalog (Huber et al., 2016), with the exception of the following. References for spectra: [1] (Hawley et al., 1996), [2] (Reid et al., 2008), [3] (Reid et al., 2004); [4] (Lépine and Gaidos, 2011); [5] (Kraus and Hillenbrand, 2007), [6] (Schmidt et al., 2010), [7] (Gray et al., 2003); [8] (Davison et al., 2015); [9] (Lépine et al., 2013); [10] (Kirkpatrick et al., 1991); [11] (Faherty et al., 2009); [12] (Pesch, 1968); [13] (Alonso-Floriano et al., 2015); [14] (Stephenson, 1986*a*); [15] (Cruz and Reid, 2002); [16] (Shkolnik et al., 2009).

Name	EPIC ID	K2 Field	RA (J2000)	DEC (J2000)	SpT	P d	M $M_\odot$	R $R_\odot$	T_{eff} (K)	$log(g)$ (cgs)
LHS 2420	201611969	1	11:31:32.845	+02:13:42.86	M2.5V [9]		0.319	0.301	3740	4.977
LP 804-27	205204563	2	16:12:41.781	–18:52:31.83	M3V [7]		0.445	0.391	3930	4.86
GJ 3954	205467732	2	16:26:48.160	–17:23:33.6	M4.5V		0.304	0.286	3772	4.995
IL Aqr	206019387	3	22:53:16.7	–14:15:49.3	M4V [1]	95	0.21	0.22	3472	5.07
LP 760-3	206050032	3	22:28:54.401	–13:25:17.86	M6.5V [10]		0.09	0.113	2617	5.271
2MASSI J2214-1319	206053352	3	22:14:50.707	–13:19:59.080	M7.5 [11]		0.078	0.098	2211	5.349
Wolf 1561 A	206262336	3	22:17:18.9	–08:48:12.5	M4V+M5V [1]		0.22	0.23	3495	5.06
HG 7-26	210317378	4	3:52:34.340	+11:15:38.807	M1 [12]	0.192	0.396	0.358	3788	4.917
NLTT 12593	210434433	4	4:07:54.80	+14:13:00.7	M2.5V [13]	1.073	0.424	0.382	3844	4.896
G 6-33	210460280	4	3:45:54.83	+14:42:52.1	M1.5 [9]		0.511	0.454	4028	4.821
LP 415-363	210489654	4	4:20:47.988	+15:14:09.073	M4V [13]	82.6	0.391	0.351	3751	4.917
MCC 428	210579749	4	3:43:45.247	+16:40:02.166	M0V [14]		0.504	0.449	3898	4.836

Continued on next page

Table 4.1 – continued from previous page

Name	EPIC ID	K2 Field	RA (J2000)	DEC (J2000)	SpT	P d	M $M_\odot$	R $R_\odot$	T_{eff} (K)	$log(g)$ (cgs)
GJ 3225	210758829	4	03:26:45.0	+19:14:40.1	M4.5V [1]	0.454	0.13	0.15	3027	5.19
2MASS J0326+1919	210764183	4	03:26:44.5	+19:19:31.0	M8.5V [2]		0.08	0.10	2192	5.34
LP 414-108	210811310	4	04:10:38.1	+20:02:23.5	M0.5V+M0.5V [3]		0.43	0.37	3971	4.89
LP 357-206	210894955	4	3:55:36.90	+21:18:48.30	M5 [15]	7.916	0.240	0.248	3550	5.014
2MASSJ0335+2342	211046195	4	3:35:02.087	+23:42:35.61	M8.5V [16]	0.472	0.084	0.106	2432	5.310
LT Tau	211069418	4	03:42:56.5	+24:04:58.1	M3.5V [4]		0.32	0.30	3675	4.97
V497 Tau	211077349	4	03:42:02.9	+24:12:36.3	M3V [4]		0.44	0.40	3876	4.87
V692 Tau	211082433	4	03:56:30.4	+24:17:18.8	M4-5V [4]		0.26	0.26	3567	5.03
V631 Tau	211112686	4	03:44:24.8	+24:46:06.3	M1V [4]	3.27	0.37	0.34	3700	4.93
V* MY Tau	211117230	4	3:44:27.293	+24:50:38.26	M0 [16]	0.4	0.427	0.381	3811	4.894
2MASS J0831+1025	211329075	5	08:31:56.0	+10:25:41.7	M9V [2]		0.08	0.10	2209	5.34
GJ 3508	211642294	5	8:37:07.961	+15:07:45.5257	M3V [9]		0.427	0.385	3861	4.892
LP 426-35	211945363	5	08:57:15.4	+19:24:17.7	M5V [5]		0.35	0.32	3738	4.96
2MASS J0909+1940	211963497	5	09:09:48.2	+19:40:42.9	L1 [6]		0.08	0.10	2098	5.36
AX Cnc	211970427	5	08:39:09.9	+19:46:58.9	M2 [5]	4.854	0.45	0.41	3881	4.87

Continued on next page

Table 4.1 – continued from previous page

Name	EPIC ID	K2 Field	RA (J2000)	DEC (J2000)	SpT	P d	M $M_\odot$	R $R_\odot$	T_{eff} (K)	$log(g)$ (cgs)
2MASS J0831+2024	212009427	5	08:31:29.9	+20:24:37.5	M0V [5]	1.55	0.58	0.51	4116	4.78
2MASS J0839+2044	212029094	5	08:39:18.1	+20:44:21.3	M1V [5]		0.34	0.32	3785	4.96
L 762-51	212285603	6	13:45:50.7	–17:58:05.6	M3.5V [1]		0.31	0.30	3646	4.99
LP 737-14	212518629	6	13:16:45.47	–12:20:20.4	M3.5V [13]		0.281	0.273	3577	5.005
BD-05 3740	212776174	6	13:38:58.7	–06:14:12.5	M0.5V [7]		0.45	0.40	3847	4.88
2MASSI J1332-0441	212826600	6	13:32:24.427	–4:41:12.690	M7.5 [6]		0.079	0.101	2264	5.328
GJ 1224	228162462	9	18:07:32.927	–15:57:46.46	M4V [8]		0.14			

4.3 Data Analysis

4.3.1 Rotation Period

From the sample of 32 stars, only five have rotation periods previously recorded in the literature, see Table 4.1. The two most important factors in determining the level of activity in a low mass star are age and rotation period. The rotation period can be determined from low mass stars if they have starspots whose rotation can produce a change in brightness as the starspots are expected to be darker than the photosphere (in the same way as sunspots).

The first objective is to determine or constrain the rotation period from the K2 data. The method used to determine the rotation is initially through the Lomb-Scargle periodogram producing a power spectrum of the lightcurve of the source, followed by a fine tuning iterative process involving phase folding. The value of the rotation obtained via the power spectrum is used in the phase folding of segments of the lightcurve originating from the start, middle and end of the K2 data. Phase zero is first obtained by eye and through an iteration of phase folding the three segments of data, a best fit for the rotation period, P_{rot}, and phase zero, t_0, is obtained. The phase folding of segments is used due to the changing nature of the lightcurve over the observation period iterating until all sections have phase zero at the minimum. These values can be used to produce a mean folded lightcurve and will be used during the analysis of flaring activity on the targets.

The uncertainty on the rotation period is estimated by determining the Full Width at Half Max (FWHM) of the corresponding peak on the power spectrum. The FWHM is estimated through a Gaussian fit onto the peak and the following relationship:

$$FWHM = 2\sqrt{2ln(2)}\sigma \tag{4.1}$$

where σ is the FWHM of the Gaussian. Through Gaussian error propagation the error on the period can be calculated using Equation 4.2 and the values are shown in Table 4.2.

$$\delta P = P^2 \times FWHM \tag{4.2}$$

As described in §2.2.1, data which had been corrected by the EVEREST pipeline was utilised which corrects for instrumental effects that are present in K2 data. As a result, for each photometric point there are parameters including time, raw and corrected flux, counts and a quality flag (as noted in §2.2.1). Our first goal is to search for and identify the stellar rotation period which is much longer than the duration of any stellar flare. Therefore, any photometric point which did not possess a quality flag of zero was removed (i.e. QUALITY $\neq$ 0).

The stellar rotation period derived for the sample using K2 data are shown in Table 4.2: they range from 0.34 days to greater than 70 days. There are six stars in the sample where the rotational modulation was incomplete (i.e. only a portion of the rotation was observed) so, it is only possible for us to say the rotation period is greater than the observation length itself i.e. greater than 70 days. There is no correlation between rotation period and spectral type. For instance, stars with a rotation period less than 1 day have spectral types in the range M0–M8.5. Other examples of rapid rotation in late type active stars include the M7 dwarf 2MASS J0335+23 (Gizis et al., 2017) which has a very rapid rotation period of 0.22 days, which is presumably due to its young age (24 Myr). Gizis et al. (2017) find 22 flares in the K2 lightcurve of 2MASS J0335+23 showing it is active.

Taking a sample of ∼12,000 main sequence stars observed using *Kepler*, Nielsen et al. (2013) found M dwarfs had a median period of 15.4 days, although with a considerable spread in the overall distribution. Out of all of the stars only a handful show rotation periods which are not in agreement with the literature (compare column 7 in Table 4.1 with column 2 in Table 4.2). For some objects, the difference can be substantial, for example, HG 7-26 (EPIC 210317378) had a reported period of 0.192 days (Newton et al., 2016) compared to 24.5 days as derived from the K2 data. However, this source was classed as a 'Non detection or undetermined detection' in the catalogue of Newton et al. (2016), which indicates that they could not positively identify a periodic modulation within their data. This underlines the need for a continuous sequence of photometric measurements, such as provided by K2, to reliably determine rotation periods.

4.3.2 Flare Identification

The flare identification process was completed using Flares By EYE (FBEYE), a suite of `IDL` programs created by J.R.A. Davenport (Davenport et al., 2014). FBEYE scans each lightcurve and flags up any point which is over a 2.5σ threshold, identifying potential flares which consist of 2 or more consecutive flagged points. Within the flare finding algorithm, potential flares are required to consist of two or more consecutive flagged points; It is important to note here all of the flares within this sample (and subsequent samples) are composed of many more points and 2 is simply the minimum requirement. In addition, users can manually classify flares present in the lightcurve via an interactive display. Once complete, this produces a comprehensive list of flares per star along with properties for each flare such as start and stop time, flux peak and equivalent duration. The lightcurves which are used for this process were complete, meaning all photometric points were used regardless of their quality flag due to potential flaring events having quality flags which are not zero. The `EVEREST` quality flags and FBEYE flare list were then compared directly to assess the likelihood of the flare being a real event.

Any photometric point with quality flags which were a result of thruster firing or known instrumental effects were removed from further analysis. Any point which had a flag of `EVEREST` bits 23 and 25 (which may have been due to cosmic rays or a real stellar flare) were kept. Events which consisted of only one photometric point were removed and events which did not have profiles consistent with being a likely stellar flare (i.e. sharp rise and exponential decay) were also removed.

The data for each star was analysed in a consistent manner and for each the number of flares, the range in the duration and amplitude of the flares are shown in Table 4.2. In addition, the normalised flare number which represents the number of flares expected on each star if the observation duration was 78.3 days is included. The duration of each flare was calculated from the start and stop times and the amplitude represents the flux peak of each flare all of which were obtained from the output of FBEYE. Sources 2MASS J0831+1025, 2MASS J0909+1940 and L 762-51 did not show any flares and were omitted from Table 4.2 – these sources did also not show complete rotational cycles and so the rotational periods could not be determined.

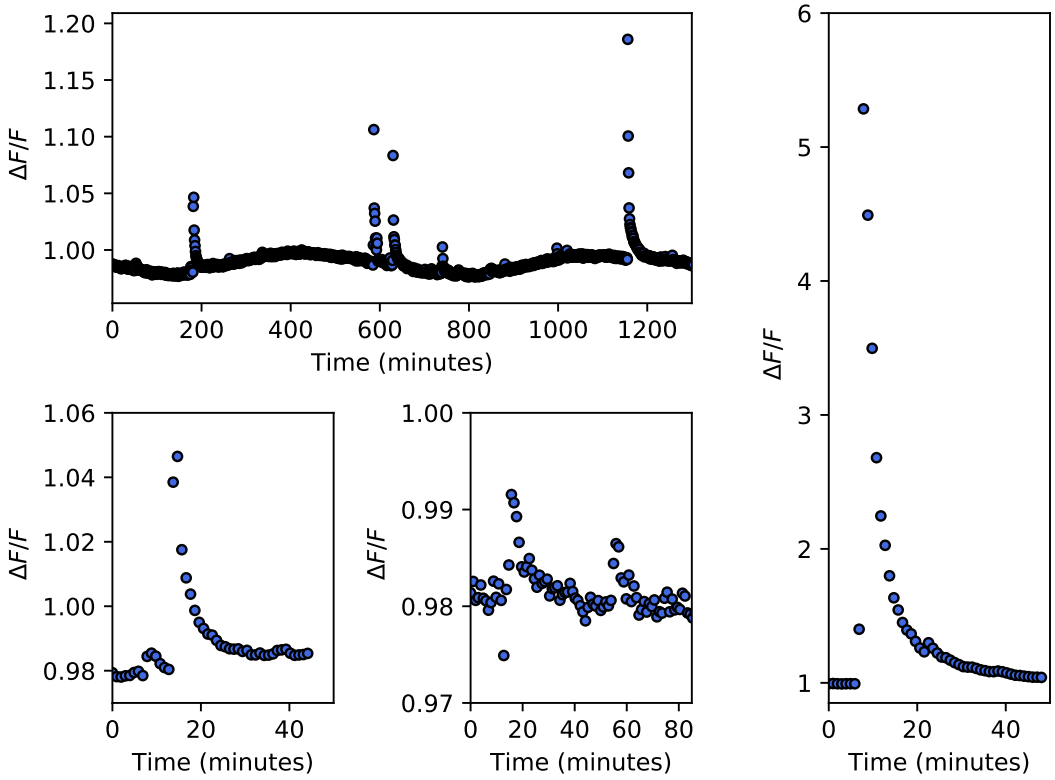

Figure 4.1: A sample of flares of varying magnitude from the flare star GJ 3225 (EPIC 210758829) a M4.5 star with a rotation period of 0.45 days. The upper left plot shows a small section of the lightcurve of the star demonstrating the frequency of the flares and also the range in magnitude. Far right is the largest flare seen in the K2 lightcurve of this star with a peak normalised flux of 4.32. The bottom two plots show smaller amplitude, short duration flares which dominate the lightcurve.

Examples of some flares from GJ 3225 (EPIC 210758829) are shown in Figure 4.1. Of particular interest is the largest flare from this star with a normalised flux peak of 4.32 ($\sim$ 1.6 mag), where a rapid rise (approximately 1 min) and clear slow decay (approximately 10 min) can be seen which is similar to a classical stellar flare profile.

It is expected that stars with shorter rotation periods will display greater levels of flaring activity. This is the case with this particular sample of M dwarfs (Figure 4.2), however, the star with the most flares does not have the fastest rotation. After a rotation period of approximately 10 days there is a drop off in the number of flares seen on the star, which is consistent with the findings of Stelzer et al. (2016). In order to create a complete picture of this sample of M dwarfs the ages of the stars would need to be determined, as although the activity of the stars depends on rotation, this in turn depends on age.

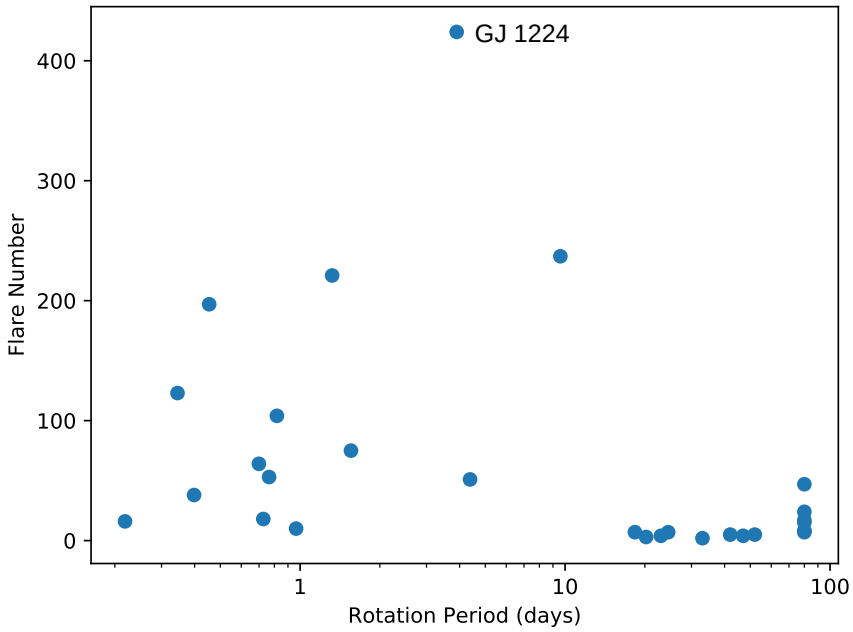

Figure 4.2: The number of flares as a function of the rotation period for all stars showing flaring activity. As other studies have found, stars with rotation periods longer than ∼10 d are less active. The most active star is GJ 1224, P_{rot} =3.9 days.

Work similar to this has been carried out on long and short cadence *Kepler* data of various known flare stars, for example Hawley et al. (2014) studied 5 M dwarf stars with spectral types from M1 - M5. They found three of the stars with spectral types of M1 - M3 showed very little activity with flare numbers between 2 and 12 and rotation periods in the order of days. Of the three stars remaining with spectral types of M4 and M5, they showed high levels of flaring activity with flares in the order of hundreds and rotation periods less than a day. In particular GJ 1243, a well studied M4 flare star, showed 833 flares and a rotation period of 0.6 days during the 2 month of short 1 minute cadence *Kepler* data. Ramsay et al. (2013) also looked at this star using short cadence *Kepler* data from Q14 observing a small number of large amplitude flares and a great number of low amplitude short duration flares.

4.3.3 Flare Energies

To determine the energy of the stellar flares, the quiescent luminosity of the star, L_*, must be calculated in the *Kepler* band-pass. To construct a template spectral energy distribution

for each star PanStarrs magnitudes g, r, i and z are used (see Table 4.A.1). The PanStarrs magnitudes (Chambers et al., 2016) represent the mean quiescent magnitude of the star calculated over an average of multiple measurements. This ensures the effects of flares or rotation has been removed from the magnitudes. A polynomial was fitted to the Panstarrs data and determined the flux in the *Kepler* band-pass in the same manner as Kowalski et al. (2013). The quiescent luminosity is then computed by multiplying the flux by $4\pi d^2$, where the distance (d) is determined by inverting the parallax from the *Gaia* Data 2 release (Gaia Collaboration, 2016, 2018), (see Table 4.B.1). Additionally, the Bayesian analysis approach was used as described by Astraatmadja and Bailer-Jones (2016) and implemented in the `STILTS` suite of software (Taylor, 2006), and find that, as expected for sources within 200 pc, the distances determined using the inversion and the Bayesian approach are entirely consistent.

The energy of the flares, $E_{\rm flare}$, can then be determined by the multiplication of the luminosity of the star, L_*, in erg/s and the equivalent duration, t, in seconds. The equivalent duration (Gershberg, 1972) is defined as the area under the flare lightcurve in units of seconds, which is different to the flare duration, and is obtained through the FBEYE suite of programs. FBEYE uses a Trapezoidal summation of the area under the flare lightcurve which is converted into seconds.

A wide range of flare energies are seen in the 31 flaring M dwarfs. The most energetic flare is observed in V497 Tau at $\sim 5.9\times10^{34}$ erg and the flare with the lowest energy at $\sim 1.3\times10^{29}$ erg is seen in IL Aqr. The range of energies seen in the sample are comparable to energies seen in other work similar to this. Using *Kepler* data, Hawley et al. (2014) showed flares with energies in the range of $\sim 2 \times 10^{28} - 2 \times 10^{33}$ erg on the M dwarf GJ 1243. Other stars in their sample were consistent with this but less extreme. In addition, Lurie et al. (2015) investigated the M5 binary system GJ 1245 also using 9 months of short cadence *Kepler* data, finding a total of 1288 flares on both stars with an energy range of $\sim 1 \times 10^{30} - 1 \times 10^{33}$ erg. For comparison, these large scale flares of order of 10^{34} erg are the equivalent to extremely large X1000 class flares, in terms of the solar flare GOES classification. Zeeman-Doppler imaging was also completed for GJ 1245A and B finding two different magnetic field topologies (see Gastine et al., 2013, for further details). GJ 1245 A possesses a strong dipole dominated field where GJ 1245 B has a weaker multipolar field. However,

Table 4.2: For the stars in the survey which show flaring activity their properties including their observed rotation period; the number of flares together with their duration, amplitude and energy are indicated. Since the length of each observation differs by a small amount, the normalised flare number which is the number of flares expected on each star if the observation duration was 78.3 d has been included.
Note For a handful of sources the apparent modulation period is longer than the observation length meaning only an lower limit to the rotation period could be determined. For stars with no evidence for a modulation no rotation period could be determined.

EPIC ID	Rotation Period (P_{rot})	No. of	Normalised	Duration Range	Amplitude Range	$log(E_{Kp})$
	days	flares	Flare No.	minutes	Flux	ergs
201611969	$>$ 70	15	14.33	11.8 – 35.3	0.0009 – 0.0095	31.17 – 32.18
205204563	42:	5	4.72	8.83 – 20.6	0.0003 – 0.0030	29.12 – 31.05
205467732	1.321 $\pm$ 0.021	221	205.35	8.83 – 91.2	0.0003 - 1.3694	30.60 – 33.49
206019387	$>$ 70	47	39.27	10.8 – 81.4	0.0004 – 0.0151	30.01 – 31.77
206050032	$>$ 70	17	14.21	10.8 – 32.4	0.0274 – 0.6937	31.25 – 32.52
206053352	–	8	6.78	11.8 – 30.4	0.2254 – 6.7031	31.19 – 32.27
206262336	9.6 $\pm$ 1.2	237	194.73	8.78 – 46.1	0.0018 – 1.2462	29.45 – 33.06
210317378	24.5:	7	6.06	12.8 – 21.6	0.0069 – 0.0582	31.39 – 32.28
210434433	47:	4	3.49	14.7 – 24.5	0.0041 – 0.0207	31.02 – 32.11
210460280	45:	1	0.87	29.42	0.0024	31.47
210489654	$>$ 80	24	20.90	10.8 – 39.2	0.0037 – 0.0632	31.06 – 32.28
210579749	23:	4	3.43	12.8 – 42.2	0.0014 – 0.0027	31.37 – 31.95

Continued on next page

Table 4.2 – continued from previous page

EPIC ID	Rotation Period (P_{rot})	No. of	Normalised	Duration Range	Amplitude Range	$log(E_{Kp})$
	days	flares	Flare No.	minutes	Flux	ergs
210758829	0.4539 ± 0.0027	197	170.68	8.78 – 106	0.0023 – 4.3192	30.09 – 33.46
210764183	0.966 ± 0.011	10	8.77	8.78 – 45.9	0.2365 – 5.1922	31.95 –
210811310	33:	2	1.75	10.8	0.0013 – 0.0028	30.88 – 31.16
210894955	0.726 ± 0.006	18	15.81	10.8 – 30.4	0.0455 – 2.3884	30.65 – 32.58
211046195	0.2185 ± 0.0006	16	14.02	0.98 – 2888	0.0437 – 4.5665	31.15 – 34.57
211069418	0.8177 ± 0.0086	104	90.48	8.78 – 63.8	0.0101 – 0.4138	31.65 – 33.81
211077349	0.6992 ± 0.0061	64	55.75	8.78 – 75.6	0.0142 – 3.8455	31.69 – 34.77
211082433	0.3447 ± 0.0015	123	107.23	8.78 – 71.6	0.0097 – 0.4683	31.17 – 33.51
211112686	0.7639 ± 0.0073	53	46.34	8.78 – 94.0	0.0103 – 0.4311	31.99 – 34.24
211117230	0.398 ± 0.002	38	32.72	8.83 – 76.5	0.0045 – 0.2136	32.08 – 34.28
211642294	52:	5	4.49	20.6 – 103	0.0023 – 0.0196	31.15 – 34.42
211945363	$>$ 70	8	7.39	10.8 – 31.2	0.0025 – 0.0231	31.19 – 31.98
211970427	4.38 ± 0.24	51	47.31	8.78 – 64.8	0.0101 – 0.3572	32.04 – 34.09
212009427	1.556 ± 0.029	75	69.34	8.78 – 76.5	0.0068 – 0.0967	32.14 – 34.29
212029094	20.22 ± 5.03	3	2.78	14.7 – 22.5	0.0019 – 0.0087	31.19 – 31.66

Continued on next page

Table 4.2 – continued from previous page

EPIC ID	Rotation Period (P_{rot})	No. of	Normalised	Duration Range	Amplitude Range	$log(E_{Kp})$
	days	flares	Flare No.	minutes	Flux	ergs
212518629	80:	1	0.96	27.46	0.0106	31.46
212776174	18.35 $\pm$ 5.03	7	6.58	10.8 – 20.6	0.0007 – 0.0038	31.21 – 31.99
212826600	–	7	6.79	12.8 – 41.2	0.0015 – 0.8707	32.15 – 33.31
228162462	3.9 $\pm$ 0.2	424	355.31	8.78 – 165	0.0015 – 0.8707	29.32 – 32.74

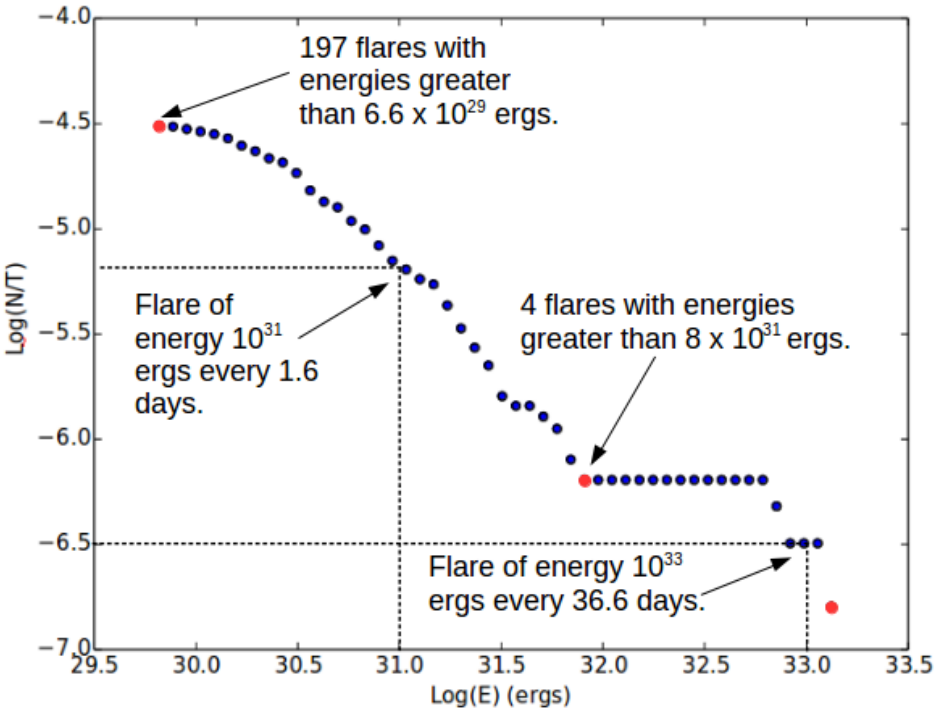

Figure 4.3: A cumulative frequency plot as a function of energy for all flares on the star GJ 3225. Key features are noted on this plot as an example of the information it can display.

despite these differences in magnetic field topology, both stars show similar flare number overall in their lightcurve and in flares per day.

4.3.4 Flare Frequency

Some of the stars in the sample show flares of incredibly high energies and so, it is important to understand how often these large events are seen and which stars show these large scale events. This is done by calculating a cumulative Flare Frequency Distribution (FFD) of the flares with respect to their energy.

Figure 4.3 shows this relationship for GJ 3225, pointing out some key features of the plot. All of the flares are binned by energy and then the cumulative frequency is calculated for each bin increasing as the energy decreases. This shows that higher energy flares are a lot less frequent than lower energy flares and this is universal for all stars in the sample. Another useful feature is the ability to predict how often you will see flares of particular energies on the star. Some examples are shown in Figure 4.3, such as flares of energies greater than 10^{33} erg will be seen approximately every 36.6 days on GJ 3225.

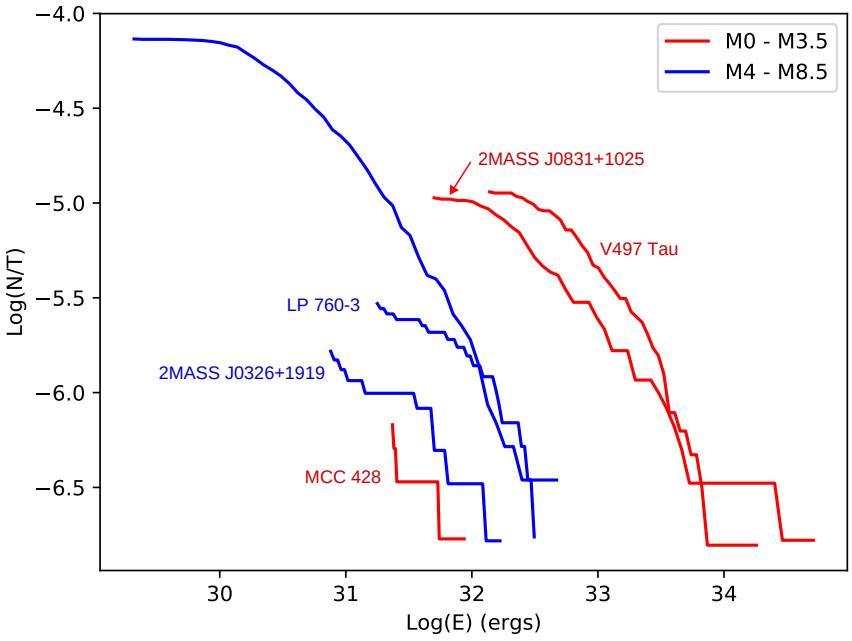

Figure 4.4: The cumulative FFD in minutes for a small selection of the M dwarf sample with various spectral type, rotation and flare number. This indicates the flare rate does not exclusively depend on the spectral type.

The cumulative frequency can be calculated for flares of all energies on all stars and plotted similarly to the previous figure. Figure 4.4 shows the FFD of all energies for a selection of 6 M dwarfs from the sample, including: LP 760-3, MCC 428, 2MASS J0326+1919, V497 Tau, 2MASS J0831+2024 and GJ 1224. For example V497 Tau will emit a flare of energy $> 10^{34}$ erg every 36.6 days and similarly GJ 1224 will emit a flare of 10^{30} erg every 0.14 days. The two stars showing the highest energy flares have a much faster rotation period of less than a couple of days than the other stars and are both M0-M3.5 stars.

The less active stars with only a handful of flares are a mixture of spectral types and posses rotation periods of days. Overall, this tells us the flare rate of these stars does not depend on the spectral type. A flattening trend is noticed in Figure 4.4 at various energies depending on the star. This has been mentioned in previous work suggesting higher and lower energy flares follow a different power law slope. Therefore, in SC data it is not due to a detection limit but is in fact a real feature. Despite attempts to find correlations between the slope of the power law and stellar parameters no significant correlation was found. The stellar parameters investigated included the mass, rotation period and spectral type, however, none of these

showed any potential trends indicating a correlation.

4.4 Rotational Phase

Stars with starspots can show a periodic change in brightness as the star rotates due to the starspots being cooler than the surrounding photosphere. If stellar flares originate from the starspot, one might naively expect more flares would be seen at rotation minimum where the starspot is most visible. However, if a star has a low rotation angle (i.e. one of its rotation poles is close to being face on), spots near the pole would be visible at all phases, and flares would be seen at all rotation phases. To investigate this further, the rotation phase of the flares which were identified in the previous section are determined and analysed.

For this analysis, stars with rotation periods shorter than the observation length were selected. Due to this, eight of the sources are omitted from this analysis and any further investigations due to the K2 lightcurve showing incomplete modulation which led to the rotation period being unable to be confirmed. The lightcurves are phase folded and binned using the rotation period shown in Table 4.2 and the phase zero calculated previously, yielding rotation cycles covering all of the K2 lightcurve showing a minimum at ϕ=0.0. The resulting phase folded and binned lightcurves are shown in Figure 4.5. Flares are present at practically all rotational phases for all stars. In many cases there are high energy flares present at rotation maximum, where you would expect the starspot to be least visible. Many of the lightcurves show a roughly sinusoidal modulation suggesting the presence of one prominent starspot, although several sources, such as Wolf 1561 A (which is in a triple system) show evidence for a second starspot. The fact that all the stars shown in Figure 4.5 show a clear modulation suggests they are not observed at low rotation angles.

In order to determine whether the phase distribution of the flares is random the χ^2_ν statistic is used. Here χ^2_ν is used as a variance test, measuring how far a set of random numbers are spread from the average value. The rotational phase is split into 10 bins and so, the number of flares observed on each star is used to determine the average number of flares you would expect to see in each phase bin if they are randomly distributed. If there is a preference for a phase bin then there will be a higher number of flares

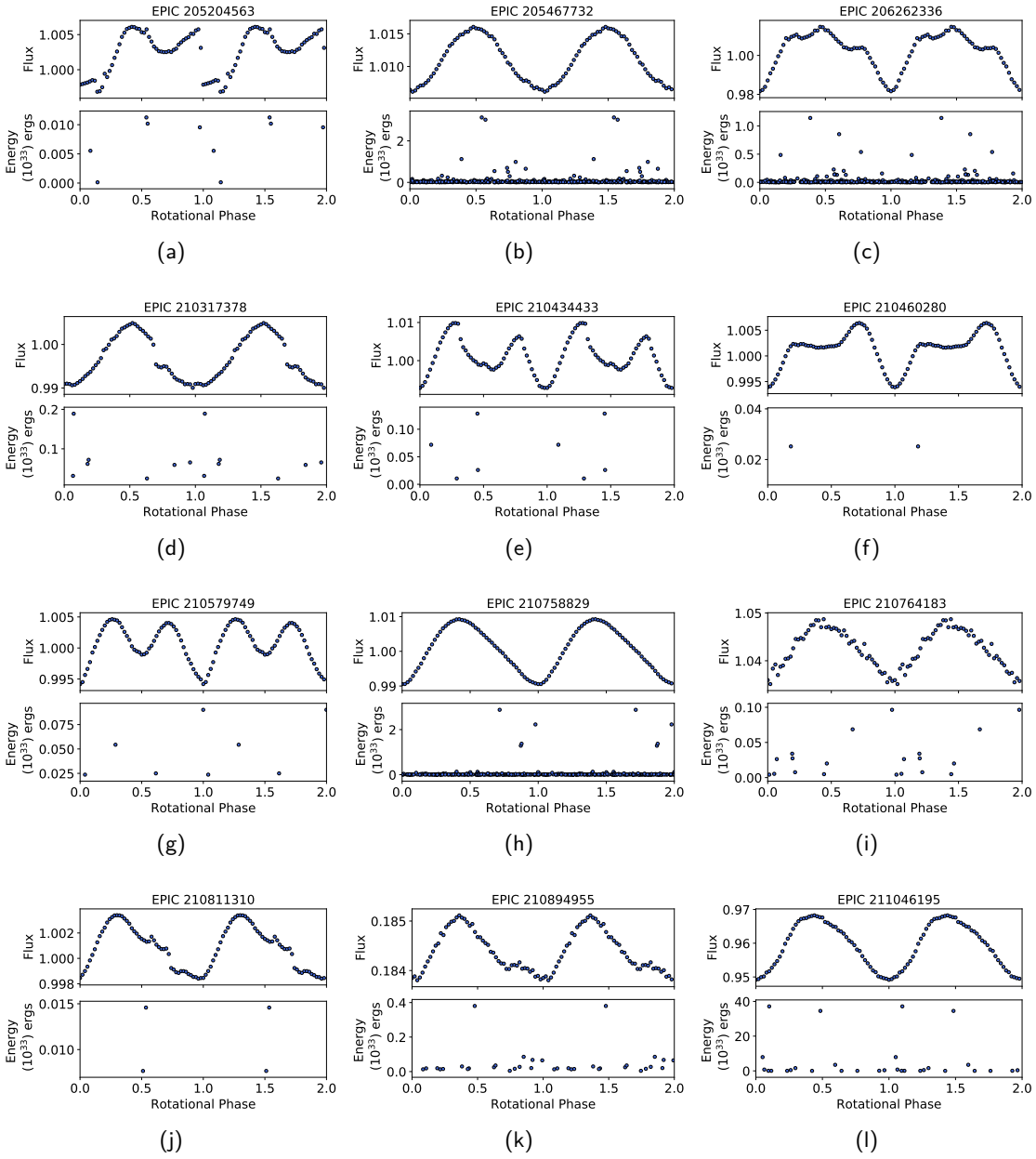

Figure 4.5: The top panels show the phased and binned lightcurves on the rotation period such that there are 50 bins per rotation phase. The bottom panels show the phase of the flares with the energy. The data is plotted twice so they cover rotation phase 0.0–2.0 where 1.0–2.0 is a repeat of 0.0–1.0. The star in panel (a) shows three rotation cycles with a long term trend.

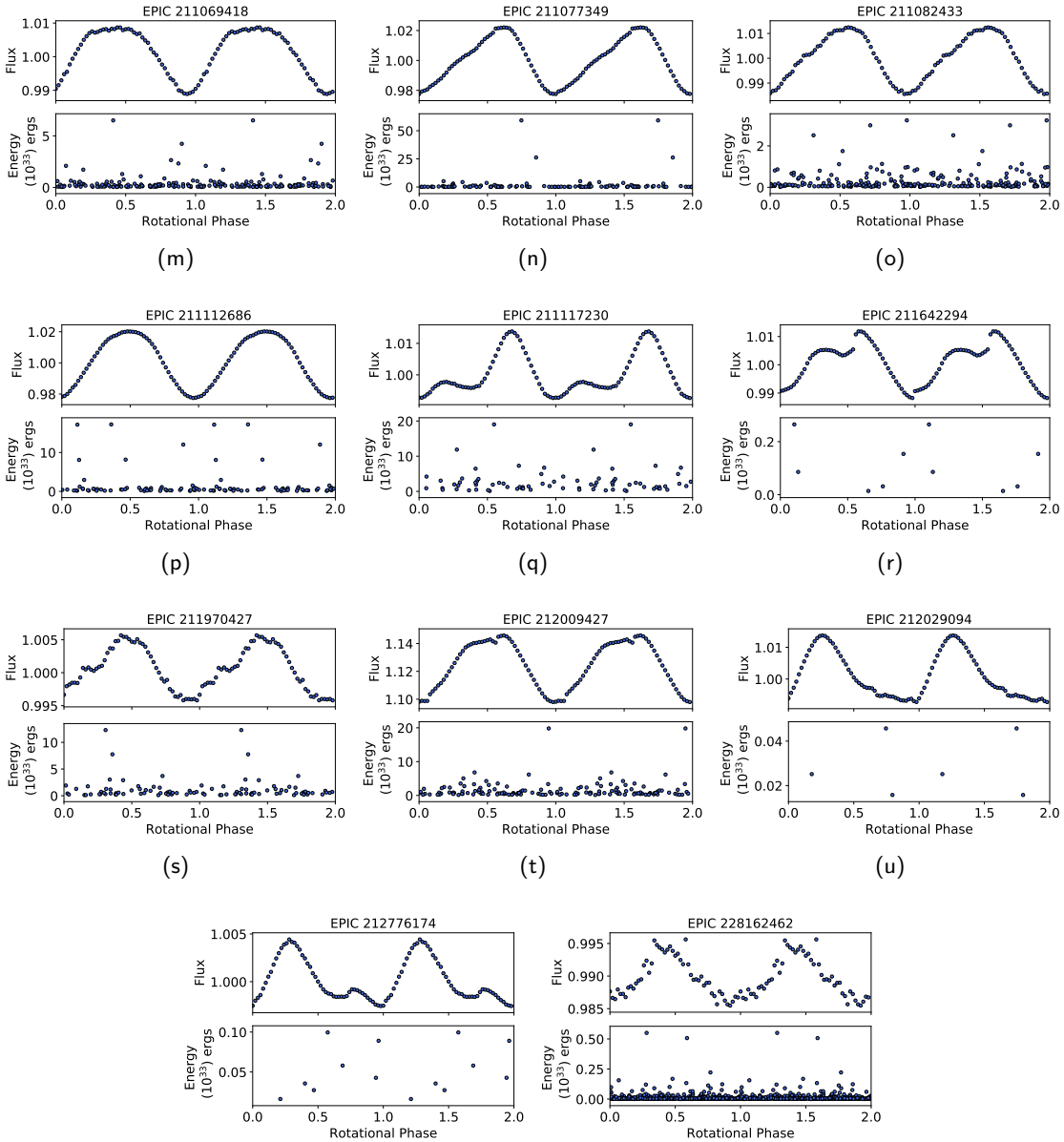

Figure 4.5: Continued

Table 4.3: For the stars shown in Figure 4.5 (with the exception of EPIC 210460280 which has only one flare) the χ^2_ν values are shown for whether each rotation phase bin (split into ten) had flares which were randomly distributed by phase. The flares are split into low and high energy where the cut off is determined by the median energy of all the flares for each star. None of the stars in the sample show a preference for flares at a certain rotational phase.

EPIC ID	median energy (erg)	Reduced Chi-Squared		
		low	high	all
205204563	9.5×10^{30}	0.78	2.00	1.00
205467732	2.3×10^{31}	1.17	1.17	0.55
206262336	6.5×10^{30}	0.92	1.13	0.61
210317378	6.2×10^{31}	0.78	1.22	0.97
210434433	4.9×10^{31}	0.89	0.89	1.22
210579749	3.9×10^{31}	0.89	0.89	0.67
210758829	6.7×10^{30}	1.14	0.30	0.62
210764183	2.3×10^{31}	1.44	1.00	1.11
210811310	1.1×10^{31}	1.00	1.00	2.00
210894955	1.9×10^{31}	1.10	1.35	0.47
211046195	3.7×10^{32}	0.33	0.78	0.78
211069418	1.8×10^{32}	0.93	1.33	0.65
211077349	3.1×10^{32}	0.82	0.82	1.15
211082433	1.2×10^{32}	1.11	0.39	0.72
211112686	4.8×10^{32}	0.58	1.21	1.18
211117230	1.9×10^{33}	0.87	0.99	0.69
211642294	8.6×10^{31}	0.78	0.89	1.00
211970427	5.5×10^{32}	0.82	0.82	1.24
212009427	7.8×10^{32}	0.54	0.81	0.33
212029094	2.5×10^{31}	1.00	0.89	1.52
212776174	4.3×10^{31}	1.22	0.78	0.97
228162462	4.6×10^{30}	0.83	0.48	0.94

present within the bin in comparison to the average flare number. Therefore, χ^2_ν will be much greater than one as there is a smaller spread in the flares within the phase bins.

Flares were split up into high and low energy with a cut-off determined by the median energy of all flares from each star. In addition, the rotational phase was split into 10 bins and χ^2_ν was determined for each star in the low, high and all energy categories, where the degrees of freedom, ν, is 9. Table 4.3 shows the results for both high and low energy flares and also all flares in each star overall. Regarding low, high and all flare categories, none of the stars show a preference for rotational phase even at a 2σ confidence level. Therefore, there is no evidence for the flares having any preference for rotational phase, which surprisingly indicates many flares may not originate from the large starspot. I now go on to investigate possible causes for this.

4.5 Discussion

I have analysed flaring activity from a sample of 31 M dwarfs covering a range of spectral types using K2 short cadence data. Overall, the rotation periods have been derived (or placed lower limits on) for 29 of these stars using the K2 lightcurves, many for the first time. In addition to this the flare characteristics (energy, duration and phase of the rotation cycle) are used to compute a statistical analysis of flares of this sample.

It is known, from previous studies (e.g. Mohanty and Basri, 2003; McLean et al., 2012), that faster rotating stars show greater flaring activity. Moreover, activity drops for stars with rotation periods $>$ 10 days (Stelzer et al., 2016). Our findings are consistent with these results. However, the work has identified an area which has not previously been studied in great detail. If flares originate from the same starspot which causes the rotational modulation, one would expect to observe a clear correlation of flares with rotational phases: this is not what is observed here. None of the stars in the sample show evidence for flares being preferentially seen at certain rotation phases. This result is unexpected and seems to point to the conclusion that the majority of flares do not originate from the prominent starspot.

Where do flares originate on these active stars and how are they generated? Three possible scenarios are considered to explain this finding. Firstly, there is the potential of magnetic interaction with a second star in a binary system. It is possible for interactions between the M dwarf and a binary companion causing increased magnetic activity between the stars and in turn the generation of flares at locations other than a dominant starspot/active region. As summarised by Kouwenhoven et al. (2009), 30–40 % of M dwarfs are members of a binary system. For late M dwarfs and brown dwarfs this drops to 10 - 30 %. This suggests less than a dozen of the sample will be in a binary system and hence binarity is unlikely to play a prominent role in resolving this question.

Our second scenario is that magnetic interaction could occur with a planet orbiting the M dwarf. Dressing and Charbonneau (2015) present an updated occurrence rate for planets orbiting early M dwarfs as 2.5 planets per M dwarf star. Depending on the number of planets orbiting the host star (and the mass, radius and magnetic field of the planet), it could be

induced magnetic activity between the star-planet system which causes the increased flaring activity. However, both the first and second scenario would depend on a small separation between the orbiting star or planet to allow for any magnetic interaction.

Now the likely separation between the photosphere of the M dwarf and the magnetic interaction region is considered. In the multi-scale field scenario of Yadav et al. (2015), only the large scale field (lower order multiple) would interact with any orbiting planets and the location of any 'null points' (where the global topology of the magnetic field changes) would be in a transitional region where the long range dipole field becomes weaker than the quadrupole (higher order) field. As the null point induced by the planet is also associated with the dipole field it cannot be too close to the stellar surface. Moreover, this kind of null point would not be associated with the dominant stellar spot (which is not created by the dipole field component). Furthermore, the reconnection region would not easily be eclipsed by the star so, it is natural that no correlation with the phases and the flares is found.

A third possibility is the presence of polar spots on the M dwarf. Depending on the viewing geometry and the relative inclination of the rotational and magnetic moment axes of the star, polar spots could be seen at all phases, interacting with emerging active regions and spot free regions as the star rotates, causing continuously visible flaring activity. Through solar observations we know the Sun does not posses polar spots, so the presence of polar spots on M dwarfs would support the view that the generation of the magnetic field in these stars differs from than of the Sun.

Despite the absence of polar spots on the Sun, Schrijver and Title (2001) model the formation of polar spots on rapidly rotating (6 d) Sun-like stars due to the poleward migration of the magnetic field. Their models predicted very active stars possessing polar caps with topologies of one polarity encircling another. This magnetic configuration could generate very large filaments, flares and Coronal Mass Ejections. Despite the differences between rapidly rotating Sun-like stars and fully convective low mass stars, the work of Schrijver and Title (2001) highlighted that a global poloidal field and a shear underneath/next to it in a perpendicular direction, a local dynamo can occur. Hence, this could lead to flare activity.

Next, the formation of polar spots on fully convective low mass stars is considered as another

possible scenario. Yadav et al. (2015) investigated the conditions necessary for formation of polar spots in convection driven dynamos. This directly applies to many stars in the sample as they are fully convective, and a magnetic field driven by the α^2 dynamo mechanism. As a result of their parameter study, they determine three key features for large spot formation in fully convective stars: i) rotation driven convection, ii) many scale heights in the convection zone, iii) a dynamo producing an axial-dipole field. All of the stars posses these properties and so, could this be the solution to the key problem noticed in the rotational phase of the flares?

Yadav et al. (2015) also show a self-consistent distributed dynamo can spontaneously generate high-latitude dark spots when a large-scale magnetic field, generated in the bulk of the convection zone, interacts with and locally quenches flow near the surface. This is similar to findings reported by Schrijver and Title (2001), who explored the migration of surface magnetic fields towards the poles. Rapid rotation is vital for the formation of such dark polar spots. However, if there is a global poloidal field and a shear underneath/next to it in a perpendicular direction, a local dynamo can occur.

Such flare activity from the polar regions could be caused by large-scale 2D vortices within the poloidal fields which thread through the temperature inversion layer (in the polar regions) acting in a similar way to charged particles when they experience a force across the field lines perpendicular to their motion. When such 2D vortices are formed they may wind up the field line with them and when these eddies encounter the rim of the polar cap (whose axis is not aligned with the rotation axis of the star) magnetic reconnection may occur generating flares.

There has been much work completed on the magnetic structures of M dwarfs including the study of their surface magnetic fields. Zeeman Doppler Imaging (ZDI: Semel, 1989) is a technique which can be used to map the large-scale magnetic topologies of stars. Overall, studies such as Donati et al. (2008) and Morin et al. (2010) have found a broad variety of magnetic field topologies including complex magnetic field structures. Therefore, there are a multitude of possibilities within the magnetic field conditions of these stars which are producing the flaring activity observed. In addition, the dynamo mechanism of the star also plays an important role as this is how these varying magnetic field geometries can be explained.

Overall, I have outlined three scenarios to explain the lack of rotational phase preference for flares in the M dwarf sample. In order to test the theories further I would need to compare results from stars with low and high inclination. Davenport et al. (2015) and Silverberg et al. (2016) reported observations of GJ 1243 which has a high rotation inclination and a high latitude spot. With many thousands of flares being detected, no correlation with its 0.59 day rotational period was found. A sample of stars with well defined inclination values is the next step in allowing us to distinguish between the three scenarios to explain the main result.

4.6 Conclusion

Previous observations of activity levels in fast and slow rotators suggest a rotation-dependent transition in the magnetic properties of the atmosphere of M dwarfs, where the transition corresponds to approximately 10 days. Using K2 SC observations of a sample of 34 M dwarfs, an interesting result has been found. There is no correlation between the rotation phase and the number of flares. Given these stars all show significant rotational modulation amplitude due to a starspot, this is a surprise.

New wide field surveys which are red sensitive will be suited to exploring these issues in greater detail and with larger sample sizes. For instance, the New Generation Transit Survey (NGTS) (Wheatley et al., 2017) has a field of view of 96 square degree and is red sensitive. Although its prime goal is the detection of Neptune and super-Earth size exo-planets it will obtain long duration lightcurves of many red dwarfs.

The Transiting Exoplanet Survey Satellite (TESS) (Ricker et al., 2015) was launched on the 18th April 2018. TESS will be sensitive to stars brighter than $V \sim$12 and will have 27 day observation blocks covering $24^\circ \times 96^\circ$ of sky with a cadence of 1 min for many objects. In the next chapter I look further into the starspot/stellar flare relationship using SC data from *TESS* on a sample of 149 M dwarfs.

Appendix

4.A PanStarrs Magnitudes

Table 4.A.1: For all the stars in the sample here presents the corresponding PanStarrs magnitudes (Chambers et al., 2016) in the g, r i, and z bands with errors which are also taken from the PanStarrs catalogue. These magnitudes are used to create a template spectrum of each star and used in the calculation of the quiescent *Kepler* luminosity.

Name	EPIC ID	g	r	i	z
LHS 2420	201611969	13.0682 ± 0.0010	11.7446 ± 0.0010	10.0773	10.6904 ± 0.1852
LP 804-27	205204563	12.2986 ± 0.0010	11.0668 ± 0.1391	9.8560 ± 0.1723	9.0415 ± 0.0378
GJ 3954	205467732	15.0310 ± 0.0034	13.7505 ± 0.0029	12.2592 ± 0.3998	11.1509 ± 0.0210
IL Aqr	206019387	11.0744 ± 0.0150	8.9746 ± 0.0692	8.4762 ± 0.0394	8.1422 ± 0.2303
LP 760-3	206050032	12.2150	11.5380	11.2720	11.1370
2MASSI J2214-1319	206053352	20.8604 ± 0.0406	19.4495 ± 0.0081	16.9408 ± 0.0041	15.7102 ± 0.0042
Wolf 1561 A	206262336	14.2094 ± 0.0001	13.5603 ± 0.0784	11.3962 ± 0.0352	10.4803 ± 0.0635
HG 7-26	210317378	14.3808 ± 0.0065	13.2037 ± 0.0107	12.1530 ± 0.0701	11.4553 ± 0.0371
NLTT 12593	210434433	13.6522 ± 0.0005	12.3198 ± 0.0010	11.9320	10.7620 ± 0.0397
G 6-33	210460280	12.5168 ± 0.0055	11.6516 ± 0.0404	12.2169 ± 0.0385	11.8217 ± 0.0991
LP 415-363	210489654	14.4373 ± 0.0057	13.3156 ± 0.0037	11.8085 ± 0.0385	13.3588 ± 0.0012
MCC 428	210579749	11.2964 ± 0.0520	10.0182 ± 0.0124	9.3745 ± 0.2068	8.5127 ± 0.0229
GJ 3225	210758829	15.5532 ± 0.0024	14.2847 ± 0.0037	12.5702 ± 0.0183	11.9246 ± 0.1065
2MASS J0326+1919	210764183	21.4785 ± 0.1072	19.7707 ± 0.0250	17.1323 ± 0.0032	15.7071 ± 0.0027
LP 414-108	210811310	13.7311 ± 0.0100	12.5716 ± 0.0599	12.3544 ± 0.1876	12.2010 ± 0.3246
LP 357-206	210894955	18.4372 ± 0.0077	17.1264 ± 0.0034	14.9935 ± 0.0013	14.0026 ± 0.0041
2MASS J0335+2342	211046195	19.5600 ± 0.0100	18.2366 ± 0.0054	15.6818 ± 0.0029	14.4760 ± 0.0047
LT Tau	211069418	16.8460 ± 0.0065	15.6460 ± 0.0035	14.2525 ± 0.0012	13.3161 ± 0.0017
V497 Tau	211077349	17.0385 ± 0.0053	15.7580 ± 0.0126	14.5928 ± 0.0049	14.0379 ± 0.0036
V692 Tau	211082433	16.7380 ± 0.0118	15.5423 ± 0.0052	13.8039 ± 0.0004	12.8970
V631 Tau	211112686	15.9072 ± 0.0060	14.7119 ± 0.0089	13.8246 ± 0.0100	13.3578 ± 0.0050
V* MY Tau	211117230	14.6712 ± 0.0068	13.5257 ± 0.0010	12.8800	12.4340
GJ 3508	211642294	12.3840 ± 0.0010	11.7487 ± 0.0461	10.0195 ± 0.0502	11.4547 ± 0.0000
LP 426-35	211945363	14.0742 ± 0.0024	13.3732 ± 0.4861	11.3541 ± 0.0010	11.9661 ± 0.0010
AX Cnc	211970427	16.6625 ± 0.0041	15.4590 ± 0.0008	14.2677 ± 0.0010	13.7382 ± 0.0034
2MASS J0831+2024	212009427	15.3423 ± 0.0041	14.1807 ± 0.0014	13.3870	13.0250 ± 0.0079
2MASS J0839+2044	212029094	17.0009 ± 0.0051	15.7975 ± 0.0017	14.7718 ± 0.0023	14.3082 ± 0.0030
LP 737-14	212518629	14.3029 ± 0.0051	13.0944 ± 0.0010	11.7148 ± 0.0400	12.1497 ± 0.0010
BD-05 3740	212776174	11.4172 ± 0.0406	9.2114 ± 0.0875	9.3707 ± 0.0523	9.1667 ± 0.0487
2MASSI J1332-0441	212826600	20.2436 ± 0.0221	18.7220 ± 0.0132	16.0798 ± 0.0023	14.7831 ± 0.0025
GJ 1224	228162462	14.1926 ± 0.0010	13.0493 ± 0.0098	11.1694 ± 0.0134	10.8942

4.B Gaia Parallaxes

Table 4.B.1: Parallaxes along with their associated errors from *Gaia* Data release 2 (Gaia Collaboration, 2016, 2018) which are then inverted to calculate the distances to the stars in the sample. The errors on the quiescent luminosity includes the error on the distance and the PanStarrs magnitude. Three of the stars did not have parallaxes in the *Gaia* DR2 catalogue and so these distances were taken from the EPIC Catalogue (Huber et al., 2016) and marked with an asterisk.

Name	Parallax	Parallax Error	Distance	$log(L_{star})$
	mas	mas	pc	erg/s
201611969	35.48	0.06	28.18 ± 0.04	31.679 ± 0.006
205204563	68.78	0.12	14.54 ± 0.03	31.266 ± 0.007
205467732	–	–	28.3*	30.88
206019387	213.87	0.08	4.676± 0.002	30.864 ± 0.001
206050032	91.89	0.09	10.88 ± 0.01	30.564 ± 0.004
206053352	25.3	0.2	39.47 ± 0.31	29.261 ± 0.032
206262336	89.20	0.13	11.21 ± 0.02	30.385 ± 0.006
210317378	28.59	0.06	34.97 ± 0.08	31.119 ± 0.009
210434433	32.36	0.06	30.90 ± 0.06	31.188 ± 0.008
210460280	27.61	0.04	36.22 ± 0.06	31.389 ± 0.006
210489654	34.72	0.15	28.80 ± 0.12	31.011 ± 0.016
210579749	58.01	0.05	17.24 ± 0.01	31.661 ± 0.003
210758829	55.20	0.09	18.12 ± 0.03	30.330 ± 0.007
210764183	34.12	0.42	29.31 ± 0.36	28.936 ± 0.049
210811310	19.07	0.04	52.45 ± 0.12	31.477 ± 0.009
210894955	34.69	0.13	28.83 ± 0.11	29.763 ± 0.015
211046195	19.53	0.15	51.21 ± 0.40	29.988 ± 0.032
211069418	8.13	0.65	122.9 ± 9.9	31.355 ± 0.321
211077349	7.34	0.07	136.3 ± 1.3	31.306 ± 0.038
211082433	12.62	0.17	79.24 ± 1.09	31.131 ± 0.055
211112686	7.47	0.05	133.9 ± 0.9	31.623 ± 0.028
211117230	7.58	0.05	131.9 ± 0.9	32.016 ± 0.027
211642294	56.10	0.06	17.82 ± 0.02	31.307 ± 0.004
211945363	–	–	37.7*	31.41
211970427	5.28	0.15	189.3 ± 5.4	31.721 ± 0.113
212009427	5.43	0.04	184.2 ± 1.2	32.083 ± 0.026
212029094	5.39	0.06	185.3 ± 2.1	31.513 ± 0.045
212518629	45.5	1.2	21.98 ± 0.58	30.832 ± 0.105
212776174	41.31	0.05	24.21 ± 0.03	32.022 ± 0.005
212826600	–	–	109*	30.49
228162462	125.59	0.07	7.962± 0.004	30.156 ± 0.002

5 Origins of Stellar Flares on M dwarfs with *TESS*

The research outlined in this chapter has been published in the Monthly Notices of the Royal Astronomical Society as Doyle et al., 2019, MNRAS, 489(1), 437-445.

5.1 Introduction

For over nine years, the *Kepler* mission provided a wealth of time variability information for several hundreds of thousands of stars (Borucki et al., 2010). This data set has provided a wide range of advances in stellar astrophysics and exoplanet research. With the loss of its second reaction wheel in 2014, *Kepler* was re-purposed as K2 and began to take observations of fields along the ecliptic for $\sim$70 - 80 days. However, in October 2018, it ran out of consumables and NASA announced the retirement of the satellite, ending its mission. Fortunately, *TESS* had been launched in April 2018 with short cadence 2-min data being available in early 2019.

As mentioned previously, the lightcurves of low mass M dwarfs can show periodic changes in their brightness as the star rotates. This is widely thought to be the result of active regions hosting spots which are cooler than their surroundings rotating in and out of view (McQuillan et al., 2013). From observations of the Sun, it is known flares typically originate in active regions which host spots so, it is natural to expect flares to originate also from the prominent starspots in low mass M dwarfs . However, recent studies, such as Davenport et al. (2014), (Lurie et al., 2015) and Doyle et al. (2018), have shown evidence seriously challenging this view. There was no correlation found between the flare number and the rotational phase in any of the M dwarfs observed using *Kepler* or K2, suggesting flares could occur without the

association with a large, dominant starspot active region.

In the previous study (henceforth Chapter 4), K2 short cadence (1 min) data was used to investigate the rotational phase of flares in a sample of 34 M dwarfs. Utilising a simple chi-squared test, the phase distribution of the flares was investigated and deemed to be random. Overall, it was concluded none of the stars in the sample showed any preference for rotational phase. The result suggests flares on low mass M dwarfs maybe generated through a different mechanism than present in our Sun.

In this chapter, *TESS* short cadence (2-minute) photometric data from a selection of M dwarfs made in sectors 1 - 3 are used with a prime goal of investigating whether there is a preferential rotational phase for flares from these low mass stars. This sample will be compared to the previous K2 study, were I will discuss in greater detail the potential causes of the findings.

5.2 M dwarf Sample Selection

There are a number of strategies for identifying active low mass stars in *TESS* data. For instance Günther et al. (2019) searched for flares in all of the 2-min cadence *TESS* data and then used the temperature extracted from the *TESS* Input Catalog (Stassun et al., 2018) to identify cool main sequence stars. Here, stars which have been observed in 2-min cadence mode using *TESS* and have a MV spectral type in the `SIMBAD` catalogue[1] are identified. By considering the original publications which provided the spectral classifications in the `SIMBAD` catalog, the stars in the sample have a spectral type accurate to within one spectral subclass. The *TESS* Input Catalog was also used to remove stars which were likely giants and wrongly classed in the `SIMBAD` catalogue using the luminosity and radii values.

Our target stars were also cross-referenced with the SkyMapper Southern Sky Survey (Wolf et al., 2018). Those which did not possess Gaia DR2 (Gaia Collaboration, 2018) parallaxes or SkyMapper data were not considered further. The SkyMapper multi-colour magnitudes were converted to flux and then fitted using a polynomial producing a template spectrum which was convolved with the *TESS* band-pass to derive the stars quiescent flux, similar to Chapter 4. The Gaia parallaxes were inverted to provide distances to each star which was used to

[1] http://simbad.u-strasbg.fr/simbad/

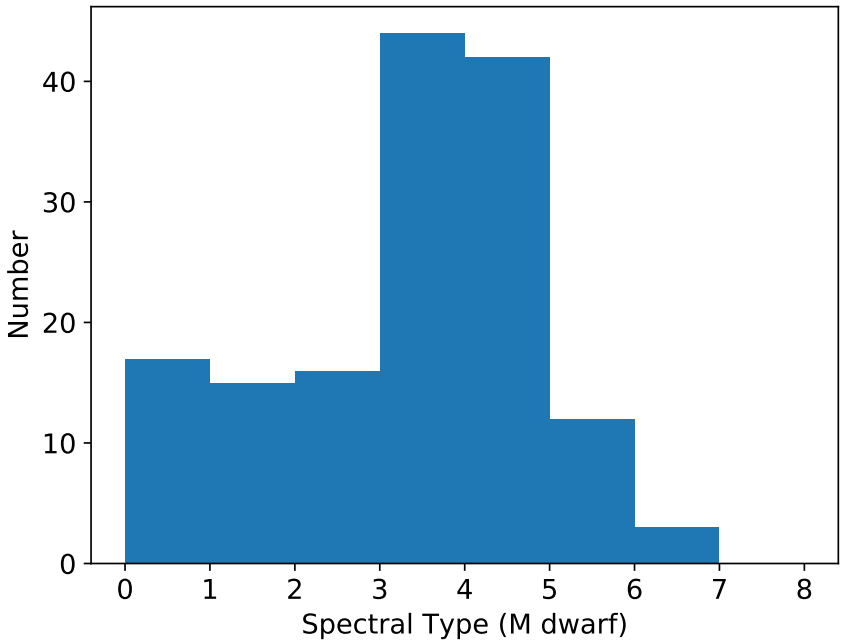

Figure 5.1: A histogram showing the spread of M dwarf spectral types within the TESS 2-min cadence sample.

determine the quiescent stellar luminosity.

The final sample of low mass stars observed at 2-min cadence with *TESS* consists of 167 M dwarfs. Each sector is observed for $\sim$ 27 days with 28 percent of the sample being observed in more than one sector. The complete list of the low mass star *TESS* sample, including a range of stellar properties, is provided in Table 5.1 and Figure 5.1 shows the spread of the spectral types within the sample.

5.3 Tess Data

The data preparation for each *TESS* lightcurve is discussed in §2.2.2. Each lightcurve was initially examined by eye to determine whether there was evidence for a rotational modulation and any flare-like events. Some sources which showed complex lightcurves (such as BY Dra variables) were not considered further. Additionally, the 18 stars which showed no modulation but did show flares in their *TESS* lightcurve were not included as the rotational phase of the flares could not be determined, see Table 5.A.1. This leaves a final sample of 149 M dwarfs

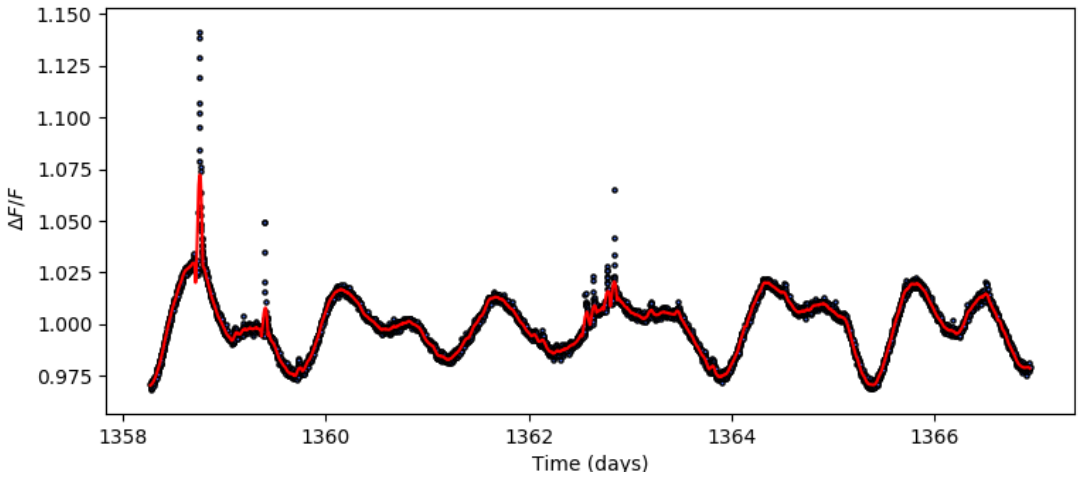

Figure 5.2: A section of the *TESS* lightcurve for 2MASS J0030-6236 (TIC 231914259) from sector 1 which covers $\sim$ 9 days. This star has a spectral type, M2V and rotation period, P_{rot}, of 1.43 days. The black points represent the *TESS* data points which have a cadence of 2-mins and the red line is the Savitzky-Golay filtered, smoothed data and shows evidence of multiple spots and flares of varying magnitudes. It is important to note the rotational modulation within this particular star suggests the presence of multiple active regions/starspots on the stellar disk.

stars remaining in the sample for this study.

5.4 Rotation Period

Large variations in brightness can be observed in the lightcurves of M dwarfs which are widely explained by the presence of spots (Oláh et al., 1997). These large, dominant starspot(s), hosted in active regions, come in and out of view as the star rotates producing quasi-sinusoidal changes in brightness, see Figure 5.2. Observations with high enough cadence and length present one way of determining a stars rotation period. Thousands of low mass stars now have derived accurate rotation periods through *Kepler* and K2 observations (e.g. McQuillan et al., 2014).

For each of the stars in the sample the rotational period, P_{rot}, is determined using the same process discussed in §4.3.1.The software package `Period` (Dhillon et al., 2001) package which runs a Lomb-Scargle (LS) periodogram was used initially, followed by an iterative process involving the phase folding of sections from the start and end of the lightcurve. Phase zero, ϕ_0, is also defined as the minimum of the flux of the rotational modulation which is initially

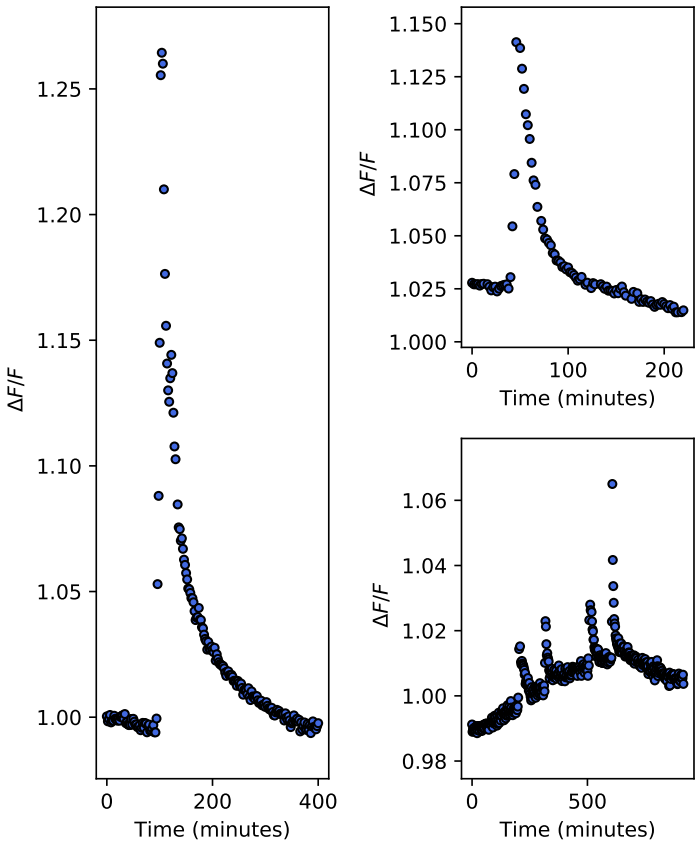

Figure 5.3: A selection of flares of varying magnitudes and duration from the M2.2 dwarf 2MASS J0030-6236 (TIC 231914259). This star was observed in sectors 1 & 2 for a total duration of $\sim$ 54 days, has a rotation period, P_{rot}, of 1.43 days and a total flare number of 58. The far left panel shows the largest flare from this star which a normalised flux peak of $\sim$ 1.27 and the remaining panels contain flares with lower energies.

determined by eye. The iterative process allows us to fine tune P_{rot} and ϕ_0 to fit the start and end of the data which ultimately derives the best fit to the data as a whole. Error estimates on the period are in the order of a few percent which ensures the phase of all the flares are reliable.

Table 5.1 shows the stellar properties of the sample including P_{rot} and ϕ_0. The rotation periods of the sample range from 0.1 to 17.4 days. This includes 9 ultra-fast rotators with $P_{rot} < 0.3$ days and 53 with $P_{rot} < 1$ day. For stars with other stars spatially nearby, there is a small possibility in which the variability is due to the nearby star, this is discussed in more detail in §2.2.2.

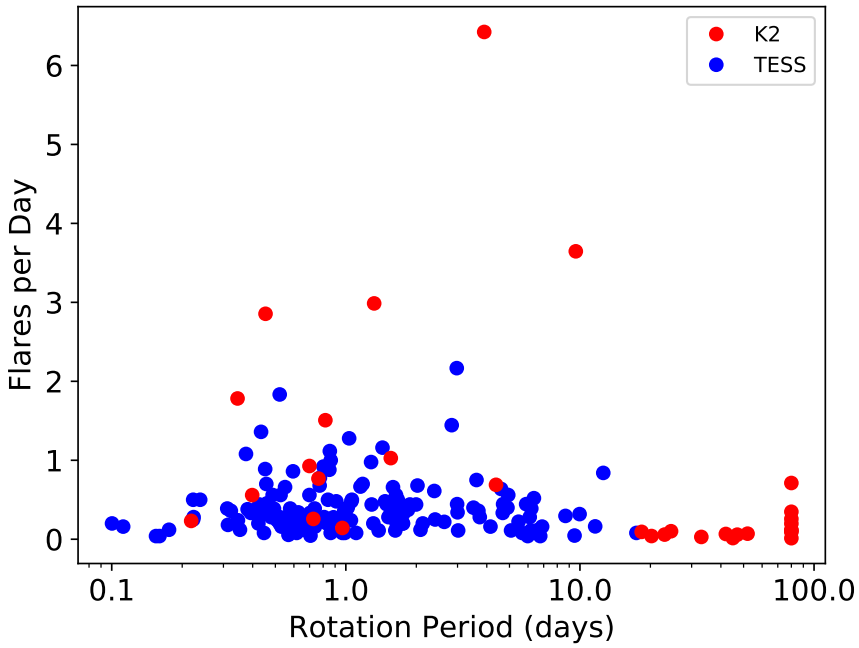

Figure 5.4: Here the normalised number of flares per day for each star is shown as a function of rotation period. The red represent the stars from Paper 1 using K2 short cadence data, and the blue the 149 targets from this study using *TESS* 2-min cadence data.

5.5 Stellar Flares

For each star in the sample, the flares present in each lightcurve along with their energies in the *TESS* band-pass need to be identified. The approach to identifying flares is the same as Chapter 4 using FBEYE (Davenport et al., 2014). A selection of flares of varying magnitudes can be seen in Figure 5.3 from the M2V dwarf 2MASS J0030-6236 (TIC 231914259) which has a rotation period, $P_{rot} = 1.43$ days. Overall, 1765 flares from the 149 flaring dwarf stars are catalogued with a range of magnitudes and durations (see Table 5.1). For stars which showed no modulation, 69 flares are catalogued and shown in Table 5.A.1.

Figure 5.4 shows the normalised flare number per day for each star in the sample according to the stellar rotational period. Additionally, the M dwarfs from Chapter 4 are overplotted which were observed using short cadence K2 data. Similar to Chapter 4, a drop in flare number for stars with $P_{rot} > 10$ days is found, however, the sample is limited in this respect due to the observation length of *TESS* being 27 days for each sector. On average the flare rate of the *TESS* stars is lower than that of the K2 stars which is attributed to its lower sensitivity, as

discussed in §2.2.3.

The energies of the flares are determined as the equivalent duration of each flare multiplied by the quiescent luminosity of the star. Amongst the sample of 149 M dwarfs, a wide range in flaring energies are observed. The lowest energy flare is $\sim 6 \times 10^{29}$ erg and is observed in the M3 star PMJ 01538-149 (TIC 92993104) from sector 3 with $P_{rot} = 3$ days. Similarly, the highest energy flare is $\sim 2 \times 10^{35}$ erg from an M3 star GSC 08494-00369 (TIC 201897406) observed in sector 2 with $P_{rot} = 3.5$ days. All of the properties including the luminosities of the stars and range of flare energies can be found in Table 5.1.

Table 5.1: The stellar properties of the first low mass stars observed by *TESS* detailing the number of flares, rotation periods, quiescent luminosity, energy range and duration range of the flares. The apparent magnitude in the *TESS* band-pass, T_{mag}, is taken from the *TESS* Input Catalog (TIC) along with the TIC ID (Stassun et al., 2018). The distances are derived from the Gaia Data Release 2 parallaxes (Gaia Collaboration, 2016, 2018) and the spectral types are obtained from the SIMBAD catalogue. For the full table please refer to Appendix A.1.

Name	TIC ID	sector	Ra (deg)	Dec (deg)	No. of Flares	SpT	T_{mag}	Parallax (mas)	Distance (pc)	P_{rot} (days)	$log(L_{star})$ (erg/s)	$log(E_{flare})$ (erg)	Duration minutes
2MASS J2151-2807	053851254	1	327.8703	-28.1304	5	1.5	12.02	12.2990	81.3074	1.7537	31.74	32.98 – 34.55	14.0 – 172.00
2MASS J2114-4213	126945045	1	318.6401	-42.2318	9	3.9	13.11	15.1340	66.0764	0.4134	31.16	32.16 – 33.36	8.0 – 48.00
2MASS J2117-4444	139090254	1	319.3919	-44.7433	4	4.5	10.88	56.9728	17.5522	0.5308	30.82	31.47 – 31.95	14.0 – 20.00
2MASS J2150-5113	139984208	1	327.669	-51.2277	6	3.7	12.0	22.4897	44.4648	1.0513	31.26	32.20 – 32.87	18.0 – 38.00
FS2003 0345	150188736	1,3	93.7286	-60.6552	2	0.5	10.44	26.0053	38.4537	9.4832	31.75	33.78 – 34.06	102.0 – 168.00
GSC 08894-00426	150359500	3	96.4838	-60.0569	23	5.0	9.71	74.3690	13.4465	1.0331	31.11	31.57 – 33.20	12.0 – 130.00
Smethells 119	161356637	1	343.8646	-52.3032	2	0.5	9.56	42.0588	23.7762	17.425	31.68	31.93 – 32.73	14.0 – 40.00
WOH S 209	179038379	1,3	78.9968	-67.2733	7	0.0	12.62	16.1301	61.9959	11.616	31.28	32.44 – 33.91	16.0 – 134.00
BPM 45048	206327797	1	354.0652	-48.5836	4	3.5	9.67	40.0092	24.9943	0.1119	31.64	33.18 – 34.08	14.0 – 46.00
WT 2220	206537793	1	332.923	-20.7367	7	3.0	11.16	24.1987	41.3245	1.5203	30.70	31.55 – 32.33	12.0 – 48.00
UPM J0113-5939	206544316	1	18.4189	-59.6598	9	3.7	11.6	23.1900	43.1220	0.3227	31.39	32.36 – 34.93	8.0 – 180.00
UCAC4 265-194917	207082763	1	331.9728	-37.0737	22	3.0	10.75	29.7125	33.6559	0.8505	31.50	32.16 – 34.21	14.0 – 130.00
LEHPM 5245	215197039	1	343.2486	-39.3812	5	0.0	10.96	20.9295	47.7795	2.1316	31.74	32.61 – 33.77	12.0 – 108.00
WISE J0250-6545	220523369	1,2,3	42.5936	-65.7653	22	3.2	11.94	19.7575	50.6137	1.2892	31.41	32.07 – 34.58	12.0 – 180.00
GSC 08859-00633	220539110	1,2,3	43.447	-61.5878	34	3.0	9.93	24.1223	41.4554	0.773	31.98	32.08 – 34.49	8.0 – 106.00
2MASS J0256-6343	220556639	1,2,3	44.197	-63.7174	43	4.0	11.48	16.6797	59.9531	0.5947	31.74	32.04 – 34.68	6.0 – 148.00
UCAC4 110-129613	229807000	1	352.2412	-68.0431	27	2.5	10.74	21.7164	46.0481	0.3745	31.79	31.59 – 34.31	8.0 – 90.00
2MASS J2329-6749	229807051	1	352.324	-67.8336	6	3.5	12.48	21.7647	45.9460	1.0224	31.10	32.55 – 33.90	26.0 – 220.00
FS2003 1156	231267979	1	334.6657	-53.4444	17	2.5	10.66	21.9142	45.6325	2.0233	31.83	32.45 – 33.90	12.0 – 82.00
2MASS J2110-5811	231632372	1	317.5259	-58.1972	3	4.0	12.63	19.8774	50.3084	0.5896	31.12	32.54 – 32.85	20.0 – 22.00
Smethells 165	231867117	1	6.0384	-62.1848	8	0.0	9.56	22.6086	44.2310	1.7568	32.20	32.87 – 34.50	22.0 – 200.00
UPM J0027-6157	231910539	1,2	6.8898	-61.955	33	4.0	12.04	23.0563	43.3721	0.55	31.22	31.82 – 33.75	8.0 – 140.00

5.6 Rotational Phase

For all stars in the sample, they display a clear rotational modulation which is attributed as being due to the presence of a large dominant starspotflregion rotating into and out of view. From studies of solar flares it is known numerous and more energetic flares of energies ($\geq 10^{32}$ erg) occur in active regions which possess complex sunspot configurations (Zirin and Liggett, 1982; McIntosh, 1990). Therefore, you would expect to observe the same behaviour from M dwarfs which host a large, dominant spot as part of a complex active region. In Chapter 4, I investigated the preference for rotational phase for a small group of M dwarfs observed in short cadence by K2 and found no correlation between flare number and rotational phase, despite the clear presence of large dominant starspot(s)flregion. For this sample of M dwarfs observed using *TESS*, the same analysis as Chapter 4 is used to determine if any of the flares show a preference for certain rotational phases which coincide with the dominant starspotflregion.

The χ^2_ν statistic is utilised as a means of assessing the rotational phase distribution of the flares. In order to do this the sample is split depending on the number of flares present in the lightcurves of each star using the overall mean number of flares as an indicator. Any star which possessed $>$ 12 flares in its *TESS* lightcurve was considered to be an active M dwarf and remaining sources are grouped together for the rotational phase analysis of the flares. Additionally, the flares from all 149 low mass dwarf stars as a whole is also investigated and these results discussed individually.

5.6.1 Individual Cases

From the sample, 45 stars show 13 or more flares in their lightcurves so, the phase distribution of these flares can be tested individually. Out of this 45, ten have a star which was up to 1.5 mag fainter and within 42$''$ of the target. For each of these stars, their lightcurves are phase folded and binned using rotation periods and phase zeros obtained previously. The flares are then split into low and high energy, where the cut-off was determined from a histogram distribution of all flares which levelled off at $10^{33.5}$ erg. This information can be displayed

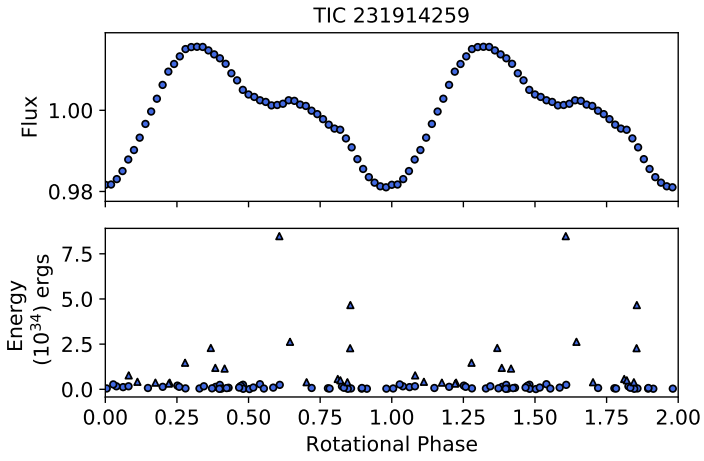

Figure 5.5: The rotational phase distribution for 2MASS J0030-6236 (TIC 231914259) observed in sectors 1 & 2 (where the rotational phase coverage $\phi = 1.0 - 2.0$ is a repeat). The upper panel shows the phase folded, binned lightcurve where phase zero is defined as flux minimum and $P_{rot} = 1.43$ days. The lower panel shows the phase distribution of the flares as a function of energy where triangle symbols represent flares of energies $> 3.16 \times 10^{33}$ erg and circles $< 3.16 \times 10^{33}$ erg.

in plots similar to Figure 5.5 which show the rotational phase distribution of the flares as a function of energy. In this particular example, 2MASS J0030-6236 (TIC 231914259) shows a total of 58 flares, 17 of which are considered to be high energy, which are spread across all rotational phases.

A simple χ^2_ν test is used to assess the randomness within the rotational phase distribution of the flares. The rotational phase, ϕ, is split into 10 bins (degrees of freedom is 9) of 0.1 between $\phi = 0.0 - 1.0$ and χ^2_ν is calculated for high energy, low energy and all flares. As an example, 2MASS J0030-6236 (Figure 5.5) has χ^2_ν of 1.31, 1.32 and 1.48 for high, low and all flares: none are significant. For full details of this method please refer to §4.4. Overall, out of the 45 M dwarfs none show flares which have a preference for rotational phase indicating the flares are not associated with a large, dominant starspotflregion.

5.6.2 The Remaining Sources

The 104 remaining M dwarfs in the sample which show ≤ 12 or less flares in their lightcurves, are grouped together to asses the rotational phase distribution of the flares as a whole. Phase zero, ϕ_0, is defined for each star to be the minimum of the rotational modulation, making a

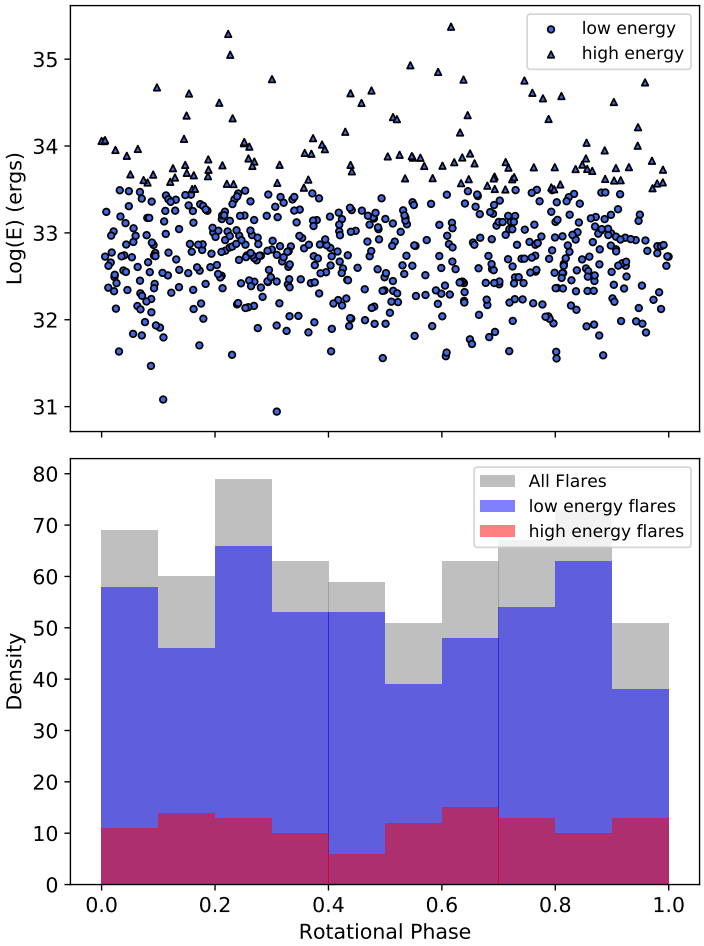

Figure 5.6: The rotational phase distribution for all stars which show < 12 flares in their *TESS* lightcurves, where ϕ is defined as flux minimum 0.0 which represents rotational minimum. The upper panel shows the rotational phase distribution as a function of energy where triangle symbols represent flares of energies $> \ 3.16 \times 10^{33}$ erg and circles $< \ 3.16 \times 10^{33}$ erg. The lower panel shows the histogram of the rotational phase distribution.

comparison of the flare phase distribution for varying stars possible. Figure 5.6 shows the flare rotational phase distribution as a function of energy for all flares from the remaining 104 stars, along with the histogram of the distribution where the rotational phase has been split into 10 bins of 0.1 between $\phi = 0.0 - 1.0$. Flares were also split into low and high energy using the cut off mentioned previously of $10^{33.5}$ erg. The χ^2_ν test is applied to this sample of flares yeilding values of 1.25, 0.57 and 0.57 for all, high and low flare groups respectively. Again, these χ^2_ν values for high and low energy flares indicate there is no correlation between rotational phase and flare number amongst this group of flares from 104 stars.

This was repeated, splitting the stars into spectral type categories of $<$ M4 and $>$ M4 with no

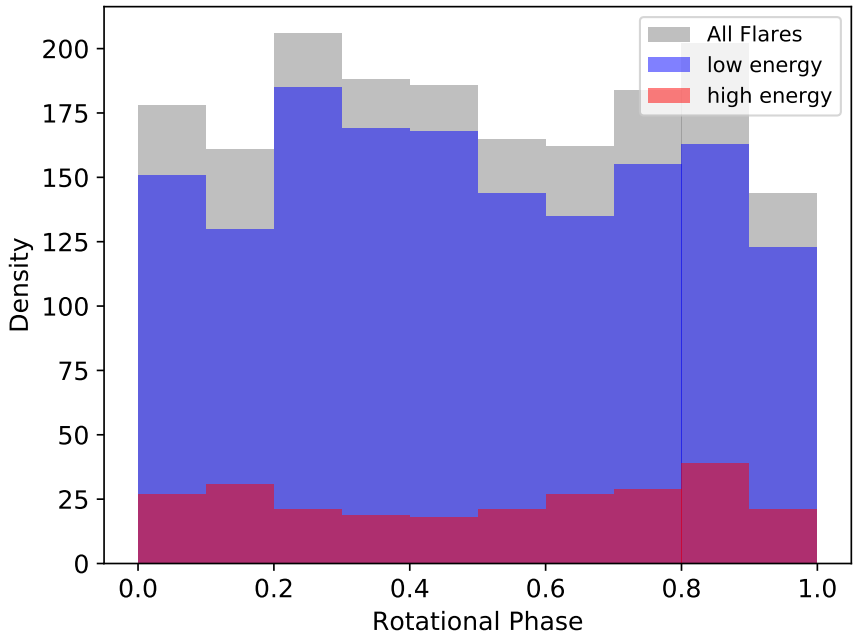

Figure 5.7: The rotational phase distribution for all 1776 flares from the sample of 149 stars. The histogram of this distribution is shown using bins of $\phi = 0.1$ where there is no evidence of any correlation between flare number and rotational phase in high, low or all flares.

preference for flare rotational phase found in either of these groups. Similarly, the stars were split by rotational period, for example 0 - 0.5 days, 0.5 - 1 days and so on, with no evidence of any correlation being found using the χ^2_ν test. In addition, using Gaia targets with nearby stars were identified and are removed yeilding values of the χ^2_ν test to be 1.13, 0.945 and 0.945 for all, high and low flares respectively: the conclusions, therefore, are not affected.

To summarise, no evidence was found of any correlation between flare number and rotational phase in the grouped remaining 104 M dwarfs which show ≤ 12 flares in their lightcurves. When splitting this group up by spectral type or rotational period, again, no correlation was found and the χ^2_ν statistical test indicated the flares are randomly distributed.

5.6.3 The Sample as a Whole

Next, the rotational phase distribution of all 1765 flares from the sample of low mass stars is analysed in its entirety to check for any correlations with flare number. As ϕ_0 is defined at flux minimum this comparison is possible. I do not find any correlation between flare number

and rotational phase and the χ^2_ν test indicates the flares are randomly distributed. Figure 5.7 shows the histogram distributions of the rotational phase for all flares which displays a uniform spread amongst the phase bins of $\phi = 0.1$. This was repeated for phase bins of $\phi = 0.2$ and $\phi = 0.01$ and again no correlation was found.

In a similar analysis, Roettenbacher and Vida (2018) look at the number of flares occurring in bins of phase $\phi = 0.01$, for all stars in their sample of 119. They do find a correlation between rotational phases which represent a visible starspot and flare number. This is observed as a peak in the histogram distribution for flares of flux increases between 1% and 5% only and not in higher energy flares of flux increases $> 5\%$. However, their sample differs greatly from this one as it consists of main sequence stars from late-F to mid-M observed in long cadence (30-min) by *Kepler*.

Similarly, in Roettenbacher and Vida (2018) they only select stars for their sample which exhibit one spot structure at a time in their lightcurve. From the sample of 149 M dwarfs which show rotational modulation in their lightcurves, 77% show a clear sinusoidal pattern indicative of the presence of one large starspot, where the remaining 23% have lightcurves which would have arisen from multiple spots. To address this, all stars which showed any evidence for multiple spots within their lightcurves were removed: the conclusions do not change.

5.7 Ultra-Fast Rotators

Rapidly rotating low mass stars are expected to produce increased levels of activity which are strongly related to their dynamo mechanism (Hartmann and Noyes, 1987; Maggio et al., 1987). Activity, including Hα, Ca II and X-ray emission, is observed to saturate in rapid rotators where there is a decline in activity observed as rotation decreases, known as the rotation-activity paradigm (Soderblom et al., 1993; Stauffer et al., 1997; Kiraga and Stepien, 2007; Yang et al., 2017). A further downward trend from the saturated plateau, known as super-saturation, has also been observed in rapidly rotating stars (James et al., 2000). This suggests a decline in activity despite their rapid rotation and goes against the rotation-activity paradigm.

From Figure 5.4, I noticed a small group of nine stars which have rotation periods, $P_{rot} < 0.3$

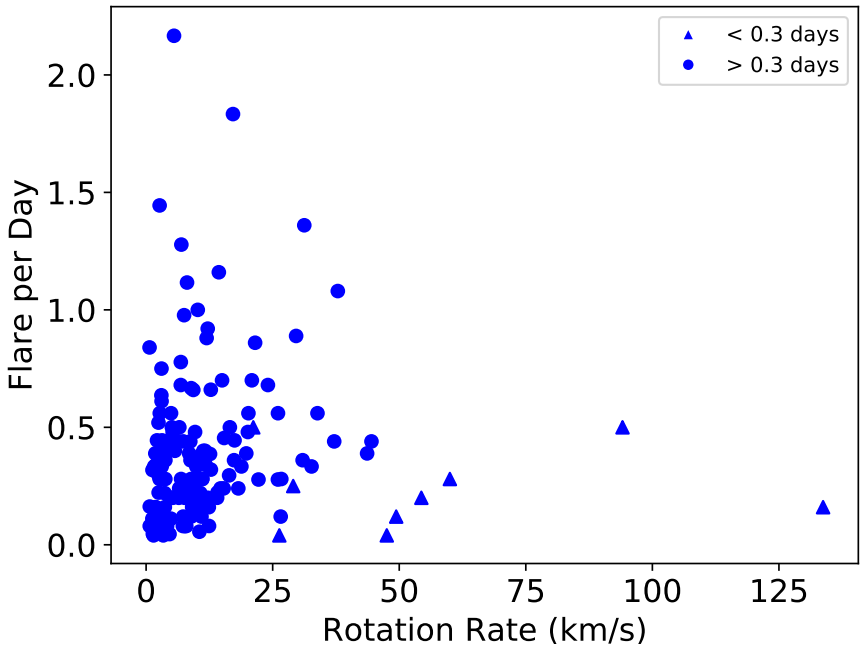

Figure 5.8: The normalised flares per day of each star in the *TESS* sample as a function of rotation rate.

days and spectral types in the range from M1 to M6 which produce a very low number of flares. To investigate this further the rotational velocity, Ω, was determined for all stars in the sample as $\Omega = 2\pi R/P_{rot}$ which has units of km/s. R is the radius of the star derived from the Stefan-Boltzmann Law using the temperature derived from Gaia DR2 and P_{rot} is the rotation period. Although there is some uncertainty in determining Ω, Figure 5.8 shows that the stars with $P_{rot} < 0.3$ days also have high rotational velocities. Upon calculating the break-up velocity for the fastest two rotators in this group (TIC 206327797: $\Omega = 133$ km/s and TIC 183596242: $\Omega = 94$ km/s) it can be said these stars are both stable, rotating between 0.24 – 0.34 of the break-up velocity. Secondly, I am surprised to find that the flare rate decreases with increasing rotational velocity. You would expect the stars with higher rotational velocity to show greater flaring activity. At this point I am unable to explain this finding which will therefore require further investigation, see §7.4.3 for more details.

I look to determine stellar ages for the small number of ultra-fast rotators as another indicator to explain the lack of flaring activity. To do this Gyrochronology (Barnes, 2007) is used, which utilises a relationship between the age, colour and rotation period of main sequence stars. For

the purposes of this work, `stardate` (Morton, 2015; Angus, 2019) a python package, is used which combines isochrone fitting with gyrochronology. For the nine ultra-fast rotators, the ages are estimated to within the range of 3 Myr to 2 Gyr. If these are taken at face value it raises serious questions for how such a rapid rotator could be as old as 2 Gyr, and conversely how such a young fast rotator can show only few flares. However, although the uncertainties in determining the ages of solar-type stars are reasonably well understood, the spread in period against age for low mass stars is much higher. With this caveat in mind, it is concluded that age may not be the primary cause for the lack of flaring activity in these stars. Rather, this suggests it may be related to their magnetic field configuration.

Kochukhov and Lavail (2017) recently investigated the global and small-scale magnetic field configuration of the nearby M dwarf binary GJ65 AB. Despite nearly identical masses and rotation rates ($P_{rot} = 0.2432$ days for GJ65 A and $P_{rot} = 0.2269$ days for GJ65 B (Barnes et al., 2017)), the secondary exhibits an axisymmetric, dipolar-like global field with an average strength of 1.3 kG while the primary has a much weaker, more complex, and non-axisymmetric 0.3 kG field. Furthermore, GJ 65 B flares more frequently than GJ 65 A and is also an order of magnitude brighter in its steady radio emission (Audard et al., 2003). Despite their rotation rate both of these stars possess dramatically different magnetic field configurations along with varying degrees of magnetic activity. This suggests the magnetic field configuration of the stars plays an important role in their magnetic activity, more so than their rotation period or age. However, it is likely that all three factors are connected.

An alternative explanation is that flares from these objects emit mostly in blue wavelengths. A preliminary check has been made for a few known ultra-fast rotators (KIC 6752578, KIC 6791060 and KIC 9825598) from literature observed by *Kepler* and find they too show a low number of flares. However, these sources have only been observed in long cadence (30-min), compared to *TESS* short cadence at 2-min, which could be the reason for not observing the short duration flares if they are present. Additional work is needed via checking the flare activity on the same object as observed by *Kepler* and *TESS*, see §7.4.3 and Ramsay et al. (2020) for further details.

5.8 Discussion

I have analysed the magnetic activity of a sample of 149 low mass stars observed in 2-min cadence by *TESS*. Rotation periods for 90 percent of stars were successfully derived for the sample as a result of rotational modulation present in their lightcurves. In addition, the flare characteristics (energy, duration, rotational phase, etc.) have been catalogued for each star and this information used to compute a statistical analysis on the flaring activity. No evidence of a correlation between rotational phase and flare number was found for any individual star in the sample or collectively as the entire catalogue of 149 stars. Even when targets with nearby stars were removed there is still no trend present with regards to rotational phase and flare number. Furthermore, when the sample is restricted to only those which show evidence of one starspot, still no evidence for a correlation between rotational phase and flare number was found. This result is consistent with the findings in Chapter 4 and with a larger sample size this solidifies the initial finding. In Chapter 4, three scenarios were proposed to explain the lack of correlation between phase and flare number including binarity, presence of exo-planets and polar spots. Here I will discuss these three scenarios in greater detail while also introducing a number of others which have come to light since.

Firstly, there is the possibility of star-star and star-planet interactions being a cause of the constant flaring activity at all rotational phases observed in the samples of M dwarfs from both K2 and *TESS*. Fischer and Saur (2019) look to identify signatures of star-planet interaction (SPI) in the K2 lightcurve of the TRAPPIST-1 system. They discuss four mechanisms which cause temporal variability of SPI lightcurves, two by orbital positions of planets and two due to the stellar magnetic field. Overall, their results hint at a possibility of a quasi-periodic occurrence of flares with the orbiting planet TRAPPIST-1c. However, this result is inconclusive due to various factors but is a promising potential find for further studies. Similarly, Route (2019) used multi-wavelength observations to study the SPI in the HD 189733 system. The star in this system is a very active BY Dra type variable with a Jupiter mass planet orbiting at a distance of 0.031 AU. Through physical and statistical analysis, Route (2019) concludes there is no existence of SPI within this system and stellar activity on HD 189733A is not correlated at certain orbital phases.

In earlier work, Doyle et al. (1992), Van den Oord et al. (1998) and Byrne et al. (1998) showed that for a star with radius ∼0.3R$_\odot$, a field strength of ∼2.5kG (typical values for an M dwarf), the maximum amount of stored energy is $\sim 10^{37}(l/R_\odot)$ erg where l is the length of a filament and $R_\odot$ is the solar radius. Thus for a filament whose length is ∼30% of the star's radius this equates to $\sim 10^{36}$ erg. This is more than sufficient to explain the large flare energies for flares on M dwarfs. Regarding the possibility of a filament located between the star and a nearby planet this allows a factor of $(1.6a/R_*)^2$, where a is the binary separation and R_* is the star's radius. However, despite these studies SPI is still a relatively new area of research and is difficult to observe. Hopefully further observations with missions like *TESS* will provide the observations needed to prove SPIs.

As mentioned previously, Roettenbacher and Vida (2018) conducted a similar study to investigate the connection between starspots and flares in main-sequence stars. They use a sample of late-F to mid-M stars observed using long cadence (30-min) lightcurves over 4 years. From their sample of 119 stars, 2447 flares were detected with only lower energy flares occurring predominantly with the large starspot. They propose this could be a result of more energetic flares being observed on disk and close to/over the limb, whereas less energetic flares would not be strong enough to be seen over the limb. In the present data there is no difference in the rotational phase versus either the large or small flares. Furthermore, Mariska and McTiernan (1999) reported that in most instances, occulted solar limb flares were indistinguishable from non-occulted limb flares, although the hard X-ray spectra averaged over the entire event had a softer spectral index in the occulted limb flares thus indicating an occultation of the hard X-rays. Kuhar et al. (2015) shows a good correlation between hard X-ray fluxes and the excess white light flux. It is likely the white-light emission from occulted flares may not be observable, hence this can be ruled out as an explanation for the lack of rotational modulation in the flare occurrence.

An additional scenario includes the possibility of multiple spot locations across the disk of the star. Fitting a lightcurve with a one or even two spot model does not produce the sinusoidal pattern observed in many low mass stars from *Kepler* and *TESS* (Eaton et al., 1996). If the rotation modulation was a result of one dominant, large starspot, you would almost always observe flat-top lightcurves and this is not the case. Therefore, the sinusoidal pattern which

is observed is not produced by a circular large starspot but in fact multiple active regions which hosts more/larger spots across the disk. One active region will possess either a larger spot or greater spot coverage and would be responsible for the peak and trough present in the sinusoidal lightcurve. In theory, this active region should produce higher energy flares, see McIntosh (1990). However, no correlations between low or high energy flares and the phases corresponding to the minimum of rotational modulation is observed. This suggests there are other magnetic features, such as polar spots, and/or magneto-kinetic/hydrodynamical processes at play.

Finally, there is the potential for the presence of polar spots on these low mass stars (Strassmeier, 1996). Unlike the Sun, where polar spots are not present as a result of its dynamo mechanism, polar spots can be present in these low mass stars and depending on the viewing geometry are not reflected in the lightcurve. In Chapter 4, the formation of polar spots was discussed in more detail concluding they have the potential to play an important role in flare generation. It is possible they could be interacting with multiple spot groups across the disk to produce constant flaring activity at a range of energies and at all rotational phases. Similarly Roettenbacher and Vida (2018) also suggest the presence of polar spots as an explanation for the spread in stellar flares within their sample.

I have further discussed the three scenarios proposed in Chapter 4 to explain the lack of a correlation between flare number and rotational phase. With the extended sample of 149 low mass stars observed in 2-min cadence with *TESS*, the initial finding has been solidified and two new scenarios proposed to explain its cause. However, it is likely the results obtained stem from a combination of the five scenarios, in particular multiple spot locations and polar spots will have a big role to play.

5.9 Conclusions

To summarise, a statistical analysis of stellar flares is conducted from a sample of 149 low mass stars observed in 2-min cadence by TESS. In particular, the focus is on investigating the correlation between the rotational phase and number of flares and ultimately find no evidence of any such correlation. This is unexpected as you would expect a correlation in flare number to

coincide with the minimum of rotational modulation when spot coverage is at its maximum. Therefore, explanations for the finding are outlined including star-planet interactions, polar spots and multiple spot locations.

In addition, a group of rapidly rotating stars is touched upon within the TESS sample which have $P_{rot} < 0.3$ days but very little flaring activity. The reasoning behind this is speculated and it is concluded to most likely be a result of the magnetic field configurations of the star. In order to investigate this further it would be necessary to obtain spectropolarimetry observations to derive more information on the magnetic properties of the stars.

Overall, the lack of any correlation between starspots and flare number has been solidified with a larger sample using *TESS*. This finding questions the magnetic properties which are at play on these stars to produce the flares observed. The next chapter sees the continuation of this study extending out into stellar flare analysis of solar-type stars. This includes looking not only at the rotational phase distribution of the flares but flare occurrence and stellar variability. In addition, historic GOES solar flare data is used as a benchmark to detail the close relationship between solar flares and sunspots.

Appendix

5.A Non-Rotating M dwarf Flare Stars

In this Appendix the stellar properties for the non-rotating low mass stars are detailed. This includes properties such as the number of observed *TESS* sectors, number of flares, quiescent luminosity, energy range and duration of the flares for each star.

The number of flares is obtained from the `FBEYE` suite of programs which also provides the start, stop and peak times of each flare in order to calculate the durations. The energies of the flares are determined as the equivalent duration (area under the flare lightcurve which is obtained from `FBEYE`) of each flare multiplied by the quiescent luminosity of the star. For full details of how all the stellar and flare properties are obtained please refer to §5.5.

Table 5.A.1: The stellar properties of a select few stars which showed no rotational modulation but processed flares within their lightcurves, detailing the number of flares, quiescent luminosity, energy range and duration range of the flares. The apparent magnitude in the TESS band-pass, T_{mag}, is taken from the TESS Input Catalog (TIC) along with the TIC ID (Stassun et al., 2018). The distances are derived from the Gaia Data Release 2 parallaxes (Gaia Collaboration, 2016, 2018) and the spectral types are obtained from the SIMBAD catalogue.

Name	TIC ID	sector	No. of Flares	SpT	T_{mag}	Parallax mas	Distance pc	$log(L_{star})$ erg/s	$log(E_{flare})$ erg	Duration minutes
2MASS J2148-4736	147421845	1	3	5.0	12.694	17.869 ± 0.064	55.9623 ± 0.2023	31.18	33.00 – 33.53	42.00 – 47.99
LP873-37	099566892	1	5	4.0	12.12	21.106 ± 0.076	47.3165 ± 0.1706	31.26	32.59 – 33.37	17.99 – 80.00
2MASS J2123-3908	207080123	1	4	3.5	10.879	41.090 ± 0.070	24.3365 ± 0.0418	31.26	32.51 – 33.95	45.99 – 125.99
2MASS J0119-6842	052242947	1	3	4.0	13.69	28.976 ± 0.085	34.4768 ± 0.1018	30.39	32.00 – 34.06	14.00 – 130.00
2MASS J2121-2433	302298728	1	3	5.0	12.986	34.466 ± 0.102	29.0141 ± 0.0860	30.51	32.15 – 32.69	25.99 – 32.69
2MASS J0028-6751	038820496	1	3	4.5	13.653	22.666 ± 0.059	44.1177 ± 0.1160	30.75	32.30 – 32.88	12.00 – 47.99
2MASSI J01231-6921	052256020	1	1	8.0	14.748	22.479 ± 0.189	44.4915 ± 0.3742	30.14	32.20	28.00
2MASS J0253-7959	394356010	1	7	5.5	13.652	57.101 ± 0.071	17.5128 ± 0.0218	29.87	31.11 – 33.24	11.99 – 221.99
LEHPM 4459	389051009	1	2	5.0	12.94	72.095 ± 0.081	13.8649 ± 0.0157	29.84	32.14 – 32.36	69.99 – 101.99
2XMM J2253-1721	188586529	2	10	4.0	12.948	24.485 ± 0.124	40.8420 ± 0.2068	30.82	32.29 – 33.36	17.99 – 63.99
2MASS J0219-7137	234307350	1&2	3	6.0	15.342	20.735 ± 0.135	48.2307 ± 0.3153	29.77	32.14 – 32.36	11.99 – 31.99
2MASS J2352-5229	201226029	1&2	4	4.6	13.506	23.372 ± 0.069	42.7853 ± 0.1264	30.62	32.24 – 34.02	8.00 – 317.99
WISE J0127-6032	237910557	1&2	7	4.2	12.824	19.770 ± 0.058	50.5845 ± 0.1501	31.05	31.91 – 32.90	12.00 – 54.00
2MASS J0413-5231	219229275	3	2	2.4	11.54	19.428 ± 0.036	51.4721 ± 0.0967	31.58	33.54 – 33.63	104.00 – 128.00
WISE J0202-3136	123336907	3	1	4.0	13.32	19.41 ± 0.515	51.5198 ± 1.3674	30.86	33.29	58.00
FBS 0014-091	037718790	3	4	5.0	12.15	17.969 ± 0.083	55.6504 ± 0.2589	31.38	32.52 – 34.14	17.99 – 131.99
PS 78191	011652986	3	5	3.5	11.58	29.532 ± 0.074	33.8608 ± 0.0857	31.19	32.21 – 33.20	8.00 – 37.99
2MASS J0137-4558	100100909	3	2	5.0	13.22	26.511 ± 0.706	37.7193 ± 1.0053	30.65	32.63 – 32.72	39.99 – 41.99

6 Superflares and variability in Solar-type Stars with TESS

The research outlined in this chapter has been published in the Monthly Notices of the Royal Astronomical Society as Doyle et al., 2020, MNRAS, 494(3), 3596-3610.

6.1 Introduction

Solar flares are powerful, eruptive events which are seen across the entire electromagnetic spectrum. Overall, our Sun can show flares with energy outputs ranging from 10^{24} - 10^{32} erg (Aschwanden et al., 2000). However, studies of solar-type stars using *Kepler* have revealed flares with energies exceeding 10^{32} erg, with 'superflares' having energies up to 10^{38} erg (Schaefer et al., 2000).

Maehara et al. (2012) conducted the first statistical study of flares on solar-type (G-type main sequence) stars. They used *Kepler* long cadence (LC: 30-min) lightcurves and identified 365 superflares (flares with energies $> 10^{33}$ erg) on 148 G-type stars. In addition, they fit the occurrence distribution rate of the flares with a power law and find it is similar to solar flares and flares on low mass stars. They also explore the proposed theory of hot Jupiters being important in the generation of superflares (Rubenstein and Schaefer, 2000) and find none have been discovered around their sample of solar-type stars indicating they are rare. Lastly, using derived rotation periods for each star they conclude superflares occur more frequently on young solar-type stars (younger than our Sun) as a result of faster rotation periods.

In Shibayama et al. (2013), they extend the work started by Maehara et al. (2012), searching for superflares on solar-type stars (G-type dwarfs) with *Kepler* LC data over a longer period

of 500 days. This resulted in identifying 1547 superflares on 279 solar-type stars, increasing the sample of flares by a factor of four. Overall, they confirm the previous results, identifying the distribution of occurrence rate as a function of energy to be similar to that of solar flares. Interestingly, by monitoring the brightness variation of their sample they conclude the high occurrence of superflares could be a result of extremely large starspots.

More recently, Notsu et al. (2019) presented a complete review of *Kepler* solar-type superflares including updates on a new sample using the Apache Point Observatory (APO) and Gaia DR2. The results from Gaia DR2 revealed the possibility of contamination of subgiant stars within the classification of *Kepler* solar-type stars. This is due to previous classifications using T_{eff} and $log(g)$ values from the *Kepler* Input Catalog (KIC: Brown et al. (2011)), where there are large differences between real and catalogued values. One of the other key differences was their ability to check the binarity of their new sources using APO spectroscopic observations, ruling out stars which were members of binary systems. This, in turn, rules out the generation of flares as a result of magnetic interaction between the binary system. They also investigate starspot size, concluding the majority of superflares occur on stars with larger starspots, however, they acknowledge there is some scatter. With regards to rotation period (P_{rot}), they note maximum spot size does not depend on P_{rot} but maximum flare energy does continuously decrease with slower rotation.

In solar physics, the relationship between flares and sunspots has been well established, with these phenomena being closely linked. Multiple studies, such as Maehara et al. (2012); Notsu et al. (2013); Maehara et al. (2017); Notsu et al. (2019), of solar-type stars report close links between starspots and flaring activity concluding superflares are a result of stored magnetic energy near starspots. Despite this, the relationship between flare rotational phase and starspots in solar-type stars has not been investigated in great detail. If superflares do occur near starspots due to the storage of magnetic energy then you would expect to see a correlation between starspots and flare occurrence.

In the previous studies outlined in Chapters 4 & 5, K2 & *TESS* SC photometric data was used to investigate the rotational phase of flares in a sample of 183 M dwarfs. By using simple statistical tests it was determined the phase distribution of the flares was random and did not coincide with the large starspot producing the rotational modulation. This result was

unexpected as it suggests the flares on these M dwarf stars are not correlated with the dominant large starspotflregion present on the stellar disk. As a result, this indicates the magnetic field and resulting activity on these stars may be more complex than what is observed on the Sun.

In this study, *TESS* 2-min photometric lightcurves from a sample of solar-type stars are used from observations in sectors 1 - 13 to conduct a statistical analysis of their flaring properties. The short cadence 2-min *TESS* data is important for detecting low energy, short duration flares. In addition to investigating the rotation periods, flare energies and flare frequency, the rotational phase of the flares will be explored. This analysis aims to determine whether the flares and starspots on these solar-type stars share the same strong correlation as solar flares and sunspots on the Sun. Furthermore, historic GOES data of solar flares is also utilised to investigate the relationship between solar flares and sunspots in greater detail.

6.2 Solar-Type star sample

In previous solar-type star studies, the sources were identified using their effective temperatures (T_{eff}) and $log(g)$ values from the KIC, or other associated catalogues. However, this process led to a contamination of sub-giants within the sample which were incorrectly identified due to differences between real (Gaia DR2) and catalogued values. Here solar-type stars are identified as those with spectral types ranging from F7 - K2 according to the `SIMBAD` catalogue[1], and have been observed in 2-min cadence by *TESS*.

Now the various steps are discussed which were taken to eliminate any sources which were not main sequence solar-type stars. Firstly, the sources were cross referenced with the SkyMapper Southern Sky Survey (Wolf et al., 2018) and Gaia DR2 (Gaia Collaboration, 2018). Any star which did not possess SkyMapper magnitudes or Gaia parallaxes was not considered any further. Radii and luminosity values from Gaia DR2 were used to eliminate any which are likely to be giants and hence wrongly classified within `SIMBAD`. Skymapper multi-colour magnitudes and Gaia parallaxes were used to determine the quiescent luminosity of the stars in the *TESS* bandpass. The magnitudes in the g, r, i and z bands are converted to flux and then fitted

[1] http://simbad.u-strasbg.fr/simbad/

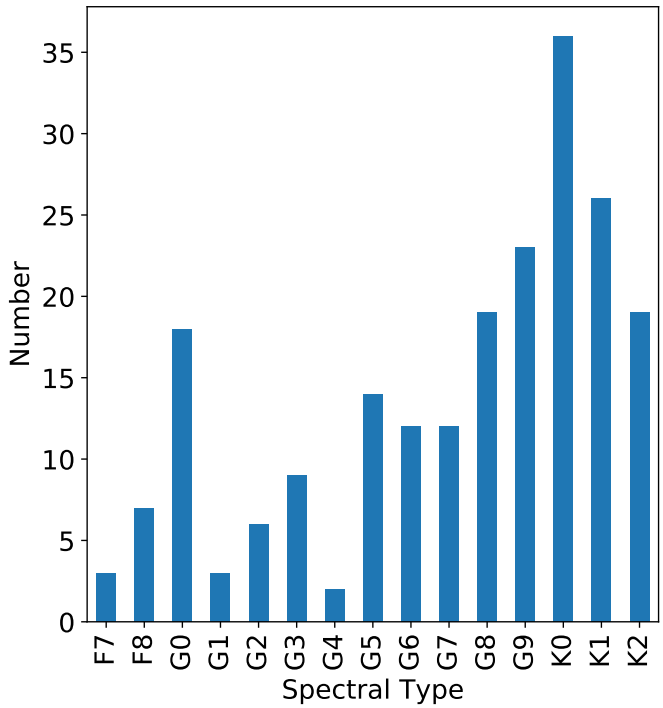

Figure 6.1: A histogram showing the spread in spectral types within the solar-type star sample observed in 2-min cadence by *TESS*.

by a polynomial to produce template spectra of each star. These are then convolved by the *TESS* bandpass providing the quiescent flux of each star in the *TESS* bandpass. By inverting the Gaia parallaxes the distances of the sample are determined and used to infer the quiescent luminosity of each star. These values along with the stellar properties of each star are provided in Table 6.1.

In this chapter, photometric *TESS* lightcurves of solar-type stars are used from sectors 1 - 13 made between 25th July 2018 - 18th July 2019. The data processing of the lightcurves is discussed in §2.2.2. Overall, 158 solar-type stars in the sample (76%) were observed in only one sector with the remaining 58 (24%) targets being observed in multiple sectors.

The *TESS* 2-min lightcurves of the remaining sources were visually inspected by eye individually to determine those which showed any signs of rotational modulation. Some sources which showed complex lightcurves or no evidence of rotational modulation were not considered further. Only a handful of these sources which did not possess rotational modulation showed any evidence of flaring activity and were omitted as the rotational period is a key aspect of the

analysis. Finally, all lightcurves were then run through a flare finding algorithm and any which did not show any flaring activity were omitted from further analysis.This process resulted in a final sample of 209 solar-type stars observed in 2-min cadence by *TESS*. The spread of spectral types within this sample is shown in Figure 6.1. Additionally, it is important to note three of the stars within the sample show evidence of belonging to an eclipsing binary in the *TESS* lightcurves. This will be discussed further near the end of the chapter in §6.8.

Due to the nature of the selection of targets for our solar-type sample there are some selection biases which should be highlighted. Firstly, only stars which had spectral types recorded in SIMBAD were initially selected: we are therefore biased towards stars which had a spectral type recorded. Secondly only those stars which display rotational modulation are selected, as it is critical for our analysis. However, this results in a bias towards active solar-type stars in our sample meaning a complete picture is not achieved. Additionally, there is a bias towards later type (G8 - K2) solar-type stars, see Figure 6.1. Finally, targets had to possess SkyMapper and Gaia data which resulted in some targets being omitted from this study which potentially could have shown rotational modulation and/or flares. Despite these selection biases, we consider that our final sample of 209 solar-type stars with spectral types between F7 and K2 (for the full stellar properties see Table 6.1) is large enough for determining the rate of super-flares from solar-type stars and whether they show any rotational phase dependence.

6.3 Stellar and Flare Properties

This section looks at both the stellar and flare properties of each star, including determining the rotation period, identifying the flares and calculating their energies. In addition, a small group of ultra-fast rotators identified within the solar-type sample is also discussed.

6.3.1 Rotation Period

The rotation periods are determined for all 209 solar-type stars in the sample using the rotational modulation observed in the lightcurve. This rotational modulation occurs as a result of large, dominant starspot(s)flregion which move in and out of view as the star rotates, changing

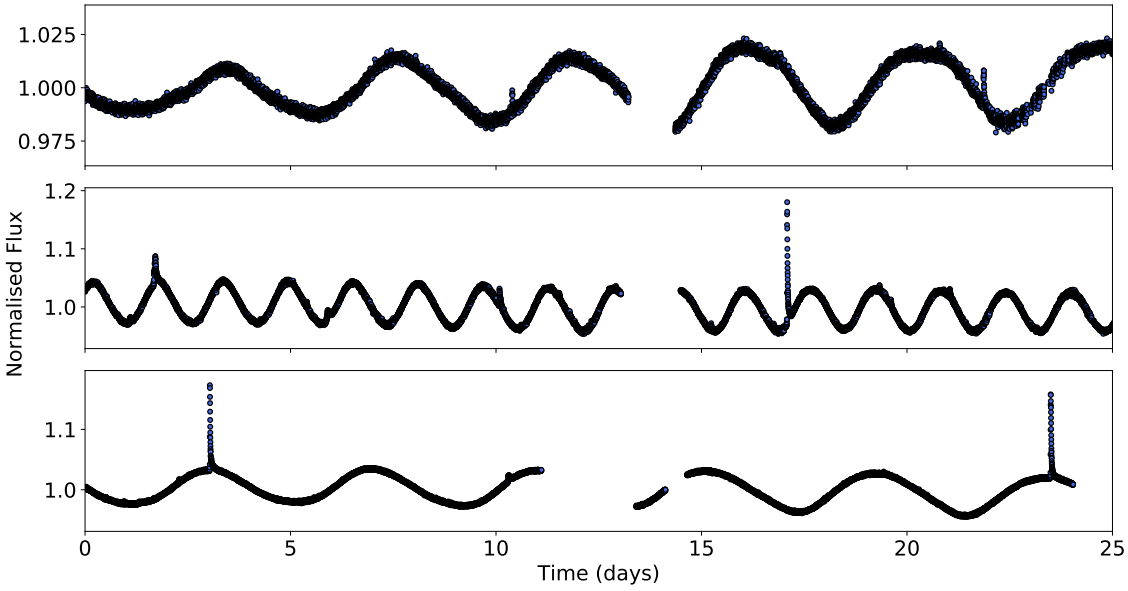

Figure 6.2: Here three examples of lightcurves are shown from the solar-type stars CD-52 10232 (top), HD 221224 (middle) and BD-19 3018 (bottom). These have spectral types K0, G5 and K0 and rotation periods 4.25 days, 1.58 days and 4.07 days respectively. As well as clear modulation within these lightcurves as a result of starspots, flares can also be seen in all three stars.

the brightness of the star periodically. Examples of this phenomenon can be seen in Figure 6.2 of several solar-type stars ranging in rotation period and spectral type.

To determine the rotation periods, P_{rot}, a Lomb-Scargle (LS) periodogram is utilised from the software package `vartools` (Hartman and Bakos, 2016). This provides an initial estimation of P_{rot}, and by phase folding and binning the lightcurve through an iterative process a final value is verified. Along with P_{rot} phase zero, ϕ_0, is also determined and represents the minimum of the flux of the rotational modulation. Overall, this process allows for the determination of both P_{rot} and ϕ_0 which is used in subsequent analysis of the magnetic activity. Errors on P_{rot} are estimated to be within a few percent. It is important to note that occasionally the LS periodogram detects half of the true period. However, as each lightcurve was visually inspected instances where this has occurred are identified and the period modified accordingly. Therefore, this does not affect the majority of stars in the sample.

The stellar properties of the sample can be seen in Table 6.1 including both P_{rot} and ϕ_0. Within the solar-type sample rotation periods range from 0.24 - 11.16 days. It is difficult to detect stars with $P_{rot} > 10$ days (the Sun has $P_{rot} \sim 27$ days), due to the observation length

of *TESS* at $\sim$ 27 days per sector although, for stars with more than one sector of data it is possible to obtain longer periods. However, despite this, it is still possible to conduct an analysis on this sample in comparison to the Sun as the comparison is done with regards to the relationship between flares and starspots.

Table 6.1: The stellar properties of the first stars in the survey observed by *TESS* detailing the rotation periods, quiescent luminosity, energy range and duration range of the flares. The apparent magnitude in the *TESS* band-pass, T_{mag}, is taken from the *TESS* Input Catalog (TIC) along with the TIC ID (Stassun et al., 2018). The distances are derived from the Gaia Data Release 2 parallaxes (Gaia Collaboration, 2016, 2018) and the spectral types are obtained from the SIMBAD catalogue. For the full table please refer to Appendix A.2.

Name	TIC ID	sector	Ra (deg)	Dec (deg)	No. of Flares	SpT	T_{mag}	Parallax (mas)	Distance (pc)	P_{rot} (days)	$log(L_{star})$ (erg/s)	$log(E_{flare})$ (erg)	Duration (minutes)
CD-5210232	161172848	1	339.8765	-52.0882	2	K0	10.03	9.4283	106.063	4.25170	32.82	33.80 – 34.26	34.00 – 70.00
HD205297	403121294	1	324.3149	-65.0393	11	G6	8.27	13.642	73.3003	1.52470	33.05	33.09 – 34.44	12.00 – 102.00
HD49855	176873028	1,2,4	100.9428	-71.9762	12	G6	8.39	17.989	55.5871	3.85670	32.78	31.73 – 34.10	8.00 – 52.00
HD42270	261236136	1,12,13	88.3725	-81.9478	19	K0	8.28	16.965	58.9431	1.88070	32.82	32.82 – 35.06	8.00 – 232.00
HD47875	167344043	all minus 11	98.6712	-69.8849	179	G4	8.50	13.893	71.9756	2.99380	33.00	32.74 – 34.74	8.00 – 184.00
HD987	266997586	1,13	3.4725	-74.6886	10	G8	8.07	21.811	45.8470	3.60860	32.70	32.74 – 33.98	14.00 – 96.00
V*VZHor	220536421	1,2,3	42.9723	-61.6173	48	K1	7.89	24.921	40.1263	2.57500	32.48	32.33 – 34.65	12.00 – 174.00
V*CSGru	278634010	1	333.8974	-39.0143	20	K0	8.43	18.595	53.7770	3.35710	32.82	32.79 – 35.00	14.00 – 284.00
HD32195	319289907	1	72.0231	-80.7790	7	F7	7.85	15.927	62.7857	1.23136	33.02	32.80 – 33.81	12.00 – 42.00
HD46920	167247077	1,5,7	97.6388	-67.6025	11	G3	8.50	13.893	71.9756	3.66670	33.02	33.13 – 34.02	14.00 – 54.00
HD202917	079403675	1	320.2084	-53.0347	9	G7	7.99	21.345	46.8489	3.38290	32.56	32.94 – 34.61	24.00 – 275.99
HD211862	270356871	1	335.1712	-28.2328	4	G1	8.54	7.0541	141.761	1.19460	33.61	34.53 – 35.59	58.00 – 168.00
CPD-571131	279614617	1	106.3013	-57.5706	2	G8	9.12	3.5490	281.769	7.37670	33.98	35.19 – 35.46	84.00 – 108.00
HD269406	179369970	1	79.9842	-71.4854	1	G5	8.90	3.9785	251.351	2.86130	33.98	35.15	64.00
CD-7776	050345701	1,13	32.3507	-76.6876	11	K1	8.99	11.405	87.6755	5.27750	33.06	33.38 – 34.95	18.00 – 160.00
HD39150	364588501	all	85.4033	-76.0723	207	G6	9.14	9.0342	110.690	2.28000	33.16	33.07 – 35.29	8.00 – 220.00
HD269921	404768019	1,2	84.6440	-68.8850	8	G7	9.50	10.653	93.8667	0.72162	32.89	33.26 – 35.17	12.00 – 174.00
CD4014901	214772274	1	341.6400	-39.4792	3	G5	8.81	13.198	75.7685	3.19250	32.97	33.89 – 34.29	50.00 – 98.00
CD-63408	309714906	1,10,11	126.0248	-63.5672	9	G5	9.19	10.027	99.7258	0.79029	33.06	33.52 – 34.67	22.00 – 96.00
HD223728	009708387	2	358.0430	-11.7210	4	G1	8.08	11.840	84.4552	2.36540	33.25	32.99 – 34.74	8.00 – 118.00
CD-3019800	012359079	2	0.8360	-29.8230	1	F8	10.76	4.2171	237.129	2.64560	33.23	34.37	38.00
V*VZRet	031850842	2	52.1536	-66.9201	2	G8	10.11	7.2042	138.807	2.31970	33.02	33.19 – 34.58	8.00 – 46.00

6.3.2 Stellar Flares

The same methods as Chapters 4 & 5 were used to identify the flares present in each lightcurve and calculate their energies in the *TESS* bandpass. This involves using FBEYE (Davenport et al., 2014) and visually checking by eye to validate they are indeed flares. This requires them to possess a classical flare shape with a sharp rise and exponential decay. Once complete, a comprehensive list of stellar flares including their start and stop times, flux peak and equivalent duration is produced for each star. Some examples of these flares can be seen in Figure 6.2 along with the rotational modulation.

The flare numbers for each star are normalised to give the number of flares per day as the observation length of each star varies as a result of being observed in multiple sectors. In Figure 6.3 the normalised flare number is plotted alongside the rotational period which shows flare number decreasing with increasing rotation period. Despite the lack of stars with $P_{rot} > 10$ days, this is consistent with other studies such as Stelzer et al. (2016) but also with Chapters 4 & 5.

In addition, the rotation rate, Ω, is also plotted as a function of the normalised flare number, see Figure 6.3. To do this, the relationship $\Omega = 2\pi R/P_{rot}$ is used where R is the radius of the star taken from the Gaia DR2 release and P_{rot} is the rotation period derived earlier. This allows for the identification of the fast rotators within the sample. In Chapter 5, a group of M dwarf ultra-fast rotators (UFRs) was discovered with $P_{rot} < 0.3$ days which surprisingly displayed a low level of flaring activity. Determining ages for these stars did not provide any explanation for their peculiar behaviour. In this sample four solar-type UFRs were identified with $P_{rot} <$ 0.4 days which also show low levels of flaring activity. At the moment, I do not have a clear explanation for this phenomenon, however, I do believe it is related to the magnetic field properties of the stars which is discussed more in §7.4.3. Since these objects are fast rotators, they are probably young, hence it is possible that the flares have their maximum energy in the blue, thus the *TESS* band-width only sees the more energetic events. Additionally, these stars could be members of syncronised binary systems which could cause the observed rapid rotation and suppress flaring activity.

Next the energies of the flares are determined within the *TESS* bandpass. These are calculated

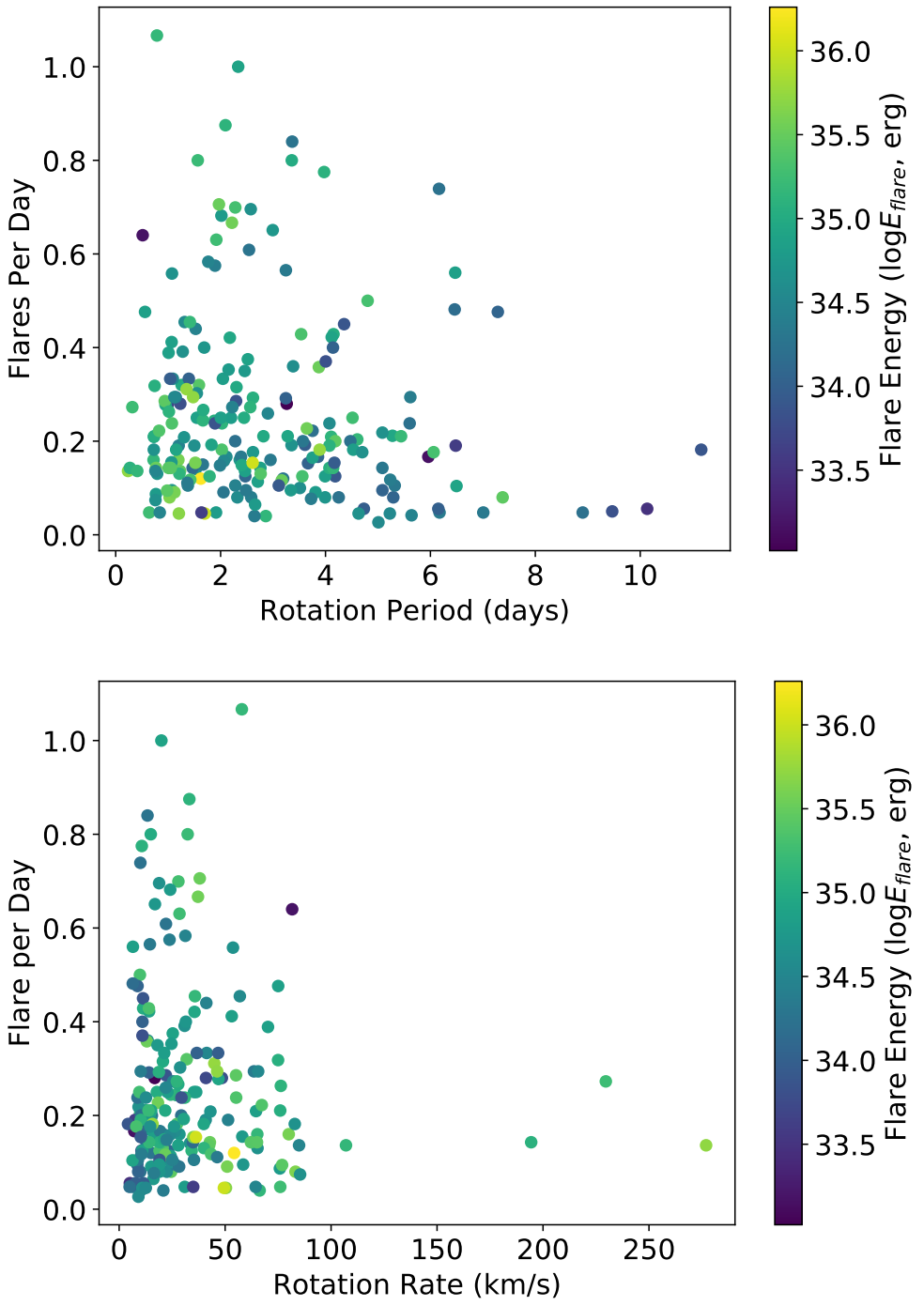

Figure 6.3: The normalised flares per day of each star in the sample as a function of rotation period, P_{rot}, (top panel) and rotation rate, Ω (lower panel). Each of the points are colour coded according to the colour bar which represents the maximum flare energy from the star.

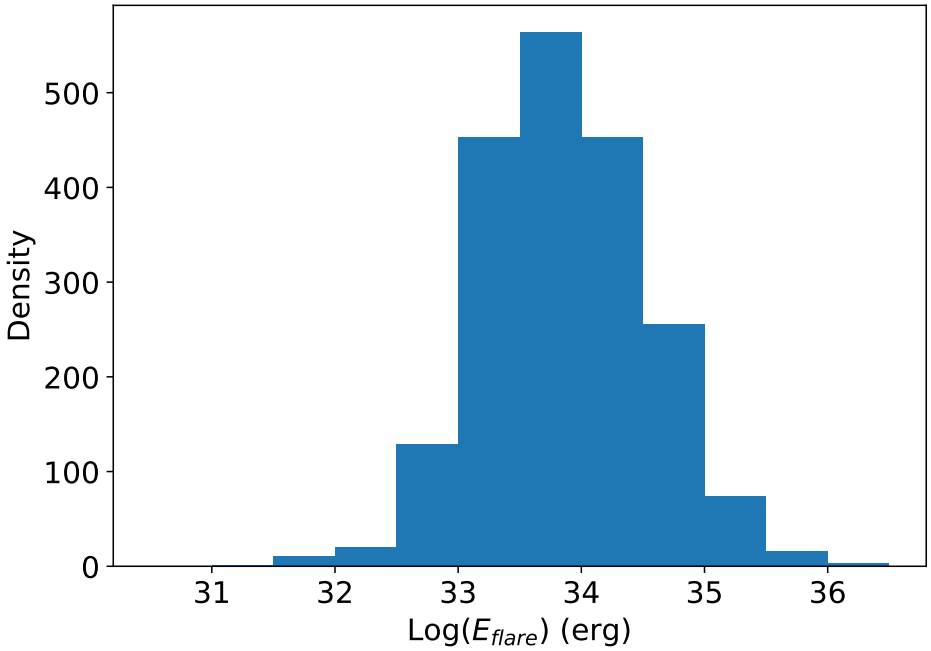

Figure 6.4: The distribution of the energies of the 1980 flares for the sample of 210 solar-type stars. This histogram was used to define the cut off between high and lower energy flares of 10^{34} erg which was used in subsequent analysis.

as the equivalent duration, area under the flare lightcurve obtained from FBEYE, multiplied by the quiescent stellar luminosity. As mentioned previously, the quiescent stellar luminosity, L_{star}, was determined from both Skymapper magnitudes and Gaia parallaxes, full details in §6.2. Within the solar-type sample a large variety of flare energies are seen ranging from $2.1 \times 10^{31} - 1.8 \times 10^{36}$ erg. Approximately 92% of the flare sample are classified as superflares with energies greater than 10^{33} erg. It is important to note here the term 'superflare' was defined according to the Carrington event which was a X45 class solar flare observed in 1859 and had an energy output of 4.5×10^{32} erg (Cliver and Dietrich, 2013). Hence, the majority of the flares exceed this energy range making them 'superflares'. Similarly, only 1.6% of the flare sample have energies less than 10^{32} erg, which is the range of solar flares, with no flares less than $10^{31.5}$ erg. The highest energy flare of 1.8×10^{36} erg was observed on the star HD 217344 (TIC 229066844) a G4 star with P_{rot} of 1.62 days. All of the flare properties for each star can be seen in Table 6.1, and the spread of flare energies can be seen in Figure 6.4.

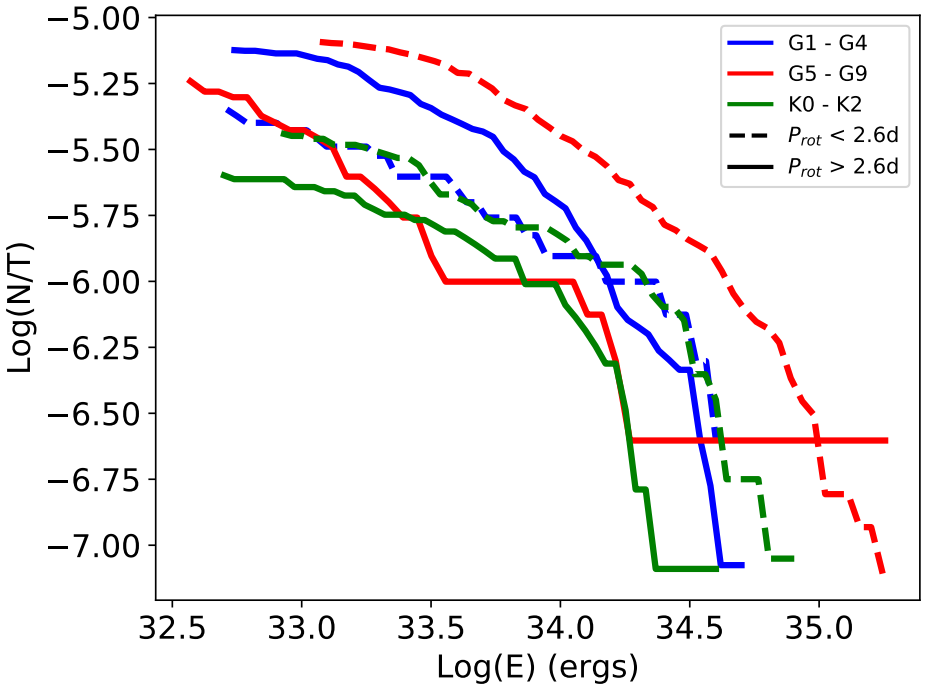

Figure 6.5: The logarithm of the cumulative flare frequency in seconds against the logarithm of flare energies for a handful of solar-type stars in the sample. These stars have varying spectral types in the ranges G1 - G4 (blue), G5 - G9 (red) and K0 - K2 (green) but each line represents a single star. In addition, these stars have different rotation periods identified by the line style where dashed represents fast rotating with $P_{rot} < 2.6$ days and solid as slowly rotating with $P_{rot} > 2.6$ days.

6.3.3 Superflare Frequency

As well as calculating the flare energies, the frequency of the superflares need to be investigated. Figure 6.5 shows the FFD for a handful of stars ranging in rotation period and spectral type. The dashed line represents stars with rotation periods less than 2.6 days and a solid line greater than 2.6 days, where 2.6 days represents the median. In addition, stars with varying spectral types are displayed by colour with G1 – G4 blue, G5 – G9 red and K0 – K2 green, where each line represents an individual star. These stars were selected as they possessed a reasonable number of flares for each of the spectral sub-types and had varying rotational periods. Now I will go into more detail about the various stars and the relationship between all six as a whole.

Firstly, as an example, the dashed red line represents the G6 type star HD 39150 (TIC 364588501) which has a rotation period of 2.28 days and 207 flares. HD 39150 will produce

a flare of energy 10^{35} approximately every 49 days whereas a flare of 10^{33} will be produced every 1.5 days. Overall, the higher the flare energy the less frequently it will be observed from the star which is consistent with the mechanism known to generate solar flares on the Sun. Prior to the flare energy release the magnetic field becomes stressed and twisted allowing for the buildup of magnetic energy. The flare is then released as thermal energy, kinetic energy and particle acceleration when the magnetic field reconfigures and simplifies through magnetic reconnection (Fletcher et al., 2011, and references therein). Therefore, it should take longer to build up and store the magnetic energy required for larger energy flares of 10^{35} erg and greater, although see §4.5 on flare waiting times.

Looking at the slowly rotating stars as a whole, the G9 type star HD 31026 (TIC 077371445; solid red line in Figure 6.5) which has a $P_{rot} = 4.8$ days and a total of 23 flares, shows a higher flare energy than the other slowly rotating stars. Oddly enough, this star was only observed in two sectors in comparison to the other slowly rotating stars at six sectors. From the FFD we can see it will take approximately 150 days for this star to produce another of the highest energy flares which is approximately 5 *TESS* sectors of observations. Therefore, it could be coincidence that *TESS* was observing this star at the right time to observe such a large flare.

In terms of the fast rotating stars, HD 39150 (TIC 364588501) has the highest flare rate and highest energy, however, it was observed in all 13 sectors. The remaining fast rotators both have the same distribution where the difference in spectral type has no effect. As a whole, the behaviour between the fast and slow rotators does change in each of the spectral type groups, where fast rotators show flares more frequently. However, within the G1 – G4 spectral group the flare frequency at lower energies is higher in the slowly rotating star.

Overall, this plot shows the spectral type of the stars does not affect the flare energies. However, it is apparent the rotation period does play a role with the faster rotating stars producing flares of higher energies and flares more frequently. This is to be expected as faster rotating stars tend to produce high energy and overall flare more frequently (with exception of the UFRs) in comparison to their slowly rotating counterparts (Hartmann and Noyes, 1987; Maggio et al., 1987).

6.3.4 Flare Effects on Habitability

The Sun can produce solar flares with energy outputs of up to 10^{32} erg. These explosive events have effects which sweep through the entire solar system. Due to Mercury's close proximity with the Sun, it's very thin exosphere is constantly being stripped away and then replenished by particles from solar flares, Coronal Mass Ejections and the solar wind (Guinan and Ribas, 2004, and references therein). On Earth, the magnetosphere protects the planet from harmful radiation and fast moving particles which originate from the Sun. In the event of a large X-class solar flare satellites can be disrupted and aurora can be seen at lower latitudes. Gas giant planets such as Jupiter and Saturn have strong internal magnetic fields and large magnetospheres so the effects of flaring activity can result in aurora and geomagnetic storms (Engvold et al., 2018).

The sample of 209 solar-type stars was cross referenced with the NASA Exoplanet Archive [2] to identify if any of the targets have known planets. Within the sample only one solar-type star, HD 44627 (TIC 260351540), is a host to known exoplanets with a spectral type and rotation period of K1 and 3.9 days. This particular planet is a wide orbiting giant with a semi-major axis of 275AU and mass of 13.5 M_{JUP} (Chauvin et al., 2005). This star produces flares with energies between 6.1×10^{32} - 3.4×10^{35} erg flaring 48 times over a period of approximately 160 days. Jupiter is at a distance of approximately 5.5AU from the Sun, therefore, the distance between the star and planet in the HD 44627 system would mean any stellar flares would have a minimal effect. In addition, as the planet is a gas giant it will more than likely possess a considerable magnetosphere similar to Jupiter.

However, there may be undiscovered exoplanets orbiting other solar-type stars in the sample. Overall, the effects of superflares on orbiting planets will depend on many factors including the star-planet separation, the energy of the flare and the composition of the planet. For example, the flux deposited by a superflare of energy 10^{35} erg on a rocky planet at a distance of 1AU will not cause any geophysical alterations. If this planet was icy, however, and if the flare was in the range of 10^{38} erg, then it could cause melting which would result in flood plains (Schaefer et al., 2000). Another key factor is the potential for the planet to have a magnetic

[2] https://exoplanetarchive.ipac.caltech.edu

field strong enough to provide protection from harmful flare events. The radiation alone from these events could cause planetary atmospheres to be constantly modified making it difficult for hosting life (Vida et al., 2019, and references therein).

6.3.5 Flare Waiting Times

Hudson (2020) investigated the flare waiting times between successive solar flares from two active regions AR 10930 (December 2006) and AR 7978 (June 1996). The purpose of this study was to establish the build up/release processes which should be present as a correlation between the waiting time and flare magnitude. Overall, Hudson (2020) does observe such a correlation which solidifies the build up/release scenario for solar flares where solar flares result from the build up of magnetic energy in the corona.

Similar work has been carried out in a stellar flare case, Hawley et al. (2014) study the flare waiting times for the low mass M dwarf GJ 1243 using two months of Kepler data. They observe a decline in the number of flares with greater waiting times between the range of 30 mins – 8 hours. As a result, they conclude GJ 1243 maintains a steady state of flaring activity which is consistent to a scenario of a number of active regions on the disk. This means some active regions are in the stages of release/decay while others are in the growth phase.

Here a similar analysis is conducted using the solar-type star HD 39150 (TIC 364588501) which shows 207 flares within a year of TESS 2-min cadence observations. Overall, a similar decline in waiting times (Figure 6.6(a)) is observed in comparison with Hawley et al. (2014), however, the range in waiting times is much greater on a scale of days. According to Hudson (2020), there should be a correlation with regards to waiting time and flare magnitude (i.e. energy). However, while some flares with longer waiting times do show higher energies, there is a wide spread amongst waiting time and energy as a whole, see Figure 6.6(b). Therefore, this is consistent with HD 39150 possessing multiple active regions on the disk at various stages in the build up/release of flaring activity. This is discussed in more detail in the subsequent sections.

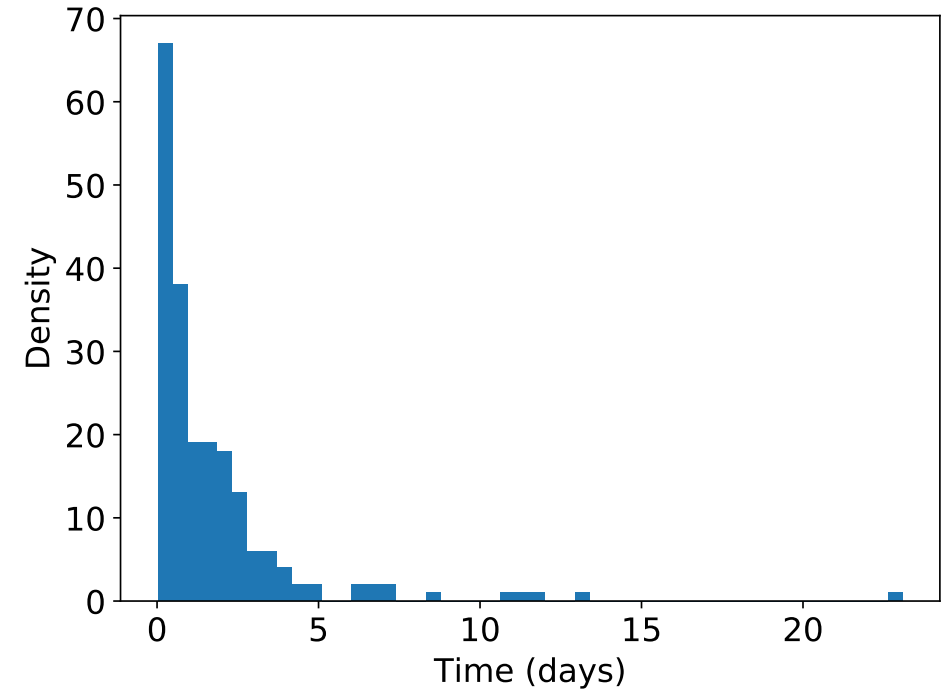

(a)

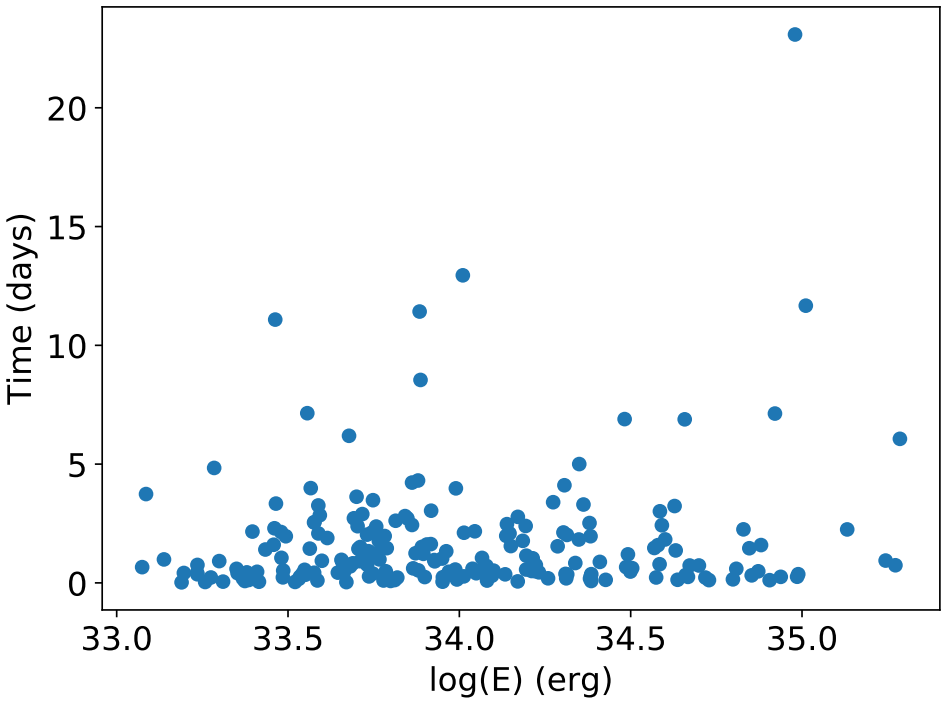

(b)

Figure 6.6: The distribution of flare waiting times (top panel) for HD 39150 (TIC 364588501) covering 207 flares during one year of TESS 2-min cadence data. Additionally, the flare waiting times as a function of energy are also shown (bottom panel) detailing no strict correlation between flare magnitude and waiting time.

6.4 Stellar Variability

The continuous viewing zone is an area of the sky where each of the *TESS* sectors in the southern and northern hemisphere overlap. This produces a region of sky with many stars being observed for approximately one year. Within the sample of solar-type stars two have been observed in the continuous viewing zone, HD 39150 (TIC 364588501) which was observed in all 13 sectors and HD 47875 (TIC 167344043) which was observed in all 13 sectors minus sector 11 where no data was collected. This provides lightcurves of these stars which span one year allowing for the investigation of long-term levels of variability within these stars.

HD 39150 (TIC 364588501) which was observed for a total of 357 days. This G6 star has a rotation period, P_{rot} = 2.28 days and a total of 207 flares with energies reaching 10^{35} erg. Figure 6.7 shows the lightcurve of this star spanning approximately 170 days, detailing the changing nature of the rotational modulation. There is evidence of multiple spot groups throughout the lightcurve sequence as the shape of the modulation changes. This could be the result of two active regions possessing spots which are rotating with marginally different periods, meaning they are slightly unsynchronised. The whole *TESS* lightcurve of this star from all sectors can be folded to one rotation period and phase zero which also suggests this scenario. In addition, the amplitude of the rotational modulation changes sector to sector suggesting the active regions are growing and decaying as the star rotates or new regions are developing/disappearing. To determine if some of the variability was due to instrumental effects the lightcurves of spatially nearby stars were examined and found no variation between different sectors. Therefore, it can be concluded the variability in HD 39150 (TIC 364588501) is intrinsic to the star. With regards to flaring activity, there seems to be an increased level towards the end of this section of lightcurve between days 125 and 155 where the flares appear more frequently and with a greater energy. Tu et al. (2020) also discuss this target noting the increase in flaring activity within sector 5, however, they do not offer any explanation regarding the reasoning behind this. This star is discussed further in §6.6.2 providing a potential explanation for the sudden increase in activity while also associating it with the rotational phase distribution of the flares.

HD 47875 (TIC 167344043) is also present within the continuous viewing zone and was ob-

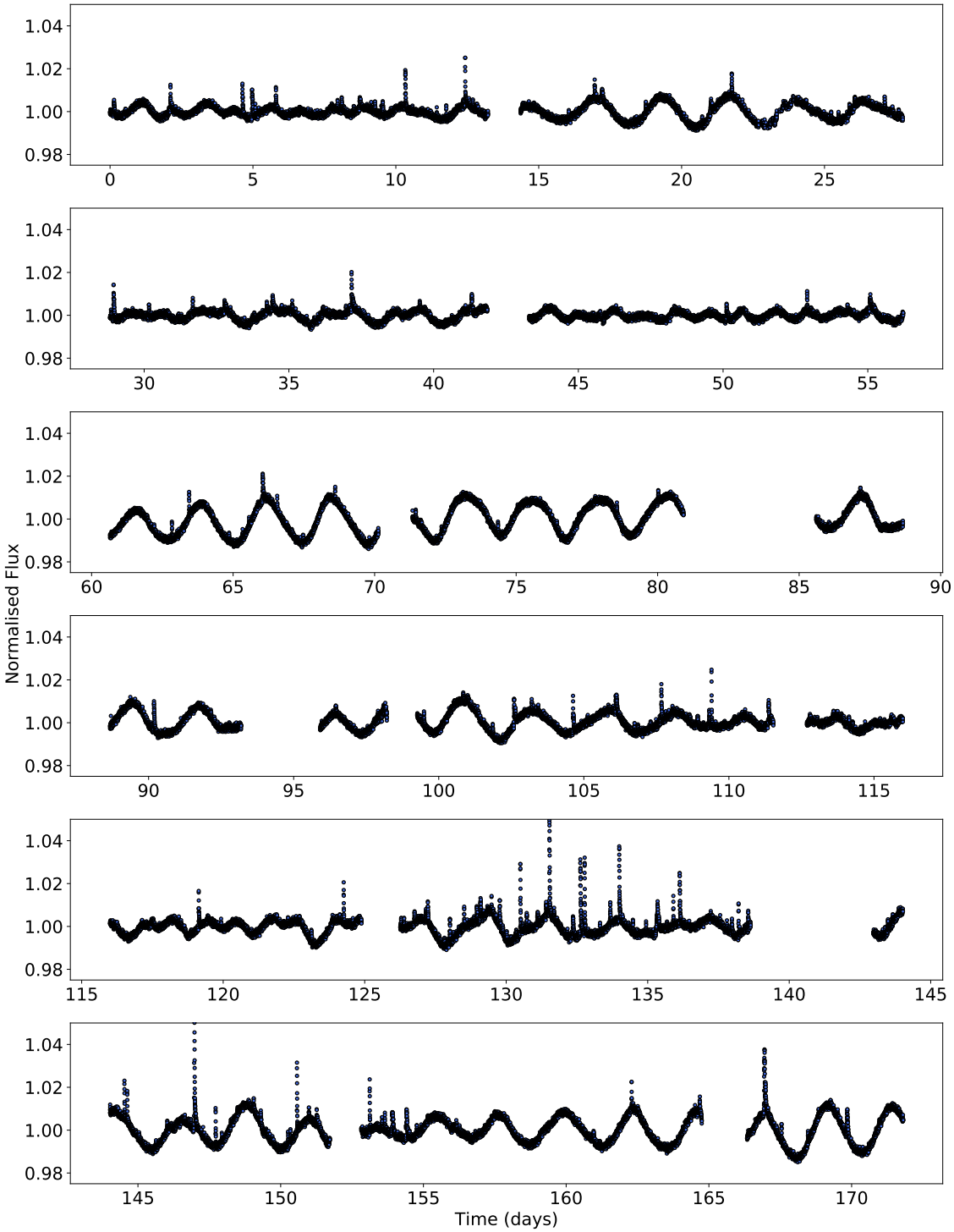

Figure 6.7: The lightcurve for HD 39150 (TIC 364588501) covering approximately 170 days detailing the magnetic variability of the star including changing spot structures and flaring.

served for a total of 330 days. This star has a spectral type of G4, P_{rot} of 2.99 days and a total of 179 flares with energies in the 10^{34} erg range. The rotational modulation of this star is constant throughout the year of observations possessing a clear sinusoidal pattern with no evidence of multiple spots. However, the amplitude of this particular star also changes producing a multiperiodic lightcurve. This would suggest there are potentially migrating spots on the disk of the star which fall into differential rotation. As a result of this phenomenon, large flares are observed as the migrating spot crosses the disk of the star.

Overall, there appears to be more variability observed within solar-type stars on timescales of months, with regards to their spotted structures, as compared to low mass stars. It is known active regions and spot structure observed on the Sun change over periods of weeks to months with no sunspots lasting years. Therefore, it is not unexpected to observe this behaviour in other stars of a similar spectral type. As *TESS* returns to the southern ecliptic in cycle 3, follow ups of these stars would be valuable to continue to monitor the changing behaviour observed. This will then lead into long term observations with the potential to determine stellar cycles which is important in understanding the overall magnetic cycle on other stars.

6.5 Starspot Areas

Determining the areas of starspots is a non-trivial process and there are many ways to do so including Zeeman Doppler Imaging (Rosén et al., 2015), Spectral Modelling (Fang et al., 2016; Gully-Santiago et al., 2017) and Planet-Transit Spot Modelling (Morris et al., 2017). In addition, it is possible to use the amplitude of the rotational modulation from lightcurves to provide a rough indication of the approximate areas of starspots on the stellar disk (Rebull et al., 2016*a*,*b*; Giles et al., 2017). However, this process underestimates for the presence of polar spots, circumpolar spots, bands of spots, spots all over the disk and a pole-on star with spot distributions. Despite this, there is still merit in determining starspot areas as it can provide some insight into the conditions needed for these large energy superflares.

In order to determine the starspot area the method described by Notsu et al. (2019) is used. Firstly the temperature of the spot must be determined which can be done by applying a relation on the difference between the photosphere and the spot (see Berdyugina, 2005, for

further details). The relationship is as follows:

$$T_{star} - T_{spot} = 3.58 \times 10^{-5} T_{star}^2 + 0.249 T_{star} - 808 \tag{6.1}$$

where T_{star} is the effective photospheric temperature obtained from Gaia DR2 and T_{spot} is the temperature of the spot. Next, T_{spot} is used to calculate the area of the starspot according to the variations within the lightcurve. This relationship is based on the assumption that there is a linear relationship between the amplitude of the modulation and the spot coverage, when estimating the magnetic energy stored around the starspots as a function of the amplitude of the modulation (see Shibata et al., 2013; Notsu et al., 2013, for further details). Therefore, the total amplitude of the rotational modulation, normalised to the average star brightness, can be expressed as:

$$\frac{\Delta F}{F} = \left[1 - \left(\frac{T_{spot}}{T_{star}}\right)^4\right] \frac{A_{spot}}{A_{star}} \tag{6.2}$$

This then rearranges to give the starspot coverage, A_{spot} as:

$$A_{spot} = \frac{\Delta F}{F} A_{star} \left[1 - \left(\frac{T_{spot}}{T_{star}}\right)^4\right]^{-1} \tag{6.3}$$

where $\Delta F/F$ is the amplitude of the normalised lightcurve, which was measured from the phase folded and binned lightcurve and A_{star} is the area of the stellar disk calculated as $2\pi R^2$ (R is taken as the Gaia DR2 radius). As an example and benchmark starspot temperature for the Sun, a G2 type solar star with a temperature of $T_{star} = 5800$ K, were calculated finding $T_{spot} = 3960$ K. This temperature is reasonable and aligns with the temperature range for sunspots at 3500 – 4550 K (Solanki, 2003). Using these relationships, it is possible to determine approximate spot areas for all 209 solar-type stars within the sample.

According to McIntosh (1990), larger more energetic solar flares occur from active regions

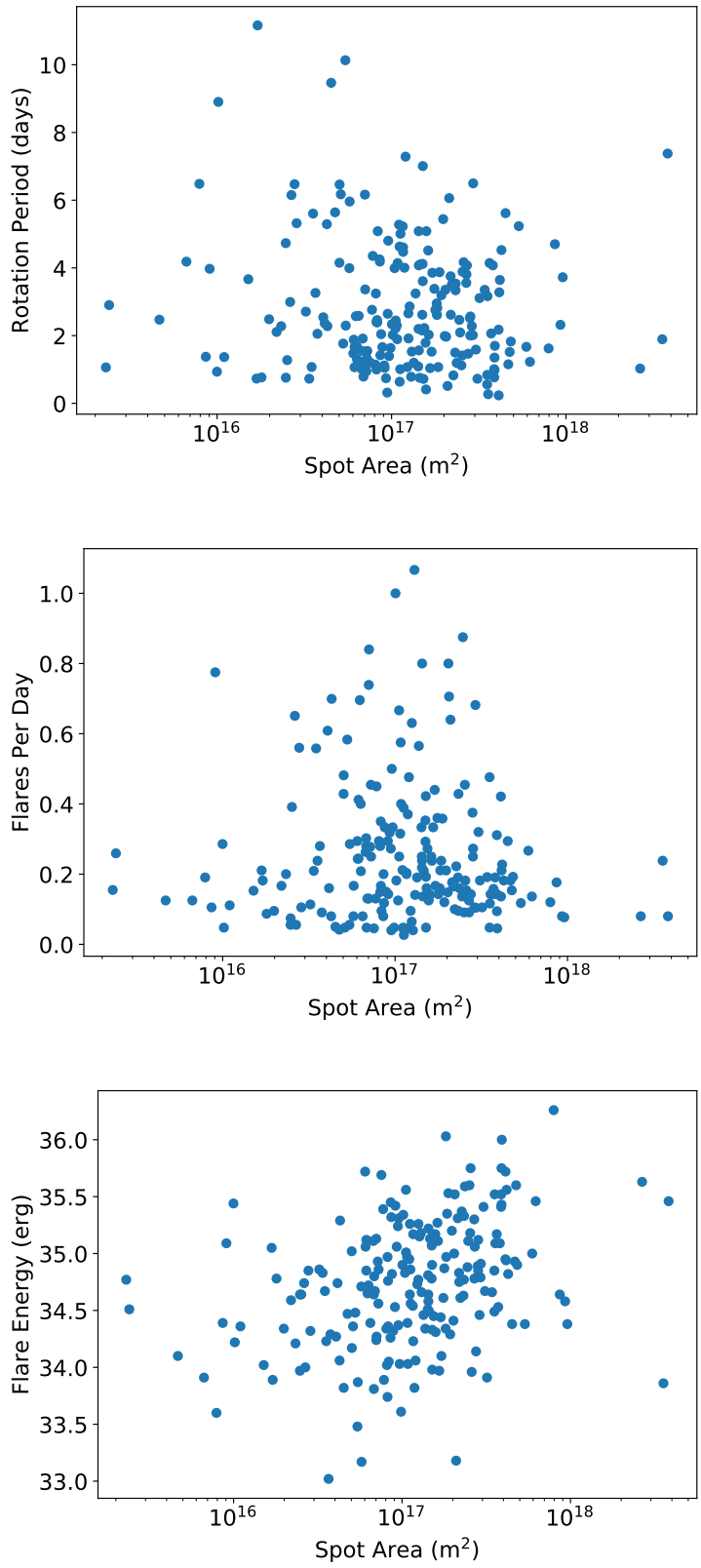

Figure 6.8: Here the spot coverage of each star calculated from the amplitude modulation of the *TESS* lightcurves is shown as a function of stellar rotation period (top panel), normalised flares per day (middle panel) and maximum flare energy (bottom panel).

which host larger spot coverages and complex spot structures. Therefore, you would expect to see the same behaviour within other solar-type stars. In Figure 6.8, the stellar spot coverages are looked at as a function of rotation period, flare number and flare energy to investigate whether the predicted behaviour is in fact observed. With regards to rotation period, you would expect a larger spot coverage to result from a faster rotation period. However, in the sample there appears to be no relation and overall there is a large spread in both rotation and spot coverage. This was tested further using the Pearson Correlation Coefficient (PCC) which yielded a result of PCC = –0.13 also indicating the lack of any correlation. The PCC is a statistical test which measures the linear relationship between two variables. A coefficient of PCC = +1 indicates a direct positive linear correlation and PC = –1 a direct negative linear correlation, with PCC = 0 indicating no correlation.

Next we look at the number of flares as a function of spot area. The expectation is that the larger the spot coverage the more flares will be observed from the star. However, this is not the case and we observe a peak in flare number at approximately 10^{17} m^2 where afterwards, there appears to be a drop in flare number for the larger spot coverages. Could this be because these larger spot coverages are producing higher energy flares less frequently? Again, this was tested with the PCC providing a value of PCC = –0.05 which indicates there is no linear relationship present. This then brings us on to look at the energy of the flares as a function of spot coverage. Although there appears to be some evidence for higher energy flares resulting from larger spot coverages (Figure 6.8), the PCC provided a result of PCC = 0.38 indicating there is a weak linear correlation present. Overall, none of the Pearson correlations for any of the plots in Figure 6.8 indicate a strong linear correlation.

The solar-type star CPD-5711 31 (TIC 279614617) is a G8 type star which was observed to have the largest starspot coverage despite only having a rotation period of 7.37 days. It was observed in *TESS* sector 1 and produces two flares during this time. This is a relatively low number considering it has the largest spot coverage of 3.8×10^{18} m^2 (which equates to 10% of the visible stellar disk) from the solar-type star sample. For context, sunspots typicaly cover 0.01 – 0.1% of the solar surface, reaching a 1% coverage during solar maximum (Strassmeier, 2009). However, it does produce two of the larger flares with energies in the 10^{35} erg range.

A similar analysis was conducted by Howard et al. (2019) and Notsu et al. (2019) where they also investigated the spot coverages of their stellar samples against various flare properties. In Howard et al. (2019) they use photometric data from Evryscope (Law et al., 2015) lightcurves of 113 cool stars to investigate rotation periods, starspot amplitudes and flare properties. They did not find a relationship between the size of the spot coverage and the energy of the flares produced but were able to constrain the minimum field strength of their late K to mid M flare stars as 0.5kG. In Notsu et al. (2019) they conduct an investigation into the relationship between superflares and rotation period, including an analysis on the spot coverages of their sample of solar-type (G-type) stars. Overall, they do see a weak relationship between flare energy and starspot coverage, concluding the superflare energy is in fact related to the starspot coverage of the star. In our sample we see evidence of a weak relationship between flare energy and starspot coverage, similar to the plots in Notsu et al. (2019). In addition, they also see that superflares tend to occur from stars with shorter rotation periods and larger starspot coverages.

6.6 Rotational Phase

One of the criteria for the solar-type sample was the presence of rotational modulation within the *TESS* lightcurve. This rotational modulation is the result of starspots which are present on the stellar disk and move in and out of view as the star rotates. In Chapters 4 & 5 I test the distribution of flares in samples of M dwarfs using a simple statistical test. Our findings show no evidence for any preference in rotational phase, indicating the flares are randomly distributed. In solar physics there is a well-established relationship between sunspots and solar flares. Therefore, it is surprising to find no such correlation amongst other flare stars.

In this study, I will use the same simple χ^2_ν test to assess the phase distribution of the flares. I will look at the flares from all 209 solar-type stars as well as several stars which possess the highest flare rate. In addition, stars which possess no evidence of multiple spots within their lightcurve will be extracted and a separate analysis will be carried out on these stars. All of this will allow a thorough analysis on the rotational phase of the flares, determining whether in solar-type stars there is a starspot/flare relationship similar to the Sun.

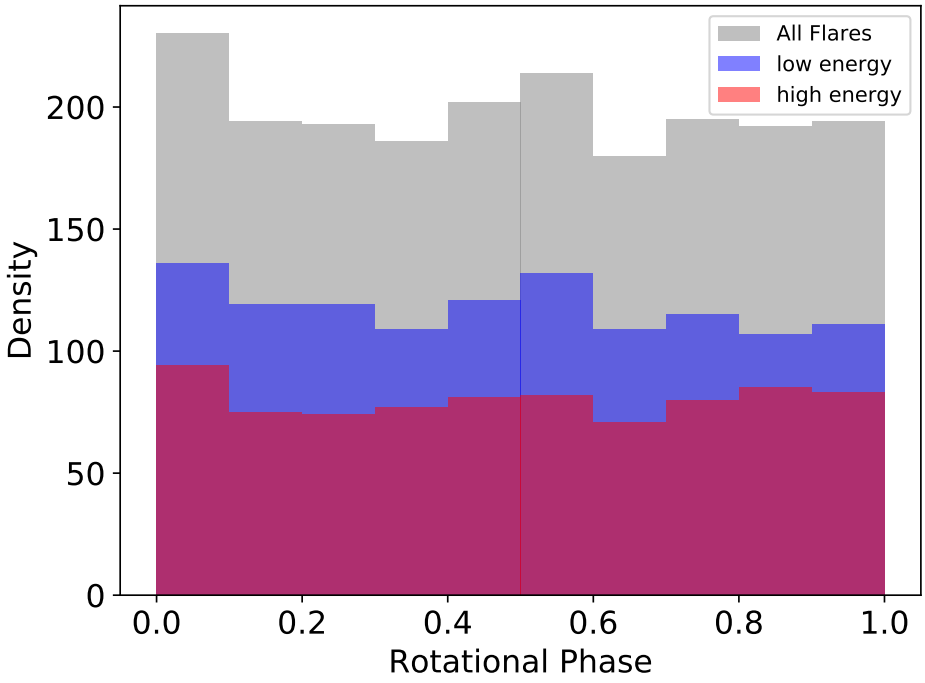

Figure 6.9: A histogram of the rotational phase distribution for all 1980 flares from the sample of 209 solar-type stars. The bin size is $\phi = 0.1$ and the spread shows no preference for any rotational phase. The cut-off for low and high energy flares was determined as 10^{34} erg.

6.6.1 The Overall Flare Sample

Taking all 209 solar-type stars in the sample with a total flare number of 1980, I can test for any preference in rotational phase. For all of the stars phase zero, $\phi = 0.0$, is defined as flux minimum of the rotational modulation allowing for this comparison. Utilising a simple χ^2_ν test (see §4.4 for full details), no correlations between flare number and rotational phase was found. The values of the χ^2_ν test are 1.22, 1.04 and 1.04 for all, low and high energy respectively, where the cut-off was determined as 10^{34} erg according to the distribution of flare energies in Figure 6.4. This indicates the flares are randomly distributed and do not coincide when the starspot is most visible. Figure 6.9 shows the histogram distributions for the flares with phase bins of $\phi = 0.1$, where a consistent spread of flares is present amongst all, high and low energies.

In Roettenbacher and Vida (2018) they conduct a similar analysis for a group of 119 main sequence stars from late-F to mid-M. However, they do find a correlation between rotational phase and flare number which is presented as a peak in their histogram plot similar to Figure

6.9. This correlation is only present in flares which have flux increases between 1% and 5% and so is not present in higher energy flares. Their sample consists of mid-M type stars, while the sample here does not, furthermore they use *Kepler* long cadence (30-min) observations whereas I have used *TESS* short cadence (2-min) lightcurves. These differences along with the addition of omitting stars which show any evidence for multiple spot structures in their analysis could be why the results differ.

As mentioned previously there is a large variation in the rotational modulation of the *TESS* lightcurves within the solar-type sample caused by the presence of multiple spots. In the sample $\sim$ 40% show a clear sinusoidal pattern as a result of one starspot structure present on the disk of the star. The remaining 60% show evidence of multiple spot structures which could potentially cause problems within the rotational phase findings of all flares from all stars. To address this all stars are removed which show any potential evidence for multiple spot structures and conduct the test on the remaining sample. This consists of 83 solar-type stars with a total of 886 flares. Our results, again, show no preference for rotational phase in the χ^2_ν test, therefore, this strengthens the conclusion that the flares do not originate from the dominant spot/active region but are randomly distribution in rotational phase.

6.6.2 Individual Case Studies

Two solar-type stars were selected from the sample which have the highest flare rate and therefore, are ideal candidates to investigate the relationship between rotational phase and flare number. Both of these stars are present in the continuous viewing zone of the *TESS* mission and their stellar variability was discussed in §6.4. However, in this section I will only be focusing on the distribution of flares within their lightcurves as a function of rotational phase. These stars are HD 47875 (TIC 167344043) and HD 39150 (TIC 364588501) with spectral types G4 and G6, flare numbers of 179 and 207 and rotation periods, P_{rot}, of 2.99 and 2.28 days, respectively. The same simple χ^2_ν test was utilised as discussed previously obtaining values for all low and high as of 1.55, 1.41 and 1.11 for HD 47875 and 0.75, 0.89 and 0.76 for HD 39150. As a result, no significant evidence of any correlations between rotational phase and flare number were found.

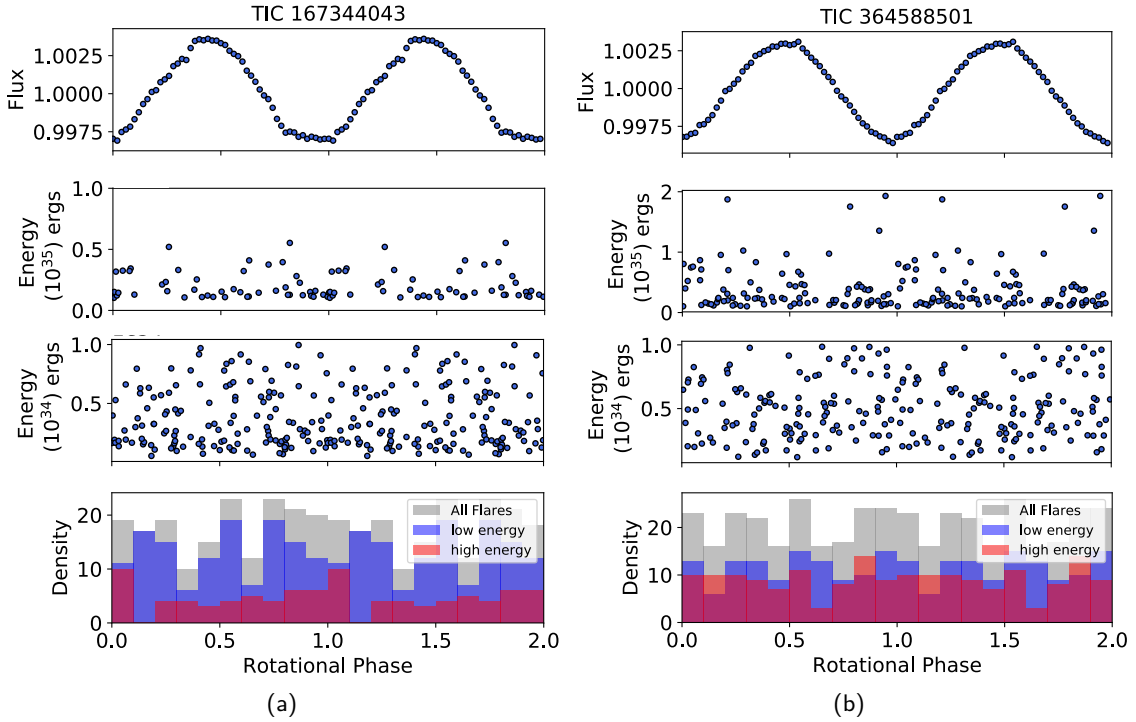

Figure 6.10: Here phase folded and binned lightcurves (upper panel) are shown along with the rotational phase distribution of the flares vs. their energy (middle panels). The top energy plot represents higher energy flares with $E_{flare} > 10^{34}$ erg and the bottom $E_{flare} < 10^{34}$ erg. In addition, a histogram distribution of the flares as a function of rotational phase is also shown for completeness. The rotational phase coverage $\phi = 1.0 - 2.0$ is simply a repeat of $\phi = 0.0 - 1.0$. (a) HD 47875 (TIC 167344043) is a G4 star with $P_{rot} = 2.99$ days and a total number of 179 flares observed over 12 *TESS* sectors. (b) HD 39150 (TIC 364588501) is a G6 star with $P_{rot} = 2.28$ days and 207 flares observed over 13 *TESS* sectors.

In Figure 6.10 the distribution of the flares as a function of their energy is shown along with the phase folded and binned lightcurves. From these plots, it is easier to see there are flares present at all rotational phases in both high and low energy. In addition, the flares are randomly distributed and there is no preference for any rotational phase even during rotational minimum when the dominant starspotflregion is most visible. Although, there is a hint of increasing high energy ($> 10^{34}$ erg) flares at phase 0.25 and 0.75.

Due to the length of the *TESS* observations for HD 39150 the analysis of flares and rotational phase is approached in a different manner than any previous studies. From Figure 6.7 it can be seen that within a few days (e.g. from day 137 to day 140), a large change in the spot structure appears. At day ∼145, there is the presence of a large dominantflregion spot structure while a few days earlier there is the emergence of multiple spots and plage activity

which reduces the spot contrast. However, the most interesting aspect is the intense flare activity from day 127 to day 138 which clearly indicates a strong link between emerging spots and flare activity. After this point the star returns to a less active state similar to what is observed at the beginning of the lightcurve. Chandra et al. (2010) showed that the triggering mechanism for intense flare activity was a combination of flux emergence, shearing between the magnetic polarities of the two flux systems (emerging and pre-existing) plus the interaction of the new emerging bi-poles with pre-existing field. With the spot structure for HD 39150 (TIC 364588501) changing rapidly on a daily basis, intense flare activity is expected.

As a result of this the χ^2_ν test was computed on the sectors of *TESS* data for HD 39150 on an individual basis and focused on the period in sectors 5 and 6 which showed the intense flaring activity. However, the values for the χ^2_ν test show no preference for rotational phase. This is to be expected as by looking at the lightcurve in Figure 6.7 during this active period there are flares present at all rotational phases. Despite this, the flares are present as a result of the emergence of multiple spots and plage activity which does suggest the link between spots and flares. However, the spot structures on these stars are more complex than a simple one spot model and so this would be the main reason behind a lack in any clear correlation.

6.7 The Solar Analogue

With the Sun being the nearest star, astronomers and physicists have been collecting detailed spatial observations to study its phenomena for nearly 150 years. Similarly, there is a wealth of historic data including sunspot number and flare properties dating back to the 1930s. Overall, these data sources provide a deep knowledge of the closest star aiding in the understanding of multiple solar phenomena and its effects on the Earth and Solar System. In this section I utilise historic X-ray data of solar flares from the GOES archive and sunspot numbers from the Sunspot Index and Long-term Solar Observations (SILSO) database to detail the close relationship between solar flares and sunspots.

The relationship between flares and sunspots is well-established and it is generally accepted these phenomena are closely related. Figure 6.11(a) sums up this close relationship where the sunspot number (red line) and flare number (blue histogram) are observed to be correlated with

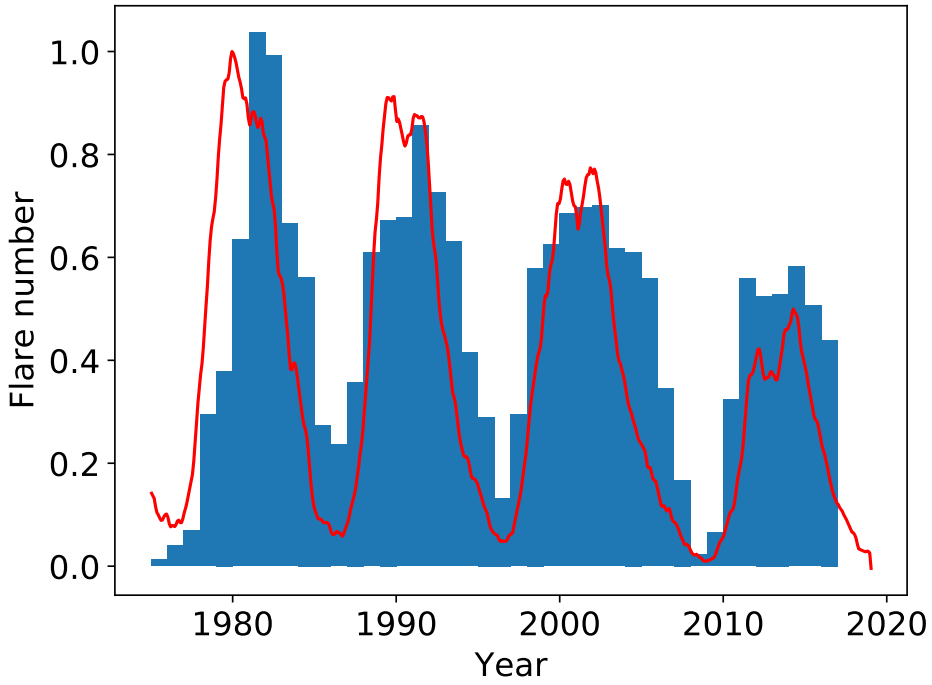

(a)

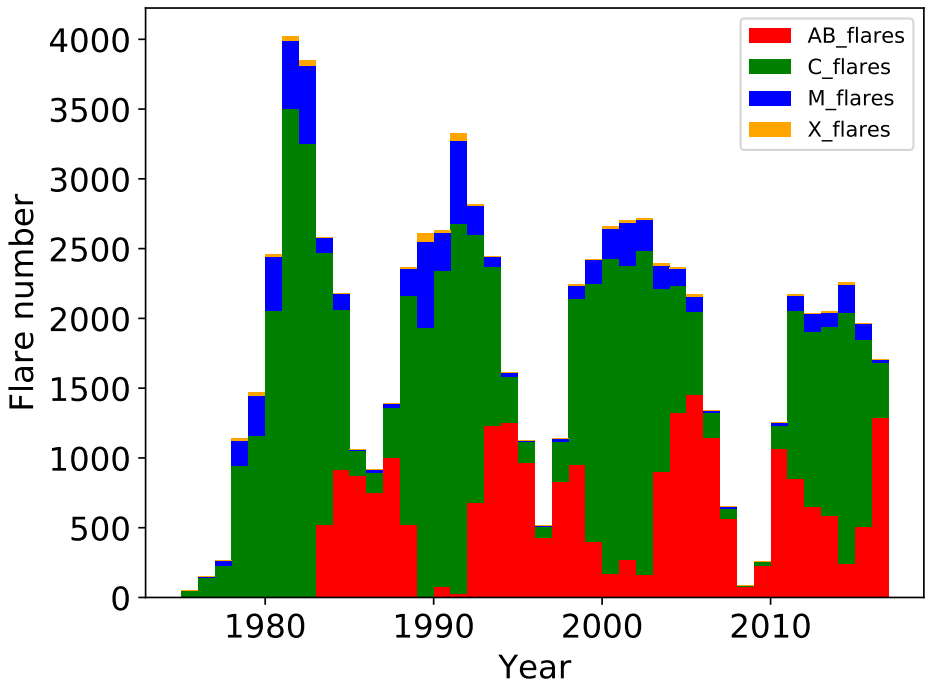

(b)

Figure 6.11: Here two plots are shown detailing the historic data of solar flares and sunspots. Plot (a) shows the sunspot number in the red solid line and the flare number as the blue histogram. These have both been normalised to 1 to allow a comparison of the data revealing the close relationship between sunspots and solar flares. Plot (b) shows the varying sub-classes of solar flares within revealing an anti-correlation between the lower A & B-class solar flares to the higher energy X, M and C-class solar flares. The data of the solar flares was obtained from the GOES for the sunspots from the SILSO database and all the data has been binned per year.

each other over the solar cycle. However, despite this, the relationship between sunspots and flares is more complicated than initially believed. In Gao and Zhong (2016) they investigated the temporal behaviour of varying classes of solar flares. Their findings show the lower B-class solar flares to be in anti-phase with all other C, M and X-class solar flares in terms of the solar cycle (see Table 6.2 for details of the various solar class flares and their respective energies). To investigate this strange behaviour, the solar sub-classes are plotted as a histogram in Figure 6.11(b) which also displays an anti-correlation amongst the A & B-class solar flares. Even more interestingly, the A & B-class flares are also out of synchronisation with the sunspot number. As suggested by Gao and Zhong (2016) this anti-correlation within low class flares could potentially be linked to the negative correlation between small and large sunspots (Nagovitsyn et al., 2012). Note, this result could also be bias due to the systematic effect of non-detection of weak flares when the Sun is bright.

This then brings us back to the lack of a correlation between stellar flares and starspots amongst the solar-type sample. The evidence of an anti-correlation between low and higher energy solar flares with regards to the solar cycle could be an explanation for the observation of stellar flares at all rotational phases. These lower energy ($< \ 10^{29}$ erg) solar flares are present when the Sun is in a solar minimum and is considered not very active. Therefore, these flares could be originating from plage regions or areas where local dynamos are at play. The higher energy ($> \ 10^{29}$ erg) solar flares are then clearly correlated with sunspots and both appear during solar maximum when the Sun is at its most active.

Applying these scenarios to our solar-type star sample could aid in explaining the lack of a correlation between rotational phase and flare number. Lower energy flares are present at all rotational phases (see Figure 6.10) which could result from plage, filaments or local dynamo regions not associated with spots which are present across the stellar disk. This is similar to what is observed on the Sun where the lower energy flares are predominately present when the Sun is less active and producing a lower number of spotted regions. The lower energy A & B class solar flares are a few orders of magnitude less energetic than those observed on the solar-type sample. However, it is possible to observe flares of energies 10^{29} erg in solar-type stars, for example using *Kepler*, see Maehara et al. (2012). Therefore, these lower energy flares could be present but not observable with *TESS* since it is less sensitive to lower energy flares

(see Section 2.2.3). As a result we note our flare sample does not contain any flares with energies less than 10^{30} erg which equates to a C-class solar flare (see Table 6.2), however, in our solar-type sample a lower energy flare is considered to be $< 10^{34}$ erg according to Figure 6.4.

Overall, the lower energy ($< 10^{34}$ erg) stellar flares from the solar-type sample could originate from plage, filaments or local dynamo regions on the stellar disk not associated with starspots. This is similar to the lower energy A & B class solar flares which are also not associated with sunspots. Therefore, the stellar flares observed at all rotational phases could be resulting from a mixture of spotted and non spotted regions resulting in no correlation between rotational phase and flare number. Alongside this, the larger energy flares are more present when there is spot activity present on the disk. This is particularly clear in the star HD 39150 in Figure 6.7 where emerging spot and plage regions cause increased flaring activity as a result of shearing between varying magnetic polarities.

All of the discussions so far centre around the relationship between solar flares and sunspots on a cycle basis. The *TESS* observations are far too short to investigate cycle periods on our sample, even the ones observed in all sectors. It will take a few years for *TESS* to build up longer term observations of stars as it returns to sectors. Therefore, can we correlate the solar flare numbers within an activity cycle to the solar rotation period? The above work regarding solar flares discusses X-ray data while with *TESS* we deal with flare observations in the optical. What is required for the Sun is a discussion on whether there is a relationship between solar flares and sunspots on the rotational period basis. Unfortunately, catalogues of solar White Light Flares (WLFs) are very much incomplete: for example Matthews et al. (2003) lists 28 flares over a one year period detected with Yohkoh, a Japanese Solar mission. The catalogue from Kuhar et al. (2015) contains 43 M and X class flares which occurred from 2011 to 2015 and were observed by both SDO/HMI and RHESSI and Namekata et al. (2017) expanded on this adding another 11 observed in 2015. Overall, this data is not sufficient for a proper analysis of the above question. Moreover, obtaining the rotation period of the Sun as an effective lightcurve in time is a difficult process and despite irradiance measurements of the solar disk being taken this is not something which is well studied in solar physics.

Flare Classification	Energy Range (ergs)
X10	$> 10^{32}$
X	10^{31} - 10^{32}
M	10^{30} - 10^{31}
C	10^{29} - 10^{30}
B	10^{28} - 10^{29}
A	$< 10^{28}$

Table 6.2: The energy range for each of the solar flare classifications, making comparisons between the stellar and solar flares easier (obtained from Notsu et al., 2019).

.

6.8 Discussion

In Chapters 4 & 5, no evidence was found for a correlation between rotational phase and flare number within a sample of 183 M dwarf flare stars. This chapter represents a similar study for a sample of 209 solar-type (F7 - K2) stars observed in 2-min cadence by *TESS* in sectors 1 - 13. Rotation periods were determined using an LS periodogram, 1980 flares were identified and classified within the sample and their energies calculated between 10^{31} - 10^{36} erg. Similar to Chapters 4 & 5, no evidence of any correlation between rotational phase and flare number was found, indicating the flares are randomly distributed and do not occur alongside the dominant starspotflregion which is responsible for the rotational modulation. However, it was noted that increased levels of activity were observed in the star HD 39150 (TIC 364588501) when evidence of emerging starspot and plage regions were observed in the rotational modulation of the lightcurve. This finding does then suggest there is a relationship between flares and starspots and agrees with the mechanism for flare generation as discussed by Chandra et al. (2010).

In Chapters 4 & 5, four possible scenarios to explain the lack of a correlation were identified including star-planet interactions, binarity, polar spots and multiple spot locations. Here I discuss these further while also bringing in other possible explanations. Firstly, there is the potential for star-planet interactions (SPI's) and interactions between two stars within a binary system. Only one of the solar-type stars in the sample, HD 44627 (TIC 260351540), has a known exoplanet. In this instance the planet is orbiting at much too great a distance (a = 275AU) to cause any SPI's with its host star. However, this does not rule out any of the other stars having undiscovered exoplanets which could cause SPI's.

Additionally, the stars in the sample could be in binary systems which could cause induced magnetic activity producing flares. Within the sample there are three stars whose *TESS* lightcurves show they are eclipsing binaries. These solar-type stars are CD-78 516, AF Cru and HD 120395 (TIC 357911163, P_{orb} = 1.63 days; TIC 309528896, P_{orb} = 1.89 days; and TIC 243662768 P_{orb} = 1.64 days respectively), which have rotation periods between 7.5 – 10 days, a spread in spectral types and show little flaring activity. The lack of flaring activity in these stars indicates that the period is long enough that interactions between the stars do not give rise to increased flaring activity.

Secondly, with the M dwarf samples in Chapters 4 & 5 I discuss the potential for polar spots which could cause flaring activity at all phases if in the line of sight. It is important to note here that after spectral type M4 ($\sim 0.3 M_{\odot}$) these stars become fully convective and so do not possess a tachocline, therefore, generating their magnetic field through a different dynamo mechanism in comparison to the Sun. However, polar spots or spots with high latitudes have never been observed on the Sun, therefore, you would assume polar spots are not possible on other solar-like stars. Despite this, in a study by Schrijver and Title (2001) they simulate that polar spots could be possible on sun-like stars where a strong polar cap field leads to suppression of convection and formation of starspots at high latitudes. As a result, there is the possibility of polar spots being present on these solar-type stars which could be interacting with active regions at lower latitudes to produce flaring activity.

This then brings us on to the theory of multiple spot locations. During solar maximum, the Sun can be observed to possess many active regions which host spots including multiple spots at one location. As a result, it is entirely possible for the solar-type stars to possess multiple spot locations which could produce flaring at all rotational phases. Evidence of multiple spots was observed in the one year lightcurve of HD 39150 (TIC 364588501) which was observed in the continuous viewing zone. In the *TESS* lightcurve of this particular star the shape of the rotational modulation is observed to change over time with the whole lightcurve being fold-able on one rotation period and phase zero. This suggests multiple spots which are slightly out of synchronisation producing the changes in the shape of the rotational modulation. As a result, increased levels of flaring activity are observed which co-align with the changes in the rotational modulation suggesting emergence of new spot regions and plage regions which interact with

each other to produce the increased flaring activity. The large spot coverage of this and other G stars suggest youth. This is consistent with a study of the solar spectral irradiance variability over the last 4 billion years (Shapiro et al., 2020). The Total Solar Irradiance (TSI) variability of the young 600 Myr old Sun was about 10 times larger than that of the present Sun with its variability been spot-dominated, while by 2.8 Gyr it's variability is faculae-dominated.

As the relationship between solar flares and sunspots is well-established I used historic X-ray GOES flare data and SILSO sunspot data to investigate this relationship further. It is found that sunspot and flare number are closely linked across the solar cycles where sunspot numbers increase as the Sun approaches solar maximum, so does the flare activity increase. Similar to Gao and Zhong (2016) I also discover the lower energy A & B class flares are anti-correlated with the higher energy X, M & C class. This is interesting as the lower energy solar flares are more prominent during solar minimum when the sunspot numbers are low. As a result, this suggests these solar flares could be originating from plage or local dynamo regions and are not associated or correlated with sunspots.

This leads us on to the earlier finding of starspots and stellar flares not being correlated on the sample of solar-type stars. The anti-correlation between high and low energy solar flares and the lack of a correlations between low energy flares and sunspots could aid in understanding the lack of a spot/flare connections in the solar-type stars. There is the potential for the lower energy flares, which are observed to occur at all rotational phases, to result from plage regions or local dynamo regions as well. However, this does not explain the lack of a correlations between higher energy flares and starspots, as they should occur together much like what is observed on a cycle by cycle basis on the Sun.

An alternative idea is that it should not be attempted to correlate flare activity with spot number as this is not the main driver of magnetic activity. In a series of papers by McIntosh et al. (2014); McIntosh and Leamon (2014) and more recently, Srivastava et al. (2018) and Dikpati et al. (2019, and references therein); these authors suggested that activity bands belonging to the 22 year magnetic activity cycle is the main driver of solar activity, with these bands interacting at the equator. The idea behind this is an 'Extended Solar Cycle' which appeared to extend the activity butterfly back in time, about 11 years before the formation of the sunspot pattern. Furthermore, these activity bands extend to much higher solar latitudes

and would require a polar dynamo which is not a widely accepted idea. The observational evidence for the extended solar cycle is based on the evolution of coronal bright points, although the origin of this work dates back several years to Wilson et al. (1988). As noted by the authors, many large solar flares do not occur at sunspot maxima (e.g. see Odenwald et al., 2006). They suggest that the longer these activity bands spent at very low latitudes, the higher the probability for large flares due to the formation of complex active regions. With faster rotators, one may have several of these activity bands, thus a series of complex active regions producing super flares.

6.9 Conclusions

In this Chapter an analysis into the statistics of superflares was conducted on a sample of 209 solar-type stars. Utilising 2-min cadence data from *TESS*, rotation periods were derived for the sample and characterised 1980 flares. Two of the targets were observed in the continuous viewing zone so, with one year of observations a short study was conducted into the variability of these stars. Our findings showed evidence of spot emergence, plage regions and migrating spots which were connected to increased levels of flaring activity. Overall, the focus was on the relationship between rotational phase and flare number finding no correlation between the two. Additionally, an analysis on historic solar flare and sunspot data was included to investigate the relationship between flares and spots on the Sun, using the results to aid in understanding the lack of a correlation in the solar-type star sample.

By June 2020, *TESS* will finish observing the northern hemisphere and will return to sectors in the southern sky. Further observations of these stars will allow for follow up studies, investigating their changing behaviour a year later. This will provide insights into the extended magnetic activity of these stars while also allowing for the search of activity cycles. Overall, the continued study of flares and starspots can aid in understanding the dynamo mechanism of other stars and how it relates to the Sun. All of this is extremely important when considering potential habitable systems which may orbit these active host stars.

In the next chapter, both the solar and stellar studies are brought together and the solar-stellar flare connection is discussed in more detail.

7 Conclusions & Future Work

Throughout this thesis I have outlined both solar and stellar flare observations providing interpretations of flares through comparisons of the two. In this Chapter, I recap on the most important results and bring together the studies on both solar and stellar flares exploring the connection between them. Additionally, the research carried out has paved the way into other avenues which are touched upon in this thesis.

7.1 The Solar-Stellar Flare Connection

Solar flares represent a sudden increase in radiation which results from a rapid reconfiguration of the coronal magnetic field. These events are extremely powerful and are observed across the entire electromagnetic spectrum, possessing energy outputs up to 10^{32} erg (Fletcher et al., 2011). The magnetic energy released from solar flares can be observed as multiple phenomena including flare ribbons, post-flare arcades and filament eruptions. Overall, the pre-flare magnetic topology is responsible for determining which of these phenomena will manifest to produce a solar flare.

In addition to solar flares, stellar flares have been observed on stars similar to the the Sun and less massive stars over many decades, with energies exceeding 10^{33} erg (e.g. (Schaefer et al., 2000). Known as 'superflares' these large outbursts can have severe consequences for any orbiting planets atmosphere, therefore, understanding their frequency and origin is vital for the existence of life. Solar-type stars have a similar interior structure to our Sun, radiative core with a convective envelope, yet they possess stronger magnetic fields - producing higher

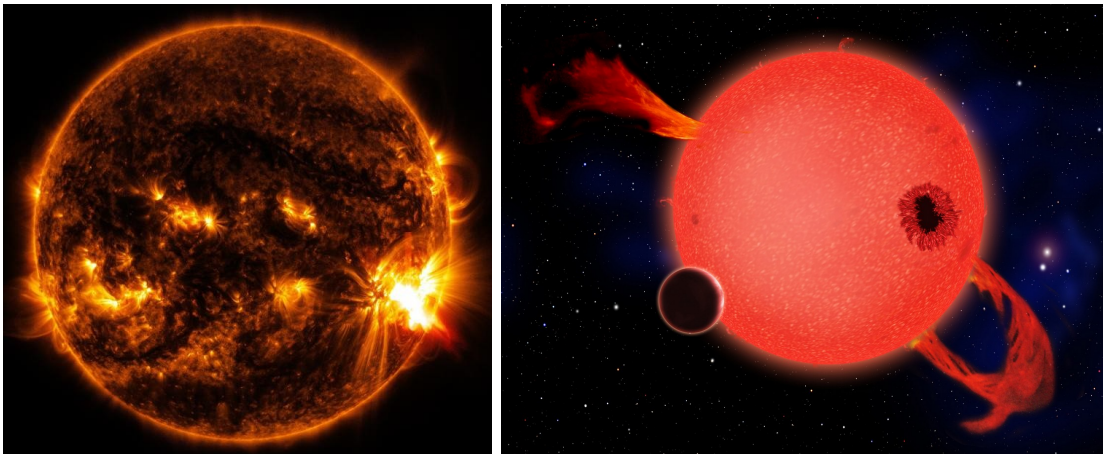

Figure 7.1: To the left shows a solar flare from the Sun on the western limb which appears as a brightening in 171Å taken by SDO/AIA. To the right is an artists impression of a flare on an M dwarf star where a large spot is also seen covering a significant area of the visible stellar disk. *Images courtesy of NASA*.

levels of activity and stronger flares (Maehara et al., 2012). The reasons behind this remain unknown, however, it is believed it relates to the stars dynamo and age. In low-mass stars with spectral types later than M4, their interiors are thought to be fully convective (Hawley et al., 2014) so they posses no tachocline (the boundary between the radiative and convective zones) and must generate their magnetic fields through a different dynamo mechanism. However, despite this, these stars can also show increased levels of flaring activity with flares reaching energies much greater than seen from our Sun.

As the Sun is our nearest star we are able to collect detailed spatial observations of its many phenomena and records of solar observations have been kept for centuries. Along with all of these observations comes a deep knowledge and understanding of the mechanisms which are at play on our nearest star and how they can affect the Earth and Solar System. In stellar physics, although the number of stars now observed by missions such as Kepler, *TESS* and Gaia has exceeded the billions, the lack of detailed and long-term observations remains an issue. The capabilities of our technology and the vast distances between us and our neighbouring stars restricts our ability to produce observations which show details of the magnetic activity. Therefore, we should be looking to use the knowledge gained from detailed solar observations to illuminate our understanding of stellar flares. In this section, we look at the solar-stellar flare connection through detailed observations of a confined solar flare event and use the results to provide insights into large scale flare events observed on other stars.

In summary, the studies of stellar flares reported in Chapters 4, 5 & 6 discuss the statistical analysis of stellar flares on both low mass and solar-type stars using one and two-minute photometric data from K2 and *TESS*. Utilising a simple statistical test, the distribution of the flares was investigated and it was concluded that none of the stars in the samples showed any preference for certain phase distributions. This was extremely unexpected, as it indicates other stars do not behave like the Sun where the relationship between solar flares and sunspots is well established. Here, using the 3D MHD simulation from Chapter 3, the conditions for large scale stellar flares on both low mass and solar-type stars is explored.

7.1.1 Scale-up of the Solar 3D MHD Simulation

In Chapter 3, a study involving a confined solar flare was carried out using ground-and-space-based observations from SST, SDO and GONG where the event was compared to a 3D MHD simulation. These observations provide the evidence to validate the simulation which can be applied to not only jets and CMEs but also confined eruptions and flares. Overall, this study explores the finer details of solar flares and their associated eruptive phenomena, providing a unique perspective when applying this knowledge to stellar flare scenarios. The simulation flare energies (i.e. magnetic field strengths) are in good agreement with what one would expect given the classification of flares observed on the Sun. Therefore, we could extrapolate the simulation to much higher energy flares.

To compare the observations of stellar flares and solar flares the key lies within the 3D MHD simulation. This simulation can be scaled up to see how it would produce flares of greater energies like the ones observed in both low mass and solar-type stars. The result of this scale up can be seen in Figure 7.2 which shows the conditions needed in both the magnetic strength and size of the parasitic polarity in order to produce flares of greater energies. Overall, our Sun can show flares with energy outputs ranging from 10^{24} - 10^{32} erg. However, studies like Chapters 4,5 & 6 of low mass and solar-type stars have revealed flares with energies exceeding 10^{32} erg, with 'superflares' having energies up to 10^{36} erg.

From Figure 7.2, it can be seen that to produce a flare of energy 10^{34} erg would require a parasitic polarity (area of strong negative field encircled by a positive field) of size 200 Mm and

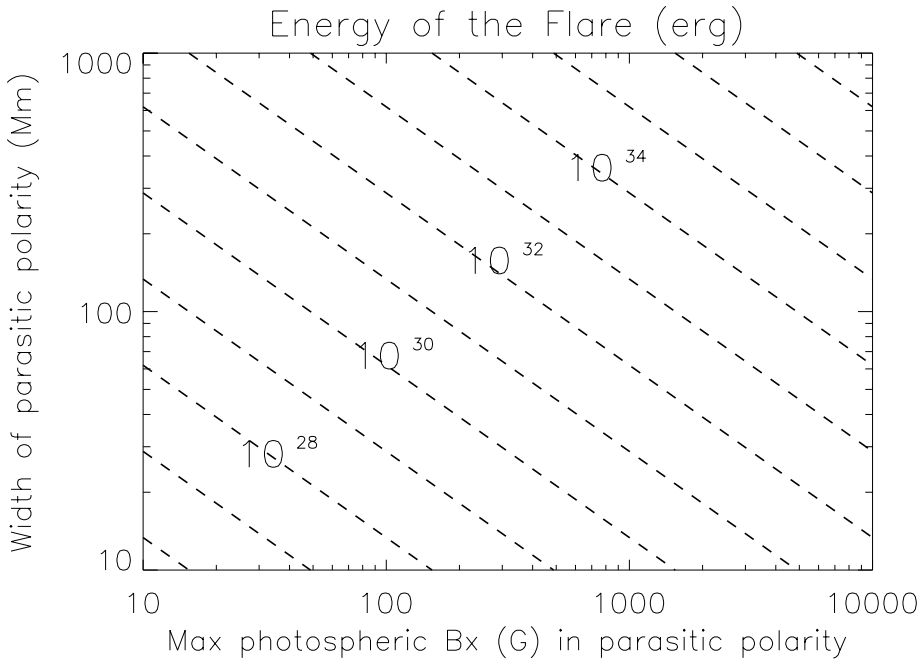

Figure 7.2: This plot represents a scale up of the solar 3D MHD simulation (see Chapter 3). The x-axis represent the field strength of the parasitic polarity and the y-axis represent the size of the parasitic polarity. The dashed lines then represent the differing energies of flares with units in erg.

field strength 2 kG. For an M dwarf with spectral type M3/M4 this means the active region hosting the parasitic polarity, which may or may not host spots, would indeed be half the size of the visible stellar disk. In terms of the Sun, the field strength of 2kG would be possible as sunspots tend to be in the region of 1kG - 4 kG, however a sunspot which is a third of the stellar disk is extremely unlikely. Despite this, Jeffers et al. (2006) calculate the spot coverage of the G2 star SV Cam using spectrophotometric data from the Hubble Space Telescope as 30%. Therefore, it may be possible for other solar-type stars to possess larger spot coverages. On the other hand you could look at producing a flare of 10^{34} erg more feasibly with a parasitic polarity of width 60 Mm, however, this would require a magnetic field strength of 10 kG. This may be unlikely on a solar-type star but would depend on the age of the stars and the magnetic configuration, however, on an M dwarf this could be entirely feasible. Shulyak et al. (2019) use Zeeman splitting to determine the magnetic field strengths of 29 active M dwarfs finding B ranging from 1 - 7 kG. These stars had rotation periods in the range of 0.1 - 10 days, with the star possessing a field of 7 kG being an M5.5 and having $P_{rot} = 0.27$ days. Therefore, a magnetic field strength of 10 kG could be possible on M dwarfs.

The flare model proposed by Aulanier et al. (2013) also fails to provide sufficient energy to explain large flare on M dwarfs and solar-type stars. They scaled up their 3D MHD simulation for eruptive flares calculating the parameters needed for larger energy flares on a solar-type star. In their highly sheared bipole model, a flare of energy 10^{34} erg would require a bipole the size of 100 Mm and field strength of 4 kG (which is similar to what we would expect with our simulation scale up for such field strengths). Overall, they conclude that solar-type stars which produce superflares with energies $> 10^{33}$ erg would require a much stronger dynamo than the Sun. However, with similar interior structures, masses and radii you would not expect other solar-type stars to differ greatly from the Sun. Therefore, there must be other factors, such as age (i.e. the stars are younger than we expect in order to have larger field strengths), which need to be taken into account.

7.1.2 Can the Sun Produce Superflares?

One important question is: Would the Sun be able to produce superflares with energies $> 10^{33}$ erg? In Shibata et al. (2013) they investigate this question using current ideas related to the mechanisms of the solar dynamo. In their calculations the Sun would need to generate a sunspot with magnetic flux of 2×10^{23} Mx to produce a 10^{34} erg flare. In order to do this it would take the Sun 40 years to store this magnetic flux and at present there is no known physical mechanism to make this possible. Overall, they conclude it is premature to say whether a 10^{35} erg flare would even be possible on the Sun given the current dynamo theories.

However, is it possible for the Sun to have produced superflares in the past? Figure 7.3 shows a sunspot drawing made by John Worchester, an English monk and chronicler, on December 8th AD 1128. He was most known for the Chronicle of John of Worcester up until his passing in AD 1140 which contains many accounts of celestial phenomena including eclipses, comets, meteor showers and aurora. The sunspot drawing represents the earliest known drawing of sunspots and it is believed Worcester observed this spot structure directly when the glare of the Sun was reduced by haze. Sunspots have been recorded by Chinese astronomers since 28 BC, however, there are no Chinese drawings which exist until after AD 1400. In the text surrounding Worcester's drawing, he describes the event as 'two black spheres against the Sun.'

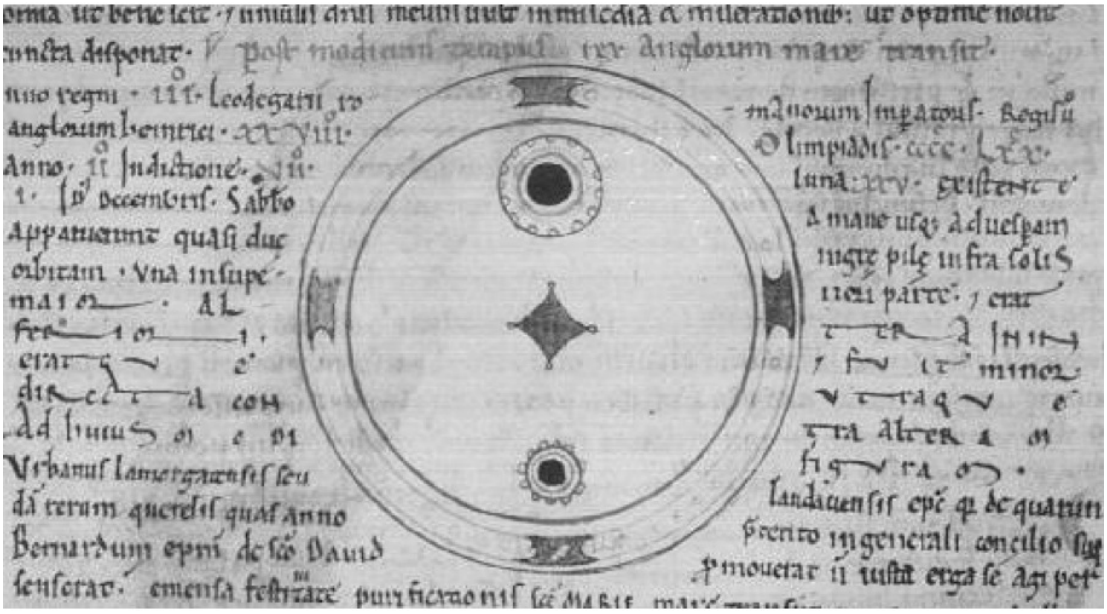

Figure 7.3: This drawing was made by John of Worcester, an English monk and chronicler, on the 8th December 1128 AD of sunspots on the solar disk. It shows two distinct sunspots on opposite side to each other where the top one is larger than the bottom. There are details of umbra and penumbra structure and the surrounding edge of the solar disk represents the solar limb. *Image courtesy of Bray et al. (1995)*.

He then goes on to say 'The first was in the upper part and large, the second in the lower and small, and each was directly opposite the other as this diagram shows' as translated by Darlington and McGurk (1995). Planetary transits can be ruled out to explain the observed spots as they were both on opposite sides of the Sun on 8th December 1128 AD and the spots were seen together.

This drawing suggests the Sun could have been capable of producing larger spots or spot groups similar to what we see in the rotational modulation of the *TESS* lightcurves. Drawings are known to be highly subjective and could be exaggerated by the artist to emphasise the significance of the feature. Therefore, it is important to bear this in mind when discussing the drawing by John Worcester and anything with regards to it is simply speculative at this point. Overall, the drawing suggests it could have been possible for the Sun to produce superflares of orders of magnitudes greater than what we observe today. Five days later, after the sunspot drawing was made, the aurora borealis was observed and recorded by a Korean astronomer almost 9,000 miles away on 13th December 1128 AD (Willis and Stephenson, 2001). This suggests the sunspots observed by John Worcester were part of an active region which was

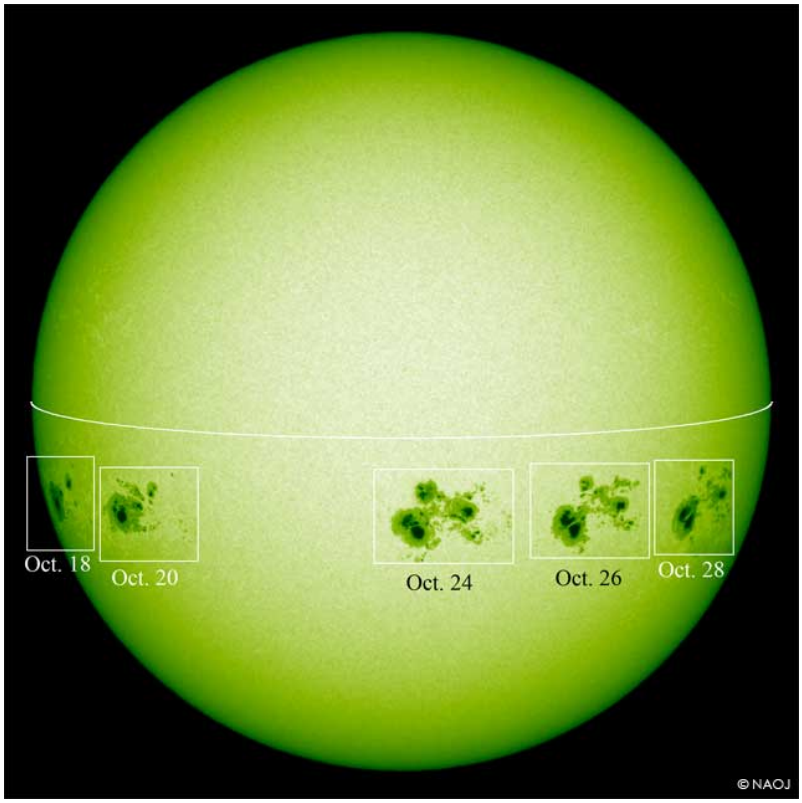

Figure 7.4: A series of white light images taken by the Solar Flare Telescope showing the AR 12192 as it progressed across the solar disk in October 2014. This particular active region hosted the largest sunspot observed in 24 years during solar cycle 24. *Image courtesy of Solar Observatory/NAOJ.*

responsible for the solar eruptions to produce the observed aurora borealis. However, the exact magnitudes of the flaring activity are unknown, from the size of the spots in Figure 7.3 and the observations of aurora borealis at lower latitudes in Korea, suggests these eruptions were substantial. The Sun has been known to produce large sunspots in the past, however, they can be rare. In October 2014 the largest sunspot and active region (AR 12192: Sarkar et al., 2017) was observed in 24 years with a size corresponding to 66 Earth cross sections, see Figure 7.4. The size of this active region was unexpected as Cycle 24 was a comparatively weak cycle (Jiang et al., 2015), however, it shows the Sun is capable of displaying larger sunspots.

Overall, this would suggest the Sun was capable of producing larger spot coverages and greater flaring activity earlier in its life. As a result, the increased flaring activity and spot coverages from the solar-type stars in the sample of Chapter 6 suggest these stars are potentially younger than the Sun. Therefore, their younger age means they are more active in comparison to the Sun. Age estimates of solar-type stars and low mass stars is a rapidly developing field,

especially in the era of *Kepler* and *TESS* were rotation periods are acquired from photometry and can be used to derive age estimates through Gyrochronology (e.g. Barnes, 2007; Morton, 2015; Angus et al., 2019). While deriving rotation periods for M dwarfs remains uncertain, there is a lot more certainty in ages determined for main sequence F, G and K stars (see Angus et al., 2019). Recently, there has been a development in studies involving stellar ages and magnetic activity. In Davenport et al. (2019) they look at the evolution of stellar flare activity with a sample of low mass main sequence stars finding that flare activity decreases as a stars rotation rate decreases, this is also linked to increasing age. In addition, Morris (2020) find that spot coverage also decreases with increasing age within a sample of F, G and K stars. This aligns with the discussions centring around the Sun, where the likelihood of it being more active earlier in its life highly plausible.

7.2 Conclusions

Throughout this thesis many different observational sources, data analysis techniques and numerical modelling have been used to investigate and discuss both solar and stellar flares. Firstly, through using one and two minute cadence photometric data from K2 and *TESS* the rotational phase of stellar flares on low mass and solar-type stars was investigated. Overall, it was established there is no preference for rotational phase within any of the stellar samples despite the presence of a large dominant spot (or group of spots) producing the observed rotational modulation. This finding was unexpected as there is a well established solar flare/sunspot connection on the Sun where these phenomena typically occur together.

Next, in a solar flare analysis, ground based SST data and space based SDO data were used to analyse the kinematics of a solar flare associated with a filament eruption and jet. These observations were qualitatively compared to a 3D MHD simulation which validated the magnetic configuration and subsequent eruption of the event. Overall, the magnetic configuration can be applied not only to jets and CMEs but also confined eruptions and flares. In turn, this simulation can be scaled up and applied to stellar scenarios replicating flare energies observed on other stars. Through this process it was difficult to replicate the higher energies with a realistic magnetic field strength and spot size suggesting superflares would require a much stronger

dynamo mechanism. Additionally, the possibility of increased spot coverage and greater flares from the Sun in the past was discussed with the likelihood of superflares occurring on much younger stars a strong possibility.

Overall, this thesis has explored the amalgamation of solar and stellar flare physics to explore the flares on other stars in greater detail. As the Sun is our nearest star we should look to using it as a benchmark for the phenomena observed on other stars. Therefore, throughout this thesis there are references to solar research comparing what we have observed on other stars to what has been studied on the Sun. In summary, there are not many astronomers who are involved in both solar and stellar research and as a result each community is not exposed enough to what the other is learning. Therefore, I hope this thesis serves as an example of the kind of research which can be done when you bring both of the disciplines together.

7.3 Summary of Original Contributions to the Field

Now I take the opportunity to detail the original contributions to the field which result from this thesis.

- Firstly, through multi-wavelength observations of a confined solar flare and helical jet and comparison with a 3D MHD model, the suggested model provides an intuitive mechanism for transferring twist/helicity in confined filament eruptions. Thus validating the applicability of the breakout model not only to jets and coronal mass ejections but also to confined eruptions and flares.

- Through multiple studies of stellar flares on both low mass and solar-type stars I discover flares do not correlate with the dominant starspot/spot groups on the disk which produce the observed rotational modulation. Overall, this suggests there are other mechanisms at play where four scenarios including binarity, multiple spots and polar spots were proposed as explanations for the finding.

- Amongst the stellar studies using *TESS* lightcurves I identified a group of ultra fast rotating M dwarf and solar-type stars which display low levels of flaring activity. This was unexpected as it is known in the field a faster rotating star is expected to be more

active as a result of its dynamo mechanism.

- During the solar-type stellar flare study, two sources were observed in the *TESS* continuous viewing zone providing year long observations of the stars. In particular, one star (TIC 364588501) showed evidence of increased flaring activity indicating a strong link between emerging spots and flare activity. The changing shape of the rotational modulation suggests flux emergence which would cause shearing between the magnetic polarities and is a known mechanism for intense flaring activity. This short study into magnetic variability showed the potential within the *TESS* data of continuous viewing zone targets.

- Finally, the running theme throughout this thesis is the amalgamation of solar and stellar flare research, using the Sun to aid in understanding the observed phenomena on other stars. The final section of this thesis discusses the scale up of a solar model to stellar flare energies showing it is difficult to replicate the conditions necessary to produce the large scale events. There are very few studies like this and overall, I believe these are important to both fields as it suggests we do not fully understand the mechanisms which are at play on other active flare stars.

These findings have paved the way into other areas of research opening potential new projects. I now go on to discuss these projects in greater detail, providing updates where work remains ongoing.

7.4 Future Work

During the three years of my PhD I have investigated a very specific aspect of stellar flares on low mass and solar-type stars. These studies have lead to many other avenues from magnetic field generation in low mass fully convective stars to stellar variability. This section looks at the potential future work which stems from the research carried out within this thesis, where some projects are already underway.

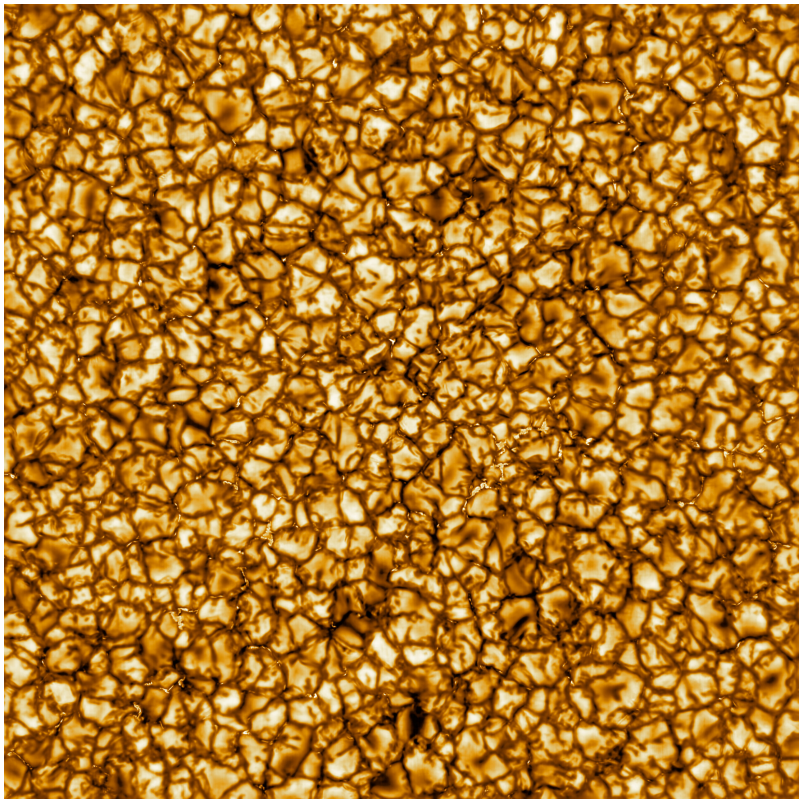

Figure 7.5: This is the first light image from the four metre Daniel K. Inouye Solar Telescope showing the granular structure on the surface of the Sun. The image itself is the highest resolution image of the Sun's surface ever taken where features as small as 30 km in size are seen for the first time. *Image courtesy of NSO/NSF/AURA*.

7.4.1 Magnetic Fields

Flares have been studied for over one hundred years, with the first record of a solar flare being observed by Richard Carrington in 1859. Known as the Carrington event, this flare produced the largest geomagnetic storm on record. It short circuited the new telegraph network worldwide and the Northern Lights were observed as far south as Cuba. This marked the first recorded space weather event, which, if repeated today would have drastic effects on communication and GPS satellites, causing chaos and potentially devastation on Earth. Flares from the Sun and other stars are commonly used as a proxy for magnetic activity. However, the question of how a magnetic field is generated on stars with different masses and interiors is still unresolved. This in turn highlights further questions, such as how do stars keep their magnetic fields and how do their structures change over time?

The Daniel K. Inouye Solar Telescope (DKIST: Tritschler et al., 2015) is the worlds largest solar

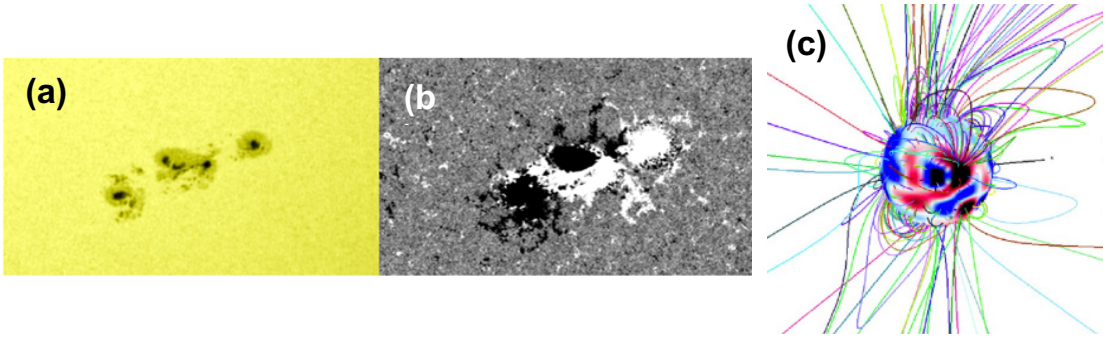

Figure 7.6: A selection of images showing the magnetic structure of spots. Panel (a) shows a section of the Sun in white light detailing a complex sunspot structure and (b) the corresponding magnetogram. *Images courtesy of NASA.* In (c) the magnetic field extrapolation of a solar-type star from Gregory et al. (2010) is shown.

telescope with a aperture of four metres based at the Haleakala Observatory on the Hawaiian island of Maui. The first light test images (see Figure 7.5) were released in January 2020 with science observations due to commence in July 2020. I have been active in developing an observation program for DKIST which I expect to lead. This program aims to aid in the understanding and modelling of the flare mechanism on low mass and solar-type stars by monitoring complex active regions likely to produce high energy solar flares. It is generally accepted that the more complex the active region and sunspot configurations, the increased chance of flaring and the possibility of releasing a higher- energy flare (see McIntosh, 1990). By monitoring active regions on the Sun and extracting their magnetic field properties we can better understand the conditions needed for such high energy flares. Obtaining magnetograms to probe the magnetic field in other stars is difficult. Therefore, we look to the Sun to provide this information using solar observations to gain an insight into the detailed physics of the flaring mechanisms on these stars.

Modelling software such as `starry` (Luger et al., 2019) can be used to map the potential spot configurations matching the observed *TESS* lightcurves from a range of stellar spectral types. This will allow for comparisons between the magnetograms from DKIST to determine whether complex spot configurations are possible on other stars. With a model of the spot configurations it is then possible to estimate what the overall field of the star would look like, if the polarity of the field is known (i.e. from ZDI maps). Using extrapolation techniques similar to those used on the Sun, magnetic maps can be created to visualise the overall field. These maps will aid in understanding the dynamo mechanisms which are also at play, especially in

low-mass stars which are fully convective.

7.4.2 Variability in Solar-Type Stars

The 11-year solar cycle is well studied in solar physics and is linked directly to sunspot number where records have been kept for over 150 years. At solar minimum there are few sunspots and overall the Sun is very quiet. However, by solar maximum there are multiple groups of spots all interacting to produce increased flaring activity. While there are still unanswered questions regarding the complexity of the solar cycle, overall it is still well understood and so far, has been relatively predictable. In terms of stellar cycles this is a much different story. While there are long-term observations of a handful of stars such as Barnard's star (Toledo-Padrón et al., 2019) and AU Mic (Ibañez Bustos et al., 2019), there is a general lack for this data amongst a larger sample of solar-type stars. As *TESS* will observe stars multiple times during its extended mission this will open many doors into the search for activity cycles much like our Sun.

In the first cycle of *TESS* observations covering the entire southern hemisphere, thousands of solar-type stars were observed which we filtered down to 209 whose lightcurves showed evidence of rotational modulation and flares. These stars formed the initial study into one of the first analyses of superflares on solar-type stars with *TESS* as discussed in Chapter 6. *TESS* will finish making observations of the northern hemisphere in April 2020 where it will then observe the southern sky again for an extended mission. Calls for proposals were submitted in early January 2020 and as a result I am looking to observe a larger sample of solar-type stars a year later to investigate their magnetic activity including flares and starspots.

I submitted a *TESS* proposal to observe 437 solar-type stars which are present in or around the *TESS* continuous viewing zone which were also observed in the first round of observations in Cycle 1. The idea for this study stemmed from the two observations of solar-type stars in the continuous viewing zone in Chapter 6, where the long term observations allowed for a more detailed study into the observed magnetic activity of the stars. In addition to the 437 solar-type continuous viewing zone targets, the 209 stars from the initial study in Chapter 6 were also included in the the proposal as a follow up. With the data set there are several aims and objectives which will be carried out:

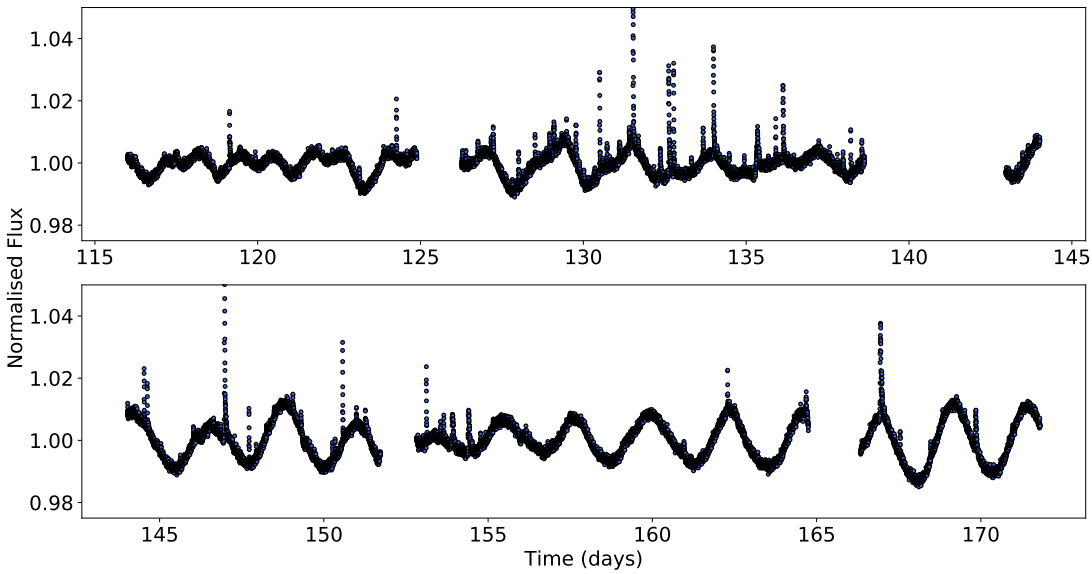

Figure 7.7: The lightcurve for TIC 364588501 covering data from Sectors 5 & 6 of Cycle 1 detailing the variability of the star including changing spot structures and increased flaring activity.

- Firstly, the rotation periods of the sample will be determined comparing them to the previous values obtained from the Cycle 1 lightcurves. Similarly, all flares will be identified and catalogued for each star which includes determining the flare properties.
- As all of the targets have been observed in Cycle 1, follow up Cycle 3 observations can be used to inform of any changes in magnetic activity. This includes using the stellar and flare properties to investigate any changes in flare number, flare energy or starspot changes observed in the rotational modulation along with any change in rotation period.
- Additionally, comparing the Cycle 3 observations with those from Cycle 1 will provide an unrivalled resource with which to search for stellar activity cycles. As *TESS* returns to sectors during its lifetime this resource will grow making the detection of stellar cycles easier.
- There are 439 solar-type stars in the sample which are present in or around the *TESS* continuous viewing zone. As a result, these targets will be observed for durations between 270 and 365 days. These observations will allow for a detailed analysis into the variability of magnetic activity within these stars over a long term. An example of one of these sources is shown in Figure 7.7 where an increase in flaring activity is observed as a result

of emerging spots and plage regions.

- Finally, I am particularly interested in looking for stars which possess rotation periods similar to the solar rotation period of $\sim$ 27 days. As this is the same as the *TESS* sector observation length stars will have to be observed in multiple sectors. Overall, within the sample, 489 solar-type stars have been observed in more than one sector with 439 being observed in more than 10 sectors including those in the continuous viewing zone. These stars are of particular interest because they will allow a direct comparison of their activity with that of the Sun.

7.4.3 Ultra Fast Rotating Low Mass Stars

In Chapter 5, a group of Ultra Fast Rotating (UFR) low mass stars with rotation periods $P_{rot} < 0.3$ days were identified which possessed a low number of flares within their *TESS* lightcurves. A similar group of UFRs was also found amongst the solar-type sample in Chapter 6, possessing $P_{rot} <$ 0.4 days which also show low levels of flaring activity. These groups are unusual as rapidly rotating stars are expected to produce increased levels of activity as this is directly related to their dynamo mechanism (Hartmann and Noyes, 1987; Maggio et al., 1987). The ages of these peculiar stars were estimated through Gyrochronology methods, however, this did not yield any answers with regards to their lack of flaring activity. Therefore, it was concluded the magnetic field configuration of the stars plays an important role in their magnetic activity, more so than their rotation period or age.

In a recent short study (Ramsay et al., 2020) we explored the flaring activity within a much larger sample of UFR low mass stars. Using data from Gaia DR2, we obtain a sample of over 13,000 stars close to the lower main sequence whittling these down to 609 stars which lie on the lower main sequence and have a periodic modulation less than 1 day. Overall, 288 out of 609 stars in the sample showed at least one flare and we find the fraction of stars which show flaring activity declines at shorter periods, with a significant drop at periods less than 0.2 days. This finding solidifies our initial discovery in Chapter 5 and details the importance of investigating the behaviour of these stars in greater detail. There are many potential reasons for this finding including the possibility of the stars being members of unknown binary systems and

the possibility of *TESS* being unable to detect lower energy flares which are present on these stars. Therefore, more data will need to be gathered of these stars including spectroscopic data to allow for a more detailed study into the magnetic activity of these peculiar UFR stars.

As a follow-up there is a proposal which has been submitted to obtain spectropolarimetry observations of these stars. This will allow for the search of evidence of magnetic fields and will be the first time a sample of UFRs have been systematically searched for evidence of magnetic fields. In addition, spectroscopic observations of these stars will enable the detection of chromospheric activity on these stars which is not delectable using *TESS*. In other studies such as Newton et al. (2017, and references herein) they found activity in UFR stars was saturated in emission such as Hα. This suggests these stars are in fact active, however, they may not show large amounts of flaring activity but there are other magnetic phenomena occurring on these stars. It is only with a full data set of observations in multiple wavelengths we can begin to unravel the mystery of the magnetic activity on these UFR stars.

A The Stellar and Flare Properties of the Low Mass and Solar-Type *TESS* Samples

In this Appendix the stellar properties for the full low mass sample (Table A.1) of Chapter 5 and solar-type sample (Table A.2) of Chapter 6 samples are detailed. This includes properties such as the number of observed *TESS* sectors, number of flares, rotation period, quiescent luminosity, energy range and duration of the flares for each star.

The apparent magnitude in the *TESS* band-pass, T_{mag}, is taken from the *TESS* Input Catalog (TIC) along with the TIC ID (Stassun et al., 2018). The distances are derived from the Gaia Data Release 2 parallaxes (Gaia Collaboration, 2016, 2018) by inverting them and the spectral types are obtained from the `SIMBAD` catalogue. SkyMapper magnitudes were converted to flux and then fitted using a polynomial to produce a template spectrum which was convolved with the *TESS* band-pass to derive the stars quiescent flux. This was then converted to quiescent luminosity using the distances determined from the Gaia parallaxes. The stellar rotation periods, P_{rot}, are obtained from the *TESS* lightcurves through a process involving a Lomb-Scargle periodogram.

With regards to the flare properties, the number of flares is obtained from the `FBEYE` suite of programs which also provides the start, stop and peak times of each flare in order to calculate the durations. The energies of the flares are determined as the equivalent duration (area under the flare lightcurve which is obtained from `FBEYE`) of each flare multiplied by the quiescent luminosity of the star. For full details of how all the stellar and flare properties are obtained please refer to Chapters 4, 5 & 6.

Table A.1: The stellar properties of all low mass stars from the study in Chapter 5 detailing the number of flares, rotation periods, quiescent luminosity, energy range and duration range of the flares.

Name	TIC ID	Sector	Ra	Dec	No. of	SpT	T_{mag}	Parallax	Distance	P_{rot}	$log(L_{star})$	$log(E_{flare})$	Duration
		(deg)	(deg)	flares			(mas)	(pc)	(days)	(erg/s)	(erg)	(minutes)	
2MASS J2151-2807	053851254	1	327.8703	-28.1304	5	1.5	12.02	12.2990	81.3074	1.7537	31.74	32.98 – 34.55	14.0 – 172.00
2MASS J2114-4213	126945045	1	318.6401	-42.2318	9	3.9	13.11	15.1340	66.0764	0.4134	31.16	32.16 – 33.36	8.0 – 48.00
2MASS J2117-4444	139090254	1	319.3919	-44.7433	4	4.5	10.88	56.9728	17.5522	0.5308	30.82	31.47 – 31.95	14.0 – 20.00
2MASS J2150-5113	139984208	1	327.669	-51.2277	6	3.7	12.0	22.4897	44.4648	1.0513	31.26	32.20 – 32.87	18.0 – 38.00
FS2003 0345	150188736	1,3	93.7286	-60.6552	2	0.5	10.44	26.0053	38.4537	9.4832	31.75	33.78 – 34.06	102.0 – 168.00
GSC 08894-00426	150359500	3	96.4838	-60.0569	23	5.0	9.71	74.3690	13.4465	1.0331	31.11	31.57 – 33.20	12.0 – 130.00
Smethells 119	161356637	1	343.8646	-52.3032	2	0.5	9.56	42.0588	23.7762	17.425	31.68	31.93 – 32.73	14.0 – 40.00
WOH S 209	179038379	1,3	78.9968	-67.2733	7	0.0	12.62	16.1301	61.9959	11.616	31.28	32.44 – 33.91	16.0 – 134.00
BPM 45048	206327797	1	354.0652	-48.5836	4	3.5	9.67	40.0092	24.9943	0.1119	31.64	33.18 – 34.08	14.0 – 46.00
WT 2220	206537793	1	332.923	-20.7367	7	3.0	11.16	24.1987	41.3245	1.5203	30.70	31.55 – 32.33	12.0 – 48.00
UPM J0113-5939	206544316	1	18.4189	-59.6598	9	3.7	11.6	23.1900	43.1220	0.3227	31.39	32.36 – 34.93	8.0 – 180.00
UCAC4 265-194917	207082763	1	331.9728	-37.0737	22	3.0	10.75	29.7125	33.6559	0.8505	31.50	32.16 – 34.21	14.0 – 130.00
LEHPM 5245	215197039	1	343.2486	-39.3812	5	0.0	10.96	20.9295	47.7795	2.1316	31.74	32.61 – 33.77	12.0 – 108.00
WISE J0250-6545	220523369	1,2,3	42.5936	-65.7653	22	3.2	11.94	19.7575	50.6137	1.2892	31.41	32.07 – 34.58	12.0 – 180.00
GSC 08859-00633	220539110	1,2,3	43.447	-61.5878	34	3.0	9.93	24.1223	41.4554	0.773	31.98	32.08 – 34.49	8.0 – 106.00
2MASS J0256-6343	220556639	1,2,3	44.197	-63.7174	43	4.0	11.48	16.6797	59.9531	0.5947	31.74	32.04 – 34.68	6.0 – 148.00
UCAC4 110-129613	229807000	1	352.2412	-68.0431	27	2.5	10.74	21.7164	46.0481	0.3745	31.79	31.59 – 34.31	8.0 – 90.00
2MASS J2329-6749	229807051	1	352.324	-67.8336	6	3.5	12.48	21.7647	45.9460	1.0224	31.10	32.55 – 33.90	26.0 – 220.00
FS2003 1156	231267979	1	334.6657	-53.4444	17	2.5	10.66	21.9142	45.6325	2.0233	31.83	32.45 – 33.90	12.0 – 82.00
2MASS J2110-5811	231632372	1	317.5259	-58.1972	3	4.0	12.63	19.8774	50.3084	0.5896	31.12	32.54 – 32.85	20.0 – 22.00
Smethells 165	231867117	1	6.0384	-62.1848	8	0.0	9.56	22.6086	44.2310	1.7568	32.20	32.87 – 34.50	22.0 – 200.00
UPM J0027-6157	231910539	1,2	6.8898	-61.955	33	4.0	12.04	23.0563	43.3721	0.55	31.22	31.82 – 33.75	8.0 – 140.00

Continued on next page

Table A.1 – continued from previous page

Name	TIC ID	Sector	Ra	Dec	No. of	SpT	T_{mag}	Parallax	Distance	P_{rot}	$log(L_{star})$	$log(E_{flare})$	Duration
		(deg)	(deg)	flares			(mas)	(pc)	(days)	(erg/s)	(erg)	(minutes)	
UCAC4 137-000439	231914259	1,2	7.6082	-62.6007	58	2.2	9.91	22.2753	44.8928	1.4341	32.10	32.11 – 34.93	6.0 – 346.00
2MASS J0153-6833	232073492	1,2	28.3553	-68.5564	10	4.5	12.9	22.5066	44.4314	0.5975	30.90	31.72 – 32.83	12.0 – 58.00
WISE J0200-6614	232083054	1,2	30.0842	-66.2339	17	4.0	12.45	21.9544	45.5490	0.6265	31.11	31.73 – 33.33	8.0 – 58.00
UPM J2222-6303	234284556	1	335.6659	-63.0576	2	3.5	11.83	22.5260	44.3931	1.1068	31.32	32.51 – 33.76	24.0 – 98.00
UCAC2 1442145	234333175	1,2	36.1037	-70.5559	12	3.3	12.12	22.7270	44.0005	0.509	31.20	31.96 – 33.40	8.0 – 88.00
2MASS J0039-6224	234495456	1,2	9.9193	-62.4035	19	4.9	13.5	26.5779	37.6252	0.3806	30.64	31.49 – 33.04	8.0 – 52.00
2MASS J0048-6526	234506344	2	12.22	-65.4427	7	3.2	12.01	20.4607	48.8742	1.0028	31.34	32.20 – 33.09	12.0 – 60.00
UCAC3 53-1665	234506911	1,2	12.3997	-63.7951	28	1.7	10.71	21.7128	46.0558	4.9401	31.79	32.20 – 34.66	12.0 – 192.00
2MASS J0118-6258	237880881	1,2	19.5279	-62.9831	12	5.1	13.4	21.7070	46.0681	0.346	30.72	31.82 – 33.78	12.0 – 422.01
2MASS J0121-6117	237883772	2	20.305	-61.2913	5	4.1	13.05	20.1895	49.5307	0.4231	30.93	32.01 – 33.46	12.0 – 116.00
UPM J0122-6318	237885807	1,2	20.689	-63.3126	35	3.5	11.43	21.9152	45.6304	0.4574	31.51	31.91 – 33.47	8.0 – 108.00
2MASS J0345-7509	238194430	1,2	56.4207	-75.1532	11	4.0	12.5	17.4263	57.3845	0.7001	31.26	31.93 – 34.73	8.0 – 214.00
2MASS J2149-6413	238813187	1	327.2708	-64.2178	3	4.5	12.15	22.6823	44.0872	0.1757	31.19	32.30 – 33.17	14.0 – 72.00
UCAC4 073-002133	238876720	2	39.6373	-75.4685	5	4.1	13.54	18.1483	55.1016	0.6325	30.83	32.18 – 33.61	12.0 – 108.00
2MASS J2137-6036	259845346	1	324.2873	-60.602	11	3.0	11.18	22.3092	44.8246	1.9957	31.60	32.06 – 34.75	12.0 – 398.00
UCAC4 114-133248	260889990	1	350.197	-67.3898	12	5.0	11.38	24.3611	41.0490	1.0561	31.36	32.19 – 33.75	12.0 – 164.00
2MASS J2317-7432	261560580	1	349.2519	-74.5363	5	3.6	12.05	22.3958	44.6512	0.8303	31.24	32.16 – 33.52	14.0 – 106.00
2MASS J2314-5405	262818859	1	348.6295	-54.0924	2	5.0	13.37	22.8336	43.7951	0.9895	30.69	32.61 – 32.79	40.0 – 86.00
1SWASP J2033-2556	269829656	1	308.4069	-25.9482	4	4.5	11.59	23.0541	43.3762	0.7382	31.40	32.45 – 33.57	12.0 – 70.00
EM* StHA 182	269940990	1	310.9218	-24.5649	6	4.1	10.15	22.8120	43.8366	1.0002	31.92	32.56 – 34.06	14.0 – 152.00
2MASS J0732-7445	271900514	1,2,3	113.1181	-74.7646	24	0.5	11.62	10.7056	93.4091	0.9104	32.03	32.04 – 34.44	8.0 – 146.00
LEHPM 5031	273369281	1	340.4959	-75.008	4	5.5	12.38	80.4417	12.4314	0.6488	30.00	30.94 – 31.82	8.0 – 52.00
UCAC3 33-129092	273416539	1	341.6457	-73.8977	5	2.3	11.12	19.9106	50.2245	1.6487	31.72	32.33 – 33.62	12.0 – 62.00

Continued on next page

Table A.1 – continued from previous page

Name	TIC ID	Sector	Ra	Dec	No. of	SpT	T_{mag}	Parallax	Distance	P_{rot}	$log(L_{star})$	$log(E_{flare})$	Duration
		(deg)	(deg)	flares			(mas)	(pc)	(days)	(erg/s)	(erg)	(minutes)	
W60 A68	277298771	1,2,3	84.5682	-69.3917	35	0.5	10.24	18.8784	52.9706	1.1798	32.07	32.50 – 34.91	12.0 – 286.00
2MASS J0023-5531	281461138	2	5.9897	-55.5291	3	4.1	12.97	23.9958	41.6740	0.6511	30.81	31.99 – 32.79	12.0 – 28.00
2MASS J2110-2710	289840926	1	317.6294	-27.1813	7	5.0	13.25	24.8489	40.2432	0.6505	30.66	32.41 – 33.10	10.0 – 60.00
2MASS J2110-2710	289840928	1	317.6316	-27.1832	7	4.5	11.98	24.7683	40.3742	0.6505	31.13	32.37 – 33.09	12.0 – 66.00
HD 270712A	294750180	1	71.0442	-70.3239	14	1.5	9.02	47.5062	21.0499	0.5263	31.81	31.72 – 34.63	10.0 – 372.00
2MASS J2345-7126	325220989	1	356.3427	-71.4474	14	3.5	11.81	22.3825	44.6778	1.6379	31.35	31.34 – 34.50	8.0 – 128.00
TYC 8543-967-1	348839788	1,2,3	98.8426	-57.6261	8	1.0	9.22	42.7725	23.3795	6.8946	31.76	31.63 – 33.87	8.0 – 208.00
2MASS J0742-6243	350142099	1,3	115.5327	-62.7317	16	4.0	11.63	38.4304	26.0211	1.8427	30.93	31.36 – 33.26	8.0 – 64.00
2MASS J2342-6224	350215424	1	355.6815	-62.4161	6	4.3	13.16	22.8689	43.7275	0.5233	30.80	31.71 – 32.89	8.0 – 48.00
UCAC3 52-533	355766445	1,2	3.8656	-64.2488	18	1.8	10.74	20.9100	47.8240	3.684	31.82	32.32 – 34.47	12.0 – 390.01
2MASS J0015-6137	355767053	1,2	3.9822	-61.6313	11	3.0	12.15	18.2189	54.8881	2.633	31.39	32.36 – 33.97	18.0 – 132.00
2MASS J0017-7032	394136141	1	4.311	-70.534	14	0.5	10.26	14.3804	69.5391	0.699	32.33	32.13 – 34.08	6.0 – 132.00
BPS CS 22956-0074	403237836	1	330.7277	-64.6794	11	1.8	10.48	22.8807	43.7050	0.4268	31.85	32.55 – 33.86	8.0 – 60.00
2MASS J2116-6005	410421717	1	319.147	-60.0868	9	3.5	11.81	21.5397	46.4259	0.9848	31.38	32.21 – 33.67	16.0 – 88.00
UCAC3 60-548	425933644	1,2	3.6996	-60.0636	28	3.6	11.35	22.5637	44.3190	0.4868	31.51	32.33 – 33.79	8.0 – 82.00
UCAC3 53-724	425937691	1,2	5.3666	-63.8525	10	5.5	13.18	22.7942	43.8708	0.1003	30.80	32.15 – 33.54	10.0 – 60.00
2MASS J2136-2049	441024908	1	324.1044	-20.8213	2	3.0	12.07	18.0365	55.4431	5.664	31.42	32.85 – 32.99	32.0 – 34.00
2MASS J2353-1844	027955268	2	358.357	-18.7449	2	6.5	13.21	27.4909	36.3757	0.6165	30.60	32.01 – 32.26	20.0 – 22.00
WOH S 6	033864387	3	65.4137	-72.5654	6	2.5	11.36	18.5936	53.7819	4.6801	31.76	32.72 – 33.96	14.0 – 98.00
2MASS J0123-4113	041862041	3	20.8874	-41.22	7	4.2	12.53	25.0455	39.9273	0.7362	30.97	32.02 – 33.44	12.0 – 140.00
TYC 6967-699-1	047465993	2	342.3711	-26.1398	11	0.0	10.29	22.1291	45.1894	1.8783	31.95	31.85 – 34.32	12.0 – 197.99
2MASS J0407-6825	025118964	2	61.9331	-68.4196	10	3.2	11.99	16.3511	61.1580	1.0187	31.55	32.55 – 33.45	14.0 – 58.00
2MASS J0321-6816	031780319	2	50.2665	-68.2799	5	4.0	11.85	18.8695	52.9956	1.3105	31.42	32.49 – 33.39	14.0 – 70.00

Continued on next page

Table A.1 – continued from previous page

Name	TIC ID	Sector	Ra	Dec	No. of	SpT	T_{mag}	Parallax	Distance	P_{rot}	$log(L_{star})$	$log(E_{flare})$	Duration
		(deg)	(deg)	flares			(mas)	(pc)	(days)	(erg/s)	(erg)	(minutes)	
G 267-34	070797900	2	1.9781	-29.9797	3	3.0	10.95	13.8030	72.4480	2.084	32.08	33.17 – 33.59	22.0 – 54.00
2MASS J0042-4252	080427281	2	10.5461	-42.882	7	2.2	11.09	18.9831	52.6784	3.7336	31.77	32.19 – 33.65	12.0 – 72.00
BPM 68724	089502706	2	356.8442	-23.2882	7	0.0	11.06	18.0639	55.3590	0.4795	31.82	32.04 – 33.62	8.0 – 46.00
CD-47 277	101936401	2	13.9852	-47.1496	7	0.0	9.48	23.8251	41.9725	6.1025	32.16	32.69 – 33.51	14.0 – 52.00
2MASS J0110-4600	102071750	2	17.7113	-46.0037	12	1.0	12.01	23.0435	43.3962	1.471	31.23	32.21 – 33.30	12.0 – 70.00
G 267-100	115242300	2	6.2696	-36.7713	21	2.5	10.12	49.9955	20.0018	12.578	31.31	31.05 – 33.40	8.0 – 124.00
2MASS J0039-3816	117874959	2	9.8998	-38.2832	13	1.4	10.18	24.8503	40.2410	6.3583	31.90	32.13 – 34.46	12.0 – 214.00
AL 442	141807839	2,3	92.8752	-72.2271	22	4.5	11.19	17.5656	56.9295	0.839	31.81	32.34 – 33.83	12.0 – 96.00
2MASS J0526-6022	149175965	2	81.6294	-60.3775	7	1.5	12.27	13.7927	72.5021	0.2237	31.58	32.92 – 34.77	12.0 – 76.00
2MASS J0033-5116	156002545	2	8.3524	-51.279	3	3.4	11.44	24.1357	41.4324	0.353	31.42	33.04 – 33.95	38.0 – 144.00
Smethells 173	156084049	2	11.3681	-51.6264	1	3.0	9.85	24.2950	41.1607	5.9834	32.04	33.78	86.0
UCAC4 204-001345	158596311	2	22.1269	-49.3528	1	4.1	12.26	23.0557	43.3732	0.1546	31.14	32.57	28.0
UPM J0234-5128	166787846	2,3	38.5786	-51.4796	20	4.3	12.38	23.1685	43.1621	0.4605	31.09	31.69 – 33.56	8.0 – 82.00
EXO 0235.2-5216	166808151	3	39.2163	-52.051	5	2.0	9.91	25.7423	38.8466	0.74	31.95	33.20 – 34.77	46.0 – 222.00
CD-39 325	183596242	3	18.3674	-38.3507	9	1.0	9.79	19.9467	50.1336	0.2228	32.20	32.33 – 33.58	8.0 – 32.00
UCAC4 172-003319	197829751	2,3	54.1984	-55.751	15	3.5	11.51	33.6599	29.7089	3.0005	31.12	32.06 – 33.77	16.0 – 244.00
2MASS J0315-5342	200740049	3	48.8485	-53.715	1	5.2	13.47	20.0661	49.8353	0.5687	30.87	33.78	98.0
2MASS J0212-5851	201753428	2,3	33.2434	-58.8551	29	2.1	10.73	20.8067	48.0614	1.5902	31.84	32.60 – 34.32	8.0 – 116.00
2MASS J0215-5627	201789285	2	33.8887	-56.4549	1	6.2	14.06	22.1146	45.2190	0.1599	30.47	32.44	28.0
UCAC4 159-002053	201795667	2,3	35.215	-58.3948	43	3.2	11.25	22.7158	44.0222	1.2818	31.55	31.00 – 34.22	6.0 – 132.00
2MASS J0232-5746	201861769	2	38.0806	-57.7699	2	4.1	12.82	21.8085	45.8537	0.8615	30.97	32.65 – 33.32	26.0 – 54.00
GSC 08494-00369	201897406	2	40.3297	-57.4217	10	3.0	11.45	11.3641	87.9964	3.5089	32.09	32.82 – 35.37	12.0 – 204.00
UCAC3 73-5378	201898220	2,3	40.5177	-53.9834	13	4.3	11.89	23.3932	42.7475	0.5676	31.27	32.02 – 33.29	10.0 – 26.00

Continued on next page

Table A.1 – continued from previous page

Name	TIC ID	Sector	Ra	Dec	No. of	SpT	T_{mag}	Parallax	Distance	P_{rot}	$log(L_{star})$	$log(E_{flare})$	Duration
		(deg)	(deg)	flares			(mas)	(pc)	(days)	(erg/s)	(erg)	(minutes)	
UCAC3 73-5376	201898222	2,3	40.5094	-53.9875	11	4.3	12.64	23.6594	42.2665	0.2228	30.96	31.84 – 33.26	8.0 – 102.00
2MASS J0247-5804	201938513	2,3	41.9442	-58.0743	14	1.8	10.77	22.3695	44.7037	9.9652	31.76	32.46 – 34.23	18.0 – 268.00
WISE J0255-5702	207138379	2,3	43.8833	-57.0479	17	4.3	12.91	21.9307	45.5982	0.4932	30.92	31.87 – 33.82	8.0 – 152.00
CD-56 1032B	220433364	2,3	73.3786	-55.8584	48	4.0	9.38	90.1653	11.0907	0.8543	31.10	31.58 – 34.12	8.0 – 142.00
CD-57 1054	220473309	2,3	75.1967	-57.2567	13	0.0	8.32	37.1736	26.9008	8.6742	32.21	32.43 – 34.64	22.0 – 210.00
2MASS J0259-6120	220558700	2	44.7624	-61.3333	2	3.9	13.31	13.2576	75.4284	0.966	31.20	32.73 – 32.97	20.0 – 36.00
2MASS J0145-5230	229141941	2,3	26.3791	-52.5052	19	3.5	12.17	22.8529	43.7581	1.6351	31.21	32.18 – 34.04	12.0 – 132.00
2MASS J0146-5339	229142295	2	26.6237	-53.6596	2	4.5	11.17	57.2911	17.4547	0.4471	30.79	31.56 – 32.69	12.0 – 88.00
GSC 08044-00859	229147927	2,3	27.1712	-48.5147	28	1.5	10.54	25.5403	39.1538	4.6058	31.73	32.02 – 34.66	10.0 – 228.00
L 173-39	231017428	2,3	27.1115	-56.9783	33	2.0	9.54	47.7678	20.9346	3.6153	31.53	31.77 – 33.60	12.0 – 142.00
2MASS J0150-5844	231020638	2,3	27.738	-58.7344	22	3.0	11.11	22.0573	45.3365	1.6675	31.64	32.28 – 34.11	14.0 – 192.00
2MASS J0150-5716	231020924	2,3	27.6902	-57.2804	2	5.5	14.2	22.4107	44.6215	0.7063	30.40	33.16 – 33.58	70.0 – 104.00
BPS CS 22882-0010	246854127	2	6.3749	-28.5739	11	0.5	11.12	11.1124	89.9896	0.4594	32.21	33.03 – 35.05	14.0 – 148.00
2MASS J0028-2733	246861224	2	7.2292	-27.5592	4	4.5	12.46	17.8506	56.0205	4.1471	31.28	32.95 – 34.04	38.0 – 276.00
TYC 6994-23-1	251828744	2	6.3228	-32.7077	5	0.0	9.54	23.9076	41.8277	1.7043	32.15	32.43 – 33.51	12.0 – 88.00
GJ 2006 A	251845153	2	6.9599	-32.5519	10	4.0	10.43	28.6591	34.8929	4.9024	31.69	32.49 – 34.85	12.0 – 190.00
GR* 9	251846450	2	7.0605	-32.4657	5	5.0	11.93	28.4686	35.1264	0.5216	31.06	31.92 – 33.39	12.0 – 104.00
2MASS J0436-7851	269797536	2	69.1381	-78.8504	7	4.0	12.65	14.3695	69.5918	0.8077	31.39	32.44 – 33.61	14.0 – 62.00
UPM J0042-5444	281670243	2	10.5429	-54.7456	5	2.9	11.38	22.6146	44.2192	1.7521	31.51	32.41 – 33.56	22.0 – 60.00
UCAC2 1093148	287584993	3	124.7472	-72.6653	2	0.0	10.96	12.3669	80.8610	6.6226	32.18	33.33 – 33.87	22.0 – 46.00
RBS 1877	326446019	2	339.3131	-26.3759	23	3.5	10.74	31.5620	31.6837	0.8022	31.47	32.04 – 33.81	10.0 – 183.99
2MASS J0305-5317	339607562	2	46.274	-53.2884	10	4.7	12.98	22.5427	44.3603	0.4444	30.88	31.62 – 33.24	8.0 – 82.00
2MASS J0144-4604	401838575	2,3	26.1337	-46.0757	8	5.5	13.96	25.8925	38.6212	0.3137	30.34	31.64 – 34.09	12.0 – 242.01

Continued on next page

Table A.1 – continued from previous page

Name	TIC ID	Sector	Ra	Dec	No. of	SpT	T_{mag}	Parallax	Distance	P_{rot}	$log(L_{star})$	$log(E_{flare})$	Duration
		(deg)	(deg)	flares			(mas)	(pc)	(days)	(erg/s)	(erg)	(minutes)	
GR* 239	434106919	2	354.4557	-12.8625	1	2.5	11.68	17.9161	55.8157	6.7665	31.58	33.03	32.0
LP 764-40 B	441056236	2	359.5583	-17.4097	34	1.0	9.7	29.9438	33.3959	0.4344	31.76	31.73 – 33.79	6.0 – 114.00
UCAC4 420-002082	010863087	3	25.9384	-6.0447	18	3.5	10.36	46.8488	21.3453	0.862	31.28	31.56 – 33.91	10.0 – 90.00
2MASS 0122-2439 b	011614485	3	20.7129	-24.6647	8	3.5	11.58	29.5326	33.8609	1.4925	31.2	31.93 – 33.67	12.0 – 108.00
Barta 161 12	029853348	3	23.8085	-7.2145	6	4.3	10.59	26.8241	37.2799	0.7033	31.64	32.43 – 33.80	18.0 – 90.00
G 271-110	029855342	3	24.2308	-6.7944	9	3.5	11.31	41.7150	23.9722	1.061	30.97	32.11 – 34.51	8.0 – 204.00
2MASS J0156-2615	033625362	3	29.0863	-26.2558	2	0.0	10.66	12.5913	79.4199	6.535	32.29	32.72 – 33.89	12.0 – 60.00
LP 705-28	040047077	3	6.463	-9.9619	5	3.0	11.34	30.7317	32.5397	0.8856	31.24	32.62 – 33.60	22.0 – 120.00
UCAC4 329-000876	043451426	3	11.3504	-24.288	6	3.0	13.85	29.1234	34.3367	1.6582	30.37	31.97 – 32.90	18.0 – 48.00
LP 768-113	054003038	3	23.4919	-17.641	2	3.5	10.38	67.9564	14.7153	5.079	30.93	31.80 – 33.21	26.0 – 114.00
2MASS 0219-3925 b	077111651	3	34.8421	-39.4229	2	6.0	13.49	24.9441	40.0896	1.6266	30.62	32.49 – 33.74	20.0 – 106.00
PM J01538-1459A	092993104	3	28.4626	-14.9977	39	3.0	9.45	29.5489	33.8422	2.977	31.87	29.78 – 34.03	6.0 – 156.00
WISE J0241-3049	122608433	3	40.364	-30.8209	5	4.3	12.88	22.2480	44.9479	0.5241	30.9	31.86 – 33.17	12.0 – 74.00
UCAC3 112-6119	122671519	3	42.2198	-34.0737	16	4.0	10.9	23.8067	42.0050	0.4523	31.66	32.35 – 33.87	12.0 – 96.00
G 269-153B	140478471	3	21.1168	-33.9195	14	4.3	10.67	39.7772	25.1400	0.7751	31.22	31.93 – 32.78	12.0 – 64.00
2MASS J0249-4416	146636926	3	42.3396	-44.268	11	3.0	11.43	31.4374	31.8092	2.3871	31.2	31.81 – 33.91	12.0 – 124.00
2MASS J0305-3725	165124012	3	46.2907	-37.4183	8	1.9	10.48	5.46590	182.952	2.988	32.9	33.49 – 34.68	12.0 – 78.00
WISE J0308-3844	165162811	3	47.1651	-38.7434	3	4.3	13.0	17.7221	56.4267	0.689	31.07	32.13 – 33.36	8.0 – 60.00
UCAC3 92-4597	165941376	3	31.7579	-44.1105	6	3.5	10.8	23.3925	42.7487	0.3928	31.71	32.16 – 33.39	12.0 – 76.00
LP 767-17	167457891	3	17.6234	-15.1686	8	4.0	11.54	22.9845	43.5076	4.6964	31.35	32.39 – 33.29	14.0 – 84.00
2MASS J0332-5139	200806186	3	53.0149	-51.6652	4	2.0	11.46	13.0328	76.7295	5.467	31.84	32.86 – 33.99	20.0 – 130.00
WISE J0351-5154	206478549	3	57.8459	-51.9162	5	4.0	12.38	17.4122	57.4310	0.4246	31.34	32.34 – 33.03	14.0 – 28.00
GSC 04683-02117	248354845	3	17.8474	-5.4273	33	3.5	11.08	27.2635	36.6791	0.5218	31.47	31.16 – 34.43	6.0 – 214.00

Continued on next page

Table A.1 – continued from previous page

Name	TIC ID	Sector	Ra	Dec	No. of	SpT	T_{mag}	Parallax	Distance	P_{rot}	$log(L_{star})$	$log(E_{flare})$	Duration
		(deg)	(deg)	flares			(mas)	(pc)	(days)	(erg/s)	(erg)	(minutes)	
LP 647-46	248945338	3	20.272	-4.0357	7	0.0	10.85	10.9178	91.5935	0.5785	32.34	33.20 – 33.92	18.0 – 64.00
2MASS J0447-5134	259542669	3	71.7522	-51.5778	7	1.9	11.52	17.0613	58.6122	6.1974	31.68	32.45 – 34.16	18.0 – 184.00
2MASS J0207-1810	268765554	3	31.7834	-18.1694	9	4.0	12.57	22.3261	44.7906	0.2387	31.09	31.93 – 34.61	8.0 – 172.00
UCAC4 334-002479	268862481	3	34.2287	-23.3704	6	3.5	11.13	13.7216	72.8778	1.5547	31.95	32.92 – 34.64	14.0 – 224.00
L 34-26	272232401	3	117.3005	-76.7028	26	3.0	8.92	91.8291	10.8898	2.833	31.18	31.31 – 33.26	12.0 – 168.00
2MASS J0129-0823	299178185	3	22.4279	-8.3998	7	5.0	12.63	27.2344	36.7183	0.3115	30.83	31.94 – 33.15	12.0 – 76.00
PS78 99	326104737	3	15.9748	-28.0978	2	4.5	13.22	18.9451	52.7841	1.381	30.88	32.95 – 33.04	26.0 – 50.00
2MASS J0516-5410	382043650	3	79.1914	-54.1712	2	3.0	11.91	13.6053	73.5008	6.1785	31.73	32.97 – 33.71	32.0 – 66.00
UCAC4 149-002104	382552502	3	35.6854	-60.38	12	4.0	10.59	35.4382	28.2181	1.1546	31.41	32.08 – 34.16	12.0 – 232.00
2MASS J0424-5512	396731889	3	66.0043	-55.2061	8	2.5	11.25	13.1037	76.3143	5.8911	32.04	32.63 – 34.07	12.0 – 84.00
LP 586-73	398569617	3	15.0924	-1.4021	2	2.0	11.77	11.3719	87.9361	3.0182	31.93	32.79 – 34.61	14.0 – 104.00
GaiaDR2 2417003566064655	406351523	3	5.1769	-14.1154	4	2.0	11.31	18.8535	53.0405	0.8583	31.65	32.63 – 33.08	12.0 – 52.00

Table A.2: The stellar properties of all solar-type stars in the study from Chapter 6 detailing the rotation periods, quiescent luminosity, energy range and duration range of the flares.

Name	TIC ID	Sector	Ra	Dec	No. of	SpT	T_{mag}	Parallax	Distance	P_{rot}	$log(L_{star})$	$log(E_{flare})$	Duration
		(deg)	(deg)	flares			(mas)	(pc)	(days)	(erg/s)	(erg)	(minutes)	
CD-5210232	161172848	1	339.8765	-52.0882	2	K0	10.03	9.4283	106.063	4.25170	32.82	33.80 – 34.26	34.00 – 70.00
HD205297	403121294	1	324.3149	-65.0393	11	G6	8.27	13.642	73.3003	1.52470	33.05	33.09 – 34.44	12.00 – 102.00
HD49855	176873028	1,2,4	100.9428	-71.9762	12	G6	8.39	17.989	55.5871	3.85670	32.78	31.73 – 34.10	8.00 – 52.00
HD42270	261236136	1,12,13	88.3725	-81.9478	19	K0	8.28	16.965	58.9431	1.88070	32.82	32.82 – 35.06	8.00 – 232.00
HD47875	167344043	all minus 11	98.6712	-69.8849	179	G4	8.50	13.893	71.9756	2.99380	33.00	32.74 – 34.74	8.00 – 184.00
HD987	266997586	1,13	3.4725	-74.6886	10	G8	8.07	21.811	45.8470	3.60860	32.70	32.74 – 33.98	14.00 – 96.00
V*VZHor	220536421	1,2,3	42.9723	-61.6173	48	K1	7.89	24.921	40.1263	2.57500	32.48	32.33 – 34.65	12.00 – 174.00
V*CSGru	278634010	1	333.8974	-39.0143	20	K0	8.43	18.595	53.7770	3.35710	32.82	32.79 – 35.00	14.00 – 284.00
HD32195	319289907	1	72.0231	-80.7790	7	F7	7.85	15.927	62.7857	1.23136	33.02	32.80 – 33.81	12.00 – 42.00
HD46920	167247077	1,5,7	97.6388	-67.6025	11	G3	8.50	13.893	71.9756	3.66670	33.02	33.13 – 34.02	14.00 – 54.00
HD202917	079403675	1	320.2084	-53.0347	9	G7	7.99	21.345	46.8489	3.38290	32.56	32.94 – 34.61	24.00 – 275.99
HD211862	270356871	1	335.1712	-28.2328	4	G1	8.54	7.0541	141.761	1.19460	33.61	34.53 – 35.59	58.00 – 168.00
CPD-571131	279614617	1	106.3013	-57.5706	2	G8	9.12	3.5490	281.769	7.37670	33.98	35.19 – 35.46	84.00 – 108.00
HD269406	179369970	1	79.9842	-71.4854	1	G5	8.90	3.9785	251.351	2.86130	33.98	35.15	64.00
CD-7776	050345701	1,13	32.3507	-76.6876	11	K1	8.99	11.405	87.6755	5.27750	33.06	33.38 – 34.95	18.00 – 160.00
HD39150	364588501	all	85.4033	-76.0723	207	G6	9.14	9.0342	110.690	2.28000	33.16	33.07 – 35.29	8.00 – 220.00
HD269921	404768019	1,2	84.6440	-68.8850	8	G7	9.50	10.653	93.8667	0.72162	32.89	33.26 – 35.17	12.00 – 174.00
CD4014901	214772274	1	341.6400	-39.4792	3	G5	8.81	13.198	75.7685	3.19250	32.97	33.89 – 34.29	50.00 – 98.00
CD-63408	309714906	1,10,11	126.0248	-63.5672	9	G5	9.19	10.027	99.7258	0.79029	33.06	33.52 – 34.67	22.00 – 96.00
HD223728	009708387	2	358.0430	-11.7210	4	G1	8.08	11.840	84.4552	2.36540	33.25	32.99 – 34.74	8.00 – 118.00
CD-3019800	012359079	2	0.8360	-29.8230	1	F8	10.76	4.2171	237.129	2.64560	33.23	34.37	38.00
V*VZRet	031850842	2	52.1536	-66.9201	2	G8	10.11	7.2042	138.807	2.31970	33.02	33.19 – 34.58	8.00 – 46.00

Continued on next page

Table A.2 – continued from previous page

Name	TIC ID	Sector	Ra	Dec	No. of	SpT	T_{mag}	Parallax	Distance	P_{rot}	$log(L_{star})$	$log(E_{flare})$	Duration
		(deg)	(deg)	flares			(mas)	(pc)	(days)	(erg/s)	(erg)	(minutes)	
V*CCPhe	149248196	2	22.0371	-52.6389	16	K1	8.27	65.319	15.3093	0.51423	31.73	31.32 – 33.18	4.00 – 54.00
HD44920	150299548	2,4,5	95.0966	-61.5987	11	F7	8.84	9.2923	107.616	1.06210	33.25	32.91 – 34.77	8.00 – 90.00
V*CCPhe	158595208	2	22.0371	-52.6389	14	K1	8.27	25.098	39.8438	6.47300	32.56	32.43 – 34.85	12.00 – 216.00
HD218203	204322922	2	346.6068	-23.1674	2	G5	9.38	10.356	96.5605	5.29210	32.99	33.18 – 34.06	12.00 – 38.00
HD8558	206592394	2	20.8395	-57.4809	21	G7	7.86	22.068	45.3145	3.36480	32.64	32.35 – 34.27	10.00 – 96.00
BD-166129	240764987	2	340.1419	-15.7894	2	K2	10.21	4.7902	208.759	1.02727	33.32	34.29 – 35.63	18.00 – 86.00
CD-571654	294098955	2,3,13	107.7109	-57.6128	10	G2	9.94	6.9925	143.010	1.52820	33.10	33.53 – 34.66	14.00 – 90.00
HD217344	229066844	2	345.1177	-33.7459	3	G4	7.75	11.972	83.5240	1.62240	33.31	34.98 – 36.26	84.00 – 276.00
HD71864	307490251	2,9	126.1584	-70.1596	4	G2	8.86	10.298	97.1006	0.76700	33.16	33.73 – 34.78	32.00 – 88.00
CD-50245	322051377	2	13.8558	-49.9491	2	G9	9.37	12.935	77.3084	2.58333	32.78	33.40 – 34.39	26.00 – 124.00
GSC08912-01753	348898049	2	106.0602	-62.9025	7	K2	10.64	8.5281	117.259	1.00030	32.64	32.86 – 33.74	8.00 – 40.00
HD48189A	375034557	2	99.5010	-61.5330	7	G0	6.48	47.806	20.9177	3.26030	32.03	31.73 – 33.02	12.00 – 94.00
HD10922	401840741	2	26.5340	-46.9481	8	G9	8.58	12.892	77.5657	1.25680	32.97	32.74 – 34.98	8.00 – 136.00
HD215964	419010038	2	342.3162	-20.9784	4	G3	9.06	9.6872	103.229	2.95120	33.17	33.50 – 34.34	18.00 – 66.00
HD221224	434096244	2	352.5323	-17.2842	8	G5	9.59	10.941	91.3977	1.58730	32.86	33.31 – 35.41	18.00 – 174.00
HD224374	441054134	2	359.3468	-16.0956	2	G0	8.83	7.9618	125.599	3.99250	33.45	33.64 – 34.71	18.00 – 86.00
BD-12243	010802452	3	20.1351	-11.4684	3	G9	7.69	28.302	35.3321	5.96039	32.44	32.77 – 33.17	38.00 – 58.00
HD26864	152504097	3	63.1825	-47.5656	1	G3	8.11	16.478	60.6851	10.13283	32.90	33.48	52.00
CD-481289	152589104	3,5	64.8087	-47.8534	13	K0	9.53	12.776	78.2711	1.54700	32.71	32.82 – 34.64	14.00 – 122.00
CD-421064	153046829	3	49.1878	-42.5256	4	G7	8.58	12.512	79.9194	3.75288	33.14	33.40 – 34.20	18.00 – 84.00
CD-371123	175491080	3,4	45.1952	-37.1338	31	G9	9.77	10.184	98.1884	3.97364	32.84	32.82 – 35.09	6.00 – 168.00
TYC8511-2197-1	219389540	3,4,5,6,13	77.0287	-53.2711	28	G3	10.18	6.3930	156.421	1.54700	33.09	33.42 – 34.86	12.00 – 70.00
HD13183	219998026	3	31.8260	-53.1991	18	G7	8.00	20.187	49.5349	2.33540	32.82	32.44 – 34.90	8.00 – 174.00

Continued on next page

Table A.2 – continued from previous page

Name	TIC ID	Sector (deg)	Ra (deg)	Dec flares	No. of	SpT	T_{mag} (mas)	Parallax (pc)	Distance (days)	P_{rot} (erg/s)	$log(L_{star})$ (erg)	$log(E_{flare})$ (minutes)	Duration
CD-601850	281582156	3,8,9,10,11,13	115.9286	-61.1213	41	K0	9.95	10.038	99.6165	2.30289	32.79	32.92 – 34.97	8.00 – 148.00
CD-55899	293166952	3,4,5,9	66.6895	-55.3708	14	K1	9.54	9.2338	108.297	3.75287	33.00	33.04 – 34.83	12.00 – 144.00
CD-571709	339668420	3,6,9,13	110.3488	-57.3435	22	K0	9.85	9.2531	108.071	4.60582	32.89	33.08 – 35.17	12.00 – 302.00
V*XZPic	350520348	3,10	86.3056	-59.9232	23	K0	8.37	20.889	47.8721	1.89370	32.65	32.38 – 34.39	6.00 – 130.00
HD15045	001114345	4	36.2987	-10.4737	4	G5	8.34	15.234	65.6392	6.48254	32.97	32.69 – 33.60	8.00 – 38.00
HD32372	013955147	4	75.2163	-41.0184	6	G5	8.71	12.825	77.9672	2.29540	32.96	32.71 – 33.87	12.00 – 54.00
GSC05289-01010	036828969	4	42.0924	-11.2867	3	G7	10.73	4.1612	240.315	1.00896	33.24	34.11 – 35.41	20.00 – 174.00
CD-261578	044797824	4	62.4543	-26.0221	4	K0	9.77	7.3229	136.557	1.49898	33.15	33.75 – 34.63	22.00 – 106.00
CD-27963	065416676	4	41.1103	-26.9978	1	G7	10.32	6.5182	153.416	0.63874	33.03	35.26	134.00
HD31026	077371445	4,5	72.6480	-41.0471	23	G9	8.14	19.675	50.8239	4.80332	32.75	32.57 – 35.31	12.00 – 358.00
CD-251599	089187590	4	57.5754	-24.8096	7	K0	10.06	8.6082	116.168	1.08959	32.86	33.18 – 34.51	12.00 – 66.00
HD22213	093122097	4	53.5685	-12.0689	7	G8	8.02	19.392	51.5671	1.39428	32.99	33.12 – 34.03	18.00 – 84.00
HD23208	121011020	4	55.6659	-20.5454	9	G8	8.39	17.606	56.7966	4.15212	32.92	32.83 – 35.02	12.00 – 90.00
CD-35926	122576779	4	40.3086	-35.4194	1	F8	9.73	6.0561	165.122	6.17415	33.32	34.36	40.00
CD-361309	142889317	4	52.0312	-35.9121	4	F8	8.81	9.5960	104.210	1.20055	33.17	34.10 – 34.46	58.00 – 108.00
CD-371224	159923666	4	49.0130	-37.4229	3	G8	9.29	10.091	99.0943	2.75869	33.02	33.27 – 34.87	14.00 – 82.00
HD24329	166791648	4	57.7131	-34.7995	3	G8	8.63	11.812	84.6568	5.08471	33.00	33.88 – 34.31	68.00 – 90.00
HD25156	166874846	4,5	59.6637	-31.5953	18	G0	8.77	15.294	65.3821	1.27745	32.84	32.71 – 34.64	8.00 – 142.00
CD-311688	168696027	4	61.4675	-31.6439	5	G6	9.33	8.2426	121.320	2.02595	33.16	33.47 – 35.11	22.00 – 148.00
HD17781	274000285	4	42.6701	-21.5519	2	G3	9.01	13.195	75.7857	5.08491	32.89	33.50 – 34.05	28.00 – 72.00
HD55279	278024057	4,7,10,11,12,13	105.1270	-79.6958	31	K2	9.10	15.674	63.7999	5.08462	32.66	32.70 – 34.64	10.00 – 154.00
HD19491	299886628	4	46.5230	-48.7968	2	F7	7.67	14.310	69.8768	2.48360	33.23	33.57 – 34.34	34.00 – 72.00
V*FQCet	302384263	4	33.0789	-13.5121	1	K1	9.64	12.228	81.7742	7.00811	32.73	34.33	34.00

Continued on next page

Table A.2 – continued from previous page

Name	TIC ID	Sector	Ra	Dec	No. of	SpT	T_{mag}	Parallax	Distance	P_{rot}	$log(L_{star})$	$log(E_{flare})$	Duration
		(deg)	(deg)	flares			(mas)	(pc)	(days)	(erg/s)	(erg)	(minutes)	
CD-371559	321100884	4	60.1266	-37.3824	2	F8	10.09	4.8887	204.553	1.07180	33.37	34.51 – 34.73	46.00 – 52.00
HD26980	007586485	5	63.5943	-38.3171	14	G3	8.49	12.542	79.7315	1.76509	33.13	33.12 – 34.48	14.00 – 110.00
HD30689	009293388	5	72.3599	-10.5925	1	F8	8.56	10.759	92.9446	5.64072	33.18	34.47	68.00
V*TYCol	020096356	5,6	89.4617	-38.0677	48	G6	8.89	13.882	72.0316	0.78629	32.97	32.78 – 35.18	8.00 – 286.01
CD-382198	021540586	5,6	86.3177	-38.6136	14	G9	10.24	5.8574	170.724	1.35144	33.13	33.84 – 35.75	22.00 – 188.00
HD39012	021626512	5	86.9560	-40.0633	3	G7	8.06	21.216	47.1333	4.18509	32.80	32.75 – 33.91	14.00 – 64.00
CD-292164	030946945	5	79.4708	-29.5753	3	K1	10.22	6.0715	164.703	1.78948	33.09	33.40 – 35.12	12.00 – 120.00
CD-332281	078055898	5,6	80.4462	-33.1345	19	K0	9.50	8.3331	120.003	4.11864	33.12	33.18 – 34.90	12.00 – 148.00
V*AGLep	092845906	5	82.5796	-19.2755	21	G5	8.92	8.8455	113.051	2.09255	33.32	33.51 – 35.11	20.00 – 114.00
HD34866	139396805	5	79.9056	-22.2495	3	G6	8.59	12.403	80.6257	2.47119	33.13	33.46 – 34.10	28.00 – 62.00
V*ATCol	144499196	5	84.2723	-39.5407	9	K1	8.67	12.818	78.0141	2.51917	33.02	33.29 – 34.89	20.00 – 164.00
HD27679	152370762	5	65.2932	-24.5393	5	G2	8.76	11.794	84.7853	1.30387	33.01	33.64 – 34.70	28.00 – 130.00
CD-441568	153797977	5	66.8357	-44.3442	3	K1	9.88	11.324	88.3033	3.99183	32.71	32.83 – 34.83	8.00 – 158.00
HD272836	259645014	5,6	73.2719	-48.7440	9	K2	9.66	11.849	84.3910	4.47363	32.76	33.12 – 34.23	14.00 – 126.00
HD44627	260351540	5,6,7,8,11,12	94.8040	-58.0541	48	K1	8.27	19.952	50.1200	3.87276	32.71	32.79 – 35.53	12.00 – 306.00
HD275012	290717316	5,6	84.3353	-48.5864	11	G5	10.54	7.5514	132.425	1.66329	32.79	33.37 – 35.12	14.00 – 190.00
BD-171085	442868242	5	79.8508	-17.7484	7	K0	8.59	16.709	59.8469	3.24345	32.78	32.69 – 34.02	12.00 – 82.00
HD274263	453856222	5	82.8350	-42.8454	4	G0	10.10	6.2087	161.064	2.10955	33.14	33.67 – 34.59	18.00 – 64.00
HD274576	007491381	6	82.2140	-46.4719	5	G6	9.92	7.6517	130.689	2.19919	33.01	33.90 – 34.81	22.00 – 174.00
CD-333188	052641430	6	101.1104	-33.9805	3	G2	8.94	9.0204	110.859	1.66202	33.27	33.83 – 34.32	22.00 – 48.00
HD295290	053417036	6	100.0932	-3.5333	16	G0	8.19	16.434	60.8472	1.56450	32.93	33.23 – 35.22	18.00 – 152.00
V*AILep	093126844	6	85.0865	-19.6697	8	G2	8.44	13.672	73.1390	1.68774	33.03	33.36 – 34.72	26.00 – 152.00
CD-402458	119289797	6,7	96.5288	-41.0482	9	K0	9.28	10.082	99.1818	4.10799	33.04	33.48 – 35.13	20.00 – 158.00

Continued on next page

Table A.2 – continued from previous page

Name	TIC ID	Sector	Ra	Dec	No. of	SpT	T_{mag}	Parallax	Distance	P_{rot}	$log(L_{star})$	$log(E_{flare})$	Duration
		(deg)	(deg)	flares			(mas)	(pc)	(days)	(erg/s)	(erg)	(minutes)	
HD46670	141977935	6	96.3874	-76.4264	1	G5	9.52	9.0618	110.353	9.46622	33.07	33.82	38.00
TYC7066-1037-1	143141922	6	89.5492	-35.0137	5	G9	10.50	7.3448	136.150	2.44630	32.83	33.08 – 35.01	8.00 – 208.00
CD-37984	148002142	6	99.9449	-37.8361	8	K1	9.99	9.9577	100.424	4.14250	32.79	33.04 – 34.03	12.00 – 60.00
TYC7627-2190-1	148091129	6,7	100.3270	-38.3434	9	K2	10.39	8.5322	117.203	0.72818	32.77	33.32 – 34.83	16.00 – 124.00
CD-283484	173088921	6	102.4391	-28.9880	4	G7	9.86	7.0118	142.616	4.18702	33.12	33.60 – 35.45	16.00 – 186.00
CD-442217	235073057	6	86.0327	-44.7926	2	K1	10.70	3.8597	259.087	3.51162	33.31	34.27 – 34.61	38.00 – 48.00
CD-521641	319466859	6,12	100.3021	-52.1273	9	K0	9.88	9.7491	102.573	3.35240	32.82	32.82 – 34.66	8.00 – 54.00
HD37551	354571604	6	84.3039	-42.7155	9	G7	8.85	12.471	80.1815	4.35440	32.98	33.23 – 33.89	18.00 – 40.00
HD62237	094515514	7	115.6107	-16.2835	10	G6	8.93	8.0146	124.772	1.31474	33.36	33.44 – 34.56	12.00 – 66.00
HD51797	130297425	7	104.0981	-46.7818	4	K0	8.90	10.454	95.6489	4.52854	33.05	33.54 – 34.82	28.00 – 154.00
HD271037	140891597	7	76.7105	-72.3531	3	K0	10.12	6.9180	144.550	0.23559	33.06	34.02 – 35.72	12.00 – 82.00
HD47582	156920968	7	99.2843	-45.5908	6	G0	9.03	9.7585	102.474	2.22309	33.12	33.46 – 34.45	20.00 – 60.00
TYC8557-1251-1	260848905	7,8,9	118.8818	-54.6140	4	G9	10.62	7.9038	126.521	2.65811	32.72	34.07 – 34.77	34.00 – 132.00
CD-521363	270677813	7	87.7549	-52.6368	1	G9	9.79	7.4602	134.045	1.20462	33.12	35.69	184.00
TYC8549-141-1	279570232	7	105.9600	-58.4573	2	G9	10.95	4.6574	214.713	1.12176	33.06	34.28 – 35.60	48.00 – 122.00
CD-482844	355359026	7	109.4323	-48.4860	2	G0	9.56	6.8847	145.249	2.05498	33.29	34.27 – 34.29	40.00 – 46.00
BD-012318	078234015	8	148.6296	-1.7643	12	G0	9.03	7.6399	130.891	2.21649	33.30	33.52 – 35.56	12.00 – 160.00
CPD-541712	118541883	8,10	129.2956	-55.3028	12	G9	10.40	6.6159	151.150	2.61735	32.97	33.10 – 35.07	8.00 – 184.00
CD-423328	123029030	8	113.3382	-42.9284	5	K1	10.63	7.1379	140.097	0.94990	32.81	33.65 – 34.93	20.00 – 172.00
HD48139	142087340	8	98.4252	-74.7009	1	K1	9.23	11.165	89.5600	4.73137	32.95	33.97	32.00
BD-032892	143400356	8	154.8007	-4.0789	1	K2	8.94	14.258	70.1321	6.15083	32.92	34.00	64.00
CD-541693	294157702	8	108.0720	-54.7693	3	G8	9.77	10.093	99.0717	2.38861	32.86	33.21 – 34.36	14.00 – 64.00
TYC8570-1980-1	342169848	8,9	122.7889	-55.9322	14	G8	10.57	7.0611	141.620	2.46030	32.84	33.26 – 34.76	8.00 – 72.00

Continued on next page

Table A.2 – continued from previous page

Name	TIC ID	Sector (deg)	Ra (deg)	Dec flares	No. of	SpT	T_{mag} (mas)	Parallax (pc)	Distance (days)	P_{rot} (erg/s)	$log(L_{star})$ (erg)	$log(E_{flare})$ (minutes)	Duration
CPD-551885	383664368	8,9,10	135.0141	-55.6400	18	G5	10.13	7.1017	140.811	0.93549	33.03	33.23 – 35.44	8.00 – 156.00
HD77883	401683991	8,9	135.8518	-48.6880	8	G0	8.50	10.189	98.1374	2.27807	32.95	33.16 – 34.21	18.00 – 82.00
HD83988	409973553	8	145.3938	-17.8867	7	K0	8.22	12.880	77.6361	1.00832	33.01	33.17 – 34.86	16.00 – 110.00
CD-287670	022011809	9	147.6530	-29.5578	7	K2	10.42	8.2598	121.069	1.03950	32.80	33.03 – 33.97	8.00 – 74.00
BD-042994	047425894	9	164.9403	-5.3703	5	K1	9.72	10.845	92.2058	5.60462	32.82	33.17 – 34.23	12.00 – 58.00
HD297669	132965136	9	149.2058	-49.3719	7	G7	9.82	7.6077	131.445	0.74195	33.08	33.92 – 35.06	28.00 – 102.00
HD297762	138700126	9	151.3481	-48.9887	4	K0	9.57	12.026	83.1497	11.16298	32.78	33.15 – 33.89	18.00 – 70.00
CD-386968	151737954	9,10	167.4166	-39.1131	24	G3	9.33	8.3258	120.108	1.07342	33.21	33.04 – 34.67	8.00 – 66.00
CD-66395	167123841	9	96.3016	-66.4861	3	K0	10.08	7.3391	136.256	0.27057	33.02	34.26 – 35.09	26.00 – 72.00
CD-287948	168067848	9	152.5082	-29.0583	5	K2	9.10	12.014	83.2300	1.07184	32.98	33.12 – 35.35	12.00 – 160.00
BD-193018	294257082	9	156.9052	-20.4531	4	K0	9.20	15.800	63.2879	4.07436	32.70	33.20 – 35.09	20.00 – 156.00
BD-133153	296862547	9	158.5020	-13.9039	1	G6	10.07	8.5779	116.578	8.90320	32.89	34.22	46.00
CPD-522481	298690606	9,10	143.1086	-52.6276	29	G8	10.16	7.5620	132.240	1.91863	33.09	33.36 – 35.26	8.00 – 110.00
CPD-69912	307490261	9	126.7141	-70.1668	3	K0	9.90	9.8514	101.508	0.76819	32.83	34.36 – 35.52	54.00 – 136.00
CD-248341	315095307	9	145.2244	-24.9683	7	K0	9.99	10.525	95.0038	2.04374	32.75	33.02 – 34.82	8.00 – 124.00
HD309751	360709162	9,10	142.9363	-65.2479	5	G3	9.46	7.1288	140.276	2.70900	33.28	34.13 – 34.86	26.00 – 106.00
HD70614	364425576	9	69.5673	-72.3700	1	G0	9.13	8.6724	115.307	1.91327	33.25	34.80	70.00
TYC8590-1193-1	383134735	9,10	134.1312	-57.0112	11	K0	11.06	6.3409	157.707	4.51493	32.76	33.60 – 35.27	14.00 – 192.00
CD-494008	400598180	9	134.4671	-49.6973	4	G9	9.73	7.9022	126.547	2.02249	33.19	33.53 – 35.34	20.00 – 146.00
CD-427422	021827610	10	181.6368	-42.7975	15	K0	9.88	9.3091	107.421	2.01540	32.87	33.07 – 34.79	12.00 – 130.00
CD-426814	162091088	10	168.2007	-42.6871	10	G9	8.92	16.311	61.3083	0.55942	32.75	33.17 – 34.85	8.00 – 92.00
HD49078B	167524561	10	100.5282	-64.5246	3	K0	10.28	8.1150	123.228	0.41113	32.77	34.20 – 35.17	18.00 – 134.00
CD-407581	178725301	10	194.0509	-41.3722	1	K2	10.58	7.3079	136.838	4.63048	32.78	34.64	86.00

Continued on next page

Table A.2 – continued from previous page

Name	TIC ID	Sector	Ra	Dec	No. of	SpT	T_{mag}	Parallax	Distance	P_{rot}	$log(L_{star})$	$log(E_{flare})$	Duration
		(deg)	(deg)	flares			(mas)	(pc)	(days)	(erg/s)	(erg)	(minutes)	
CPD-535235	273817886	10	189.2453	-54.2050	3	K0	9.51	8.5173	117.408	2.46519	33.09	33.11 – 34.88	8.00 – 154.00
2MASSJ0850-7554	282051790	10,11	132.5222	-75.9104	8	G9	9.86	9.7257	102.820	1.15305	32.86	33.46 – 34.93	14.00 – 110.00
TYC8984-2245-1	295777692	10,11	171.9802	-66.4346	6	K1	9.85	9.1115	109.751	2.76320	32.88	33.13 – 35.39	12.00 – 280.00
CPD-494947	334300225	10	183.0463	-49.8357	2	K2	10.34	7.7910	128.353	3.80981	32.83	33.87 – 34.78	32.00 – 110.00
CD-506815	334684206	10	183.6418	-51.1702	5	G9	9.53	8.4191	118.777	3.64417	33.05	33.98 – 35.56	32.00 – 214.00
CD-612010	355235442	10,11	130.5019	-62.3073	6	K0	10.10	7.8761	126.966	1.22680	32.94	32.48 – 35.46	14.00 – 164.00
V*V479Car	359740883	10	140.8954	-61.1932	4	K1	9.19	10.308	97.0111	3.88801	33.06	34.07 – 35.75	54.00 – 276.00
RXJ0523.2-5751	382157212	10	80.8149	-57.8495	1	K2	10.82	5.6694	176.385	0.84029	32.92	34.49	58.00
CD-542644	385626253	10	138.3202	-55.4842	3	G5	9.56	7.5765	131.987	0.75664	33.15	34.03 – 34.49	34.00 – 58.00
CD-554499	390229592	10	183.7176	-55.7844	1	G9	8.87	8.6815	115.187	1.69898	33.31	36.00	206.00
CD-69783	398085117	10,11	160.3454	-69.6786	12	G8	9.51	10.567	94.6333	1.66888	32.93	33.48 – 35.00	20.00 – 108.00
CPD-681388	399639698	10	164.4552	-69.2333	3	K1	9.31	8.5919	116.388	3.55809	33.16	34.10 – 35.30	48.00 – 190.00
CD-574328	433448211	10	182.8806	-58.2815	6	G9	9.37	9.1014	109.873	2.56581	33.12	33.67 – 35.12	20.00 – 204.00
HD110817	449355457	10,11	191.2779	-47.7162	5	K1	9.38	8.3654	119.540	3.16514	33.15	33.56 – 35.52	22.00 – 257.99
V*V570Car	465075473	10,11	162.4514	-64.7745	6	G9	10.77	6.5122	153.557	1.21373	32.80	33.86 – 35.13	26.00 – 178.00
2MASSJ1530-3022	054810190	11	232.6995	-30.3683	4	K2	10.36	8.7401	114.415	3.27936	32.70	33.68 – 34.94	20.00 – 90.00
V*LTLup	076652075	11	228.9389	-33.5334	2	K0	9.79	8.5707	116.676	2.27993	32.96	33.84 – 34.46	32.00 – 72.00
CD-469327	127089264	11	216.7730	-47.2395	5	G9	9.80	8.3031	120.436	4.07489	33.00	32.55 – 34.58	12.00 – 84.00
HD126670	127249954	11	217.0386	-44.2383	4	G8	9.03	8.3430	119.861	5.44068	33.29	33.34 – 35.20	20.00 – 168.00
CD-439198	128414141	11	219.3354	-44.1684	4	G8	9.17	11.353	88.0793	0.73208	32.99	33.19 – 35.05	12.00 – 142.00
V*LYLup	148158169	11	229.8165	-40.9356	4	K0	10.32	7.5000	133.333	2.81639	32.90	33.38 – 34.97	12.00 – 114.00
HD133938	160701354	11	227.1603	-44.0146	5	G6	9.62	6.0880	164.257	1.01438	33.34	33.97 – 35.11	26.00 – 84.00
HD125328	179951420	11	214.9650	-41.0501	2	G3	9.53	8.8325	113.218	1.37580	33.06	34.07 – 34.39	42.00 – 52.00

Continued on next page

Table A.2 – continued from previous page

Name	TIC ID	Sector	Ra	Dec	No. of	SpT	T_{mag}	Parallax	Distance	P_{rot}	$log(L_{star})$	$log(E_{flare})$	Duration
		(deg)	(deg)	flares			(mas)	(pc)	(days)	(erg/s)	(erg)	(minutes)	
HD136122	225707690	11	229.9515	-28.7459	2	G2	9.16	11.548	86.5906	5.31983	32.90	33.97 – 34.32	58.00 – 60.00
CD-478710	241739877	11	208.6751	-48.3495	9	K2	10.05	8.8269	113.290	3.53553	32.84	33.48 – 35.33	18.00 – 232.00
HD120395	243662768	11	207.5315	-44.8513	1	G0	7.63	18.280	54.7037	1.63547	33.07	33.61	28.00
CD-517268	244882956	11	196.6669	-51.9942	10	K1	9.64	8.6378	115.770	7.28528	33.01	33.47 – 34.06	20.00 – 54.00
CD-458100	248129790	11	193.6307	-46.1268	3	G0	9.05	7.4902	133.507	1.04984	33.37	33.67 – 35.42	18.00 – 186.00
CD-517878	261389834	11	209.8074	-51.8776	3	G0	8.94	8.3318	120.022	4.07487	33.33	33.94 – 35.06	26.00 – 102.00
V*KNLup	272456799	11	229.9854	-30.1071	8	G0	8.40	9.7792	102.257	2.17630	33.29	33.61 – 34.95	22.00 – 120.00
V*AFCru	309528896	11	184.7782	-63.1650	5	G9	8.94	15.086	66.2853	1.89303	33.09	33.34 – 33.86	12.00 – 22.00
CD-498410	312617539	11	210.8953	-50.1780	3	K0	9.38	10.291	97.1647	4.14512	32.96	33.31 – 35.17	12.00 – 170.00
CD-691055	335376063	11,12	194.6060	-70.4804	12	K0	8.95	10.548	94.7984	2.00349	33.11	33.50 – 34.85	22.00 – 124.00
CPD-691926	343709282	11,12	206.7859	-70.3519	5	K0	9.90	10.980	91.0747	6.49783	32.72	33.48 – 34.91	26.00 – 158.00
CD-78516	357911163	11	192.8917	-79.0258	1	F8	9.67	6.3774	156.803	5.22653	33.30	34.54	40.00
CD-3012033	371122327	11	228.1852	-31.2802	2	K2	10.53	6.9606	143.665	3.10899	32.85	33.72 – 33.91	28.00 – 30.00
CPD-631286	375310963	11	151.7320	-63.8690	4	K0	10.09	7.3234	136.548	0.72632	32.98	33.87 – 34.67	26.00 – 72.00
CPD-632126	379329149	11	181.0596	-64.3143	10	G8	9.38	9.2469	108.144	1.41421	33.11	33.78 – 35.18	28.00 – 132.00
CD-8480	405077613	11,12,13	112.7469	-84.3240	2	G9	9.10	14.459	69.1596	5.00877	32.77	33.15 – 34.56	20.00 – 130.00
2MASSJ1245-5410	419778517	11	191.4532	-54.1829	3	K2	10.32	8.9603	111.603	1.46594	32.71	34.01 – 34.14	38.00 – 72.00
CD-545780	430829746	11	219.4591	-54.9616	2	K1	9.66	8.5428	117.057	3.33916	33.02	33.53 – 34.77	18.00 – 120.00
2MASSJ1410-2355	438863006	11	212.7066	-23.9249	3	K2	9.94	10.619	94.1655	2.06367	32.74	32.99 – 34.53	12.00 – 122.00
CPD-662366	448165364	11,12	208.5306	-67.5625	7	G6	10.15	7.3277	136.468	2.40420	32.98	33.82 – 34.97	18.00 – 78.00
HD307772	460765494	11	158.6244	-62.5992	6	G7	9.72	6.7652	147.815	0.31717	33.20	33.66 – 35.24	12.00 – 98.00
CD-5110295	022836043	12	248.4599	-51.3172	3	K2	9.67	9.9367	100.637	6.06104	32.99	34.50 – 35.31	64.00 – 174.00
HD144732	067822383	12	242.1095	-28.4305	7	G0	9.20	8.3941	119.131	1.06628	33.20	33.38 – 34.85	16.00 – 106.00

Continued on next page

Table A.2 – continued from previous page

Name	TIC ID	Sector	Ra	Dec	No. of	SpT	T_{mag}	Parallax	Distance	P_{rot}	$log(L_{star})$	$log(E_{flare})$	Duration
		(deg)	(deg)	flares			(mas)	(pc)	(days)	(erg/s)	(erg)	(minutes)	
HD321958	079358659	12	251.6678	-38.1476	5	G9	10.12	5.7738	173.196	1.47641	33.28	33.86 – 35.72	24.00 – 180.00
HD143637	093700013	12	240.6838	-30.6672	5	G1	8.48	9.4977	105.288	1.14518	33.17	33.32 – 34.34	18.00 – 78.00
HD156097	152346470	12	259.2415	-31.1512	12	G5	8.83	8.5735	116.638	1.96856	33.48	33.83 – 35.52	20.00 – 158.00
CD-3510498	179051609	12	236.6716	-36.3133	2	K1	10.33	6.6890	149.499	1.42170	32.98	34.14 – 35.32	40.00 – 208.00
CD-3910162	179622269	12	236.9239	-40.3076	5	K1	10.17	7.5901	131.750	5.61745	32.91	33.40 – 34.38	14.00 – 66.00
TYC8696-1949-1	190372855	12	235.3795	-53.5084	4	K2	9.86	9.6009	104.156	1.51825	33.07	33.71 – 35.60	20.00 – 211.99
CD-3311099	210541258	12	244.9606	-33.9127	3	G6	9.44	7.2617	137.708	2.61724	33.21	33.83 – 34.75	28.00 – 140.00
CD-3410971	210845898	12	245.9068	-34.6729	5	G0	8.83	8.1376	122.886	1.11805	33.33	33.69 – 34.53	18.00 – 58.00
HD329929	270107026	12	236.7156	-49.3182	3	K0	9.50	7.8124	128.001	4.70033	33.04	33.45 – 34.64	18.00 – 98.00
CD-79137	293466528	12,13	50.3399	-79.2859	5	G5	9.67	6.4382	155.322	0.98023	33.29	33.94 – 35.43	12.00 – 120.00
V*MVLup	295911223	12	237.4966	-36.4994	2	K2	10.37	7.1809	139.258	5.23443	32.88	33.38 – 34.38	22.00 – 54.00
HD155915	304437284	12	259.5604	-60.4581	4	G8	8.61	16.779	59.5969	4.16963	32.71	32.88 – 33.96	18.00 – 72.00
CD-3510827	318035342	12	243.4916	-36.3039	6	K0	10.15	7.9771	125.358	2.15249	32.89	33.19 – 34.78	22.00 – 140.00
2MASSJ1314-6846	338248268	12	198.5044	-68.7774	4	G9	10.12	4.8027	208.216	2.61080	33.33	34.34 – 36.03	40.00 – 341.99
CPD-681894	339812943	12	200.5308	-69.6368	2	K1	9.19	10.115	98.8631	3.72475	33.03	34.18 – 34.38	54.00 – 66.00
CD-547336	360323842	12	262.4794	-54.2639	5	K1	8.69	14.758	67.7557	1.82592	32.77	33.62 – 34.90	62.00 – 162.00
HD177996	061275837	13	287.2105	-42.4288	17	K1	7.12	27.920	35.8155	6.16424	32.63	32.40 – 34.24	12.00 – 130.00
HD163029	076313563	13	269.3830	-57.6646	10	K0	7.90	23.734	42.1333	4.00502	32.71	32.68 – 33.82	22.00 – 110.00
HD180445	097914505	13	289.5533	-38.3851	14	G8	7.69	23.121	43.2500	2.54197	32.66	32.60 – 34.27	14.00 – 114.00
HD180524	097919620	13	289.6781	-41.7082	13	G8	9.69	9.7275	102.801	3.24435	32.89	33.31 – 34.34	14.00 – 58.00
HD170132	119676968	13	277.7483	-55.5485	13	K0	8.66	16.180	61.8047	6.46270	32.71	32.59 – 34.17	14.00 – 124.00
HD198610	318213519	13	314.8254	-78.1811	3	G0	8.45	10.822	92.4009	1.36713	33.32	33.40 – 34.36	18.00 – 54.00
HD183253	319904128	13	293.0046	-58.9164	6	G8	9.33	10.036	99.6373	0.82663	33.02	33.69 – 35.37	26.00 – 172.00

Continued on next page

Table A.2 – continued from previous page

Name	TIC ID	Sector	Ra	Dec	No. of	SpT	T_{mag}	Parallax	Distance	P_{rot}	$log(L_{star})$	$log(E_{flare})$	Duration
		(deg)	(deg)	flares			(mas)	(pc)	(days)	(erg/s)	(erg)	(minutes)	
CPD-791037	346704136	13	296.7666	-78.9621	4	G8	10.59	6.8583	145.808	1.98853	32.88	33.34 – 34.41	12.00 – 78.00
CD-84117	369959289	13	173.5587	-85.1208	7	F8	8.97	8.9034	112.316	2.90160	33.31	33.59 – 34.51	18.00 – 96.00
HD157963	407575771	13	264.1054	-77.6012	2	G0	8.77	8.5680	116.713	0.75829	33.40	33.22 – 34.64	8.00 – 94.00

Abbreviations

AIA	Atmospheric Imaging Assembly
APO	Apache Point Observatory
AR	Active Region
ARMS	Adaptively Refined Magnetohydrodynamics
BBSO	Big Bear Solar Observatory
BY Dra	A late-type variable main sequence star
CCD	Charge-Coupled Device
CHROMIS	CHROMospheric Imaging Spectrometer
CME	Coronal Mass Ejection
CR	Circular Ribbon
CRISP	CRisp Imaging SpectroPolimeter
DKIST	Daniel K. Inouye Solar Telescope
EPIC	Ecliptic Plane Input Catalog
EUV	Extreme Ultraviolet
EVEREST	EPIC Variability Extraction and Removal for Exoplanet Science Targets
EXOSAT	European X-ray Observatory Satellite
FBEYE	Flares By EYE
FDHA	Full Disk H-alpha

FFD	Flare Frequency Distribution
FFI	Full Frame Image
FOV	Field Of View
FR	Flare Ribbon
FWHM	Full Width Half Maximum
GOES	Geostationary Operational Environmental Satellite
GONG	Global Oscillations Network Group
GPS	Global Positioning System
GUI	Graphical User Interface
Hα	H-alpha
HMI	Helioseismic and Magnetic Imager
HXR	Hard X-Rays
`IDL`	Interactive Data Language
KIC	Kepler Input Catalog
LC	Long Cadence
LS	Lomb Scargle
MAST	Mikulski Archive for Space Telescopes
MDI	Michelson Doppler Imager
MHD	MagnetoHydroDynamics
MOMFBD	Multi-Object Multi-Frame Blind Deconvolution
NOAA	National Oceanic and Atmospheric Administration
PCC	Pearson Correlation Coefficient

PIL Polarity Inversion Line

RHESSI Reuven Ramaty High Energy Solar Spectroscopic Imager

RR Remote Ribbon

`SIMBAD` An astronomical database for objects beyond the Solar System

SSWIDL Solar SoftWare Interactive Data Language

SC Short Cadence

SDO Solar Dynamics Observatory

SILSO Sunspot Index and Long-term Solar Observations

SOHO Solar and Heliospheric Observatory

SPI Star-Planet Interaction

SST Swedish Solar Telescope

SXR Soft X-Rays

TESS Transiting Exoplanet Survey Satellite

TIC TESS Input Catalog

TSI Total Solar Irradiance

UFR Ultra Fast Rotator

UV Ultraviolet

WLF White Light Flare

ZDI Zeeman Doppler Imaging

Symbols and Units

P_{rot}	Rotation Period
T_{eff}	Effective Temperature
Ω	Rotational Velocity
χ^2_ν	Reduced Chi-Squared
ϕ_0	Phase Zero
$log(g)$	Surface Gravity
Å	Angstrom: 1Å= 10^{10}m
AU	Astronomical Unit: 1AU = 1.49$\times 10^{11}$m
Dec	Declination
erg	Unit of Energy: 1erg = 10^{-7}J
G	Gauss
K	Kelvin
mas	milliarcsecond
Mx	Maxwell unit of Magnetic Flux: 1Mx = 1Gauss cm^2
pc	unit of length, parsec: 1pc = 3.0857$\times 10^{16}$m
ppm	Parts Per Million
Ra	Right Ascension
rms	Root Mean Square
SpT	Spectral Type

References

Aberasturi, M., Caballero, J., Montesinos, B., Gálvez-Ortiz, M., Solano, E. and Martín, E. (2014), 'Search for bright nearby m dwarfs with virtual observatory tools', *The Astronomical Journal* **148**(2), 36.

Agüeros, M. A., Covey, K. R., Lemonias, J. J., Law, N. M., Kraus, A., Batalha, N., Bloom, J. S., Cenko, S. B., Kasliwal, M. M., Kulkarni, S. R. et al. (2011), 'The factory and the beehive. i. rotation periods for low-mass stars in praesepe', *The Astrophysical Journal* **740**(2), 110.

Alonso-Floriano, F., Morales, J., Caballero, J., Montes, D., Klutsch, A., Mundt, R., Cortés-Contreras, M., Ribas, I., Reiners, A., Amado, P. et al. (2015), 'Carmenes input catalogue of m dwarfs-i. low-resolution spectroscopy with cafos', *Astronomy & Astrophysics* **577**, A128.

Amari, T., Canou, A., Aly, J.-J., Delyon, F. and Alauzet, F. (2018), 'Magnetic cage and rope as the key for solar eruptions', *Nature* **554**(7691), 211–215.

Angus, R. (2019), 'stardate: a tool for measuring precise stellar ages.', Github.
URL: https://stardate.readthedocs.io/en/latest/

Angus, R., Aigrain, S., Foreman-Mackey, D. and McQuillan, A. (2015), 'Calibrating gyrochronology using kepler asteroseismic targets', *Monthly Notices of the Royal Astronomical Society* **450**(2), 1787–1798.

Angus, R., Morton, T. D., Foreman-Mackey, D., van Saders, J., Curtis, J., Kane, S. R., Bedell, M., Kiman, R., Hogg, D. W. and Brewer, J. (2019), 'Toward precise stellar ages: Combining isochrone fitting with empirical gyrochronology', *The Astronomical Journal* **158**(5), 173.

Antiochos, S. K. (1990), 'Heating of the corona by magnetic singularities', *Mem. Societa Astronomica Italiana* **61**(2), 369–382.

Antiochos, S. K. (1998), 'The Magnetic Topology of Solar Eruptions', *Astrophysical Journal, Letters* **502**(2), L181–L184.

Antiochos, S. K., DeVore, C. R. and Klimchuk, J. A. (1999), 'A Model for Solar Coronal Mass Ejections', *Astrophysical Journal* **510**, 485–493.

Archontis, V. and Hood, A. W. (2013), 'A Numerical Model of Standard to Blowout Jets', *Astrophysical Journal, Letters* **769**, L21.

Aschwanden, M. J., Boerner, P., Schrijver, C. J. and Malanushenko, A. (2013), 'Automated temperature and emission measure analysis of coronal loops and active regions observed with the atmospheric imaging assembly on the solar dynamics observatory (sdo/aia)', *Solar Physics* **283**(1), 5–30.

Aschwanden, M. J., Tarbell, T. D., Nightingale, R. W., Schrijver, C. J., Kankelborg, C. C., Martens, P., Warren, H. P. et al. (2000), 'Time variability of the "quiet" sun observed with trace. ii. physical parameters, temperature evolution, and energetics of extreme-ultraviolet nanoflares', *Astrophysical Journal* **535**(2), 1047.

Astraatmadja, T. L. and Bailer-Jones, C. A. L. (2016), 'Estimating Distances from Parallaxes. III. Distances of Two Million Stars in the Gaia DR1 Catalogue', *Astrophysical Journal* **833**, 119.

Audard, M., Güdel, M. and Skinner, S. L. (2003), 'Separating the x-ray emissions of uv ceti a and b with chandra', *Astrophysical Journal* **589**(2), 983.

Aulanier, G., Démoulin, P., Schrijver, C., Janvier, M., Pariat, E. and Schmieder, B. (2013), 'The standard flare model in three dimensions-ii. upper limit on solar flare energy', *Astronomy & Astrophysics* **549**, A66.

Barnes, J., Jeffers, S., Haswell, C., Jones, H., Shulyak, D., Pavlenko, Y. V. and Jenkins, J. S. (2017), 'Surprisingly different star-spot distributions on the near equal-mass equal-rotation-rate stars in the m dwarf binary gj 65 ab', *Monthly Notices of the Royal Astronomical Society* **471**(1), 811–823.

Barnes, S. A. (2003), 'On the rotational evolution of solar-and late-type stars, its magnetic origins, and the possibility of stellar gyrochronology', *Astrophysical Journal* **586**(1), 464.

Barnes, S. A. (2007), 'Ages for illustrative field stars using gyrochronology: viability, limitations, and errors', *Astrophysical Journal* **669**(2), 1167.

Baykan, N. and Özçelik, C. (2006), 'Management of drought', *Water resources management: Risks and Challenges for the 21st century, Turkey* pp. 55–62.

Beichman, C. A., Chester, T., Gillett, F. C., Low, F. J., Matthews, K. and Neugebauer, G. (1990), 'The nature of unidentified 12 micron IRAS sources at high Galactic latitudes', *Astronomical Journal* **99**, 1569–1584.

Berdyugina, S. V. (2005), 'Starspots: a key to the stellar dynamo', *Living Reviews in Solar Physics* **2**(1), 8.

Bergfors, C., Brandner, W., Bonnefoy, M., Schlieder, J., Janson, M., Henning, T. and Chauvin, G. (2016), 'Characterization of close visual binaries from the astralux large m dwarf survey', *Monthly Notices of the Royal Astronomical Society* **456**(3), 2576–2585.

Bergfors, C., Brandner, W., Janson, M., Daemgen, S., Geissler, K., Henning, T., Hippler, S., Hormuth, F., Joergens, V. and Kohler, R. (2010), 'Lucky imaging survey for southern m dwarf binaries', *å* **520**, A54.

Beuzit, J.-L., Ségransan, D., Forveille, T., Udry, S., Delfosse, X., Mayor, M., Perrier, C., Hainaut, M.-C., Roddier, C., Roddier, F. et al. (2004), 'New neighbours-iii. 21 new companions to nearby dwarfs, discovered with adaptive optics', *å* **425**(3), 997–1008.

Bianchi, L., Conti, A. and Shiao, B. (2014), 'The ultraviolet sky: An overview from the GALEX surveys', *Advances in Space Research* **53**, 900–912.

Bice, C. P. and Toomre, J. (2020), 'Probing the influence of a tachocline in simulated m-dwarf dynamos', *arXiv preprint arXiv:2001.05555* .

Blow, G., Chen, P., Edwards, D., Evans, D. and Frueh, M. (1982), 'Photoelectric observations of lunar occultations. xiii', *Astrophysical Journal* **87**, 1571–1584.

Bogdan, T., Gilman, P. A., Lerche, I. and Howard, R. (1988), 'Distribution of sunspot umbral areas-1917-1982', *Astrophysical Journal* **327**, 451–456.

Bopp, B. W. and Moffett, T. (1973), 'High time resolution studies of uv ceti.', *Astrophysical Journal* **185**, 239–252.

Bornmann, P. L., Speich, D., Hirman, J., Matheson, L., Grubb, R., Garcia, H. A. and Viereck, R. (1996), Goes x-ray sensor and its use in predicting solar-terrestrial disturbances, *in* 'GOES-8 and Beyond', Vol. 2812, International Society for Optics and Photonics, pp. 291–299.

Borucki, W. J., Koch, D., Basri, G., Batalha, N., Brown, T., Caldwell, D., Caldwell, J., Christensen-Dalsgaard, J., Cochran, W. D., DeVore, E. et al. (2010), 'Kepler planet-detection mission: introduction and first results', *Science* **327**(5968), 977–980.

Boudreault, S., Lodieu, N., Deacon, N. and Hambly, N. (2012), 'Astrometric and photometric initial mass functions from the ukidss galactic clusters survey–iii. praesepe', *Monthly Notices of the Royal Astronomical Society* **426**(4), 3419–3434.

Bray, J., Darlington, R. R., McGurk, P. et al. (1995), *The Chronicle of John of Worcester: The annals from 1067 to 1140 with the Gloucester interpolations and the continuation to 1141*, Vol. 3, Oxford University Press.

Bray, R. J. and Loughhead, R. E. (1964), *Sunspots*, Chapman and Hall London.

Brown, A. G., Vallenari, A., Prusti, T., De Bruijne, J., Mignard, F., Drimmel, R., Babusiaux, C., Bailer-Jones, C., Bastian, U., Biermann, M. et al. (2016), 'Gaia data release 1-summary of the astrometric, photometric, and survey properties', *Astronomy & Astrophysics* **595**, A2.

Brown, T. M., Latham, D. W., Everett, M. E. and Esquerdo, G. A. (2011), 'Kepler input catalog: photometric calibration and stellar classification', *Astrophysical Journal* **142**(4), 112.

Byrne, P., Eibe, M. and Van den Oord, G. (1998), Evidence of prominences on cool late-type stars, *in* 'International Astronomical Union Colloquium', Vol. 167, Cambridge University Press, pp. 226–234.

Cameron, R., Dikpati, M. and Brandenburg, A. (2017), 'The global solar dynamo', *Space Science Reviews* **210**(1-4), 367–395.

Cargill, P. J., Mariska, J. T. and Antiochos, S. K. (1995), 'Cooling of solar flares plasmas. 1: Theoretical considerations', *The Astrophysical Journal* **439**, 1034–1043.

Carrington, R. C. (1859), 'Description of a singular appearance seen in the sun on september 1, 1859', *Monthly Notices of the Royal Astronomical Society* **20**, 13–15.

Carroll, B. W. and Ostlie, D. A. (2006), *An introduction to modern astrophysics*, Cambridge University Press.

Cayrel de Strobel, G. (1996), 'Stars resembling the sun', *Astronomy and Astrophysics Reviews* **7**(3), 243–288.

Chabrier, G. and Küker, M. (2006), 'Large-scale-dynamo in low-mass stars and brown dwarfs', *Astronomy & Astrophysics* **446**(3), 1027–1037.

Chambers, K. C., Magnier, E., Metcalfe, N., Flewelling, H., Huber, M., Waters, C., Denneau, L., Draper, P., Farrow, D., Finkbeiner, D. et al. (2016), 'The pan-starrs1 surveys', *arXiv preprint arXiv:1612.05560* .

Chandra, R., Schmieder, B., Aulanier, G. and Malherbe, J. (2010), A flaring twisted emerging flux region, *in* 'Magnetic Coupling between the Interior and Atmosphere of the Sun', Springer, pp. 523–524.

Charbonneau, P. (2010), 'Dynamo models of the solar cycle', *Living Reviews in Solar Physics* **7**(1), 3.

Chauvin, G., Lagrange, A.-M., Zuckerman, B., Dumas, C., Mouillet, D., Song, I., Beuzit, J.-L., Lowrance, P. and Bessell, M. (2005), 'A companion to ab pic at the planet/brown dwarf boundary', *Astronomy & Astrophysics* **438**(3), L29–L32.

Chen, J. (2017), 'Physics of erupting solar flux ropes: coronal mass ejections (cmes)—recent advances in theory and observation', *Physics of Plasmas* **24**(9), 090501.

Chen, P. F. (2011), 'Coronal mass ejections: Models and their observational basis', *Living Reviews in Solar Physics* **8**(1), 1.

Chen, Y., Du, G., Zhao, D., Wu, Z., Liu, W., Wang, B., Ruan, G., Feng, S. and Song, H. (2016), 'IMAGING a MAGNETIC-BREAKOUT SOLAR ERUPTION', *The Astrophysical Journal* **820**(2), L37.

Cheung, M. C., Boerner, P., Schrijver, C., Testa, P., Chen, F., Peter, H. and Malanushenko, A. (2015), 'Thermal diagnostics with the atmospheric imaging assembly on board the solar dynamics observatory: a validated method for differential emission measure inversions', *The Astrophysical Journal* **807**(2), 143.

Cliver, E. W. and Dietrich, W. F. (2013), 'The 1859 space weather event revisited: limits of extreme activity', *Journal of Space Weather and Space Climate* **3**, A31.

Cox, A. N., Livingston, W. C. and Matthews, M. S. (1991), *Solar Interior and Atmosphere*, University of Arizona Press.

Cruz, K. L. and Reid, I. N. (2002), 'Meeting the cool neighbors. iii. spectroscopy of northern nltt stars', *The Astronomical Journal* **123**(5), 2828.

Cutri, R., Skrutskie, M., Van Dyk, S., Beichman, C., Carpenter, J., Chester, T., Cambresy, L., Evans, T., Fowler, J., Gizis, J. et al. (2003), 'Vizier online data catalog: 2mass all-sky catalog of point sources (cutri+ 2003)', *VizieR Online Data Catalog* **2246**, 0.

Darlington, R. R. D. and McGurk, P. (1995), *The chronicle of John of Worcester*, Clarendon Press.

Davenport, J. R. (2016), 'The kepler catalog of stellar flares', *Astrophysical Journal* **829**(1), 23.

Davenport, J. R. A., Hebb, L. and Hawley, S. L. (2015), 'Detecting Differential Rotation and Starspot Evolution on the M Dwarf GJ 1243 with Kepler', *Astrophysical Journal* **806**, 212.

Davenport, J. R., Covey, K. R., Clarke, R. W., Boeck, A. C., Cornet, J. and Hawley, S. L. (2019), 'The evolution of flare activity with stellar age', *Astrophysical Journal* **871**(2), 241.

Davenport, J. R., Hawley, S. L., Hebb, L., Wisniewski, J. P., Kowalski, A. F., Johnson, E. C., Malatesta, M., Peraza, J., Keil, M., Silverberg, S. M. et al. (2014), 'Kepler flares. ii. the temporal morphology of white-light flares on gj 1243', *Astrophysical Journal* **797**(2), 122.

Davison, C. L., White, R. J., Henry, T. J., Riedel, A. R., Jao, W.-C., Bailey, III, J. I., Quinn, S. N., Cantrell, J. R., Subasavage, J. P. and Winters, J. G. (2015), 'A 3D Search for Companions to 12 Nearby M Dwarfs', *Astronomical Journal* **149**, 106.

de la Cruz Rodriguez, J., Löfdahl, M. G., Sütterlin, P., Hillberg, T. and van der Voort, L. R. (2015), 'Crispred: A data pipeline for the crisp imaging spectropolarimeter', *Astronomy & Astrophysics* **573**, A40.

De Pontieu, B., McIntosh, S., Hansteen, V. H., Carlsson, M., Schrijver, C. J., Tarbell, T. D., Title, A. M., Shine, R. A., Suematsu, Y., Tsuneta, S. et al. (2007), 'A tale of two spicules: the impact of spicules on the magnetic chromosphere', *Publications of the Astronomical Society of Japan* **59**(sp3), S655–S652.

DeForest, C., Hagenaar, H., Lamb, D., Parnell, C. and Welsch, B. (2007), 'Solar magnetic tracking. i. software comparison and recommended practices', *The Astrophysical Journal* **666**(1), 576.

Delfosse, X., Forveille, T., Beuzit, J.-L., Udry, S., Mayor, M. and Perrier, C. (1998), 'New neighbours. i. 13 new companions to nearby m dwarfs', *arXiv preprint astro-ph/9812008* .

DeVore, C. R. and Antiochos, S. K. (2008), 'Homologous Confined Filament Eruptions via Magnetic Breakout', *Astrophysical Journal* **680**, 740–756.

Dhillon, V., Privett, G. and Duffey, K. (2001), 'Period–a time-series analysis package', *Starlink User Note* **167**.

Dikpati, M. and Charbonneau, P. (1999), 'A babcock-leighton flux transport dynamo with solar-like differential rotation', *Astrophysical Journal* **518**(1), 508.

Dikpati, M., McIntosh, S. W., Chatterjee, S., Banerjee, D., Yellin-Bergovoy, R. and Srivastava, A. (2019), 'triggering the birth of new cycle's sunspots by solar tsunami', *Scientific reports* **9**(1), 2035.

Donati, J.-F., Forveille, T., Cameron, A. C., Barnes, J. R., Delfosse, X., Jardine, M. M. and Valenti, J. A. (2006), 'The large-scale axisymmetric magnetic topology of a very-low-mass fully convective star', *Science* **311**(5761), 633–635.

Donati, J.-F., Morin, J., Petit, P., Delfosse, X., Forveille, T., Aurière, M., Cabanac, R., Dintrans, B., Fares, R., Gastine, T. et al. (2008), 'Large-scale magnetic topologies of early m dwarfs', *Monthly Notices of the Royal Astronomical Society* **390**(2), 545–560.

Doyle, J., Van den Oord, G. and Kellett, B. (1992), 'Dynamic phenomena on the rs canum venaticorum binary ii pegasi in august 1989. ii-an interpretation', *Astronomy and Astrophysics* **262**, 533–543.

Doyle, L. (2017), Spectroscopic studies of arcade flares with EIS and EVE, PhD thesis, University of Glasgow.

Doyle, L., Ramsay, G., Doyle, J. G. and Wu, K. (2019), 'Probing the origin of stellar flares on m dwarfs using tess data sectors 1–3', *Monthly Notices of the Royal Astronomical Society* **489**(1), 437–445.

Doyle, L., Ramsay, G., Doyle, J., Wu, K. and Scullion, E. (2018), 'Investigating the rotational phase of stellar flares on m dwarfs using k2 short cadence data', *Monthly Notices of the Royal Astronomical Society* **480**(2), 2153–2164.

Doyle, L., Wyper, P. F., Scullion, E., McLaughlin, J. A., Ramsay, G. and Doyle, J. G. (2019), 'Observations and 3d magnetohydrodynamic modeling of a confined helical jet launched by a filament eruption', *The Astrophysical Journal* **887**(2), 246.

Dressing, C. D. and Charbonneau, D. (2015), 'The occurrence of potentially habitable planets orbiting m dwarfs estimated from the full kepler dataset and an empirical measurement of the detection sensitivity', *Astrophysical Journal* **807**(1), 45.

Druett, M., Scullion, E., Zharkova, V., Matthews, S., Zharkov, S. and Van der Voort, L. R. (2017), 'Beam electrons as a source of hα flare ribbons', *Nature communications* **8**, 15905.

Durney, B. R., De Young, D. S. and Roxburgh, I. W. (1993), 'On the generation of the large-scale and turbulent magnetic fields in solar-type stars', *Solar Physics* **145**(2), 207–225.

Eaton, J. A., Henry, G. W. and Fekel, F. C. (1996), 'Random spots on chromospherically active stars', *Astrophysical Journal* **462**, 888.

Emslie, A. G., Dennis, B. R., Holman, G. D. and Hudson, H. S. (2005), 'Refinements to flare energy estimates: A followup to "Energy partition in two solar flare/CME events" by A. G. Emslie et al.', *Journal of Geophysical Research (Space Physics)* **110**(A11), A11103.

Engvold, O. (2015), Description and classification of prominences, *in* 'Solar prominences', Springer, pp. 31–60.

Engvold, O., Vial, J.-C. and Skumanich, A. (2018), *The Sun as a Guide to Stellar Physics*, Elsevier.

Faherty, J. K., Burgasser, A. J., Cruz, K. L., Shara, M. M., Walter, F. M. and Gelino, C. R. (2009), 'The Brown Dwarf Kinematics Project I. Proper Motions and Tangential Velocities for a Large Sample of Late-Type M, L, and T Dwarfs', *Astronomical Journal* **137**, 1–18.

Fang, X.-S., Zhao, G., Zhao, J.-K., Chen, Y.-Q. and Bharat Kumar, Y. (2016), 'Stellar activity with lamost–i. spot configuration in pleiades', *Monthly Notices of the Royal Astronomical Society* **463**(3), 2494–2512.

Filippov, B. P. (1998), Causes and effects of filament eruptions, *in* 'International Astronomical Union Colloquium', Vol. 167, Cambridge University Press, pp. 342–349.

Fischer, C. and Saur, J. (2019), 'Time-variable electromagnetic star–planet interaction: The trappist-1 system as an exemplary case', *Astrophysical Journal* **872**(1), 113.

Fisher, G. H. and Welsch, B. T. (2008), Flct: A fast, efficient method for performing local correlation tracking, *in* 'Subsurface and Atmospheric Influences on Solar Activity', Vol. 383, p. 373.

Fletcher, L., Dennis, B. R., Hudson, H. S., Krucker, S., Phillips, K., Veronig, A., Battaglia, M., Bone, L., Caspi, A., Chen, Q. et al. (2011), 'An observational overview of solar flares', *Space science reviews* **159**(1-4), 19.

Fletcher, L. and Hudson, H. (2001), 'The magnetic structure and generation of euv flare ribbons', *Solar Physics* **204**(1-2), 69–89.

Frith, J., Pinfield, D., Jones, H., Barnes, J., Pavlenko, Y., Martin, E., Brown, C., Kuznetsov,

M., Marocco, F., Tata, R. et al. (2013), 'A catalogue of bright (k_j 9) m dwarfs', *Monthly Notices of the Royal Astronomical Society* **435**(3), 2161–2170.

Gaia Collaboration, Brown, A. G. A. e. a. (2016), 'Gaia data release 1-summary of the astrometric, photometric, and survey properties', *Astronomy and Astrophysics* **595**, A2.

Gaia Collaboration, Brown, A. G. A. e. a. (2018), 'Gaia data release 2-summary of the contents and survey properties', *Astronomy and Astrophysics* **616**, A1.

Gao, P.-X. and Zhong, J. (2016), 'The curious temporal behavior of the frequency of different class flares', *New Astronomy* **43**, 91–94.

Gastine, T., Morin, J., Duarte, L., Reiners, A., Christensen, U. and Wicht, J. (2013), 'What controls the magnetic geometry of m dwarfs?', *Astronomy and Astrophysics* **549**, L5.

Gershberg, R. (1972), 'Some results of the cooperative photometric observations of the uv cet-type flare stars in the years 1967–71', *Astrophysics and Space Science* **19**(1), 75–92.

Gershberg, R. E. (2005), *Solar-type activity in main-sequence Stars*, Springer Science & Business Media.

Gershberg, R. E., Katsova, M., Lovkaya, M., Terebizh, A. and Shakhovskaya, N. (1999), 'Catalogue and bibliography of the uv cet-type flare stars and related objects in the solar vicinity', *Astronomy and Astrophysics Supplement Series* **139**(3), 555–558.

Gershberg, R. and Shakhovskaya, N. (1983), 'Characteristics of activity energetics of the uv cet-type flare stars', *ApSS* **95**(2), 235–253.

Giles, H. A., Collier Cameron, A. and Haywood, R. D. (2017), 'A kepler study of starspot lifetimes with respect to light-curve amplitude and spectral type', *Monthly Notices of the Royal Astronomical Society* **472**(2), 1618–1627.

Gillon, M., Triaud, A. H., Demory, B.-O., Jehin, E., Agol, E., Deck, K. M., Lederer, S. M., De Wit, J., Burdanov, A., Ingalls, J. G. et al. (2017), 'Seven temperate terrestrial planets around the nearby ultracool dwarf star trappist-1', *Nature* **542**(7642), 456–460.

Gizis, J. E., Paudel, R. R., Mullan, D., Schmidt, S. J., Burgasser, A. J. and Williams, P. K. G. (2017), 'K2 Ultracool Dwarfs Survey II: The White Light Flare Rate of Young Brown Dwarfs', *ArXiv e-prints* .

Gray, R. O., Corbally, C. J., Garrison, R. F., McFadden, M. T. and Robinson, P. E. (2003), 'Contributions to the Nearby Stars (NStars) Project: Spectroscopy of Stars Earlier than M0 within 40 Parsecs: The Northern Sample. I.', *Astronomical Journal* **126**, 2048–2059.

Gregory, S., Jardine, M., Gray, C. and Donati, J. (2010), 'The magnetic fields of forming solar-like stars', *Reports on Progress in Physics* **73**(12), 126901.

Guarcello, M., Micela, G., Sciortino, S., López-Santiago, J., Argiroffi, C., Reale, F., Flaccomio, E., Alvarado-Gomez, J., Antoniou, V., Drake, J. et al. (2019), 'Simultaneous kepler/k2 and xmm-netwon observations of superflares in the pleiades', *A&A* .

Güdel, M., Audard, M., Reale, F., Skinner, S. L. and Linsky, J. L. (2004), 'Flares from small to large: X-ray spectroscopy of proxima centauri with xmm-newton', *Astronomy and Astrophysics* **416**(2), 713–732.

Guglielmo, F., Epchtein, N., Le Bertre, T., Fouqué, P., Hron, J., Kerschbaum, F. and Lepine, J. (1993), 'Identification of 106 new infrared carbon stars in the iras point source catalog-near-infrared photometry and their space distribution in the galaxy', *Astronomy and Astrophysics Supplement Series* **99**, 31–69.

Guinan, E. F. and Ribas, I. (2004), Evolution of the solar magnetic activity over time and effects on planetary atmospheres, *in* 'Symposium-International Astronomical Union', Vol. 219, Cambridge University Press, pp. 423–430.

Gully-Santiago, M. A., Herczeg, G. J., Czekala, I., Somers, G., Grankin, K., Covey, K. R., Donati, J., Alencar, S. H., Hussain, G. A., Shappee, B. J. et al. (2017), 'Placing the spotted t tauri star lkca 4 on an hr diagram', *Astrophysical Journal* **836**(2), 200.

Günther, M. N., Zhan, Z., Seager, S., Rimmer, P. B., Ranjan, S., Stassun, K. G., Oelkers, R. J., Daylan, T., Newton, E., Gillen, E., Rappaport, S., Ricker, G. R., Latham, D. W., Winn, J. N., Jenkins, J. M., Glidden, A., Fausnaugh, M., Levine, A. M., Dittmann, J. A.,

Quinn, S. N., Krishnamurthy, A. and Ting, E. B. (2019), 'Stellar Flares from the First Tess Data Release: Exploring a New Sample of M-dwarfs', *arXiv e-prints* .

Guo, J., Lin, J. and Deng, Y. (2014), 'The dependence of flares on the magnetic classification of the source regions in solar cycles 22–23', *Monthly Notices of the Royal Astronomical Society* **441**(3), 2208–2211.

Hale, G. E., Ellerman, F., Nicholson, S. B. and Joy, A. H. (1919), 'The magnetic polarity of sun-spots', *Astrophysical Journal* **49**, 153.

Hannah, I. G. and Kontar, E. P. (2012), 'Differential emission measures from the regularized inversion of hinode and sdo data', *Astronomy & Astrophysics* **539**, A146.

Hansen, O. and Blanco, V. (1975), 'Classification of 831 two-micron sky survey.', *The Astronomical Journal* **80**, 1011–1025.

Haro, G. (1976), 'An observational approach to stellar evolution.-i.(flare stars and related objects).', *Boletin del Instituto de Tonantzintla* **2**, 3.

Haro, G. and Chavira, E. (1973), 'New flare stars in the pleiades region (1972-1973)', *Information Bulletin on Variable Stars* **788**.

Haro, G. and Gonzalez, G. (1972), 'A re-examination of the pleiades tonantzintla photographic material: 1963-1970. ii', *Boletin de los Observatorios Tonantzintla y Tacubaya* **6**, 149–154.

Harra, L. K., Schrijver, C. J., Janvier, M., Toriumi, S., Hudson, H., Matthews, S., Woods, M. M., Hara, H., Guedel, M., Kowalski, A. et al. (2016), 'The characteristics of solar x-class flares and cmes: a paradigm for stellar superflares and eruptions?', *Solar Physics* **291**(6), 1761–1782.

Hartman, J. D. and Bakos, G. Á. (2016), 'Vartools: A program for analyzing astronomical time-series data', *Astronomy and Computing* **17**, 1–72.

Hartmann, L. W. and Noyes, R. W. (1987), 'Rotation and magnetic activity in main-sequence stars', *Annual review of astronomy and astrophysics* **25**(1), 271–301.

Harvey, J., Bolding, J., Clark, R., Hauth, D., Hill, F., Kroll, R., Luis, G., Mills, N., Purdy, T., Henney, C. et al. (2011), Full-disk solar h-alpha images from gong, *in* 'Bulletin of the American Astronomical Society', Vol. 43.

Harvey, J., Hill, F., Hubbard, R., Kennedy, J., Leibacher, J., Pintar, J., Gilman, P., Noyes, R., Toomre, J., Ulrich, R. et al. (1996), 'The global oscillation network group (gong) project', *Science* **272**(5266), 1284–1286.

Hassanin, A. and Kliem, B. (2016), 'HELICAL KINK INSTABILITY IN a CONFINED SOLAR ERUPTION', *The Astrophysical Journal* **832**(2), 106.

Hawley, S. L., Davenport, J. R., Kowalski, A. F., Wisniewski, J. P., Hebb, L., Deitrick, R. and Hilton, E. J. (2014), 'Kepler flares. i. active and inactive m dwarfs', *Astrophysical Journal* **797**(2), 121.

Hawley, S. L., Gizis, J. E. and Reid, I. N. (1996), 'The Palomar/MSU Nearby Star Spectroscopic Survey.II.The Southern M Dwarfs and Investigation of Magnetic Activity', *Astronomical Journal* **112**, 2799.

Heise, J., Brinkman, A., Schrijver, J., Mewe, R., Gronenschild, E., Den Boggende, A. and Grindlay, J. (1975), 'Evidence for x-ray emission from flare stars observed by ans', *Astrophysical Journal* **202**, L73–L76.

Henden, A. A., Levine, S. E., Terrell, D., Smith, T. C. and Welch, D. (2012), 'Data Release 3 of the AAVSO All-Sky Photometric Survey (APASS)', *Journal of the American Association of Variable Star Observers (JAAVSO)* **40**, 430.

Herzenberg, A. (1958), 'Geomagnetic dynamos', *Philosophical Transactions of the Royal Society of London. Series A, Mathematical and Physical Sciences* **250**(986), 543–583.

Høg, E., Fabricius, C., Makarov, V. V., Urban, S., Corbin, T., Wycoff, G., Bastian, U., Schwekendiek, P. and Wicenec, A. (2000), 'The tycho-2 catalogue of the 2.5 million brightest stars', *Astronomy and Astrophysics* **355**, L27–L30.

Hog, E., Kuzmin, A., Bastian, U., Fabricius, C., Kuimov, K., Lindegren, L., Makarov, V. and Roeser, S. (1998), 'The tycho reference catalogue', *Astronomy and Astrophysics* **335**, L65–L68.

Houdebine, E. (1991), '"homothetiques" white light flares on a dme star', *Information bulletin on variable stars* **3643**.

Houdebine, E., Mullan, D., Paletou, F. and Gebran, M. (2016), 'Rotation–activity correlations in k and m dwarfs. i. stellar parameters and compilations of v sin i and p/sin i for a large sample of late-k and m dwarfsbased on observations available at observatoire de haute provence and the european southern observatory databases and on hipparcos parallax measurements.', *The Astrophysical Journal* **822**(2), 97.

Howard, W. S., Corbett, H., Law, N. M., Ratzloff, J. K., Glazier, A. L., Fors, O., del Ser, D. and Haislip, J. (2019), 'Evryflare i: Long-term evryscope monitoring of flares from the cool stars across half the southern sky', *arXiv preprint arXiv:1904.10421* .

Howell, S. B., Sobeck, C., Haas, M., Still, M., Barclay, T., Mullally, F., Troeltzsch, J., Aigrain, S., Bryson, S. T., Caldwell, D. et al. (2014), 'The k2 mission: Characterization and early results', *Publications of the ASP* **126**(938), 398.

Huang, Z., Madjarska, M. S., Koleva, K., Doyle, J. G., Duchlev, P., Dechev, M. and Reardon, K. (2014), 'Hα spectroscopy and multiwavelength imaging of a solar flare caused by filament eruption', *Astronomy and Astrophysics* **566**, A148.

Huber, D., Bryson, S. T., Haas, M. R., Barclay, T., Barentsen, G., Howell, S. B., Sharma, S., Stello, D. and Thompson, S. E. (2016), 'The k2 ecliptic plane input catalog (epic) and stellar classifications of 138,600 targets in campaigns 1–8', *Astrophysical Journal, Supplement* **224**(1), 2.

Hudson, H. S. (2020), 'A correlation in the waiting-time distributions of solar flares', *Monthly Notices of the Royal Astronomical Society* **491**(3), 4435–4441.

Ibañez Bustos, R., Buccino, A., Flores, M., Martinez, C., Maizel, D., Messina, S. and Mauas, P. (2019), 'First long-term activity study of au microscopii: a possible chromospheric cycle', *Monthly Notices of the Royal Astronomical Society* **483**(1), 1159–1167.

Ita, Y., Deguchi, S., Fujii, T., Kameya, O., Miyoshi, M., Nakada, Y., Nakashima, J. and Parthasarathy, M. (2001), 'Sio maser survey of agb stars in the north galactic cap', *Astronomy & Astrophysics* **376**(1), 112–123.

Jackson, R. and Jeffries, R. (2013), 'On the relationship between the size and surface coverage of starspots on magnetically active low-mass stars', *Monthly Notices of the Royal Astronomical Society* **431**(2), 1883–1890.

James, D. J., Jardine, M. M., Jeffries, R. D., Randich, S., Collier Cameron, A. and Ferreira, M. (2000), 'X-ray emission from nearby m-dwarfs: the super-saturation phenomenon', *Monthly Notices of the Royal Astronomical Society* **318**(4), 1217–1226.

Janvier, M., Savcheva, A., Pariat, E., Tassev, S., Millholland, S., Bommier, V., McCauley, P., McKillop, S. and Dougan, F. (2016), 'Evolution of flare ribbons, electric currents, and quasi-separatrix layers during an x-class flare', *Astronomy & Astrophysics* **591**, A141.

Jeffers, S., Cameron, A. C., Barnes, J. and Aufdenberg, J. (2006), 'Dense spot coverage and polar caps on sv cam', *Astrophysics and Space Science* **304**(1-4), 371–373.

Ji, H., Wang, H., Schmahl, E. J., Moon, Y.-J. and Jiang, Y. (2003), 'Observations of the failed eruption of a filament', *The Astrophysical Journal* **595**(2), L135–L138.

Jiang, J., Cameron, R. H. and Schuessler, M. (2015), 'The cause of the weak solar cycle 24', *Astrophysical Journal, Letters* **808**(1), L28.

Jones, B. (1981), 'Proper-motion membership probabilities for pleiades flare stars', *Astrophysical Journal* **86**, 290–297.

Joshi, N. C., Srivastava, A. K., Filippov, B., Kayshap, P., Uddin, W., Chandra, R., Choudhary, D. P. and Dwivedi, B. N. (2014), 'CONFINED PARTIAL FILAMENT ERUPTION AND ITS REFORMATION WITHIN a STABLE MAGNETIC FLUX ROPE', *The Astrophysical Journal* **787**(1), 11.

Judge, P. (2008), 'An explanation of the solar transition region', *The Astrophysical Journal Letters* **683**(1), L87.

Karoff, C., Metcalfe, T. S., Santos, Â. R., Montet, B. T., Isaacson, H., Witzke, V., Shapiro, A. I., Mathur, S., Davies, G. R., Lund, M. N. et al. (2018), 'The influence of metallicity on stellar differential rotation and magnetic activity', *The Astrophysical Journal* **852**(1), 46.

Karpen, J. T., Antiochos, S. K. and DeVore, C. R. (2012), 'The Mechanisms for the Onset and Explosive Eruption of Coronal Mass Ejections and Eruptive Flares', *Astrophysical Journal* **760**, 81.

Keller, S. C., Schmidt, B. P., Bessell, M. S., Conroy, P. G., Francis, P., Granlund, A., Kowald, E., Oates, A., Martin-Jones, T., Preston, T. et al. (2007), 'The skymapper telescope and the southern sky survey', *Publications of the Astronomical Society of Australia* **24**(1), 1–12.

Khalaj, P. and Baumgardt, H. (2013), 'The stellar mass function, binary content and radial structure of the open cluster praesepe derived from ppmxl and sdss data', *Monthly Notices of the Royal Astronomical Society* **434**(4), 3236–3245.

Kiraga, M. and Stepien, K. (2007), 'Age-rotation-activity relations for m dwarf stars based on asas photometric data', *AcA* **57**(149).

Kirkpatrick, J. D., Henry, T. J. and McCarthy Jr, D. W. (1991), 'A standard stellar spectral sequence in the red/near-infrared-classes k5 to m9', *The Astrophysical Journal Supplement Series* **77**, 417–440.

Kliem, B. and Török, T. (2006), 'Torus Instability', *Physical Review Letters* **96**(25), 255002.

Knizhnik, K., Antiochos, S., DeVore, C. and Wyper, P. (2017), 'The mechanism for the energy buildup driving solar eruptive events', *The Astrophysical Journal* **851**.

Koch, D. G., Borucki, W., Dunham, E., Geary, J., Gilliland, R., Jenkins, J., Latham, D., Bachtell, E., Berry, D., Deininger, W. et al. (2004), Overview and status of the kepler mission, *in* 'SPIE Astronomical Telescopes+ Instrumentation', International Society for Optics and Photonics, pp. 1491–1500.

Kochukhov, O. and Lavail, A. (2017), 'The global and small-scale magnetic fields of fully convective, rapidly spinning m dwarf pair gj65 a and b', *Astrophysical Journal, Letters* **835**(1), L4.

Koen, C., Kilkenny, D., Van Wyk, F. and Marang, F. (2010), 'Ubv (ri) c jhk observations of hipparcos-selected nearby stars', *Monthly Notices of the Royal Astronomical Society* **403**(4), 1949–1968.

Kouwenhoven, M., Brown, A., Goodwin, S., Zwart, S. P. and Kaper, L. (2009), 'Exploring the consequences of pairing algorithms for binary stars', *Astronomy and Astrophysics* **493**(3), 979–1016.

Kowalski, A. F., Hawley, S. L., Wisniewski, J. P., Osten, R. A., Hilton, E. J., Holtzman, J. A., Schmidt, S. J. and Davenport, J. R. (2013), 'Time-resolved properties and global trends in dme flares from simultaneous photometry and spectra', *The Astrophysical Journal Supplement Series* **207**(1), 15.

Kraus, A. L. and Hillenbrand, L. A. (2007), 'The Stellar Populations of Praesepe and Coma Berenices', *Astronomical Journal* **134**, 2340–2352.

Kuhar, M., Krucker, S., Oliveros, J. C. M., Battaglia, M., Kleint, L., Casadei, D. and Hudson, H. S. (2015), 'Correlation of hard x-ray and white light emission in solar flares', *Astrophysical Journal* **816**(1), 6.

Kumar, P., Karpen, J. T., Antiochos, S. K., Wyper, P. F., DeVore, C. R. and DeForest, C. E. (2018), 'Evidence for the Magnetic Breakout Model in an Equatorial Coronal-hole Jet', *Astrophysical Journal* **854**, 155.

Kumar, P., Karpen, J. T., Antiochos, S. K., Wyper, P. F., DeVore, C. R. and DeForest, C. E. (2019), 'Multiwavelength Study of Equatorial Coronal-hole Jets', *Astrophysical Journal* **873**(1), 93.

Kunkel, W. (1972), 'Observations of southern flare stars', *IBVS* **748**.

Lang, P., Jardine, M., Morin, J., Donati, J.-F., Jeffers, S., Vidotto, A. and Fares, R. (2014), 'Modelling the hidden magnetic field of low-mass stars', *Monthly Notices of the Royal Astronomical Society* **439**(2), 2122–2131.

Larmor, J. (1919), 'How could a rotating body such as the sun become a magnet', *Rep. Brit. Adv. Sci.* pp. 159–160.

Law, N. M., Fors, O., Ratzloff, J., Wulfken, P., Kavanaugh, D., Sitar, D. J., Pruett, Z., Birchard, M. N., Barlow, B. N., Cannon, K. et al. (2015), 'Evryscope science: exploring the potential of all-sky gigapixel-scale telescopes', *Publications of the Astronomical Society of the Pacific* **127**(949), 234.

Lawrence, A., Warren, S., Almaini, O., Edge, A., Hambly, N., Jameson, R., Lucas, P., Casali, M., Adamson, A., Dye, S. et al. (2007), 'The ukirt infrared deep sky survey (ukidss)', *Monthly Notices of the Royal Astronomical Society* **379**(4), 1599–1617.

Lemen, J. R., Title, A. M., Akin, D. J., Boerner, P. F., Chou, C., Drake, J. F., Duncan, D. W., Edwards, C. G., Friedlaender, F. M., Heyman, G. F., Hurlburt, N. E., Katz, N. L., Kushner, G. D., Levay, M., Lindgren, R. W., Mathur, D. P., McFeaters, E. L., Mitchell, S., Rehse, R. A., Schrijver, C. J., Springer, L. A., Stern, R. A., Tarbell, T. D., Wuelser, J.-P., Wolfson, C. J., Yanari, C., Bookbinder, J. A., Cheimets, P. N., Caldwell, D., Deluca, E. E., Gates, R., Golub, L., Park, S., Podgorski, W. A., Bush, R. I., Scherrer, P. H., Gummin, M. A., Smith, P., Auker, G., Jerram, P., Pool, P., Soufli, R., Windt, D. L., Beardsley, S., Clapp, M., Lang, J. and Waltham, N. (2012), *The Atmospheric Imaging Assembly (AIA) on the Solar Dynamics Observatory (SDO)*, Springer US, New York, NY, pp. 17–40.

Lépine, S. and Gaidos, E. (2011), 'An All-sky Catalog of Bright M Dwarfs', *Astronomical Journal* **142**, 138.

Lépine, S., Hilton, E. J., Mann, A. W., Wilde, M., Rojas-Ayala, B., Cruz, K. L. and Gaidos, E. (2013), 'A spectroscopic catalog of the brightest (j¡ 9) m dwarfs in the northern sky', *The Astronomical Journal* **145**(4), 102.

Liu, L., Wang, Y., Zhou, Z., Dissauer, K., Temmer, M. and Cui, J. (2018), 'A comparative study between a failed and a successful eruption initiated from the same polarity inversion line in AR 11387', *The Astrophysical Journal* **858**(2), 121.

Llama, J., Jardine, M. M., Wood, K., Hallinan, G. and Morin, J. (2018), 'Simulating radio emission from low-mass stars', *The Astrophysical Journal* **854**(1), 7.

Lodieu, N., Deacon, N. and Hambly, N. (2012), 'Astrometric and photometric initial mass functions from the ukidss galactic clusters survey–i. the pleiades', *Monthly Notices of the Royal Astronomical Society* **422**(2), 1495–1511.

Luger, R., Agol, E., Foreman-Mackey, D., Fleming, D. P., Lustig-Yaeger, J. and Deitrick, R. (2019), 'Starry: Analytic occultation light curves', *The Astronomical Journal* **157**(2), 64.

Luger, R., Agol, E., Kruse, E., Barnes, R., Becker, A., Foreman-Mackey, D. and Deming, D. (2016), 'EVEREST: Pixel Level Decorrelation of K2 Light Curves', *Astronomical Journal* **152**, 100.

Luger, R., Kruse, E., Foreman-Mackey, D., Agol, E. and Saunders, N. (2018), 'An update to the everest k2 pipeline: short cadence, saturated stars, and kepler-like photometry down to kp= 15', *The Astronomical Journal* **156**(3), 99.

Lurie, J. C., Davenport, J. R., Hawley, S. L., Wilkinson, T. D., Wisniewski, J. P., Kowalski, A. F. and Hebb, L. (2015), 'Kepler flares iii: stellar activity on gj 1245a and b', *The Astrophysical Journal* **800**(2), 95.

Lynch, B. J., Antiochos, S. K., DeVore, C. R., Luhmann, J. G. and Zurbuchen, T. H. (2008), 'Topological Evolution of a Fast Magnetic Breakout CME in Three Dimensions', *Astrophysical Journal* **683**, 1192–1206.

Maehara, H., Notsu, Y., Notsu, S., Namekata, K., Honda, S., Ishii, T. T., Nogami, D. and Shibata, K. (2017), 'Starspot activity and superflares on solar-type stars', *Publications of the Astronomical Society of Japan* **69**(3).

Maehara, H., Shibayama, T., Notsu, S., Notsu, Y., Nagao, T., Kusaba, S., Honda, S., Nogami, D. and Shibata, K. (2012), 'Superflares on solar-type stars', *Nature* **485**(7399), 478.

Maggio, A., Sciortino, S., Vaiana, G., Majer, P., Bookbinder, J., Golub, L., Harnden Jr, F. and Rosner, R. (1987), 'Einstein observatory survey of x-ray emission from solar-type stars-the late f and g dwarf stars', *Astrophysical Journal* **315**, 687–699.

Mamajek, E. E. and Hillenbrand, L. A. (2008), 'Improved age estimation for solar-type dwarfs using activity-rotation diagnostics', *Astrophysical Journal* **687**(2), 1264.

Marcy, W, G., Butler, Paul, R., Vogt, S, S., Fischer, D. and Lissauer, J, J. (1998), 'A planetary companion to a nearby m4 dwarf, gliese 876', *Astrophysical Journal* **505**, 147–149.

Mariska, J. T. (1992), *The solar transition region*, Vol. 23, Cambridge University Press.

Mariska, J. T. and McTiernan, J. M. (1999), 'Hard and soft x-ray observations of occulted and nonocculted solar limb flares', *Astrophysical Journal* **514**(1), 484.

Martin, D. C., Fanson, J., Schiminovich, D., Morrissey, P., Friedman, P. G., Barlow, T. A., Conrow, T., Grange, R., Jelinsky, P. N., Milliard, B., Siegmund, O. H. W., Bianchi, L., Byun, Y.-I., Donas, J., Forster, K., Heckman, T. M., Lee, Y.-W., Madore, B. F., Malina, R. F., Neff, S. G., Rich, R. M., Small, T., Surber, F., Szalay, A. S., Welsh, B. and Wyder, T. K. (2005), 'The Galaxy Evolution Explorer: A Space Ultraviolet Survey Mission', *Astrophysical Journal, Letters* **619**, L1–L6.

Masson, S., Pariat, E., Aulanier, G. and Schrijver, C. J. (2009), 'The Nature of Flare Ribbons in Coronal Null-Point Topology', *Astrophysical Journal* **700**, 559–578.

Masson, S., Pariat, É., Valori, G., Deng, N., Liu, C., Wang, H. and Reid, H. (2017), 'Flux rope, hyperbolic flux tube, and late extreme ultraviolet phases in a non-eruptive circular-ribbon flare', *Astronomy & Astrophysics* **604**, A76.

Matthews, S., van Driel-Gesztelyi, L., Hudson, H. and Nitta, N. (2003), 'A catalogue of white-light flares observed by yohkoh', *Astronomy and Astrophysics* **409**(3), 1107–1125.

McCarthy, M. and Treanor, P. (1966), M stars in the region of the pleiades, *in* 'Symposium-International Astronomical Union', Vol. 24, Cambridge Univ Press, pp. 367–367.

McIntosh, P. S. (1990), 'The classification of sunspot groups', *Solar Physics* **125**(2), 251–267.

McIntosh, S. W. and Leamon, R. J. (2014), 'On magnetic activity band overlap, interaction, and the formation of complex solar active regions', *The Astrophysical Journal Letters* **796**(1), L19.

McIntosh, S. W., Wang, X., Leamon, R. J., Davey, A. R., Howe, R., Krista, L. D., Malanushenko, A. V., Markel, R. S., Cirtain, J. W., Gurman, J. B. et al. (2014), 'Deciphering solar magnetic activity. i. on the relationship between the sunspot cycle and the evolution of small magnetic features', *The Astrophysical Journal* **792**(1), 12.

McLean, M., Berger, E. and Reiners, A. (2012), 'The radio activity-rotation relation of ultracool dwarfs', *Astrophysical Journal* **746**(1), 23.

McQuillan, A., Aigrain, S. and Mazeh, T. (2013), 'Measuring the rotation period distribution of field M dwarfs with Kepler', *Monthly Notices of the Royal Astronomical Society* **432**, 1203–1216.

McQuillan, A., Mazeh, T. and Aigrain, S. (2014), 'Rotation periods of 34,030 kepler main-sequence stars: the full autocorrelation sample', *Astrophysical Journal, Supplement* **211**(2), 24.

Menzel, W. P. and Purdom, J. F. (1994), 'Introducing goes-i: The first of a new generation of geostationary operational environmental satellites', *Bulletin of the American Meteorological Society* **75**(5), 757–782.

Micela, G., Sciortino, S., Harnden Jr, F., Kashyap, V., Rosner, R., Prosser, C., Damiani, F., Stauffer, J. and Caillault, J.-P. (1998), 'Vizier online data catalog: Rosat hri observations of the pleiades (micela+ 1999)', *VizieR Online Data Catalog* **334**, 10751.

Micela, G., Sciortino, S., Harnden Jr, F., Kashyap, V., Rosner, R., Prosser, C., Damiani, F., Stauffer, J. and Caillault, J.-P. (1999), 'Deep rosat hri observations of the pleiades', *Astronomy and Astrophysics* **341**, 751–767.

Million, C., Fleming, S. W., Shiao, B., Seibert, M., Loyd, P., Tucker, M., Smith, M., Thompson, R. and White, R. L. (2016), 'gPhoton: The GALEX Photon Data Archive', *Astrophysical Journal* **833**, 292.

Mohanty, S. and Basri, G. (2003), 'Rotation and activity in mid-m to l field dwarfs', *Astrophysical Journal* **583**(1), 451.

Monet, D. G., Levine, S. E., Canzian, B., Ables, H. D., Bird, A. R., Dahn, C. C., Guetter, H. H., Harris, H. C., Henden, A. A., Leggett, S. K., Levison, H. F., Luginbuhl, C. B., Martini, J., Monet, A. K. B., Munn, J. A., Pier, J. R., Rhodes, A. R., Riepe, B., Sell, S., Stone, R. C., Vrba, F. J., Walker, R. L., Westerhout, G., Brucato, R. J., Reid, I. N., Schoening, W., Hartley, M., Read, M. A. and Tritton, S. B. (2003), 'The USNO-B Catalog', *Astronomical Journal* **125**, 984–993.

Moore, R. L., Cirtain, J. W., Sterling, A. C. and Falconer, D. A. (2010), 'Dichotomy of Solar Coronal Jets: Standard Jets and Blowout Jets', *Astrophysical Journal* **720**, 757–770.

Moore, R. L., Sterling, A. C., Falconer, D. A. and Robe, D. (2013), 'The cool component and the dichotomy, lateral expansion, and axial rotation of solar x-ray jets', *The Astrophysical Journal* **769**(2), 134.

Moore, R. L., Sterling, A. C., Hudson, H. S. and Lemen, J. R. (2001), 'Onset of the Magnetic Explosion in Solar Flares and Coronal Mass Ejections', *Astrophysical Journal* **552**, 833–848.

Moreno-Insertis, F. and Galsgaard, K. (2013), 'Plasma Jets and Eruptions in Solar Coronal Holes: A Three-dimensional Flux Emergence Experiment', *Astrophysical Journal* **771**, 20.

Morin, J., Donati, J.-F., Petit, P., Delfosse, X., Forveille, T. and Jardine, M. (2010), 'Large-scale magnetic topologies of late m dwarfs', *Monthly Notices of the Royal Astronomical Society* **407**(4), 2269–2286.

Morris, B. M. (2020), 'A relationship between stellar age and spot coverage'.

Morris, B. M., Davenport, J. R., Giles, H. A., Hebb, L., Hawley, S. L., Angus, R., Gilman, P. A. and Agol, E. (2019), 'The solar benchmark: rotational modulation of the sun reconstructed from archival sunspot records', *Monthly Notices of the Royal Astronomical Society* **484**(3), 3244–3250.

Morris, B. M., Hebb, L., Davenport, J. R., Rohn, G. and Hawley, S. L. (2017), 'The starspots of hat-p-11: Evidence for a solar-like dynamo', *Astrophysical Journal* **846**(2), 99.

Morton, R. J., Verth, G., Jess, D. B., Kuridze, D., Ruderman, M. S., Mathioudakis, M. and Erdélyi, R. (2012), 'Observations of ubiquitous compressive waves in the sun's chromosphere', *Nature Communications* **3**(1), 1–8.

Morton, T. D. (2015), 'isochrones: Stellar model grid package', Astrophysics Source Code Library.

Mullan, D. and Houdebine, E. (2020), 'A transition of dynamo modes in m dwarfs: narrowing down the spectral range where the transition occurs', *arXiv preprint arXiv:2001.08721* .

Munari, U., Henden, A., Frigo, A., Zwitter, T., Bienaymé, O., Bland-Hawthorn, J., Boeche, C., Freeman, K. C., Gibson, B. K., Gilmore, G. et al. (2014), 'Apass landolt-sloan bvgri photometry of rave stars. i. data, effective temperatures, and reddenings', *The Astronomical Journal* **148**(5), 81.

Nagovitsyn, Y. A., Pevtsov, A. A. and Livingston, W. C. (2012), 'On a possible explanation of the long-term decrease in sunspot field strength', *Astrophysical JournalLetter* **758**(1), L20.

Namekata, K., Sakaue, T., Watanabe, K., Asai, A., Maehara, H., Notsu, Y., Notsu, S., Honda, S., Ishii, T. T., Ikuta, K. et al. (2017), 'Statistical studies of solar white-light flares and comparisons with superflares on solar-type stars', *Astrophysical Journal* **851**.

Nelson, B. E., Robertson, P. and Pritchard, S. (2015), 'An empirically derived three-dimensional laplace resonance in the gj 876 planetary system', *IAU General Assembly* **22**, 58089.

Newton, E. R., Irwin, J., Charbonneau, D., Berlind, P., Calkins, M. L. and Mink, J. (2017), 'The hα emission of nearby m dwarfs and its relation to stellar rotation', *Astrophysical Journal* **834**(1), 85.

Newton, E. R., Irwin, J., Charbonneau, D., Berta-Thompson, Z. K., Dittmann, J. A. and West, A. A. (2016), 'The Rotation and Galactic Kinematics of Mid M Dwarfs in the Solar Neighborhood', *Astrophysical Journal* **821**, 93.

Nielsen, M., Gizon, L., Schunker, H. and Karoff, C. (2013), 'Rotation periods of 12 000 main-sequence kepler stars: Dependence on stellar spectral type and comparison with v sin i observations', *Astronomy and Astrophysics* **557**, L10.

Notsu, Y., Maehara, H., Honda, S., Hawley, S. L., Davenport, J. R., Namekata, K., Notsu, S., Ikuta, K., Nogami, D. and Shibata, K. (2019), 'Do kepler superflare stars really include slowly rotating sun-like stars?—results using apo 3.5 m telescope spectroscopic observations and gaia-dr2 data', *Astrophysical Journal* **876**(1), 58.

Notsu, Y., Shibayama, T., Maehara, H., Notsu, S., Nagao, T., Honda, S., Ishii, T. T., Nogami, D. and Shibata, K. (2013), 'Superflares on solar-type stars observed with kepler ii. photometric variability of superflare-generating stars: a signature of stellar rotation and starspots', *Astrophysical Journal* **771**(2), 127.

November, L. J. and Simon, G. W. (1988), Precise proper-motion measurement of solar granulation, Technical report, AIR FORCE GEOPHYSICS LAB HANSCOM AFB MA.

Odenwald, S., Green, J. and Taylor, W. (2006), 'Forecasting the impact of an 1859-calibre superstorm on satellite resources', *Advances in Space Research* **38**(2), 280–297.

Oláh, K., Kovári, Z., Bartus, J., Strassmeier, K., Hall, D. and Henry, G. (1997), 'Time-series photometric spot modeling. iii. thirty years in the life of hk lacertae.', *Astronomy and Astrophysics* **321**, 811–821.

Onehag, A., Heiter, U., Gustafsson, B., Piskunov, N., Plez, B. and Reiners, A. (2012), 'M-dwarf metallicities. a high-resolution spectroscopic study in the near infrared', *å* **542**, A33.

Ossendrijver, M. (2003), 'The solar dynamo', *Astronomy and Astrophysics Reviews* **11**(4), 287–367.

Panesar, N. K., Sterling, A. C., Moore, R. L. and Chakrapani, P. (2016), 'Magnetic Flux Cancelation as the Trigger of Solar Quiet-region Coronal Jets', *Astrophysical Journal, Letters* **832**, L7.

Pant, V., Datta, A., Banerjee, D., Chandrashekhar, K. and Ray, S. (2018), 'Twisting/swirling motions during a prominence eruption as seen from sdo/aia', *The Astrophysical Journal* **860**(1), 80.

Parenti, S. (2014), 'Solar prominences: observations', *Living Reviews in Solar Physics* **11**(1), 1.

Pariat, E., Antiochos, S. K. and DeVore, C. R. (2009), 'A Model for Solar Polar Jets', *Astrophysical Journal* **691**, 61–74.

Parker, E. N. (1955), 'Hydromagnetic dynamo models.', *Astrophysical Journal* **122**, 293.

Parsamyan, É. and Oganyan, G. (1993), 'Spectral classification of pleiades flare stars', *Astrophysics* **36**(4), 293–305.

Pesch, P. (1968), 'Late k-and early m-dwarf stars in the hyades', *The Astrophysical Journal* **151**, 605–610.

Pesnell, W. D. (2015), *Solar dynamics observatory (SDO)*, Springer.

Pesnell, W. D., Thompson, B. J. and Chamberlin, P. C. (2012), *The Solar Dynamics Observatory (SDO)*, Springer US, New York, NY, pp. 3–15.

Pettersen, B. (1991), 'The nearby flare stars', *Memorie della Societa Astronomica Italiana* **62**, 217–242.

Phillips, K. J. (1995), *Guide to the Sun*, Cambridge University Press.

Press, W. H., Teukolsky, S. A., Vetterling, W. T. and Flannery, B. P. (1992), *Numerical recipes in C. The art of scientific computing*.

Prusti, T., De Bruijne, J., Brown, A. G., Vallenari, A., Babusiaux, C., Bailer-Jones, C., Bastian, U., Biermann, M., Evans, D., Eyer, L. et al. (2016), 'The gaia mission', *Astronomy & Astrophysics* **595**, A1.

Pucci, F. and Velli, M. (2013), 'Reconnection of quasi-singular current sheets: The "ideal" tearing mode', *The Astrophysical Journal Letters* **780**(2), L19.

Ramsay, G., Doyle, J. and Doyle, L. (2020), 'Tess observations of southern ultra fast rotating low mass stars', *Monthly Notices of the Royal Astronomical Society, submitted* .

Ramsay, G. and Doyle, J. G. (2015), 'The view from k2: questioning the traditional view of flaring on early dm stars', *Monthly Notices of the Royal Astronomical Society* **449**(3), 3015–3020.

Ramsay, G., Doyle, J. G., Hakala, P., Garcia-Alvarez, D., Brooks, A., Barclay, T. and Still, M. (2013), 'Short-duration high-amplitude flares detected on the M dwarf star KIC 5474065', *Monthly Notices of the Royal Astronomical Society* **434**, 2451–2457.

Raouafi, N., Patsourakos, S., Pariat, E., Young, P., Sterling, A., Savcheva, A., Shimojo, M., Moreno-Insertis, F., DeVore, C., Archontis, V. et al. (2016), 'Solar coronal jets: observations, theory, and modeling', *Space Science Reviews* **201**(1-4), 1–53.

Rebull, L., Stauffer, J., Bouvier, J., Cody, A., Hillenbrand, L., Soderblom, D., Valenti, J., Barrado, D., Bouy, H., Ciardi, D. et al. (2016*a*), 'Rotation in the pleiades with k2. i. data and first results', *Astrophysical Journal* **152**(5), 113.

Rebull, L., Stauffer, J., Bouvier, J., Cody, A., Hillenbrand, L., Soderblom, D., Valenti, J., Barrado, D., Bouy, H., Ciardi, D. et al. (2016*b*), 'Rotation in the pleiades with k2. ii. multiperiod stars', *Astrophysical Journal* **152**(5), 114.

Reeves, K. K., McCauley, P. I. and Tian, H. (2015), 'Direct Observations of Magnetic Recon-

nection Outflow and CME Triggering in a Small Erupting Solar Prominence', *Astrophysical Journal* **807**, 7.

Reid, I. N., Cruz, K. L., Allen, P., Mungall, F., Kilkenny, D., Liebert, J., Hawley, S. L., Fraser, O. J., Covey, K. R., Lowrance, P., Kirkpatrick, J. D. and Burgasser, A. J. (2004), 'Meeting the Cool Neighbors. VIII. A Preliminary 20 Parsec Census from the NLTT Catalogue', *Astronomical Journal* **128**, 463–483.

Reid, I. N., Cruz, K. L., Kirkpatrick, J. D., Allen, P. R., Mungall, F., Liebert, J., Lowrance, P. and Sweet, A. (2008), 'Meeting the Cool Neighbors. X. Ultracool Dwarfs from the 2MASS All-Sky Data Release', *Astronomical Journal* **136**, 1290–1311.

Reid, I. N., Gizis, J. E. and Hawley, S. L. (2002), 'The palomar/msu nearby star spectroscopic survey. iv. the luminosity function in the solar neighborhood and m dwarf kinematicsbased partly on observations made at the 60 inch (1.5 m) telescope at palomar mountain, which is jointly owned by the california institute of technology and the carnegie institution of washington.', *Astrophysical Journal* **124**(5), 2721.

Reylé, C. and Robin, A. (2004), 'New nearby stars in the liverpool-edinburgh high proper motion survey selected by denis photometry', *Astronomy and Astrophysics* **421**(2), 643–648.

Richardson, J. D. (2010), The solar wind and its interaction with the interstellar medium, *in* 'Heliophysical Processes', Springer, pp. 83–98.

Ricker, G. R., Winn, J. N., Vanderspek, R., Latham, D. W., Bakos, G. Á., Bean, J. L., Berta-Thompson, Z. K., Brown, T. M., Buchhave, L., Butler, N. R., Butler, R. P., Chaplin, W. J., Charbonneau, D., Christensen-Dalsgaard, J., Clampin, M., Deming, D., Doty, J., De Lee, N., Dressing, C., Dunham, E. W., Endl, M., Fressin, F., Ge, J., Henning, T., Holman, M. J., Howard, A. W., Ida, S., Jenkins, J. M., Jernigan, G., Johnson, J. A., Kaltenegger, L., Kawai, N., Kjeldsen, H., Laughlin, G., Levine, A. M., Lin, D., Lissauer, J. J., MacQueen, P., Marcy, G., McCullough, P. R., Morton, T. D., Narita, N., Paegert, M., Palle, E., Pepe, F., Pepper, J., Quirrenbach, A., Rinehart, S. A., Sasselov, D., Sato, B., Seager, S., Sozzetti, A., Stassun, K. G., Sullivan, P., Szentgyorgyi, A., Torres, G., Udry, S. and Villasenor, J. (2015), 'Transiting Exoplanet Survey Satellite (TESS)', *Journal of Astronomical Telescopes, Instruments, and Systems* **1**(1), 014003.

Rodono, M., Cutispoto, G., Pazzani, V., Catalano, S., Byrne, P., Doyle, J., Butler, C., Andrews, A., Blanco, C., Marilli, E. et al. (1986), 'Rotational modulation and flares on rs cvn and by dra-type stars. i-photometry and spot models for by dra, au mic, ar lac, ii peg and v 711 tau (= hr 1099)', *Astronomy and Astrophysics* **165**, 135–156.

Roettenbacher, R. M. and Vida, K. (2018), 'The connection between starspots and flares on main-sequence kepler stars', *Astrophysical Journal* **868**(1), 3.

Rosén, L., Kochukhov, O. and Wade, G. A. (2015), 'First zeeman doppler imaging of a cool star using all four stokes parameters', *Astrophysical Journal* **805**(2), 169.

Ross, F. E. (1928), 'New proper-motion stars,(sixth list)', *Astrophysical Journal* **38**, 117–120.

Route, M. (2019), 'The rise of rome. i. a multiwavelength analysis of the star–planet interaction in the hd 189733 system', *Astrophysical Journal* **872**(1), 79.

Rubenstein, E. P. and Schaefer, B. E. (2000), 'Are superflares on solar analogues caused by extrasolar planets?', *Astrophysical Journal* **529**(2), 1031.

Rust, D. M. (2001), 'A new paradigm for solar filament eruptions', *Journal of Geophysical Research: Space Physics* **106**(A11), 25075–25088.

Santos, A., Cunha, M., Avelino, P., García, R. and Mathur, S. (2017), 'Starspot signature on the light curve-learning about the latitudinal distribution of spots', *Astronomy and Astrophysics* **599**, A1.

Sarkar, R., Srivastava, N. and Dhara, S. K. (2017), 'On the dynamics of the largest active region of the solar cycle 24', *Proceedings of the International Astronomical Union* **13**(S335), 32–35.

Schaefer, B. E., King, J. R. and Deliyannis, C. P. (2000), 'Superflares on ordinary solar-type stars', *The Astrophysical Journal* **529**(2), 1026.

Scharmer, G. B., Bjelksjo, K., Korhonen, T., Lindberg, B. and Petterson, B. (2003), The 1-meter swedish solar telescope, *in* 'Proceedings of SPIE', Vol. 4853, pp. 341–350.

Scharmer, G. B., Kiselman, D., Löfdahl, M. G. and Rouppe van der Voort, L. (2003), First results from the swedish 1-m solar telescope, *in* 'Solar Polarization', Vol. 307, p. 3.

Scharmer, G. B., Narayan, G., Hillberg, T., de la Cruz Rodriguez, J., Löfdahl, M. G., Kiselman, D., Sütterlin, P., van Noort, M. and Lagg, A. (2008), 'Crisp spectropolarimetric imaging of penumbral fine structure', *The Astrophysical Journal Letters* **689**(1), L69.

Scherrer, P. H., Schou, J., Bush, R. I., Kosovichev, A. G., Bogart, R. S., Hoeksema, J. T., Liu, Y., Duvall, T. L., Zhao, J., Title, A. M., Schrijver, C. J., Tarbell, T. D. and Tomczyk, S. (2012), 'The Helioseismic and Magnetic Imager (HMI) Investigation for the Solar Dynamics Observatory (SDO)', *Solar Physics* **275**, 207–227.

Schmidt, S. J., West, A. A., Hawley, S. L. and Pineda, J. S. (2010), 'Colors and Kinematics of L Dwarfs from the Sloan Digital Sky Survey', *Astronomical Journal* **139**, 1808–1821.

Schmieder, B., Démoulin, P. and Aulanier, G. (2013), 'Solar filament eruptions and their physical role in triggering coronal mass ejections', *Advances in Space Research* **51**(11), 1967–1980.

Scholz, A., Irwin, J., Bouvier, J., Sipőcz, B. M., Hodgkin, S. and Eislöffel, J. (2011), 'Rotation periods for very low mass stars in praesepe', *Monthly Notices of the Royal Astronomical Society* **413**(4), 2595–2605.

Schrijver, C. J. and Title, A. M. (2001), 'On the Formation of Polar Spots in Sun-like Stars', *Astrophysical Journal* **551**, 1099–1106.

Scullion, E., Popescu, M., Banerjee, D., Doyle, J. G. and Erdélyi, R. (2009), 'Jets in polar coronal holes', *Astrophysical Journal* **704**(2), 1385.

See, V., Matt, S. P., Folsom, C. P., Saikia, S. B., Donati, J.-F., Fares, R., Finley, A. J., Hébrard, É. M., Jardine, M. M., Jeffers, S. V. et al. (2019), 'Estimating magnetic filling factors from zeeman–doppler magnetograms', *The Astrophysical Journal* **876**(2), 118.

Semel, M. (1989), 'Zeeman-doppler imaging of active stars. i-basic principles', *Astronomy and Astrophysics* **225**, 456–466.

Shapiro, A. V., Shapiro, A. I., Gizon, L., Krivova, N. A. and Solanki, S. K. (2020), 'Solar-cycle irradiance variations over the last four billion years'.

Shibata, K., Ishido, Y., Acton, L., Strong, K., Hirayama, T., Uchida, Y., Mcallister, A., Matsumoto, R., Tsuneta, S., Shimizu, T. et al. (1993), Observations of x-ray jets using yohkoh soft x-ray telescope, *in* 'International Astronomical Union Colloquium', Vol. 141, Cambridge University Press, pp. 343–346.

Shibata, K., Isobe, H., Hillier, A., Choudhuri, A. R., Maehara, H., Ishii, T. T., Shibayama, T., Notsu, S., Notsu, Y., Nagao, T. et al. (2013), 'Can superflares occur on our sun?', *Publications of the ASJ* **65**(3), 49.

Shibata, K. and Magara, T. (2011), 'Solar flares: magnetohydrodynamic processes', *Living Reviews in Solar Physics* **8**(1), 6.

Shibata, K., Nitta, N., Strong, K., Matsumoto, R., Yokoyama, T., Hirayama, T., Hudson, H. and Ogawara, Y. (1994), 'A gigantic coronal jet ejected from a compact active region in a coronal hole', *The Astrophysical Journal* **431**, L51–L53.

Shibata, K. and Uchida, Y. (1986), 'Sweeping-magnetic-twist mechanism for the acceleration of jets in the solar atmosphere', *Solar Physics* **103**, 299–310.

Shibayama, T., Maehara, H., Notsu, S., Notsu, Y., Nagao, T., Honda, S., Ishii, T. T., Nogami, D. and Shibata, K. (2013), 'Superflares on solar-type stars observed with kepler. i. statistical properties of superflares', *The Astrophysical Journal Supplement Series* **209**(1), 5.

Shimojo, M., Hashimoto, S., Shibata, K., Hirayama, T., Hudson, H. S. and Acton, L. W. (1996), 'Statistical study of solar x-ray jets observed with the yohkoh soft x-ray telescope', *Publications of the Astronomical Society of Japan* **48**, 123–136.

Shkolnik, E., Liu, M. C. and Reid, I. N. (2009), 'Identifying the young low-mass stars within 25 pc. i. spectroscopic observations', *The Astrophysical Journal* **699**(1), 649.

Shulyak, D., Reiners, A., Nagel, E., Tal-Or, L., Caballero, J., Zechmeister, M., Béjar, V., Cortés-Contreras, M., Martin, E., Kaminski, A. et al. (2019), 'Magnetic fields in m dwarfs from the carmenes survey', *Astronomy and Astrophysics* **626**, A86.

Shulyak, D., Seifahrt, A., Reiners, A., Kochukhov, O. and Piskunov, N. (2011), 'Rotation, magnetism and metallicity of m dwarf systems', *Monthly Notices of the Royal Astronomical Society* **418**(4), 2548–2557.

Silva, A. V. R. (2003), 'Method for Spot Detection on Solar-like Stars', *Astrophysical Journal, Letters* **585**, L147–L150.

Silverberg, S. M., Kowalski, A. F., Davenport, J. R. A., Wisniewski, J. P., Hawley, S. L. and Hilton, E. J. (2016), 'Kepler Flares. IV. A Comprehensive Analysis of the Activity of the dM4e Star GJ 1243', *Astrophysical Journal* **829**, 129.

Soderblom, D. R., Stauffer, J. R., Hudon, J. D. and Jones, B. F. (1993), 'Rotation and chromospheric emission among f, g, and k dwarfs of the pleiades', *Astrophysical Journal, Supplement* **85**, 315–346.

Solanki, S. (1999), Spots and plages: the solar perspective, *in* 'Solar and Stellar Activity: Similarities and Differences', Vol. 158, p. 109.

Solanki, S. K. (2003), 'Sunspots: an overview', *The Astronomy and Astrophysics Review* **11**(2-3), 153–286.

Srivastava, A. K., McIntosh, S. W., Arge, N., Banerjee, D., Cliver, E., Dikpati, M., Dwivedi, B. N., Guhathakurta, M., Karak, B., Leamon, R. J. et al. (2018), 'The extended solar cycle: Muddying the waters of solar/stellar dynamo modeling or providing crucial observational constraints?', *Frontiers in Astronomy and Space Sciences* **5**, 38.

Stassun, K. G., Oelkers, R. J., Pepper, J., Paegert, M., De Lee, N., Torres, G., Latham, D. W., Charpinet, S., Dressing, C. D., Huber, D. et al. (2018), 'The tess input catalog and candidate target list', *The Astronomical Journal* **156**(3), 102.

Stauffer, J. R., Hartmann, L. W., Fazio, G. G., Allen, L. E., Patten, B. M., Lowrance, P. J., Hurt, R. L., Rebull, L. M., Cutri, R. M., Ramirez, S. V. et al. (2007), 'Near-and mid-infrared photometry of the pleiades and a new list of substellar candidate members', *Astrophysical Journal, Supplement* **172**(2), 663.

Stauffer, J. R., Hartmann, L. W., Prosser, C. F., Randich, S., Balachandran, S., Patten, B. M., Simon, T. and Giampapa, M. (1997), 'Rotational velocities and chromospheric/coronal activity of low-mass stars in the young open clusters ic 2391 and ic 2602', *Astrophysical Journal* **479**(2), 776.

Steenbeck, M., Krause, F. and Rädler, K.-H. (1966), 'Berechnung der mittleren lorentz-feldstärke für ein elektrisch leitendes medium in turbulenter, durch coriolis-kräfte beeinflußter bewegung', *Zeitschrift für Naturforschung A* **21**(4), 369–376.

Stelzer, B., Damasso, M., Scholz, A. and Matt, S. P. (2016), 'A path towards understanding the rotation–activity relation of m dwarfs with k2 mission, x-ray and uv data', *Monthly Notices of the Royal Astronomical Society* **463**(2), 1844–1864.

Stephenson, C. (1986*a*), 'Dwarf k and m stars of high proper motion found in a hemispheric survey', *The Astronomical Journal* **92**, 139–165.

Stephenson, C. B. (1986*b*), 'Late m stars found in a hemispheric survey', *The Astrophysical Journal* **301**, 927–937.

Sterling, A. C. and Moore, R. L. (2005), 'Slow-rise and fast-rise phases of an erupting solar filament, and flare emission onset', *The Astrophysical Journal* **630**(2), 1148.

Sterling, A. C., Moore, R. L., Falconer, D. A. and Adams, M. (2015), 'Small-scale filament eruptions as the driver of X-ray jets in solar coronal holes', *Nature* **523**(7561), 437–440.

Strassmeier, K. G. (1996), Observational evidence for polar spots, *in* 'Symposium-International Astronomical Union', Vol. 176, Cambridge University Press, pp. 289–298.

Strassmeier, K. G. (2009), 'Starspots', *Astronomy and Astrophysics Reviews* **17**(3), 251–308.

Sun, X., Hoeksema, J. T., Liu, Y., Aulanier, G., Su, Y., Hannah, I. G. and Hock, R. A. (2013), 'Hot spine loops and the nature of a late-phase solar flare', *The Astrophysical Journal* **778**(2), 139.

Tayler, R. J. (1997), *The Sun as a star*, Cambridge University Press.

Taylor, M. B. (2006), STILTS - A Package for Command-Line Processing of Tabular Data, *in* C. Gabriel, C. Arviset, D. Ponz and S. Enrique, eds, 'Astronomical Data Analysis Software and Systems XV', Vol. 351 of *Astronomical Society of the Pacific Conference Series*, p. 666.

Toledo-Padrón, B., González Hernández, J., Rodríguez-López, C., Suárez Mascareño, A., Rebolo, R., Butler, R., Ribas, I., Anglada-Escudé, G., Johnson, E., Reiners, A. et al. (2019),

'Stellar activity analysis of barnard's star: very slow rotation and evidence for long-term activity cycle', *Monthly Notices of the Royal Astronomical Society* **488**(4), 5145–5161.

Török, T. and Kliem, B. (2005), 'Confined and Ejective Eruptions of Kink-unstable Flux Ropes', *Astrophysical Journal, Letters* **630**(1), L97–L100.

Tregloan-Reed, J. and Unda-Sanzana, E. (2019), 'Simulations of starspot anomalies within tess exoplanetary transit light curves-i. detection limits of starspot anomalies in tess light curves', *Astronomy & Astrophysics* **630**, A114.

Tritschler, A., Rimmele, T., Berukoff, S., Casini, R., Craig, S., Elmore, D., Hubbard, R., Kuhn, J., Lin, H., McMullin, J. et al. (2015), Dkist: observing the sun at high resolution, *in* '18th Cambridge Workshop on Cool Stars, Stellar Systems and the Sun', pp. 933–944.

Tu, C.-Y., Zhou, C., Marsch, E., Xia, L.-D., Zhao, L., Wang, J.-X. and Wilhelm, K. (2005), 'Solar wind origin in coronal funnels', *Science* **308**(5721), 519–523.

Tu, Z.-L., Yang, M., Zhang, Z. and Wang, F. (2020), 'Superflares on solar-type stars from the first year observation of tess', *The Astrophysical Journal* **890**(1), 46.

Van Cleve, J. E., Howell, S. B., Smith, J. C., Clarke, B. D., Thompson, S. E., Bryson, S. T., Lund, M. N., Handberg, R. and Chaplin, W. J. (2016), 'That's How We Roll: The NASA K2 Mission Science Products and Their Performance Metrics', *Publications of the ASP* **128**(7), 075002.

Van den Oord, G., Byrne, P. and Eibe, M. (1998), Prominence-like clouds near hk aqr, *in* 'International Astronomical Union Colloquium', Vol. 167, Cambridge University Press, pp. 251–254.

Van Leeuwen, F. (2007), 'Validation of the new hipparcos reduction', *Astronomy & Astrophysics* **474**(2), 653–664.

Van Noort, M., Van Der Voort, L. R. and Löfdahl, M. G. (2005), 'Solar image restoration by use of multi-frame blind de-convolution with multiple objects and phase diversity', *Solar Physics* **228**(1-2), 191–215.

Vanderburg, A. and Johnson, J. A. (2014), 'A Technique for Extracting Highly Precise Photometry for the Two-Wheeled Kepler Mission', *Publications of the ASP* **126**, 948.

VanderPlas, J. T. and Ivezic, Ž. (2015), 'Periodograms for multiband astronomical time series', *Astrophysical Journal* **812**(1), 18.

Vida, K., Oláh, K., Kővári, Z., van Driel-Gesztelyi, L., Moór, A. and Pál, A. (2019), 'Flaring activity of proxima centauri from tess observations: Quasiperiodic oscillations during flare decay and inferences on the habitability of proxima b', *The Astrophysical Journal* **884**(2), 160.

Vissers, G. and Van Der Voort, L. R. (2012), 'Flocculent flows in the chromospheric canopy of a sunspot', *The Astrophysical Journal* **750**(1), 22.

Walker, A. R. (1981), 'Flare activity of proxima centauri', *Monthly Notices of the Royal Astronomical Society* **195**(4), 1029–1035.

Weber, M., Deluca, E., Golub, L. and Sette, A. (2004), 'Temperature diagnostics with multichannel imaging telescopes', *Proceedings of the International Astronomical Union* **2004**(IAUS223), 321–328.

West, A. A., Morgan, D. P., Bochanski, J. J., Andersen, J. M., Bell, K. J., Kowalski, A. F., Davenport, J. R., Hawley, S. L., Schmidt, S. J., Bernat, D. et al. (2011), 'The sloan digital sky survey data release 7 spectroscopic m dwarf catalog. i. data', *The Astronomical Journal* **141**(3), 97.

West, F. R. (2001), 'Letter to the editor favorable times predicted for searching for transits of gliese 876= il aquarii by its giant planets', *JAAVSO* **29**, 151.

Wheatley, P. J., Pollacco, D. L., Queloz, D., Rauer, H., Watson, C. A., West, R. G., Chazelas, B., Louden, T. M., Bannister, N., Bento, J., Burleigh, M., Cabrera, J., Eigmüller, P., Erikson, A., Genolet, L., Goad, M., Grange, A., Jordán, A., Lawrie, K., McCormac, J., Neveu, M. and Walker, S. (2014), Next Generation Transit Survey (NGTS), *in* M. Booth, B. C. Matthews and J. R. Graham, eds, 'Exploring the Formation and Evolution of Planetary Systems', Vol. 299 of *IAU Symposium*, pp. 311–312.

Wheatley, P. J., West, R. G., Goad, M. R., Jenkins, J. S., Pollacco, D. L., Queloz, D., Rauer, H., Udry, S., Watson, C. A., Chazelas, B. et al. (2017), 'The next generation transit survey (ngts)', *Monthly Notices of the Royal Astronomical Society* **475**(4), 4476–4493.

Willis, D. M. and Stephenson, F. R. (2001), 'Solar and auroral evidence for an intense recurrent geomagnetic storm during december in ad 1128'.

Wilson, P., Altrocki, R., Harvey, K., Martin, S. and Snodgrass, H. (1988), 'The extended solar activity cycle', *Nature* **333**(6175), 748.

Winters, J. G., Henry, T. J., Lurie, J. C., Hambly, N. C., Jao, W.-C., Bartlett, J. L., Boyd, M. R., Dieterich, S. B., Finch, C. T., Hosey, A. D. et al. (2014), 'The solar neighborhood. xxxv. distances to 1404 m dwarf systems within 25 pc in the southern sky', *The Astronomical Journal* **149**(1), 5.

Wolf, C., Onken, C. A., Luvaul, L. C., Schmidt, B. P., Bessell, M. S., Chang, S.-W., Da Costa, G. S., Mackey, D., Martin-Jones, T., Murphy, S. J. et al. (2018), 'Skymapper southern survey: First data release (dr1)', *Publications of the Astronomical Society of Australia* **35**.

Woods, T., Eparvier, F., Hock, R., Jones, A., Woodraska, D., Judge, D., Didkovsky, L., Lean, J., Mariska, J., Warren, H. et al. (2010), Extreme ultraviolet variability experiment (eve) on the solar dynamics observatory (sdo): Overview of science objectives, instrument design, data products, and model developments, *in* 'The Solar Dynamics Observatory', Springer, pp. 115–143.

Wright, N. J., Drake, J. J., Mamajek, E. E. and Henry, G. W. (2011), 'The stellar-activity-rotation relationship and the evolution of stellar dynamos', *Astrophysical Journal* **743**(1), 48.

Wyper, P., DeVore, C., Karpen, J. and Lynch, B. (2016), 'Three-dimensional simulations of tearing and intermittency in coronal jets', *Astrophysical Journal* **827**(1), 4.

Wyper, P. F., Antiochos, S. K. and DeVore, C. R. (2017), 'A universal model for solar eruptions', *Nature* **544**, 452–455.

Wyper, P. F., DeVore, C. R. and Antiochos, S. K. (2018), 'A Breakout Model for Solar Coronal Jets with Filaments', *Astrophysical Journal* **852**, 98.

Yadav, R. K., Gastine, T., Christensen, U. R. and Reiners, A. (2015), 'Formation of starspots in self-consistent global dynamo models: Polar spots on cool stars', *Astronomy and Astrophysics* **573**, A68.

Yang, H., Liu, J., Gao, Q., Fang, X., Guo, J., Zhang, Y., Hou, Y., Wang, Y. and Cao, Z. (2017), 'The flaring activity of m dwarfs in the kepler field', *Astrophysical Journal* **849**(1), 36.

Yang, S. and Zhang, J. (2018), 'Mini-filament Eruptions Triggering Confined Solar Flares Observed by ONSET and SDO', *Astrophysical Journal, Letters* **860**, L25.

Young, P. and Muglach, K. (2014), 'Solar dynamics observatory and hinode observations of a blowout jet in a coronal hole', *Solar Physics* **289**(9), 3313–3329.

Zacharias, N., Finch, C., Girard, T., Henden, A., Bartlett, J., Monet, D. and Zacharias, M. (2012), 'Vizier online data catalog: Ucac4 catalogue (zacharias+, 2012)', *VizieR Online Data Catalog* **1322**, 0.

Zacharias, N., Finch, C., Girard, T., Henden, A., Bartlett, J., Monet, D. and Zacharias, M. (2013), 'The fourth us naval observatory ccd astrograph catalog (ucac4)', *The Astronomical Journal* **145**(2), 44.

Zechmeister, M. and Kürster, M. (2009), 'The generalised Lomb-Scargle periodogram. A new formalism for the floating-mean and Keplerian periodograms', *Astronomy and Astrophysics* **496**, 577–584.

Zhou, Z., Cheng, X., Zhang, J., Wang, Y., Wang, D., Liu, L., Zhuang, B. and Cui, J. (2019), 'Why do torus-unstable solar filaments experience failed eruptions?', *The Astrophysical Journal* **877**(2), L28.

Zirin, H. and Liggett, M. A. (1982), 'Delta spots and great flares', *Solar Physics* **113**(1-2), 267–283.